A multiscale systems pharmacology framework to assess the prophylactic utility of antivirals against HIV-1

Dissertation
zur Erlangung des Grades eines
Doktors der Naturwissenschaften (Dr. rer. nat.)

am Fachbereich Mathematik und Informatik
der Freie Universität Berlin

vorgelegt von

Sulav Duwal

Berlin, 2018

Betreuer:	**Dr. Max von Kleist**	(Freie Universität Berlin)
Erstgutachter:	**Dr. Max von Kleist**	(Freie Universität Berlin)
Zweitgutachterin:	**Prof. Susanna Röblitz**	(University of Bergen)
Drittgutachter:	**Prof. Christof Schütte**	(Freie Universität Berlin)

Tag der Disputation: 18. Dezember 2018

Acknowledgements

First and foremost, I would like to thank my supervisor, Dr. Max von Kleist for introducing me to the amazing field of HIV research & systems pharmacology and for nurturing my interest. He shared his passion with me and what began as a bachelor's thesis led to the master's and finally to this doctoral thesis, where I could appreciate the breadth and depth of many topics. I am very grateful for his continuous guidance and support throughout my journey, and for many memorable times, which I would cherish forever.

I thank Vikram, Wei and Stefanie for their time and collaborations. I wish to thank Akil Jackson for connecting us to our collaboration partners. I had a great pleasure collaborating with Laura Dickinson and Saye Khoo and I am thankful to them. I am very grateful to Han for proofreading parts of the thesis and for providing me valuable feedbacks. I thank Maureen and Lisa for proofreading the German summary of my work.

The Biocomputing group at the Freie Universität Berlin occupies a special place in my heart. I literally grew up here. I thank the members of the Biocomputing Group for the wonderful time. Many of them allowed me into their lives and became friends. I owe a special thanks to Kaveh, Maureen and Stefan (klein) for being there for all sort of things. I thank Nada, Evgenia, Marjan, Han, Johnny, Christian, Nadya, Patrick, Stefan (groß), Vikram, Victor, Illusi, Pooja, Wei, Kasia and Iurii for their friendships. I would cherish all those winter seminars, Berlin Philharmonic, karaoke evenings, mensa, coffee breaks and parties.

I am thankful to Prof. Christof Schütte for writing many recommendation letters. My sincere gratitude goes to Dr. Andreas Reichel for mentoring me as a master student and for encouraging me. I would like to thank Prof. Charlotte Kloft and Prof. Wilhelm Huisinga for the opportunity to join the PharMetrX graduate research training program. The time in the graduate program not only broadened and deepened my knowledge in the field but also allowed me to have many friends. I thank many friends of PharMetrX, especially Lisa, Imke, Mohammed, Katrin, Miro and Niklas. I would cherish all those PAGE conferences, cooking evenings, modelling nights and making through tough times together.

I thank my family for their relentless love, encouragement and understanding. They are my driving force. I owe a special thanks to my wife Krisha for her love and encouragement during the writing process. I feel that the words in my thesis are mine, but the energy is hers. I owe everything to my parents. The education they provided me, their support even when they barely grasp what I am doing, and their unwavering love and kindness made all this possible.

Dedicated to my grandparents and parents

Contents

CHAPTER 1

Introduction

Since the discovery of AIDS (Acquired immune deficiency syndrome) in 1981, approximately 35 million people have died from AIDS, and 36.7 million people currently live with an HIV infection, as of 2016 [1, 2]. Evidently, the HIV epidemic still poses a global risk. Despite these depressing numbers, impressive advances in drug development have been made, which have resulted in more than 25 antiretrovirals being approved for HIV treatment. These antiretrovirals belong to four major drug classes, namely entry inhibitors, reverse transcriptase inhibitors, integrase inhibitors and protease inhibitors [3]. Antiretroviral therapy has significantly reduced the mortality and morbidity of HIV infection. A proper utilization of these antiretrovirals can render HIV a chronic manageable disease, with the expected lifespan of an infected person approaching that of the general population [4]. However, the accessibility of antivirals even in resource-rich countries is not universal [5] and the financial burden of the life-long treatment is immense. In fact, the situation is even more dire, since 95% of people with HIV live in resource-constrained countries with very limited access to HIV treatment [6]. Moreover, for every infected person starting an antiretroviral treatment, there are two new infections [7], a situation which is clearly not sustainable. Ideally, a scalable effective vaccine or a complete cure could bring an end to the epidemic. Unfortunately, despite arduous efforts, the development of an effective vaccination has largely remained elusive due to the genetic variability of HIV and its capacity to evade the immune system. Though a modest success has been achieved by the RV144 clinical trial with a vaccine efficacy of 31% [8, 9], further research and improvements are required to deliver a viable effective vaccine [6].

In 2009, a remarkable case study reported an HIV infected person, who was treated for leukaemia and was completely cured of HIV [10]. The patient was dubbed 'Berliner patient'. However, subsequent attempts to cure infected individuals have failed [11]. These attempts highlight that a number of factors contributed to the successful cure of Berliner patient [12], and that in their entirety, these factors are not well understood. Evidently, more research is warranted to achieve a scalable functional cure.

While the search for a cure and a vaccine continues, preventing new infections is of paramount importance. In addition to raising awareness, the increased use of condoms, voluntary male circumcisions, and other methods, two antiretroviral-based prophylactic strategies have been recognized as important cornerstones for controlling the epidemic. The first antiretroviral-based strategy is known as 'treatment-as-prevention' and it focuses on infected individuals. It involves initiating treatment in an infected person shortly after infection [13]. As a consequence, the viral load of the treated individual decreases, which also decreases the contagiousness of the infected individual [14, 15]. The strategy was selected as the breakthrough of the year 2011 [16]. However, the preventive benefits of treatment-as-prevention may be difficult to achieve in practice, as individuals are unaware of their serostatus shortly after an infection and at the same time, they have high

viral loads and consequently are very contagious [2]. Secondly, inadequate viral suppression in the infected treated individuals, due to lack of adherence and development of viral resistance, also dampens its epidemiologic impact [2].

Some of these drawbacks mentioned above can be overcome by another antiretroviral-based prophylactic strategy known as pre-exposure prophylaxis (PrEP). This strategy involves antiviral drug administration to uninfected individuals at high risk of acquiring an HIV infection [17]. Recently, UNAIDS has recognized PrEP as one of its five pillars for reducing new infections to less than 500,000 by 2020 [2]. Truvada (emtricitabine-tenofovir disoproxil fumarate) is currently the only medication approved for PrEP. Despite its several advantages, truvada is not ideal. To improve PrEP, many next-generation regimens, including long-acting formulations, are being investigated as suitable candidates for PrEP [18]. However, most of them are patent-protected compounds and thus are expensive. The question arises whether there are patent-expired antivirals that can be repurposed as cost-effective alternatives for PrEP use and how to design roll-out schemes for these antivirals.

Necessity/Aim/Challenge of the study: Assessment of the prophylactic utility of antivirals concerns viral dynamics shortly after a viral exposure. Experimental investigation of the viral dynamics shortly after an exposure poses difficulties: These derive from the fact that most of the recently infected persons are unaware of their infections. In addition, not every exposure leads to an infection owing to the fact that HIV transmission is an inefficient stochastic process [19]. Hence, detailed studies require observing a large number of people and examining them shortly after an exposure, which is very difficult, notwithstanding ethical issues. Additionally, there is no appropriate biomarker for an exposure. Initially, although viral replication might be occurring, the assays are unable to detect the viral activity. By the time, viruses can be detected, the infection has established itself. Hence, biomarkers and assays are not available to study exposures that fail to lead to an infection.

Animal models used to study HIV transmission are insightful, but they are of limited use due to several issues [20], including physiological differences between the animal and the human, the respective viruses [21], differences between experiment set-ups and real-life scenarios. Besides being difficult to obtain, *ex vivo* human explant models also do not fully recapitulate the *in vivo* systemic infection [22]. These pre-clinical testings may not guide candidate selection, since they often fail to translate into the clinical efficacy. Undoubtedly, human clinical trials for PrEP can provide answers. However, quantifying the prophylactic efficacy in a clinical trial is ethically problematic and necessitates conducting long and large trials that require monitoring thousands of individuals over several years. This makes the systematic evaluation of candidates and deployment strategies prohibitively costly. In light of the fact that there are currently more than 25 antivirals approved for HIV treatment, several novel formulations and numerous ways to deploy them, tools are urgently needed that can reliably and rapidly determine the prophylactic utility of antivirals to prioritize candidates and to design roll-out strategies.

Despite HIV being among the most well-studied pathogens and a long history of mathematical modelling and simulation of HIV dynamics, there is a dearth of mathematical frameworks to investigate the prophylactic utility of antivirals. To this end, we intend to build a mathematical framework (pipeline) to serve as a tool to predict the prophylactic utility of antivirals. Building such a framework for PrEP is a challenging task, which requires solving modelling and simulation problems owing to the various complex processes occurring at different scales (multiscale). Since PrEP involves antiretroviral administration to an uninfected person at high risk, the framework requires modelling the time evolution of drug concentration, especially at its target-site (pharmacokinetics), viral dynamics (pharmacodynamics) shortly after a viral challenge and, if possible, molecular interactions between the pharmacologically active drug moiety and viral components.

Furthermore, it requires modelling the HIV transmission from an infected donor to an uninfected recipient. Besides these modelling questions, appropriate mathematical algorithms for simulation are required since purely deterministic approaches cannot account for the stochasticity of viral replications shortly after a challenge.

Outline of the work: We begin by providing a brief biological background on HIV in Chapter 2. In Chapter 3 and Chapter 4, we provide a concise mathematical background that introduces the state-of-art methods on simulation of coupled chemical systems and model building respectively. These chapters are intended to introduce the reader to the topic, but are far from being exhaustive and comprehensive. From Chapter 5 to Chapter 8, we provide the reasoning and development of various modules of the modelling and simulation framework in detail. In Chapter 9, we provide insights and predictions for various antiretrovirals regarding their prophylactic utility obtained from the developed framework. Finally, in Chapter 10 we discuss the results, summarize main conclusions and provide some future perspectives on this work. The various modules of the framework and related chapters are schematically depicted in the Graphical abstract below (Figure 1.1).

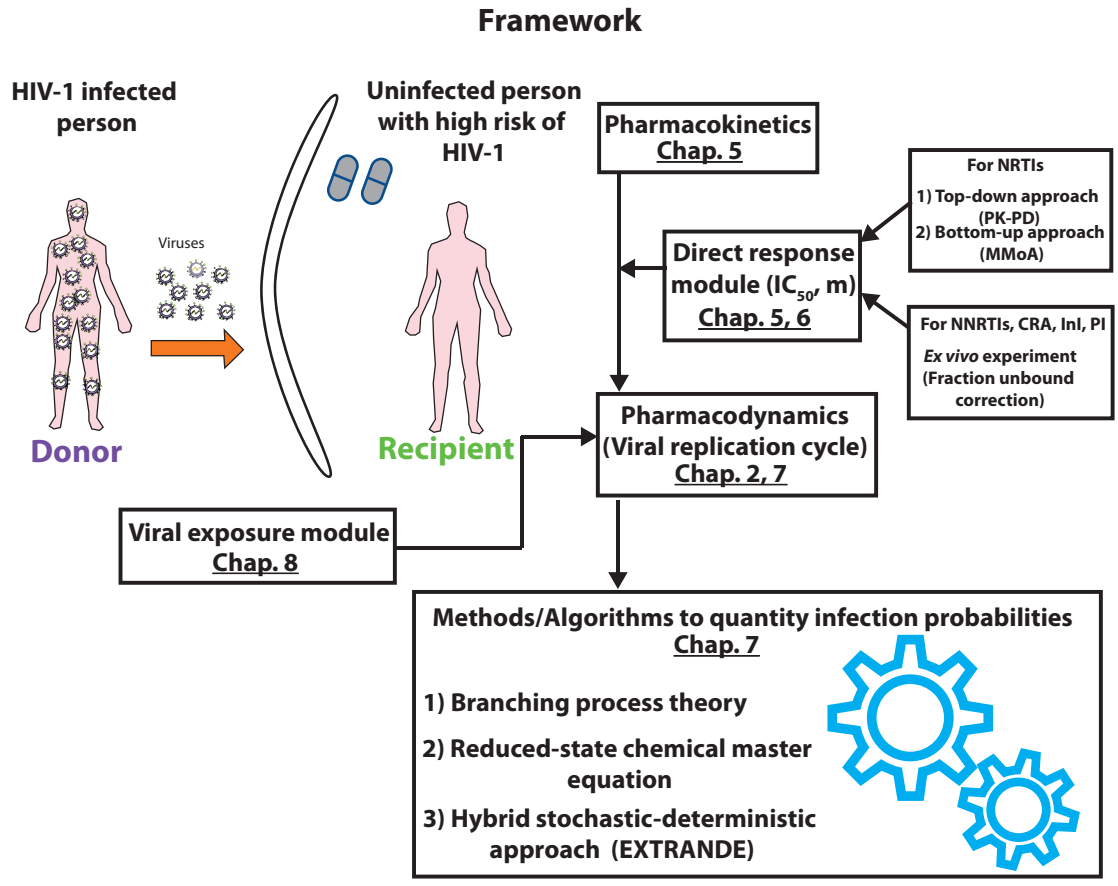

Figure 1.1: **Scheme of the multiscale systems pharmacology framework to predict the prophylactic utility of antivirals:** Various modules of the framework and related chapters.

This manuscript is based on the following publications: In the article [23], we employed 'top-down' (classical pharmacokinetic-pharmacodynamic modelling) and 'bottom-up' (molecular mechanism of action) approaches to predict *in vivo* drug potencies for nucleoside reverse transcriptase inhibitors (NRTIs), namely lamivudine (3TC), emtricitabine (FTC) and tenofovir (TFV).

We compared drug potency predictions from the top-down approach with predictions from the bottom-up approach for its validation, which was previously developed by von Kleist et al. [24].

In the article [25], we presented the multiscale systems pharmacology framework that integrates processes occurring at various scales including; 1) microscale interactions of active moiety of NRTIs with viral DNA polymerization; 2) meso- and macroscale processes, such as the drug pharmacokinetics, viral replication dynamics; and 3) population scale processes, such as viral exposure and long-term infection probabilities after repeated virus exposures, similar to a clinical trial. We used the framework to benchmark various NRTIs with a special focus on 3TC, FTC and TFV. Furthermore, we developed reduced-state viral dynamics model to circumvent the curse of dimensionality encountered in the chemical master equation (CME) approach.

We further extended the framework in articles [26, 27]. In the article [27], we employed the theory of branching processes to derive drug-class specific concentration-prophylaxis curves and to benchmark all treatment approved antivirals except NRTIs. In the article [26], we utilized the recently developed, numerically exact EXTRANDE (extra reaction algorithm for networks in a dynamic environment) algorithm [28] for simulations. The EXTRANDE algorithm is a Monte Carlo algorithm based on thinning techniques, which can also circumvent the dimensionality problem in the CME approach. Moreover, we tailored the algorithm to improve its run-time and accuracy. We used the framework to assess various deployment scenarios for dolutegravir, an integrase inhibitor which has not been hitherto tested for PrEP.

The content of the article [15] is not included in this manuscript. The article addresses the important issue of drug resistance encountered in treatment-as-prevention. Development of drug resistance in treated infected individuals can undermine the impact of treatment-as-prevention, hence treatments should be designed to avoid or delay the drug resistance development. To this end, we employed the optimal control theory to optimize and compare two distinct approaches for the treatment of HIV-1: (i) a diagnostic-guided treatment strategy, based on infrequent and patient-specific diagnostic schedules and (ii) a pro-active strategy that allows treatment adaptation prior to diagnostic ascertainment.

CHAPTER 2

HIV in a nutshell

In this chapter, we briefly present the biological background on HIV, the time course of an HIV-1 infection in a host, various antiretroviral classes and the development of mathematical models of HIV-1 dynamics.

2.1 Origin of the HIV epidemic

In 1981, a new disease was discovered that was characterized by the severe impairment of the immune system. It was termed acquired immune deficiency syndrome (AIDS). The causative agent of the disease was first discovered by Francoise Barre-Sinousse and Luc Montagnier in 1983 and subsequently by Robert Gallo's team [29, 30]. Initially, Gallo named the virus HTLV-III, whereas Montagnier's group coined the name LAV (lymphadenopathy-associated virus) for the virus. The nomenclature HIV (human immunodeficiency virus) was later agreed. Francoise Barre-Sinousse and Luc Montagnier received Nobel prize for the discovery of the virus [30].

HIV is closely related to HTLV-I and HTLV-II viruses previously discovered by Gallo's team [30]. HIV is a retrovirus, which means that its genome is in form of RNA instead of DNA. During its life cycle, the information in its genomic RNA is transcribed to DNA. The process is known as reverse transcription and at the time of its discovery, it was in direct challenge to the central dogma in the molecular biology that the information flows from DNA to RNA and from RNA to protein[I].

Though HIV was first recognized in 1983, HIV first emerged in human in the early decades of the 1900s in countries in Congo River basin [31, 32]. HIV originated from cross-species transmission of simian immunodeficiency virus (SIV) from non-human primates into humans in West and Central Africa [31]. More than 40 different non-human primate species including Gorilla and Chimpanzee have been identified harbouring SIV infections in those regions [33]. SIV is largely nonpathogenic in their natural host [34]. Cross-species transmission in human is mostly likely the result of contacts with infected blood or tissues of non-human primates in the process of hunting, butchering and keeping them as pets.

Evidences strongly suggest the occurrence of multiple independent cross-species transmissions. HIV-1 group M and N originated directly, but independently, from SIV found in chimpanzee. SIV itself emerged in Chimpanzee through recombination between SIV from red-capped mangabeys and greater spot-nosed monkeys [31]. Moreover, SIV has been recently found to be pathogenic in chimpanzee indicating that they recently acquired SIV [35]. This is further supported by the absence of SIV in two of four subspecies in chimpanzee [34]. The origin of HIV-1 group O is not completely resolved and can have either gorilla or chimpanzee origin, whereas

[I] Howard Temin and David Baltimore won the nobel prize for the discovery of reverse transcription [30].

HIV-1 group P has gorilla origin [34] [II]. HIV-2 is distantly related to HIV-1 and has originated from SIV found in sooty mangabeys monkey.

HIV-1 group M is the oldest lineage and is responsible for the global pandemic, whereas HIV-1 groups N, O and P and HIV-2 are mostly localized in West-Central Africa and non-pandemic. Analysis by Faria et al. [32] suggested that the spatial origin of HIV-1 group M is mostly likely in Kinshasa in Democratic Republic of Congo. Initially, HIV-1 group M remained large localized. Extensive use of the river system for transport and development of railway networks combined with population growth facilitated the spread of HIV-1 group M throughout the region [32]. Furthermore, a mutation in vpu gene of HIV-1 group M conferred a decisive advantage in comparison to other groups to become a global pandemic [37].

Currently, HIV-1 group M is classified into nine subtypes (A-D,F-H,J,K) and several circulating recombinant forms [34]. HIV-1 subtype C spread to South Africa and from there onward to India and other Asian countries, whereas HIV-1 group M subtype B spread to Haiti and onwards to US and other western countries [38] [III]. HIV-1 subtype B is most widely distributed [38], whereas HIV-1 subtype C is most prevalent accounting for 56 % of all the infections [36].

2.2 HIV biology

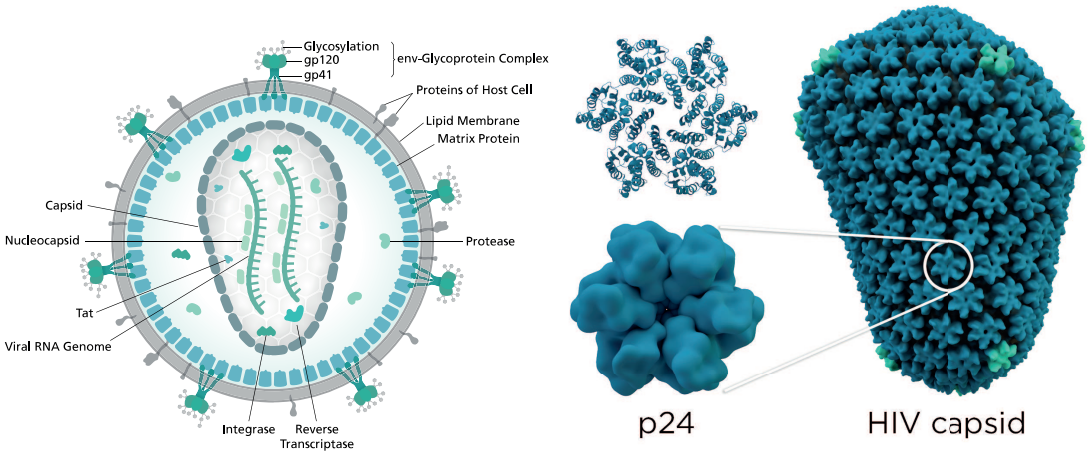

Figure 2.1: **Schematic depiction of a HIV particle and its capsid:** The leftmost panel illustrates the structure of HIV-1 particle. The outerlayer envelope of HIV-1 is of host-cell origin which is interspersed by the viral glycoprotein gp-120 and gp-41 necessary for binding with CD4 receptor and co-receptors (CCR5 and CX4). The inner layer of the envelope is made of viral matrix protein. The asymmetrical conical core of the virus particle is known as capsid. The capsid encloses the viral RNA genome, tRNAs, nucleocapsids and other enzymes. Extracted from Wikimedia [40]. The rightmost panel depicts the capsid which is made of hexamers and pentamers of p24 capsid proteins. Extracted from Wikimedia [41].

A HIV-1 particle consists of two copies of the positive sense genomic viral RNA, cellular $tRNA^{Lys3}$, viral envelope proteins, the GAG polyprotein and the three viral enzymes, namely protease, reverse transcriptase and integrase [42]. The leftmost panel in Figure 2.1 illustrates the structure of virus particle. Like all retroviruses, the two RNA copies of HIV-1 particle are 5'

[II] M in group M stands for the 'major' form. O stands for 'outlier', whereas N stands for 'neither M nor O' [36].

[III] Around the time of discovery of AIDS, a French-Canadian flight attendant Gaeten Dugas (dubbed 'patient zero') was thought to be the primary source of HIV/AIDS outbreak in US. This claim has been refuted [39]. Gilbert et al. [38] showed that Haiti had the the oldest HIV-1 epidemic outside Africa and HIV-1 first arrived there around 1966. From there onwards, spread across US for 12 years before its discovery.

capped and 3' polyadenylated full-length RNA genome [43]. The two RNA strands are noncovalently dimerized, which is essential for RNA packaging [44]. The cellular $tRNA^{Lys3}$ is required for the reverse transcription initiation [45].

The innermost region is a conical capsid, which encloses viral genomic RNA. The capsid is made of roughly 1300 protein units. All capsid proteins are identical and arrange themselves into an asymetric structure made of hexamers and pentamers [46] (see the rightmost panel in Figure 2.1). The viral genomic RNA is tightly bound to p7 nucleocapsid proteins, late assembly protein p6 and enzymes essential to the development of the virion such as reverse transcriptase and integrase. The capsid is surrounded by an envelope of host-cell origin, which also includes viral glycoproteins gp120 and gp41 necessary for the host cell entry [42].

2.2.1 Genome organisation

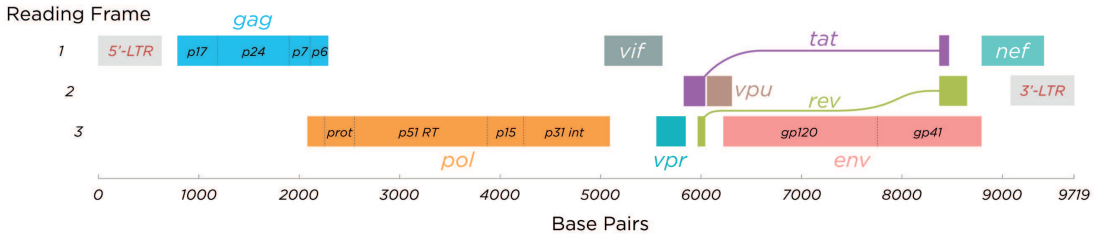

Figure 2.2: **HIV-1 genome:** The HIV-1 genome is roughly 10 kilobases in size. It consists of 9 genes, which encodes 15 viral proteins [47]. Both ends of genome have repeated non-coding sequences known as long terminal repeats. The gag codes for structural proteins namely p17, p24, p7 and p6. Pol region encodes enzymatic proteins (protease, reverse transcriptase, RNase H, integrase). The env region codes of glycoproteins (gp120 and gp41) and signal protein. Besides these genes, there are genes coding for essential regulatory proteins (tat and rev) and auxiliary proteins (vif, vpr, vpu, nef). Extracted from Wikimedia [41].

HIV-1 genome is roughly around 10,000 bases in length consisting of 9 genes (see Figure 2.2) that encodes for 15 viral proteins [47]. A repeated sequence flanks both ends of the virus genome known as long terminal repeats (LTRs), which has regulatory functions. The encoded viral proteins can be divided into three types as shown below [48]:

- Structural and enzymatic proteins: Gag codes for the precursor polyprotein called gag polyprotein. During the maturation process, the viral protease cleaves the polyprotein into matrix protein (p17), capsid protein (p24), nucleocapsid protein and spacer peptides (p1 and p2). Pol codes for viral enzymes namely reverse transcriptase, RNase H, integrase and protease. Env codes for viral envelope glycoprotein gp160 and 30 amino acid long signal protein. Gp160 is cleaved into gp120 and gp41 by the host cell protease.

- Regulatory proteins: Tat and rev are essential regulatory proteins. Tat plays an important role in regulating the reverse transcription of viral genome RNA, ensuring efficient synthesis of viral mRNAs and regulating the release of virus particles from infected cells. Rev binds to the viral genome via an arginine-rich RNA-binding motif that acts nuclear localization signals. The virus lacking rev activity are transcriptionally active but fail to express viral late genes and correspondingly fail to produce viruses.

- Accessory or auxiliary proteins: Although these proteins are not needed for the viral propagation in tissue cultures, their role in vivo is very important. Vpr is a viral protein responsible for the nuclear import of the pre-integration complex from cytoplasm. Vif is a highly

conserved phosphoprotein important for the infectivity of HIV-1 virions. Nef has multiple roles during the replication cycle of the virus. Vpu is important for a successful release of a newly formed virus. Tev is present in only few HIV-1 isolates and is believed to have similar function as tat protein.

Besides these viral proteins, there are also non-coding regions: Though these regions do not code for proteins, there is increasing evidences that they have regulatory functions [49], for e.g. 5' UTR [50]. Their role in HIV replication is a field of ongoing investigation.

As previously mentioned, HIV targets immune cells. The prime target-cells of HIV are the $CD4^+$ T helper cell. The list of cell types that are targeted by HIV besides T-cells are listed below [48, 51]:

1 $CD4^+$ macrophage cells

2 Dendric cells for example Langerhans

3 Natural killer cells/natural killer T-cells

4 Microglia and macrophages in the central nervous system.

2.2.2 Life cycle

The life cycle of HIV-1 begins with the binding of its viral envelope glycoproteins to receptors on the target-cell (CD4 and co-receptor CCR5 or CXCR4) [53]. This is followed by the fusion of viral and cellular membrane and subsequent release of the viral core into the cytoplasm of the target-cell. The cellular tRNA binds to viral RNA, which is necessary for the initiation of reverse transcription [48]. Reverse transcription is performed by reverse transcriptase. The template RNA is degraded by the RNase function of reverse transcriptase resulting in a negative-sense single stranded DNA. The negative DNA serves as a template for DNA dependent polymerization producing a double-strand viral DNA.

The viral DNA along with viral integrase and capsid proteins forms a pre-integration complex (PIC). The PIC enters the nucleus, which is an active process and involves a passage through the nuclear pore complex in non-dividing cells [54]. The capsid protein plays an important role for nuclear entry. In the nucleus, the viral DNA is integrated into the target-cell genome catalysed by integrase. The integration is carried out preferentially in the regions with a high transcription-activity.

After the integration, the viral genome is transcribed to viral mRNA. These mRNAs exit the nucleus to cytoplasm. A large number of viral mRNAs undergo multiple splicing in the nucleus before the exit. Their exit is via normal mRNA export route [42]. In the cytoplasm, they are translated to produce env and accessory proteins. Some of viral RNA are unspliced or partially spliced and exit the nucleus via a rev-dependent export pathway [42]. These partially-spliced and unspliced RNAs serve as mRNA for gag and gag-pro-pol poly proteins. Their translations produce either a 55 kDa gag precursor-protein or a 160 kDa gag-pro-pol polyprotein precursor [53]. The unspliced viral RNA can also be packed in the new virus particle functioning as the genomic material for the new virus.

Gag is the major structural protein of HIV-1 comprising roughly 50% of the mass of viral particle [42]. Gag polyprotein mediates all essential events in the virus assembly. They interact with the plasma membrane of the host cell, accumulate viral Env proteins and package viral RNA genome. Gag polyprotein guides the formation of a spherical immature particle, in which gag polyprotein molecules are projected radially inward of the virus. The virus particle is released from the host cell membrane surface in a process known as budding [42].

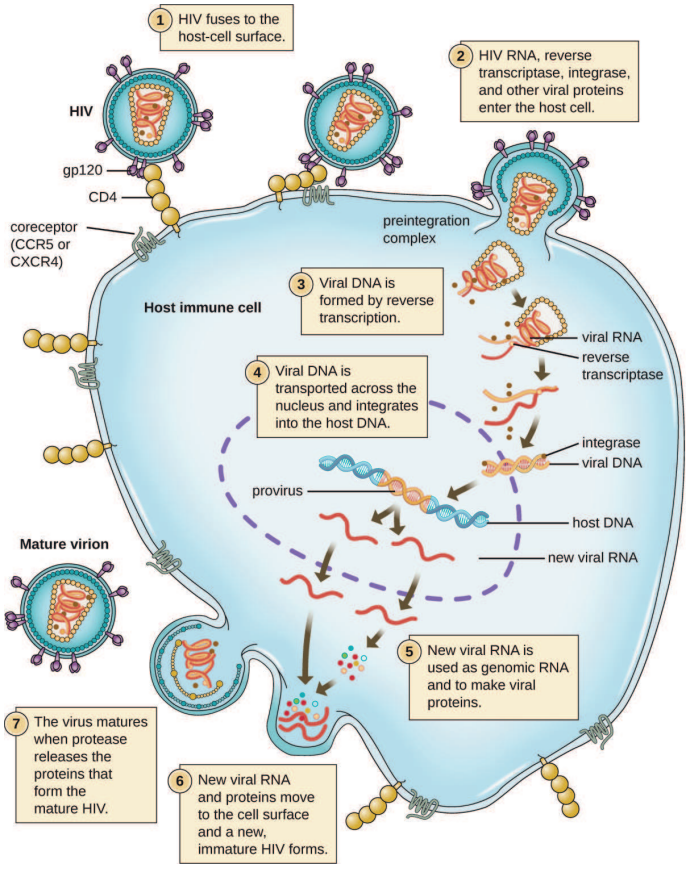

Figure 2.3: **Schematic depiction of HIV-1 life cycle:** HIV-1 fuses with the host cell by binding with the host-cell CD4 receptor and co-receptors (CCR5 and CX4) using its gp-120 and gp-41. After the fusion, the viral unpacks its core inside the host-cell. The core consists of viral RNA genome and enzymes. The genomic RNA is reverse transcribed by viral reverse transcriptase to form double stranded DNA. The DNA with other enzymes forms a pre-integration complex (PIC). The PIC is imported inside the host cell nucleus and the viral integrase mediates the integration of viral DNA in the host cell genome. The host cell machinery is hijacked and starts producing viral proteins. These assemble to form viral particles. The viral particles are released from the infected cell by the process known as budding. Extracted from NIAID [52]

During or shortly after budding off from the cell surface, the viral protease cleaves the gag polyprotein precursor into mature gag proteins (p17 matrix, p24 capsid, p7 nucleocapsid and p6) [48]. Gag cleavage triggers major changes, which include stable packaging of the dimeric RNA genome (condensation) and formation of conical capsid which is collectively referred to as viral maturation (see Figure 2.4) [42]. The maturation process prepares the recently formed immature virus particle after the budding from the host cell to form a particle able to enter and replicate inside in another host cell. The life cycle is depicted illustratively in Figure 2.3.

Ocassionally, the integrated viral genome undergoes transcriptional silencing in resting $CD4^+$ T-cells forming latently infected cells [54]. These cells are very long-living and can transition to an active transcription mode producing virus. These cells form the latent viral reservoir which is considered a major obstacle hindering the complete cure of HIV-1 infection [55, 56].

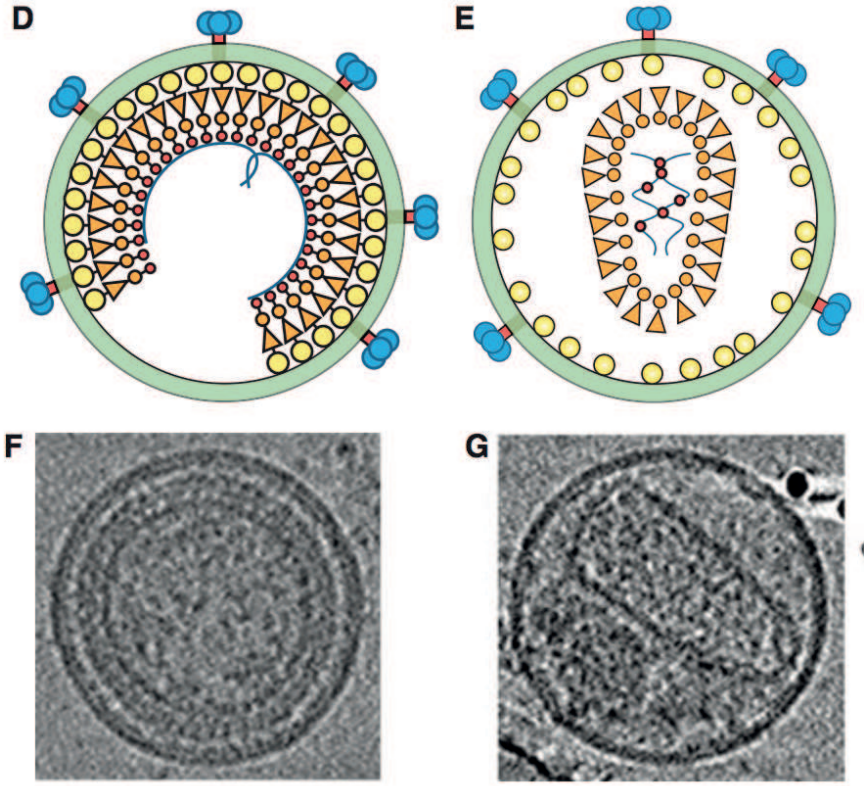

Figure 2.4: **HIV Maturation:** The left-uppermost panel schematically shows the viral assembly process. The gag polyproteins are radically projected inward, where the viral RNA is not condensely packed. The capsid is not properly formed. For comparison, the left-bottommost panel shows the immature virus particle from a cryo-EM tomographic reconstruction. The right-uppermost shows the mature virus particle, where gag polyprotein has been cleaved by viral protease and has reorganised itself to form capsid and viral RNA is densely packed. For comparison, the right-bottommost panel shows the mature virus particle. Extracted from Sundquist et al. [42].

2.3 Time course of HIV-1 infection

The time course of a HIV-1 infection in a host can be broadly divided into three sequential phases, namely acute, chronic and AIDS [57](see Figure 2.5). The acute phase occurs shortly after the infection. During the acute phase, the viremia grows exponentially reaching its peak and then starts to slowly decline. This is followed by the chronic infection phase where the plasma viremia reaches an equilibrium known as the viral set point [48]. Measurements of viremia taken in the chronic infection phase fluctuates around this constant set point. The chronic phase of infection can last for years and the infected person remains without clinical symptoms despite the high level of viremia. This is followed by AIDS when the number of $CD4^+$ has decreased significantly and the associated symptoms such as opportunistic infections and complications manifest.

The acute and early chronic infection stage can be classified into various Fiebig stages, which is guided by a sequential gain in positivity for the detection of HIV-1 antigens and HIV-1 specific antibodies assays [58, 59]. The time duration between a viral challenge and the first detection of viral RNA in the plasma is known as the eclipse phase, which is in average 10 days. The end of the eclipse phase, or Fiebig stage I marks that the viremia in the infected person has reached or crossed the lower limit of detection for plasma viral RNA. Similarly, Fiebig stages II-VI are based

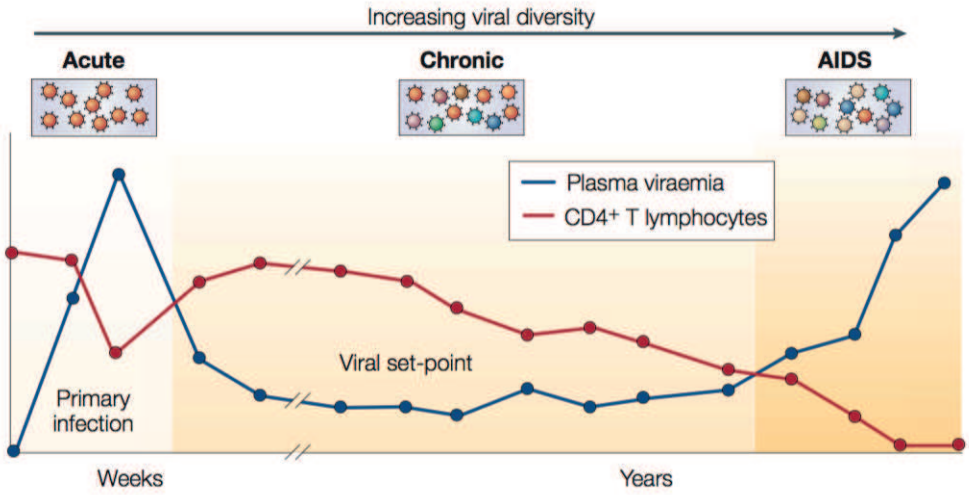

Figure 2.5: **The time course of HIV-1 infection:** The time course of HIV-1 infection can be divided into three successive phases: Acute infection phase, chronic infection phase and the manifestation of AIDS disease. The figure shows illustratively the time profile of viremia denoted by the blue line and $CD4^+$ T-cell population by the red line. With the passage of the infection, the viral diversity also increases. Extracted from Simon et al. [57].

on HIV-1 clinical diagnostic assays such as p24 and p31 viral antigens measured by enzyme-linked immunosorbent assays (ELISA), HIV-1 specific antibodies detected by ELISA and by western blotting. The viremia in the infected person peaks at 21-28 days after the viral challenge, usually in Fiebig stage III. This is followed by a slower decrease in plasma viral RNA levels.

Fiebig stage VI is marked by the positive detection of HIV-1 specific antibody by a western blotting and positive detection of p31 antigen by ELISA indicating the initiation of the early chronic infection phase. Eclipse phase and Fiebig stage I-V collectively form the acute infection phase. Figure 2.6 depicts the time course of HIV-1 with various clinical stages (eclipse and Fiebig stages) shortly after the infection respectively.

2.4 HIV-1 treatment

Within 4 years after the identification of the virus causing AIDS, Zidovudine was approved to be the first antiretroviral drug for clinical use against HIV-1 [60]. Zidovudine belongs to the nucleoside reverse transcriptase inhibitor class. The following decades saw the surge of novel antiretrovirals and currently there are more than 25 different antiretrovirals belonging to 4 major classes [3].

Initially, the treatment consisted of a single antiretroviral (monotherapy). However, the virus rapidly developed resistance against the antiretrovirals used in the monotherapy. The prospects of treatment until 1995 was to extend the life of infected individuals by months, possibly a few years [48]. With advent of protease inhibitors and non-nucleotide reverse transcriptase, the standard of care evolved from monotherapy to the administration of a cocktail or combination of antiretroviral drugs. The advent of combination therapy was known as HAART (highly active antiretroviral treatment), which reduced the mortality and morbidity associated with HIV. The first integrase inhibitor was introduced in 2007 [3]. Similarly, fusion inhibitors and a CCR5-antagonist were introduced in 2003 and 2007 respectively [60, 61]. With an increasing number of antiretrovirals,

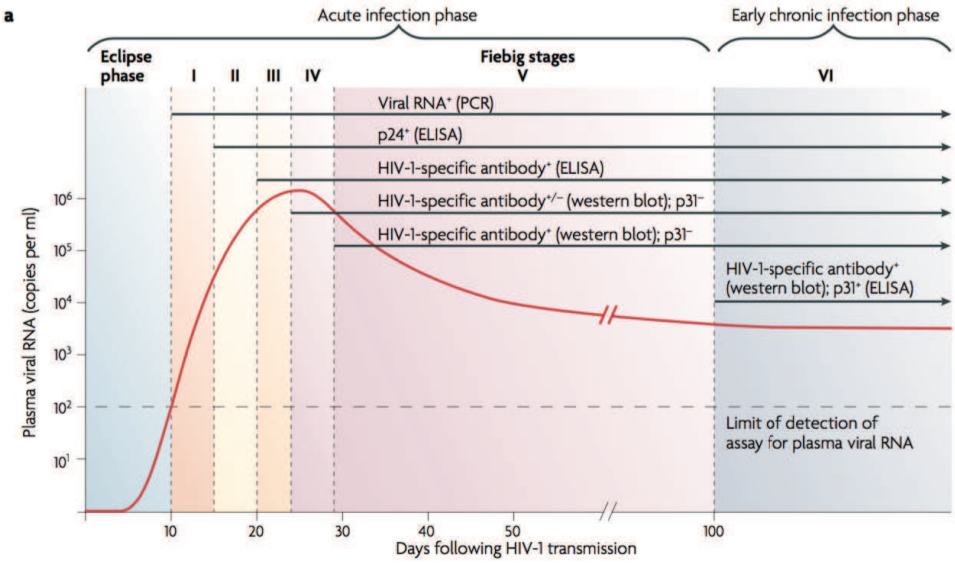

Figure 2.6: **Various clinical stages after a HIV-1 infection:** The time duration between the viral exposure and the first detection of viremia with a PCR. Following the eclipse phase, the course of HIV-1 infection can be classified in six Fiebig stages where the transition to the next Fiebig stage is marked by a step-wise gain in positivity for the detection of HIV-1 antigens and HIV-1 specific antibodies in the detection assays [58, 59]. Extracted from McMichael et al. [58].

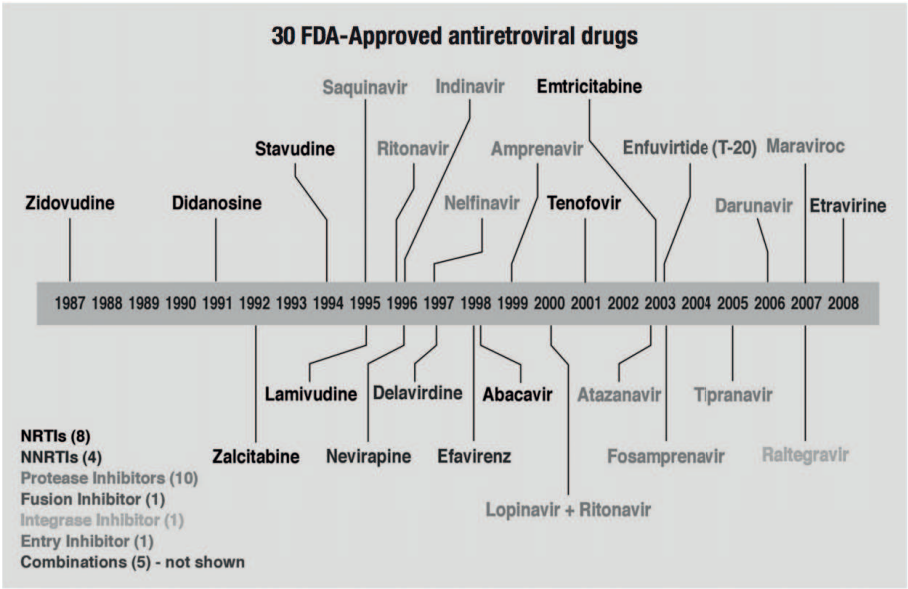

Figure 2.7: **Timeline showing antiretroviral approvals for HIV treatment:** Extracted from Palmisano [3].

HAART also improved.

HAART proved to be seminal in decreasing the morbidity and mortality of infected persons [61]. Though a complete cure cannot be achieved by antiretrovirals, they have transformed HIV-1 infection to a chronically manageable disease. In parts of the world where the access to antiretrovirals is easy, the life expectancy of HIV-1 infected person with a proper treatment is close

to that of the general population [5]. The timeline of introduction of various antivirals is depicted in Figure 2.7. Next, we provide a brief description of various antiviral classes against HIV-1.

2.4.1 Entry inhibitors

A number of viral and host cell proteins need to interact in order for a virus to enter a cell. Entry inhibitors block the viral entry by interfering with the machinery. Currently, there are two sub-classes of entry inhibitors, namely CCR5-antagonists and fusion inhibitors.

CCR5 antagonists: Researchers observed that a small subgroup of high-risk individuals is either resistant or showed delayed development of HIV-1 infection. Further investigation showed that these individuals have a homozygous mutation (a 32 base deletion) in the CCR5 co-receptor coding region resulting in the absence of CCR5 co-receptor in the cell surface [62–64]. Since CCR5 co-receptor is exploited by virus to infect a cell, its absence confers a partial immunity to the person against HIV-1. Moreover, individuals appear to be healthy without any abnormalities. This observation led to research on CCR5 antagonists (CRAs) resulting in the discovery of first CCR5-antagonist Maraviroc [65, 66]. The mechanism of action for maraviroc is that it binds to transmembrane domain of the CCR5 co-receptor [67,68]. This induces a conformational change in the co-receptor such that the HIV-binding domain is less accessible. Though the majority of HIV-1 strains exploit CCR5-receptor (CCR5-tropic virus), some are known to exploit CXCR4-receptor or both CCR5 and CXCR4 receptors. Hence, HIV-1 tropism needs to be determined before the use of maraviroc [69].

Fusion inhibitor: Unlike CCR5-antagonist which targets the host-cell receptor protein, the only known member of the fusion inhibitor subclass targets viral glycoprotein. During the fusion of virus with the host-cell surface, the viral gp-41 forms a homo-trimer helix bringing the viral and cellular membrane in close proximity [70]. Each gp-41 consists of HR1 and HR2 sub-domains. Enfuvirtide, a fusion inhibitor, is a synthetic peptide made up of 36 amino acids. It resembles an HR2 fragment of gp41 and binds to HR1 region of gp41, hence blocking helix formation critical for the fusion process. Enfurvirtide is not orally bioavailable requiring subcutaneous administration, due to which its long-term use is difficult [60]. Today, it is rarely used in the clinic.

2.4.2 Reverse transcriptase inhibitors

The two sub-classes of reverse transcriptase inhibitors (RTIs) are nucleoside reverse transcriptase inhibitor and non-nucleoside reverse transcriptase inhibitors.

Nucleoside/nucleotide reverse transcriptase inhibitors (NRTIs): Besides being the first antiviral drug class to be approved against HIV-1, nucleoside/nucleotide reverse transcriptase inhibitors (NRTIs) still are the backbone of HAART. NRTIs are administered as prodrugs [51]. Upon intracellular uptake, they need to undergo sequential phosphorylation by cellular kinases. The tri-phosphorylated NRTI resembles the natural occurring 5'-nucleoside triphosphates and competes with them for integration in the nascent viral DNA during reverse transcription. Unlike their endogenous counterparts, the tri-phosphorylated NRTI lacks the 3'-hydroxyl group necessary for forming 3'-5' phosphodiester bond with the next incoming 5'-nucleoside triphosphates [60]. Hence, upon integration in the nascent viral DNA, the reverse transcription process is halted. This is also known as chain termination. Chain termination can occur during RNA-dependent DNA polymerization as well as during DNA-dependent DNA polymerization. Currently, there are eight NRTIs approved for HIV-1 treatment: zidovudine (AZT), didanosine (ddI); zalcitabine (ddC); stavudine (d4T), lamivudine (3TC), abacavir (ABC), emtricitabine (FTC) and tenofovir disoproxil fumarate. The distribution and sale of zalcitabine has been discontinued since 2006 and ddI is rarely used today [71].

Non-nucleoside reverse transcriptase inhibitors (NNRTIs): Another sub-class of reverse transcriptase inhibitor class is known as non-nucleoside reverse transcriptase inhibitors (NNRTIs). NNRTIs bind to viral reverse transcriptase and alter the conformation of the substrate-binding site leading to reduction in its polymerase activity [72, 73]. They bind to a site in reverse transcriptase, which is close to the active catalytic site. This hinders the reverse transcriptase from normal functioning [60]. Nevirapine (NVP), delavirdine (DLV), efavirenz (EFV), etravirine (ETR) and rilpivirine (RPV) are NNRTIs currently available for HIV treatment.

2.4.3 Integrase inhibitors

Viral integrase is essential for the integration of the viral DNA in the host cell genome, namely 3' processing of viral DNA and strand transfer. All integrase inhibitors (InIs) inhibit the strand transfer process [61]. Integrase inhibitors are comprised of two essential components: (i) a metal-binding pharmacophore, which interacts with the two essential magnesium ion cofactors in the integrase and (ii) a hydrophobic group that interacts with viral DNA and enzyme in the complex [74]. They specifically bind with the integrase, when the enzyme forms a complex with viral DNA. The three approved integrase inhibitors are raltegravir, elvitegravir and dolutegravir.

2.4.4 Protease inhibitors

Viral protease plays an important role for the viral maturation. The viral protease cleaves gag poly-protein in the newly formed virus during and shortly after budding. Infected cells without functional protease can produce virus particles, however, the particles are non-infectious [53]. Protease inhibitors (PIs) inhibit the proteolytic cleavage activity of protease, hence, reduces the number of mature viruses. The site of action of protease inhibitors is intracellular and in part in the newly formed viruses. All PIs are based on 'peptidomimetic' principles, except for tipranavir. This means that they contain a hydroxyethylene scaffold, which resembles the normal peptide linkage but which itself cannot be cleaved [60]. Hence, upon binding to the viral protease they arrest the viral protease in a specific conformation. There are currently ten PIs available for HIV-1 treatment: saquinavir (SQV), ritonavir (RTV), indinavir (IDV), nelfinavir (NFV), amprenavir (APV), lopinavir (LPV), atazanvir (ATV), fosamprenavir (FPV), tipranavir (TPV) and darunavir (DRV) [61]. Ritonavir (RPV) is currently only used as a pharmacokinetic booster and older drugs SQV, APV and NFV are rarely used today due to pharmacokinetic properties which usually require multiple doses per day [75].

2.5 Mathematical modelling of HIV dynamics

The time profile of viremia in an infected person arises through complex interactions between viruses and different host cells. A viral dynamics model aims at capturing these interactions. Building a model of viral dynamics and inferring its parameters requires data from various stages of HIV-1 infection. For example, the acute infection phase captures the initial growth and decay of viremia in the recently infected person. In order to accurately determine parameters, a dense sampling of viral load at the rapid growth phase is required. However, the data in the acute infection phase is difficult to obtain, as most of the infected persons may be unaware of their infection.

Because the chronic infection phase lasts very long (years) in comparison to the acute infection phase (around 100 days), data of infected persons in the chronic infection phase is relatively easy to obtain. The hallmark of this phase is that the viral load has reached an equilibrium also

known as the set point of viremia. This equilibrium is due to the fact the production of virus in the body is balanced by the viral clearance, in another words, the system is in a steady state. However, measuring viral loads at the early chronic infection phase, where the viral load remain fairly constant, does not allow for the estimation of viral dynamics parameters.

2.5.1 Viral decay after antiretroviral treatment

In order to measure various parameters of viral dynamics, the system in steady state must be perturbed, for instance by administering antivirals that block the viral production. Perelson et al. [76, 77] performed such experiments where HIV-1 infected persons were administered potent antiretrovirals. Subsequently, the viral loads were sampled, and a model was fitted to estimate the unknown parameters.

The basic HIV-model comprised free viruses (V), uninfected and infected target T-cells (T_U, T_*) given by the following set of differential equations:

$$\begin{aligned}
\frac{d}{dt}T_U &= \lambda_T - \delta_T \cdot T_U - \beta_T \cdot V \cdot T_U \\
\frac{d}{dt}T_* &= \beta_T \cdot V \cdot T_U - \delta_{T_*} \cdot T_* \\
\frac{d}{dt}V &= N_{T_*} \cdot T_* - V \cdot CL
\end{aligned}$$

where λ_T and δ_T are the production and death rate of the uninfected target-cells T_U. The virus infects uninfected target-cells T_U with an infection rate β_T. The term δ_{T_*} is the death rate of the infected target-cells T_* and N_{T_*} is the virus production rate. The viruses are cleared at rate CL.

When the production of virus is completely blocked ($N_{T_*} = 0$) for instance with a use of 100 % effective protease inhibitor as performed by Perelson et al., the virus decays exponentially [77]. This allows to measure the viral clearance rate. The average rate of viral clearance was determined to be 23 per day, which is in line with another experiment to measure the viral clearance known as 'apheresis' [78]. Perelson et al. estimated that at least 10^{10} virions per day are produced in order to maintain the viral set point.

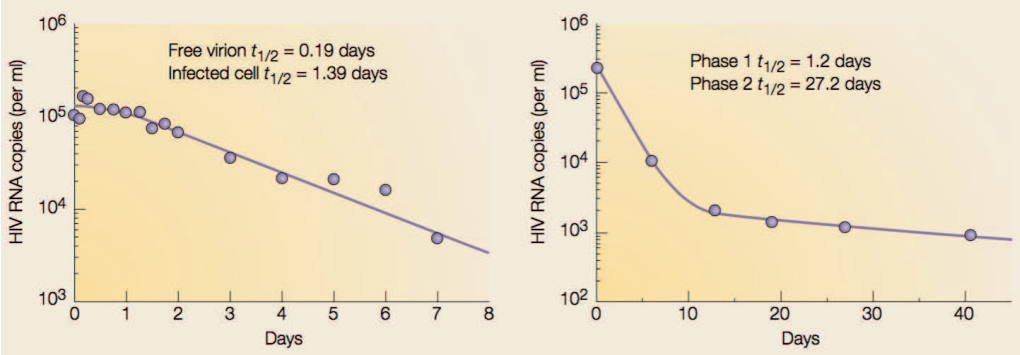

Figure 2.8: **Mono- and biphasic decays of viremia after the initiation of antiretroviral therapy**: The viremia or viral load in the infected person decay exponentially. The first and faster decay phase lasts for roughly a week (see the leftmost panel), whereas if the viral load decay is observed for a longer time period, the second slow decay is also observed (the rightmost panel). Extracted from Perelson et al. [77].

In clinical studies, when two or more antivirals are given to HIV-infected person and the viral load is observed for a longer period of time, the viral load displays a biphasic decay with an initial rapid exponential decline followed by a slower decline (see Figure 2.8). The initial decline lasts

for a week after the treatment, whereas in order to observe the second decline, viral loads need to be observed for a month or longer. The basic model with only one type of target-cells was not sufficient to explain the second exponential decline. The model required an extension with a type of longer-lived cells than T-cells. The likely candidate responsible for the second phase of decline are macrophages M_U. Accordingly, Perelson et al. [79] extended the basic model and the ODEs of the system are shown below:

$$\begin{aligned}
\frac{d}{dt}T_U &= \lambda_T - \delta_T \cdot T_U - \beta_T \cdot V \cdot T_U \\
\frac{d}{dt}M_U &= \lambda_M - \delta_M \cdot M_U - \beta_M \cdot V \cdot M_U \\
\frac{d}{dt}T_* &= \beta_T \cdot V \cdot T_U - \delta_{T_*} \cdot T_* \\
\frac{d}{dt}M_* &= \beta_M \cdot V \cdot M_U - \delta_{M_*} \cdot M_* \\
\frac{d}{dt}V &= N_{T_*} \cdot T_* + N_{M_*} \cdot M_*, -V \cdot CL
\end{aligned}$$

where λ_M, δ_M and β_M are the production-, death- and infection rates of uninfected macrophages M_U. The terms N_{M_*} and δ_{M_*} are the virus production- and death rates of infected macrophages M_*.

Similarly, observing the viral load for even longer time horizon (years) would show a third phase of decline with an extremely small rate. The candidate cells responsible for the third decay phase are latently infected cells and the model needs to be extended in a similar fashion to explain the third decay phase. Here, we forgo the details of the extension and present the details in the final model in Section 2.5.2. Next, we will briefly discuss the necessity of another extension of the viral dynamics model, where the cell infection process by the virus is broken down into smaller sub-processes.

Early non-productively and late productively infected host cells

Initially, and misleadingly, the faster decline in viral load was taken as a measure of the effectiveness of antiretroviral drugs. When raltegravir, an integrase inhibitor, was introduced, it was observed that the viral load decay was faster than the viral load decay observed for efavirenz, a reverse transcriptase inhibitor [80,81]. Hence, raltegravir was considered to be better than efavirenz.

Sedaghat et al. [82] extended the viral dynamics model and showed that the faster viral decline observed with an integrase inhibitor in comparison to a reverse transcriptase inhibitor is largely attributed to the fact that an integrase inhibitor acts later on the viral life cycle than a reverse transcriptase inhibitor. Their model distinguished early non-productively infected- (T_1, M_1) and the late productively infected cells (T_2, M_2). The ODEs for the extended model are presented below:

$$\begin{aligned}
\frac{d}{dt}T_U &= \lambda_T - \delta_T \cdot T_U - \beta_T \cdot V \cdot T_U \\
\frac{d}{dt}M_U &= \lambda_M - \delta_M \cdot M_U - \beta_M \cdot V \cdot M_U
\end{aligned}$$

$$
\begin{aligned}
\frac{\mathrm{d}}{\mathrm{d}t}\mathrm{T}_1 &= \beta_\mathrm{T} \cdot \mathrm{V} \cdot \mathrm{T}_\mathrm{U} - (\delta_{\mathrm{T}_1} + k_\mathrm{T}) \cdot \mathrm{T}_1 \\
\frac{\mathrm{d}}{\mathrm{d}t}\mathrm{M}_1 &= \beta_\mathrm{M} \cdot \mathrm{V} \cdot \mathrm{M}_\mathrm{U} - (\delta_{\mathrm{M}_1} + k_\mathrm{M}) \cdot \mathrm{M}_1 \\
\frac{\mathrm{d}}{\mathrm{d}t}\mathrm{T}_2 &= k_\mathrm{T} \cdot \mathrm{T}_1 - \delta_{\mathrm{T}_2} \cdot \mathrm{T}_2 \\
\frac{\mathrm{d}}{\mathrm{d}t}\mathrm{M}_2 &= k_\mathrm{M} \cdot \mathrm{M}_1 - \delta_{\mathrm{M}_2} \cdot \mathrm{M}_2 \\
\frac{\mathrm{d}}{\mathrm{d}t}\mathrm{V} &= \mathrm{N}_\mathrm{M} \cdot \mathrm{M}_2 + \mathrm{N}_\mathrm{T} \cdot \mathrm{T}_2 - \mathrm{V} \cdot \mathrm{CL}.
\end{aligned}
$$

The terms k_T and k_M are the rates of transformation of T_1 to T_2 and M_1 to M_2 respectively. The terms δ_{M_1}, δ_{M_2} are death rates of M_1 and M_2 cells.

In the previously discussed model without a distinction between early and late infected cells, both reverse transcriptase inhibitor and integrase inhibitor affected the parameter $\beta_\mathrm{T}/\beta_\mathrm{M}$. In the extended model presented by Sedaghat et al. [82], the reverse transcriptase inhibitor acted on parameters $\beta_\mathrm{T}/\beta_\mathrm{M}$, whereas the integrase inhibitor acted on parameters $k_\mathrm{T}, k_\mathrm{M}$. Hence, the extended model can distinguish between reverse transcriptase inhibitors and integrase inhibitors mechanistically.

2.5.2 A detailed viral dynamics model

Until now, we saw that various host cells with varying half-lives are required to account for distinct viral decay phases. Also, we saw that the extension of the model by distinguishing between early and late infected cells is required to describe the viral dynamics behaviour for reverse transcriptase and integrase inhibitors. With time, more knowledge regarding the virus life cycle was gained and novel antivirals belonging to different classes for example fusion inhibitors, CCR5 antagonists etc. were also introduced. Though the mechanism of action of fusion inhibitors, CCR5 antagonists and reverse transcriptase inhibitor differed, the previous models did not differentiate between them. This emphasized that the model must be refined by integrating additional knowledge and in such a manner that the mechanism of action of different antiviral classes are properly captured. To that end, von Kleist et al. [83] extended the viral dynamics model.

Figure 2.9 illustrates the schematics of the viral replication cycle in a host as presented in von Kleist et al. [83, 85]. T-cells and macrophages are the major target-cells of HIV. The uninfected T-cell and macrophage are represented by T_U and M_U respectively. A successful infection of a target-cell can be subsumed into two stages. The first stage involves irreversible binding to a target-cell, unpacking of viral content (genomic RNA and proteins) in the cell and completion of reverse transcription of RNA to stable DNA forming a pre-integration complex. The infected T-cell and macrophage reaching this stage are denoted by T_1 and M_1. Up to this stage, the infection is reversible. The second stage involves irreversible integration of viral DNA into target-cell genome, which hijacks the host cell machinery. After the integration, the infected host cell forms and releases virus particles. T_2 and M_2 represent the late productively infected T-cells and macrophages respectively. A portion of released virus particles are not infectious due to defective assembly such as lack of viral enzymes etc. The free infectious and non-infectious viruses are denoted by V and V_N respectively. Instead of becoming a productively infected T_2, T_1 can also form a latently infected T-cell (T_L) which does not express viral genes. The latently infected T_L can become activated transforming to productively infected T-cell and can produce virus particles. The average rates of change of the different species can be described by the system of ODEs as

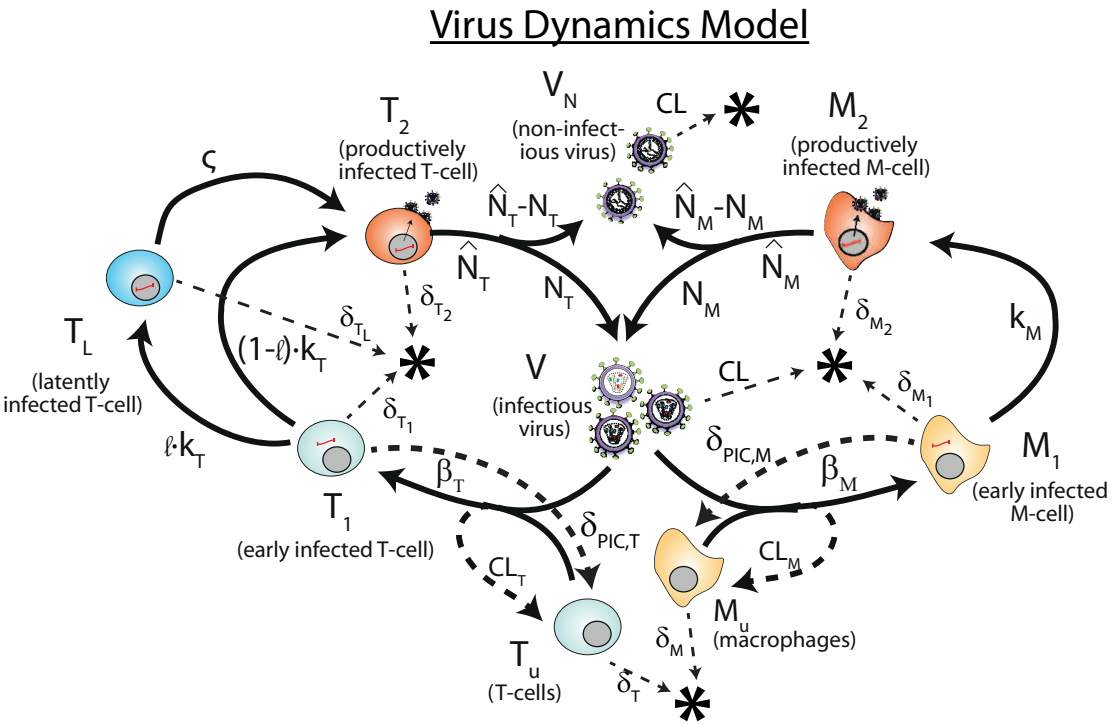

Figure 2.9: **Detailed three stage viral dynamics model:** T-cell and macrophage target-cells (T_U, M_U) are successfully infected by infectious virus V with lumped infection rate constants β_T and β_M, respectively, producing early infected cells T_1 and M_1. Infection can also be unsuccessful after the irreversible step of fusion (rate constant CL_T and CL_M, thick dashed lines), eliminating the virus and rendering the cell uninfected. In the early infected cells T_1 and M_1 essential viral proteins or DNA can be destroyed prior to integration with rate constants $\delta_{PIC,T}$ and $\delta_{PIC,M}$ (dashed lines) reverting the cell to an uninfected stage. The viral DNA can become integrated with rate constants k_T in T-cell to produce either late productively infected T_2 or latently infected cell T_L. The latently infected cell can convert to T_2 at rate ς. Similarly, M_1 can be advance to M_2 at k_M rate. The late infected cells T_2 and M_2 release new infectious- and non-infectious virus V_I and V_{NI} with rate constants N_T, $\left(\widehat{N_T} - N_T\right)$ and N_M, $\left(\widehat{N_M} - N_M\right)$, respectively. All cellular compartments x can get destroyed by the immune system with respective rate constants δ_x and the free virus gets cleared with rate constant CL (thin dashed lines). Details of viral dynamics model can be found in von Kleist et al. [83]. Adapted from Duwal et al. [84].

shown below:

$$
\begin{aligned}
\frac{\mathrm{d}}{\mathrm{d}t}\mathrm{T_U} &= \lambda_\mathrm{T} + \delta_{\mathrm{PIC,T}} \cdot \mathrm{T_1} - \delta_\mathrm{T} \cdot \mathrm{T_U} - \beta_\mathrm{T} \cdot \mathrm{V} \cdot \mathrm{T_U} \\
\frac{\mathrm{d}}{\mathrm{d}t}\mathrm{M_U} &= \lambda_\mathrm{M} + \delta_{\mathrm{PIC,M}} \cdot \mathrm{M_1} - \delta_\mathrm{M} \cdot \mathrm{M_U} - \beta_\mathrm{M} \cdot \mathrm{V} \cdot \mathrm{M_U} \\
\frac{\mathrm{d}}{\mathrm{d}t}\mathrm{T_1} &= \beta_\mathrm{T} \cdot \mathrm{V} \cdot \mathrm{T_U} - (\delta_{\mathrm{T_1}} + \delta_{\mathrm{PIC,T}} + k_\mathrm{T}) \cdot \mathrm{T_1} \\
\frac{\mathrm{d}}{\mathrm{d}t}\mathrm{M_1} &= \beta_\mathrm{M} \cdot \mathrm{V} \cdot \mathrm{M_U} - (\delta_{\mathrm{M_1}} + \delta_{\mathrm{PIC,M}} + k_\mathrm{M}) \cdot \mathrm{M_1} \\
\frac{\mathrm{d}}{\mathrm{d}t}\mathrm{T_2} &= (1-\ell) \cdot k_\mathrm{T} \cdot \mathrm{T_1} + \varsigma \cdot \mathrm{T_L} - \delta_{\mathrm{T_2}} \cdot \mathrm{T_2} \\
\frac{\mathrm{d}}{\mathrm{d}t}\mathrm{M_2} &= k_\mathrm{M} \cdot \mathrm{M_1} - \delta_{\mathrm{M_2}} \cdot \mathrm{M_2}
\end{aligned}
\tag{2.1}
$$

$$\begin{aligned}
\frac{\mathrm{d}}{\mathrm{d}t}\mathrm{T_L} &= \ell \cdot k_\mathrm{T} \cdot \mathrm{T_1} - (\delta_{\mathrm{T_L}} + \varsigma) \cdot \mathrm{T_L} \\
\frac{\mathrm{d}}{\mathrm{d}t}\mathrm{V} &= \mathrm{N_M} \cdot \mathrm{M_2} + \mathrm{N_T} \cdot \mathrm{T_2} - \mathrm{V} \cdot \Big[\mathrm{CL} + (\mathrm{CL_T} + \beta_\mathrm{T}) \cdot \mathrm{T_U} + (\mathrm{CL_M} + \beta_\mathrm{M}) \cdot \mathrm{M_U}\Big] \\
\frac{\mathrm{d}}{\mathrm{d}t}\mathrm{V_N} &= \Big[(\widehat{\mathrm{N}}_\mathrm{T} - \mathrm{N_T}) \cdot \mathrm{T_2} + (\widehat{\mathrm{N}}_\mathrm{M} - \mathrm{N_M}) \cdot \mathrm{M_2}\Big] - \mathrm{CL} \cdot \mathrm{V_{NI}},
\end{aligned}$$

where λ_T and λ_M are the birth rates of uninfected T-cells and macrophages and δ_T and δ_M are their respective death rate constants. Viruses are cleared at the rate CL by the host immune system. Unsuccessful infection of T-cell and macrophage also leads to clearance of viruses at rate $\mathrm{CL_T}$ and $\mathrm{CL_M}$ respectively. The term β(t) and β_M(t) denote the rate constants of successful infection of T-cell and macrophage by a virus to form early infected $\mathrm{T_1}$ and $\mathrm{M_1}$ respectively. In $\mathrm{T_1}$-cell, the essential components of the pre-integration complex is degraded intracellularly with rate constant $\delta_{\mathrm{PIC,T}}$, whereas integration of viral genome occurs with rate constant k_T. The integration event transforms $\mathrm{T_1}$ to productively infected T-cell ($\mathrm{T_2}$), however, a small portion ℓ is transformed to latently infected T-cell $\mathrm{T_L}$. $\mathrm{T_L}$ activates at rate ς to form $\mathrm{T_2}$. The term $\delta_{\mathrm{PIC,M}}$ and k_M are corresponding rate constants in macrophage. $\widehat{\mathrm{N}}_\mathrm{T}$ and $\widehat{\mathrm{N}}_\mathrm{M}$ denote the total number of released infectious and non-infectious virus from late infected T-cells and macrophages, whereas $\mathrm{N_T}$ and $\mathrm{N_M}$ are corresponding total number of released infectious viruses. The terms $\delta_{\mathrm{T_1}}$, $\delta_{\mathrm{T_2}}$, $\delta_{\mathrm{T_L}}$, δ_{M1} and δ_{M2} are death rate constants of $\mathrm{T_1}$, $\mathrm{T_2}$, $\mathrm{T_L}$, $\mathrm{M_1}$ and $\mathrm{M_2}$. The viral dynamics parameters can be found in Table A.1 in Appendix A.

The presented viral dynamics model encompasses the total body viremia and not only plasma viremia. The virus distributes into the plasma with total volume of 3.1 liters, where 2 % of the target-cell resides and into the interstitial space with total volume of 9.6 liters, where 98 % target-cell resides [83]. The model assumes that the interstitial space is in rapid exchange with the plasma.

2.5.3 Drug-class specific antiviral effects

The detailed viral replication cycle model allows us to mechanistically incorporate the effect of drugs belonging to different antiviral classes (derivation can be found in von Kleist et al. [83]). Let us introduce a term $D_\mathcal{K}$ which denotes a particular drug concentration at the target-site belonging to the drug class $\mathcal{K} \in \{\mathrm{CRA, RTI, InI, PI}\}$. The instantaneous effect of drugs $D_\mathcal{K}$ on their target-process is modelled using the Emax-model [86]

$$\eta_\mathcal{K}(t) = \frac{D_\mathcal{K}(t)^m}{\mathrm{IC}_{50}^m + D_\mathcal{K}(t)^m} \tag{2.2}$$

where $D_\mathcal{K}(t)$ is the target-site concentration of the drug and the term $\mathrm{IC_{50}}$ and m denote the drug concentration at which the target-process is inhibited by 50% and a hill coefficient [87] respectively. We refer this $\mathrm{IC_{50}}$ to as target-process drug potency.

In the presence of reverse transcriptase inhibitors, following parameters belonging to T-cells are affected as shown below [83]:

$$\beta_\mathrm{T}(t) = (1 - \eta_\mathrm{RTI}(t)) \cdot \beta_{\mathrm{T},\varnothing} \tag{2.3}$$

$$\mathrm{CL_T}(t) = \left(\frac{1}{\rho_{rev,\varnothing}} - (1 - \eta_\mathrm{RTI}(t))\right) \cdot \beta_{\mathrm{T},\varnothing}. \tag{2.4}$$

The parameter $\rho_{\mathrm{rev},\varnothing}$ is the probability that a virus succeeds in infecting a T-cell up to the stage where an unintegrated proviral DNA is produced. In contrast, the effect of CRA is captured as

presented below

$$\beta_{\mathrm{T}}(t) = (1 - \eta_{\mathrm{CRA}}(t)) \cdot \beta_{\mathrm{T},\varnothing} \tag{2.5}$$

$$\mathrm{CL}_{\mathrm{T}}(t) = (1 - \eta_{\mathrm{CRA}}(t)) \cdot \left(\frac{1}{\rho_{rev,\varnothing}} - 1\right) \cdot \beta_{\mathrm{T},\varnothing}. \tag{2.6}$$

Similarly, InI affects the parameter k_{T} as presented below

$$k_{\mathrm{T}}(t) = (1 - \eta_{\mathrm{InI}}(t)) \cdot k_{\mathrm{T}}, \tag{2.7}$$

whereas the protease inhibitor effect is given by

$$\mathrm{N}_{\mathrm{T}}(t) = (1 - \eta_{\mathrm{PI}}(t)) \cdot \mathrm{N}_{\mathrm{T}}. \tag{2.8}$$

respectively. The corresponding parameters for macrophages are affected in similar manner. The equations can be obtained by replacing the subscripts T by M.

2.6 Summary

HIV emerged several times in humans from independent zoonotic transmissions of simian immunodeficiency virus from non-human primates in Africa. Only HIV-1 group M managed to cause the global epidemics. HIV-1 is an obligate intracellular parasite with a compact genome, which targets mainly immune cells. The viral life cycle involves various steps where a virus hijacks the host-cell machinery to produce offspring. Currently there are four major antiviral drug classes that act on different steps in the viral life cycle. In this chapter, we provided a brief historical overview of development of HIV-1 dynamics model and description of a detailed viral dynamics model, which allows for the integration of all approved antiviral drug classes based on their mechanism of action [83, 88].

CHAPTER 3

Methods for simulating coupled chemical systems

In this chapter, we provide a brief mathematical background on chemical systems, since biological reaction networks can be viewed as chemical systems. At the microscopic level, the chemical system can be interpreted as a stochastic process, specifically a Markov jump process. Thus, we first review a Markov jump process. We also present stochastic and deterministic approaches for chemical systems. Furthermore, we discuss hybrid stochastic-deterministic approaches for a coupled system, where a part of the system behaves stochastically and another part deterministically.

3.1 Markov jump processes

Mathematical models of random phenomena require that one first specify a probability space. A probability space is a triplet $(\Omega, \mathcal{A}, \mathbb{P})$, where Ω is a sample space, $\mathcal{A}$ is a σ-algebra on Ω, and $\mathbb{P} : \mathcal{A} \to [0, 1]$ is a probability measure [1]. If a random phenomenon is known a priori to have outcomes restricted to some set $\mathbf{S}$ and if $\mathbf{S}$ can be equipped with a σ-algebra $\mathbb{S}$, then this phenomenon can be described by a random variable, i.e. a function $X : \Omega \to \mathbf{S}$ such that X is $(\mathcal{A}, \mathbb{S})$-measurable. For our purposes, we consider random variables with finite or countably infinite state spaces, i.e. $\mathbf{S} = \{0, \ldots, N\}$ for some $N \in \mathbb{N}$ or $\mathbf{S} = \mathbb{N}_0$. In both cases, we shall take $\mathbb{S}$ to be the power set of $\mathbf{S}$. In this work, we shall consider continuous-time stochastic processes on these state spaces. A continuous-time stochastic process is a family $\{X(t), t \in \mathbb{R}_+\}$ of random variables $X(t) : \Omega \to \mathbf{S}$. Given $x \in \mathbf{S}$, $\{X(t) = x\}$ refers to the event that the random variable $X(t)$ assumes the value x. We will use this notation when considering conditional probabilities later.

Given a random variable X on $(\Omega, \mathcal{A}, \mathbb{P})$, the law $\mathbb{P} \circ X^{-1}$ of X completely characterizes the statistics of the random variable. In particular, the law of a stochastic process completely characterizes its statistics. Given n time observation points $0 \leq t_0 < t_1 < \cdots < t_n$, the corresponding realization of the stochastic process of finite length n is denoted by

$$(X(t_0), X(t_1), \cdots, X(t_n)), \tag{3.1}$$

[1] The section on Markov jump processes is partly based on the manuscript by Schütte and Metzner [89].

and it obeys the following joint probability

$$\begin{aligned}\mathbb{P}(X(t_0),\cdots,X(t_n)) &= \mathbb{P}(X(t_0)) \\ &\times \mathbb{P}(X(t_1)|X(t_0)) \\ &\times \mathbb{P}(X(t_2)|X(t_0),X(t_1)) \\ &\times \cdots \\ &\times \mathbb{P}(X(t_n)|X(t_0),\cdots,X(t_{n-1})).\end{aligned} \tag{3.2}$$

We are particularly interested in a special class of continuous-time stochastic process called **Markov jump processes**. Formally, for a Markov jump process $X(t)$, the following should hold true for $0 \leq t_0 < t_1 < \cdots < t_n$:

$$\mathbb{P}(X(t_n)|X(t_0),\cdots,X(t_{n-1})) = \mathbb{P}(X(t_n)|X(t_{n-1})).$$

The above equation means that the transition from $X(t_{n-1})$ to $X(t_n)$ depends only on the previous state $X(t_{n-1})$ and does not depend on the history of the process. This memoryless property of the process is referred to as **Markov property**. This allows the joint probability as in Eqn (3.2) for a Markov process to be rewritten as shown below :

$$\begin{aligned}\mathbb{P}(X(t_0),\cdots,X(t_n)) &= \mathbb{P}(X(t_0)) \\ &\times \mathbb{P}(X(t_1)|X(t_0)) \\ &\times \mathbb{P}(X(t_2)|X(t_1)) \\ &\times \cdots \\ &\times \mathbb{P}(X(t_n)|X(t_{n-1})).\end{aligned} \tag{3.3}$$

A Markov jump process is called **homogeneous**, if the following holds

$$\mathbb{P}\left(X(t) = y|X(s) = x\right) = \mathbb{P}\left(X(t-s) = y|X(0) = x\right), \quad t > s$$

which means that the transition probability does not depend explicitly on time t and s but on the length of the interval $(t-s)$. Otherwise, the process is called inhomogeneous. For a homogeneous Markov process X, a function $\mathbf{p} : \mathbb{R}^+ \times \mathbf{S} \times \mathbf{S} \mapsto [0,1]$ can be defined by

$$\mathbf{p}(t,x,y) := \mathbb{P}\left(X(t) = y|X(0) = x\right)$$

which is called the **stochastic transition function** of X. The stochastic transition function has the following properties :

(i) The transition probabilities are non-negative i.e. $\mathbf{p}(t,x,y) \geq 0$.

(ii) Due to the conservation of probability, the transition probabilities from a state sum up to 1.

$$\sum_{y\in\mathbf{S}} \mathbf{p}(t,x,y) = 1, \quad \text{for all} \quad x \in \mathbf{S}.$$

An initial probability of a homogeneous Markov jump process to be in a particular state is defined as

$$\mathbf{p}(0,x) := \mathbb{P}(X(0) = x_0). \tag{3.4}$$

If there is a single state x_0 such that $\mathbf{p}(0,x) = 1$, then x_0 is the initial state. The vector $\mathbf{p}(0) = [\mathbf{p}(0,x)]_{x\in\mathbf{S}}$ is called the initial probability distribution and the vector $\mathbf{p}(t)$ denotes the probability distribution of a Markov jump process at time t given the initial distribution $\mathbf{p}(0)$.

Furthermore, using the Markov property it can be shown that the stochastic transition function of a homogeneous Markov process fulfills the **Chapman Kolmogorov Equation**

$$\mathbf{p}(t+s,x,y) = \sum_{\forall z \in \mathbf{S}} \mathbf{p}(s,x,z) \cdot \mathbf{p}(t,z,y) = \sum_{\forall z \in \mathbf{S}} \mathbf{p}(t,x,z) \cdot \mathbf{p}(s,z,y).$$

In words, the Chapman-Kolmogorov equation states that the probability of transition from state x to y results from the sum of all possible transitions from x to immediate states and then from the intermediate states to the end state y. Let $x, y \in \mathbf{S}$ be an arbitrary pair of states.

(i) The state x **has access to** the state y, if

$$\mathbb{P}(X(t) = y | X(0) = x) > 0 \tag{3.5}$$

for some $t > 0$.

(ii) The states x and y **communicate**, if x has access to y and y has access to x.

(iii) The Markov jump process is **irreducible**, if all pairs of states communicate.

3.1.1 Transition matrices and infinitesimal generators

For a Markov jump process, we introduce a matrix such that

$$\mathbf{P}(t) = [\mathbf{p}(t,x,y)]_{x,y \in \mathbf{S}},$$

which is known as a **transition matrix** for all $t \geq 0$. The entries of the transition matrix are non-negative and the row-wise sum of entries sum up to one. For $t = 0$, it is required that $\mathbf{P}(0)$ is an identity matrix. The set $\{\mathbf{P}(t) : t \geq 0\}$ is a semigroup known as **transition semigroup**. In terms of the transition semigroup, the Chapman-Kolmogorov equation can be expressed as:

$$\mathbf{P}(t+s) = \mathbf{P}(s) \cdot \mathbf{P}(t) = \mathbf{P}(t) \cdot \mathbf{P}(s). \tag{3.6}$$

Given a Markov jump process with a transition semigroup $\mathbf{P}(t) : t \geq 0$ and assuming its limit

$$\mathbf{Q} = \lim_{t \to 0^+} \frac{\mathbf{P}(t) - \mathrm{Id}}{t} \tag{3.7}$$

exists, this limit is known as the **infinitesimal generator** with $\mathbf{Q} = [\mathbf{q}(x,y)]_{x,y \in \mathbf{S}}$ with $-\infty \leq \mathbf{q}(x,x) \leq 0$ and $0 \leq \mathbf{q}(x,y) \leq \infty$. The entries of the generator matrix can also be defined as limits as shown below:

$$\mathbf{q}(x,x) = \lim_{t \to 0^+} \frac{\mathbf{p}(t,x,x) - 1}{t}$$

and

$$\mathbf{q}(x,y) = \lim_{t \to 0^+} \frac{\mathbf{p}(t,x,y)}{t}.$$

The infinitesimal generator matrix has the following property for the diagonal entries :

$$\mathbf{q}(x,x) = -\sum_{y \in \mathbf{S},\, y \neq x} \mathbf{q}(x,y)$$

from which it follows that the row-wise summation of entries is 0 for the infinitesimal generator matrix i.e.,

$$\sum_{y \in \mathbf{S}} \mathbf{q}(x,y) = 0.$$

Interestingly, for a Markov jump process, while the row-wise summation of the transition matrix is 1, the row-wise summation of its infinitesimal generator matrix is 0. Construction of generator- or transition matrices for an infinite Markov jump process requires appropriate boundary conditions, for instance introduction of so called 'exit states' as done by Munsky et al. [90].

3.1.2 Kolmogorov equations and master equation

Given a Markov jump process with transition semi group $\mathbf{P}(t)$ and infinitesimal generator $\mathbf{Q} = [\mathbf{q}(x, y)]$, satisfying $-\mathbf{q}(x, x) < \infty$ for all $x \in \mathbf{S}$, then, $\mathbf{P}(t)$ is differentiable for all $t \leq 0$ and satisfies so called the **Kolmogorov backward equation**

$$\frac{\mathrm{d}}{\mathrm{d}t}\mathbf{P}(t) = \mathbf{Q} \cdot \mathbf{P}(t). \tag{3.8}$$

The solution to the above Eqn (3.8) is given by

$$\mathbf{P}(t) = \mathbf{exp}(t \cdot \mathbf{Q}) \tag{3.9}$$

where the matrix exponential function is defined as

$$\mathbf{exp}(t \cdot \mathbf{Q}) = \sum_{k=0}^{\infty} \frac{(t \cdot \mathbf{Q})^k}{k!} \tag{3.10}$$

which is known to converge.

If, in addition to conditions for the Kolmogorov backward equation, the following condition

$$-\sum_{y \in \mathbf{S}} \mathbf{p}(t, x, y) \cdot \mathbf{q}(y, y) < \infty \tag{3.11}$$

is satisfied for all $t \leq 0$ and $x \in \mathbf{S}$, then the so called **Kolmogorov forward equation**

$$\frac{\mathrm{d}}{\mathrm{d}t}\mathbf{P}(t) = \mathbf{P}(t) \cdot \mathbf{Q} \tag{3.12}$$

is also valid. The Kolmogorov forward equation is particularly important as it allows us to deduce the evolution equation for an initial probability distribution $\mathbf{p}(0)$ of the Markov jump process. The derivation is shown below, which involves left-side multiplication of the forward Eqn (3.12) by the initial probability distribution :

$$\begin{aligned} \mathbf{p}_0 \cdot \frac{\mathrm{d}}{\mathrm{d}t}\mathbf{P}(t) &= \mathbf{p}_0 \cdot \mathbf{P}(t) \cdot \mathbf{Q} \\ \frac{\mathrm{d}}{\mathrm{d}t}\mathbf{p}_0 \cdot \mathbf{P}(t) &= \mathbf{p}_0 \cdot \mathbf{P}(t) \cdot \mathbf{Q} \\ \frac{\mathrm{d}}{\mathrm{d}t}\mathbf{p}(t) &= \mathbf{p}(t) \cdot \mathbf{Q}. \end{aligned} \tag{3.13}$$

Eqn (3.13) is known as the **master equation** or **chemical master equation** for a chemical system. The first reference to the master equation was in a paper by Nordsieck, Lamb and Uhlenbeck in 1940 [91]. We will revisit the master equation in the next section.

3.2 The chemical system

A chemical system at the microscopic level can be viewed as a Markov jump process. Consider a *homogeneous well-stirred* chemical system of constant volume v in a *thermal equilibrium* at a constant temperature [II]. The system consists of molecules of N_s chemical species $S_i, i = 1 \cdots N_s$

[II] The mathematical background on the chemical system is in part adapted from the Menz's dissertation [92]

interacting through N_r elementary reactions. The term R_j, $j = 1 \cdots N_r$ represents the j$^{\text{th}}$ elementary reaction. Given its stoichiometry, we can write R_j as shown below:

$$R_j : b^r_{j,1} \cdot S_1 + \cdots + b^r_{j,N_s} \cdot S_{N_s} \rightarrow b^p_{j,1} \cdot S_1 + \cdots + b^p_{j,N_s} \cdot S_{N_s}$$

where $b^r_{j,i}, b^p_{j,i} \in \mathbb{N}_0$ are known as **stoichiometric coefficients** and specify how many molecules or units of S_i are consumed and how many of S_i are produced with a single firing of R_j respectively. Obviously, if species S_i is not involved in reaction R_j, its corresponding stoichiometric coefficients are zero. Each reaction R_j can be associated with a reaction specific vector $\upsilon_j \in \mathbb{Z}^{N_s}$, where its i$^{\text{th}}$ component is defined as

$$\upsilon_{j,i} := b^p_{j,i} - b^r_{j,i}$$

which denotes the net change in the number of molecules or unit of species S_i due to a single firing of R_j. Let vector $x = [x_1, \cdots, x_{N_s}]^\top \in \mathbb{N}_0^{N_s}$ denote a possible state of the system, where x_i represents the possible numbers of molecules of a species $S_i, i = 1, \cdots N_s$. The system's dynamics are described as a continuous-time process $X(t) = [X_1(t), \cdots, X_{N_s}(t)]^\top \in \mathbb{N}_0^{N_s}$ where the i^{th} component is defined as

$$X_i(t) := \text{number of molecules or unit of species } S_i \text{ at time } t.$$

The expression $X(t) = x$ denotes that the system is in state x at time t. Firing of a reaction R_j (given that the system is in state x) changes the state to $x + \upsilon_j$.

Besides the state change vector υ_j, the other quantity characterizing R_j is its propensity function a_j, which is defined such that

$$\begin{aligned} a_j(x)\,\delta t \quad := \quad & \text{the probability that one reaction } R_j \text{ will fire somewhere} \\ & \text{inside the volume } v \text{ in the next infinitesimal time interval} \\ & [t + \delta t), \text{ given that the system is in state } x \text{ at time t.} \end{aligned} \tag{3.14}$$

The above Definition (3.14) is regarded as the **fundamental stochastic premise** of chemical kinetics because everything else in the theory follows from it via the law of probability [93].

3.3 Stochastic approach

Assume a system starts in state x_0 at time $t = 0$, i.e., $X(0) = x_0$[III]. We denote by $\boldsymbol{K}_j(t) \in \mathbb{N}_0$ the counts of firings of a reaction R_j up to the time $t \geq 0$. Utilizing the state change vector υ_j, the state of the system at time $t \geq 0$ can be achieved by updating the initial state as shown below:

$$X(t) = X(0) + \sum_{j=1}^{N_r} \upsilon_j \cdot \boldsymbol{K}_j(t) \tag{3.15}$$

with $X(0) = x_0$. In the stochastic approach, the reaction counts $\boldsymbol{K}_j(t), j = 1, \cdots, N_r$ are modelled as inhomogeneous Poisson processes [IV], with their intensities corresponding to the reaction propensity a_j, i.e.,

$$\boldsymbol{K}_j(t) = \boldsymbol{\mathcal{P}}_j\left(\int_0^t a_j(X(s))\, ds\right) \quad (j = 1, \cdots, N_r), \tag{3.16}$$

[III] Note that x_0 is reserved for an initial state vector, whereas $x_i : i \in \mathbb{N}$ denotes the i$^{\text{th}}$ component of state vector x.

[IV] A poisson process is a special kind of Markov jump process where the state space $\mathbf{S}$ is $\mathbb{N}_0$. For a comprehensive review see the book by Kingman [94].

see [92] for further details. Utilizing this, we can rewrite Eqn (3.15) as shown below

$$X(t) = X(0) + \sum_{j=1}^{N_r} \upsilon_j \cdot \mathcal{P}_j \left(\int_0^t a_j(X(s))\, ds \right) \tag{3.17}$$

which reveals the relation between the state change and reaction propensities.

3.3.1 Chemical master equation

From the fundamental premise stated in definition (3.14), the time evolution of probability $\mathbb{P}(X(t) = x|X(0) = x_0)$ can be derived as shown below :

$$\begin{aligned} \frac{\partial}{\partial t}\mathbb{P}(X(t) = x|X(0) = x_0) &= \sum_{j=1}^{N_r} a_j(x - \upsilon_j) \cdot \mathbb{P}(X(t) = x - \upsilon_j|X(0) = x_0) \\ &- \sum_{j=1}^{N_r} a_j(x) \cdot \mathbb{P}(X(t) = x|X(0) = x_0), \end{aligned} \tag{3.18}$$

which is known as the **chemical master equation (CME)**. As mentioned in the previous subsection 3.1.2, the chemical master equation is, in fact, the Kolmogorov forward equation. The chemical master equation completely characterizes the statistics of $X(t)$. Note, in the previous subsection 3.1.2, the master equation was presented in a vector form and here Eqn (3.18) denotes, in fact, the evolution of a specific entry of the vector from Eqn (3.13). Furthermore, the reaction propensities are entries of the infinitesimal generator matrix $\mathbf{Q}$ of the Markov jump process, such that

$$a_j(x) = q(x, x + \upsilon_j), \quad j = 1, \cdots, N_r \tag{3.19}$$

and

$$q(x, x) = -\sum_{j=1}^{N_r} a_j(x). \tag{3.20}$$

The CME is a set of coupled ODEs, with one equation for every possible state. This implies that the CME suffers from the **curse of dimensionality**. For instance, consider a system with 10 species where the number of each species can take any value from 0 to 99. This system has 100^{10} possible states. Hence, even for a moderately big system the curse of dimensionality can be prohibitive for the derivation of closed-form solution or even for numerical solutions.

3.3.2 Stochastic simulation algorithm

Instead of working with the chemical master equation, which is generally intractable, one can generate an ensemble of numerical realizations of the stochastic process using **Monte Carlo techniques** to approximate the statistics of the process. Gillespie [95] first presented an exact stochastic simulation algorithm. Even though a number of modifications have been introduced afterwards, the original algorithm, also known as the direct method, will be briefly presented here due to its intuitiveness and importance.

The cornerstone to generate the numerical realization of $X(t)$ is the probability function $p(\tau, j|x; t)$, defined as follows :

$$\begin{aligned} p(\tau, j|x; t)\, \delta t \quad := \quad & \text{the probability that the next reaction fires in the infinitesimal} \\ & \text{time interval } [t + \tau, t + \tau + \delta t) \text{ and the next reaction is } R_j \\ & \text{conditioned on the system being in state } x \text{ at time } t. \end{aligned} \tag{3.21}$$

This function $p(\tau, j|x;t)$ is, in fact, the joint probability density the time to the next reaction (τ) and the index of the next reaction (j) to fire conditioned on the system being in state x at time t. Applying the law of total probability to the fundamental premise permits the derivation of an exact expression for $p(\tau, j|x;t)$:

$$p(\tau, j|x;t) = a_j(x) \cdot \exp(-a_0(x) \cdot \tau) \tag{3.22}$$

where $a_0(x)$ is defined as the sum of all reaction propensities:

$$a_0(x) := \sum_{j=1}^{N_r} a_j(x).$$

Let $p(\tau|x;t)$ denote the probability that the time to the next reaction is τ, given that the system is in state x, and $p(j|\tau, x;t)$ denote the conditional probability that this reaction is R_j. From Eqn (3.22), it follows that

$$p(\tau|x;t) = \sum_{i=1}^{N_r} p(\tau, j|x;t) = a_0(x) \cdot \exp(-a_0(x) \cdot \tau), \tag{3.23}$$

which means that time to the next reaction is an exponential random variable with intensity $a_0(x)$. In other words, the time to the next reaction is the waiting time between two successive events of a Poisson process. The following relation can also be derived from Eqn (3.22)

$$p(j|\tau, x;t) = \frac{a_j(x)}{a_0(x)}, \tag{3.24}$$

which implies that the index of the next reaction to fire is an integer random variable with point probability $a_j(x)/a_0(x)$. The direct method proposed by Gillespie [95] employed the standard inversion generating method of Monte Carlo theory. The procedure is as follows: Draw two random numbers u_1 and u_2 from the standard uniform distribution $\mathcal{U}(0, 1)$ and take

$$\tau = \frac{1}{a_0(x)} \cdot \log\left(\frac{1}{u_1}\right) \tag{3.25}$$

which gives the time to the next reaction and

$$j = \text{the smallest integer such that } \sum_{j'=1}^{j} a_{j'}(x) \geq a_0(x) \cdot u_2. \tag{3.26}$$

which is the index of the next reaction to be fired. The pseudo code of stochastic simulation algorithm (direct method) as proposed by Gillespie et al [95] is given below:

(i) Set initial time $t = 0$ and initial state $X(0) = x_0$.

(ii) Evaluate the reaction propensities $a_j(X(t))$ and the sum of reaction propensities $a_0(X(t))$.

(iii) Generate a random variable $u_1 \sim \mathcal{U}(0, 1)$.

(iv) Compute the time to next reaction τ using the following equation

$$\tau = \frac{1}{a_0(x)} \cdot \log\left(\frac{1}{u_1}\right). \tag{3.27}$$

(v) Update time $t = t + \tau$.

(vi) Generate a random variable $u_2 \sim \mathcal{U}(0, 1)$.

(vii) The smallest positive integer j such that

$$\sum_{j'=1}^{j} a_{j'}(X(t)) \geq a_0(X(t)) \cdot u_2 \tag{3.28}$$

gives the index for the next reaction.

(viii) Update the state $X(t) = X(t) + \upsilon_j$.

(ix) Stop the simulation if some stopping criteria are met. If not, go to step (ii).

3.4 Deterministic approach

In the deterministic approach, the state of the system is represented by a continuous variable which evolves deterministically in time $\bar{X} = [\bar{X}_1(t), \cdots, \bar{X}_{N_s}(t)]^\top \in \mathbb{R}_+^{N_s}$ where

$$\bar{X}_i(t) := \frac{X_i(t)}{\Omega} \quad (\forall\ i = 1, \cdots, N_s) \text{ and } \Omega \in \mathbb{R}_+ \text{ is a scaling factor.}$$

Instead of representing the number of species, the variable $\bar{X}(t)$ describes some species level at time t and is given in units of Ω^{-1}. Generally, $\Omega = v \cdot N_A$ where $N_A \approx 6.023 \times 10^{23} \text{mol}^{-1}$ is the Avogadro constant and v is the volume of the system. In that case $\bar{X}(t)$ describes the molar concentration of the species at time t. Note that the description of the system by concentrations (continuous variable) deviates from the original description of the system by the number of species (discrete variable). The concentration description relies on the continuum assumption, which states that the rounding errors due to such a representation is negligible given that $X_i(t) \gg 1$ for all species [96]. In other words, the deterministic approach requires a system to be of large size in terms of the volume $\Omega \gg 1$ and the number of species $X_i(t) \gg 1$, such that the random fluctuation in the species levels due to reactions become negligible.

In fact, the representation of the chemical system by the reaction rate equation can be derived from the fundamental premise (see Eqn (3.14)), when the system is in the **thermodynamic limit** [97–99]. The limit is defined as the limit in which all species' populations $X_i(t)$ and the scaling factor related to volume Ω approach infinity, while the species level $X_i(t)/\Omega$ is a constant [93] [V].

3.4.1 Reaction rate and law of mass action

In the deterministic approach, the rate $r_j(\bar{x})$ is defined as the average number of firings of a reaction R_j per Ω and per unit time given that the system is in state $\bar{x}$ (where $\bar{x}$ denotes the species level). The general form of the reaction rates of elementary reactions is given by the **law of mass action**. The law, first proposed by Waage and Gulberg [100], states that the rate of an elementary reaction R_j is proportional to the product of molar concentration of all involved reactants raised to the power of their stoichiometric coefficients with the factor of proportionality known as **reaction**

[V] Under certain conditions, the chemical system can be approximated by a continuous stochastic equation known as **Chemical Langevin Equation (CLE)** and **Chemical Fokker-Planck Equation (CFPE)**. For the chemical system approaching the thermodynamic limit, these continuous stochastic equations lead to continuous deterministic equations also known as the **reaction rate equation**. For details, see the review by Gillespie [93].

rate constant. Let c_j denote the rate constant of an elementary reaction R_j; then according to the law of mass action the rate equation is given by

$$r_j(\bar{x}) = c_j \cdot \left(\prod_{i=1}^{N_s} (\bar{x}_i)^{b^r_{j,i}} \right). \tag{3.29}$$

Hence, the reaction rate r_j is a polynomial function of the species level. Based on the stoichiometric coefficients $b^r_{j,i}$ the reaction rate or reaction can be associated with a degree or **reaction order**. Precisely, it is defined as follows :

$$\text{Order of the reaction } R_j(|b^r_j|) := \sum_{i=1}^{N_s} b^r_{j,i}. \tag{3.30}$$

The reaction order captures how many molecules of reactants are involved in the reaction. The unit of the reaction rate constant c_j depends on the reaction order of R_j. For a zero-order reaction, the unit of c_j is equal to the inverse of the product of units of Ω and time. For a unimolecular reaction, its unit is equal to the inverse of the unit of time, whereas for bimolecular reaction the unit of reaction rate constant is equal to the unit of Ω times the inverse unit of time.

3.4.2 Reaction rate equations

Let us denote $\mathbf{\Gamma}_j(t)$ as the average number of firing of a reaction R_j per Ω over time interval $[0, t]$, with $\mathbf{\Gamma}_j(0) = 0$ for all $j = 1, \cdots, N_r$. According to the definition of a reaction rate r_j, in integral form $\mathbf{\Gamma}_j$ can defined as

$$\mathbf{\Gamma}_j(t) = \int_0^t r_j(\bar{X}(s))\, ds \tag{3.31}$$

and equivalently as the solution of the ODE

$$\frac{\mathrm{d}}{\mathrm{d}t}\mathbf{\Gamma}_j(t) = r_j(\bar{X}(t)), \text{ with } \mathbf{\Gamma}_j(0) = 0.$$

The species level $\bar{X}(t)$ are given via

$$\bar{X}(t) = \bar{X}(0) + \sum_{j=1}^{N_r} \upsilon_j \cdot \mathbf{\Gamma}_j(t) = \bar{X}(0) + \sum_{j=1}^{N_r} \upsilon_j \cdot \int_0^t r_j(\bar{X}(s))\, ds, \tag{3.32}$$

for some initial $\bar{X}(0) = \bar{x}_0$ at time $t = 0$. By differentiating Eqn (3.32) with respect to time, $\bar{X}(t)$ can be shown to be the solution of the initial value problem :

$$\frac{\mathrm{d}}{\mathrm{d}t}\bar{X}(t) = \sum_{j=1}^{N_r} \upsilon_j \cdot r_j(\bar{X}(t)), \quad \text{with } \bar{X}(0) = \bar{x}_0. \tag{3.33}$$

Eqn (3.33) denotes an ODE model of a system consisting of N_r coupled autonomous ODEs. The representation of a chemical system as a set of ODEs is also known as the **reaction rate equation** [93]. Given that all reactions are at most of first order, then all rates r_j are constant or linear functions of x. In that case, Eqn (3.33) forms a system of linear ODEs and an analytical solution might be available. Even for nonlinear ODEs, where the analytical solution is not available, there are a number of ODE solvers, which can generally handle large and more complex systems.

3.4.3 Relation between reaction rates and reaction propensities

The propensity a_j of an elementary reaction R_j is of the general form

$$a_j(x) = \alpha_j \cdot h_j(x) \tag{3.34}$$

where α_j denotes the specific probability rate constant of R_j and $h_j(x)$ gives the number of distinct combinations of R_j reactant species available in state x, which is given by the product of binomial coefficients as shown below

$$h_j(x) := \prod_{i=1}^{N_s} \begin{pmatrix} x_i \\ b^r_{j,i} \end{pmatrix}. \tag{3.35}$$

The specific probability rate constant α_j of an elementary reaction R_j is related to the reaction rate constant c_j as follows

$$\alpha_j = c_j \cdot \frac{\prod_{i=1}^{N_s} b^r_{j,i}!}{\Omega^{|b^r_j|-1}}. \tag{3.36}$$

The reaction rate c_j is independent of Ω. The relation above show the Ω-dependence of α_j. Table 3.1 shows the reaction rates and reaction propensities.

Reaction order	Propensity	Rate
0^{th}	$a_0(x) = c_0 \cdot \Omega$	$r_0(\bar{x}) = c_0$
1^{th}	$a_1(x) = c_1 \cdot x_i$	$r_1(\bar{x}) = c_1 \cdot \bar{x}_i$
2^{th}	$a_2(x) = \frac{c_{2a}}{\Omega} \cdot x_i \cdot x_j$, with $i \neq j$	$r_{2a}(\bar{x}) = c_{2a} \cdot \bar{x}_i \cdot \bar{x}_j$
2^{th}	$a_2(x) = \frac{c_{2b}}{\Omega} \cdot x_i \cdot (x_i - 1)$, if $x_i \geq 1$	$r_{2b}(\bar{x}) = c_{2b} \cdot \bar{x}_i \cdot \bar{x}_j$

Table 3.1: **Reaction rates and reaction propensities for different reaction orders.** Adapted from Menz's dissertation [92].

3.5 Hybrid stochastic-deterministic approach

In the previous sections, we discussed the stochastic and the deterministic approaches for a chemical system. However, certain chemical systems can have a subset of reactions behaving deterministically and another subset behaving stochastically. An example is a biological reaction network with metabolic and regulatory parts, where the metabolic part can be described as a continuous-state deterministic process and the regulatory part behaving as a discrete-state stochastic process. Another example is the pharmacokinetics and pharmacodynamics during PrEP (pre-exposure prophylaxis), where antiviral pharmacokinetics (a continuous-state deterministic process) influences a discrete-state stochastic viral dynamics process. Modelling the pharmacokinetics as a continuous deterministic process is common practice in the pharmacometrics/systems pharmacology field and is supported by the fact that typically large quantities of drug molecules reach the target-site. On the other hand, the viral dynamics during the initial phase after a viral exposure is known to be discrete and stochastic in nature [19]. Obviously, dealing with such systems purely using the stochastic approach (for instance SSA) will be computationally impractical, while using purely deterministic approaches will lead to incorrect results. Hence, a hybrid stochastic-deterministic approach is required to properly deal with such systems.

3.5.1 Partitioning of the system

Typically, a hybrid stochastic-deterministic approach partitions the reactions rather than the species of the chemical systems into two subsets, namely the deterministic and stochastic subsets. Such partitioning can be performed in a static or dynamic manner. The static partitioning might be motivated by biological insights. For instance, the gene regulatory reactions behave stochastically, whereas the metabolic reactions behave deterministically [101]. The static partitioning is performed before the simulation and the partition remains intact during the whole simulation period.

On the other hand, the dynamic partitioning classifies the reactions into deterministic or stochastic subsets during the simulation according to some predefined criteria, which are based on levels of the species involved in a reaction and the values of reaction propensities [92]. Though the dynamic partitioning is clearly more general than the static partitioning, it involves additional computational efforts and parameter choices.

For our purpose i.e. to assess the PrEP efficacy of various antivirals, we classify the species of the system into deterministic and stochastic subsets along with reactions in a static manner [VI]. Assume that for a given network, a partition of reactions into two disjoint subsets, namely a deterministic reaction subset $\mathcal{R}_D \neq \{\}$ and a stochastic reaction subset $\mathcal{R}_S \neq \{\}$ such that $\mathcal{R}_D \cup \mathcal{R}_S = \{1, \cdots, N_r\}$. Similarly, consider a partition of the species into a deterministic subset $\mathcal{S}_D \neq \{\}$ and a stochastic subset $\mathcal{S}_S \neq \{\}$, which are disjoint and such that $\mathcal{S}_D \cup \mathcal{S}_S = \{S_1, \cdots, S_{N_s}\}$.

In order for a species S_i to belong to the deterministic subset $\mathcal{S}_D$, the following should be valid:

(i) It should be consumed or produced during the firing of at least one deterministic reaction. In other words, there is at least one reaction with index $j \in \mathcal{R}_D$, such that the net change of S_i after firing of R_j is non-zero i.e. $\upsilon_{j,i} \neq 0$.

(ii) It should not be affected by any stochastic reaction. For any reaction with index $k \in \mathcal{R}_S$, the net change of S_i after firing of R_k is zero i.e. $\upsilon_{k,i} = 0$.

Similarly, the inverse set of rules should apply to species belonging to the stochastic species subset $\mathcal{S}_S$. Hence, we can rearrange species of $X(t)$ and write

$$X(t) = \begin{bmatrix} Y(t) \\ Z(t) \end{bmatrix} \tag{3.37}$$

where $Y(t)$ and $Z(t)$ track all the stochastic and deterministic species respectively. For our system of interest, $Y(t)$ denotes the discrete stochastic viral dynamics and $Z(t)$ denotes the continuous deterministic antiviral pharmacokinetics.

3.5.2 Stochastic chemical system with time-variant reaction propensities

Here, we are interested in the simulation of $X(t)$, where the realization of stochastic $Y(t)$ is influenced by deterministic $Z(t)$, whereas $Z(t)$ is not affected by the realization of $Y(t)$. This is motivated by the insight that the antiviral pharmacokinetics $Z(t)$ affect the viral dynamics, whereas the viral dynamics does not affect antiviral pharmacokinetics.

The simulation of antiviral pharmacokinetics $Z(t)$ is straightforward and can be performed under the deterministic approach using ODE solvers (see 3.4). However, the realization of the stochastic viral dynamics under the influence of antiviral pharmacokinetics cannot be performed

[VI] Note, it is not always straightforward to clearly classify a species as deterministic or stochastic. For instance, a species involved in two reactions, where one reaction behaves determinisitically and one stochastically.

using the stochastic approach discussed in Section 3.3. In the Subsection 3.3, we presented the algorithms assuming **time-invariant reaction propensities**. Here, *time-invariant* [VII] *reaction propensities mean that they change only when the state changes implying that the reaction propensities are constant in between two firings of reactions belonging to* $\mathcal{R}_S$. In other words, they are a function of the stochastic state only i.e, $a_j(Y(t))$.

In contrast, the reaction propensities of the viral dynamics under the influence of PK is a time dependent function or influenced by some function of time other than the state of the stochastic subsystem. They are referred to as time-variant, which means that they are not constant between two firings of reactions belonging to $\mathcal{R}_S$. The reaction propensities are explicitly denoted as $a_j(Y(t), Z(t))$ in order to show the dependence on $Z(t)$. Next, we proceed to algorithms for a stochastic system, which can account for time-variant reaction propensities.

3.5.2.1 Chemical master equation

The chemical master equation can completely describe the statistics of stochastic processes for time-variant reaction propensities as shown below :

$$\begin{aligned}\frac{\partial}{\partial t}\mathbb{P}(Y(t) = y|Y(0) = y_0; Z(t)) &= \sum_{j\in\mathcal{R}_S} a_j(y - \upsilon_j, Z(t)) \cdot \mathbb{P}(Y(t) = y - \upsilon_j|Y(0) = y_0) \\ &- \sum_{j\in\mathcal{R}_S} a_j(y, Z(t)) \cdot \mathbb{P}(Y(t) = y|Y(0) = y_0). \end{aligned} \tag{3.38}$$

However, the system above (Eqn (3.38)) still suffers from the curse of dimensionality. Solving CME still requires circumventing the aforementioned problem.

3.5.2.2 Integral-based stochastic simulation algorithm

As previously mentioned, instead of solving the CME, Monte Carlo based approaches can be utilized to approximate the statistics. However, Gillespie's original SSA requires that the reaction propensity functions are time-invariant or constant between two firing events. In case of time-variant reaction propensities finding the time to the next reaction τ requires solving the following equation [102]:

$$\sum_{j\in\mathcal{R}_S} \int_t^{t+\tau} a_j(Y(s), Z(s))\, ds = \log\left(\frac{1}{u}\right) \tag{3.39}$$

where $u \sim \mathcal{U}(0, 1)$. Usually the closed-form solution of the multidimensional integral in the above equation is not known and numerical integration methods can be employed. Accordingly, Gillespie's SSA can be adapted to account for time-variant reaction propensities using numerical integration methods. The key to generating a realization is a function

$$A_0(t + \tau|t) = \sum_{j\in\mathcal{R}_S} \int_t^{t+\tau} a_j(Y(s), Z(s)). \tag{3.40}$$

The function is non-decreasing for $\tau > 0$, since the propensities are non-negative by definition. Hence, using a random variable $u \sim \mathcal{U}(0, 1)$ the time to next reaction τ is selected such that

$$A_0(t + \tau|t) + \log(u) = 0 \quad \text{with} \quad A_0(t|t) = 0 \tag{3.41}$$

is satisfied. The pseudo-code for the direct method for time-variant reaction propensities is given as below ([101]) :

[VII] They are also called as time-homogeneous propensities.

(i) Set initial time $t = 0$ and initial state $Z(0) = z_0$ and $Y(0) = y_0$.

(ii) Generate a random variable $u_1 \sim \mathcal{U}(0, 1)$.

(iii) Set $A_0(t|t) = 0$ and solve the system of ODEs starting at time $s = t$

$$\frac{d}{ds}Z(s) = \sum_{j \in \mathcal{R}_D} \upsilon_j \cdot r_j(Z(s)) \tag{3.42}$$

$$\frac{d}{ds}A_0(s|t) = \sum_{j \in \mathcal{R}_s} a_j(Y(s), Z(s)) \tag{3.43}$$

until time $s = t + \tau$ such that $A_0(t + \tau|t) + \log(u_1) = 0$.

(iv) Update the deterministic subsystem $Z(t + \tau)$.

(v) Randomly select a reaction $j \in \mathcal{R}_S$ such that the probability of selecting reaction R_j is

$$\frac{a_j(Y(t + \tau), Z(t + \tau))}{a_0(Y(t + \tau), Z(t + \tau))}. \tag{3.44}$$

(vi) Update the stochastic subsystem $Y(t + \tau) = Y(t + \tau) + \upsilon_j$.

(vii) Update time $t = t + \tau$.

(viii) Stop the simulation if the stopping criteria are met. If not, go to step (ii).

Integral-based SSA solves Eqn (3.39) by numerically integrating and summing the number of reaction propensities. These algorithms are exact, provided that there is a negligible numerical integration error. Secondly, their computational cost increases with the number of stochastic reactions, rendering them impractical and cumbersome for moderately big systems.

3.5.2.3 Rejection-based stochastic simulation algorithm (EXTRANDE)

Another class of algorithms has been recently proposed which employs point process **thinning techniques** or so called **rejection steps** [103, 104] for the simulation of the biochemical reaction networks in dynamic environments [28, 102, 105, 106]. These algorithms do not utilize analytical solutions or numerical integrations to solve Eqn (3.39). They rely on redundant samplings leading to a small *trade off* in the computational efficiency in order to gain *exactness*. Next, we briefly discuss an exact algorithm known as EXTRANDE (extra reaction algorithm for networks in a dynamic environment [28]).

Here, we are primarily concerned with the stochastic subsystem, henceforth we use N_r for the total number of stochastic reactions instead of the total number of stochastic and deterministic reactions of the system for the sake of simplicity. Similarly, N_s denotes the number of stochastic species instead of the total number of species. The stochastic time evolution of the system's state for time-variant reaction propensities is given below

$$Y(t) = Y(0) + \sum_{j=1}^{N_r} \upsilon_j \cdot \boldsymbol{\mathcal{P}}_j\left(\int_0^t a_j\left(Y(s), Z(s)\right)\, ds\right). \tag{3.45}$$

Next, we review the central idea of the EXTRANDE algorithm presented by Voliotis et al. [28]. The idea is to augment the stochastic system of interest with an **extra reaction**, in order to make

simulation feasible while at the same time keeping the statistics of the original unaugmented system intact. The firing of the extra reaction does not change the number of species of the original system. Let the extra reaction be indexed with integer $N_r + 1$.

Let $W(t) \in \mathbb{N}_0^{N_s+1}$ be the vector that tracks the state of augmented system such that

$$W_i(t) = \begin{cases} Y_i(t) & \text{if } i = 1, \cdots, N_s \\ \text{the number of firings of extra reactions till } t & \text{if } i = N_s + 1. \end{cases} \tag{3.46}$$

This requires that the augmentation of the system should be designed in such a way that the statistics of the original or unaugmented system remain unchanged.

To that end, let us define υ'_j as the new state change vectors. For $j = 1, \cdots, N_r$, the elements of the new state change vector υ'_j are

$$\upsilon'_{j,i} = \begin{cases} \upsilon_{j,i} & \text{if } i = 1, \cdots, N_s \\ 0 & \text{if } i = N_s + 1. \end{cases} \tag{3.47}$$

For $j = N_r + 1$ i.e, the state change vector for the extra reaction is as given below:

$$\upsilon'_{j,i} = \begin{cases} 0 & \text{if } i = 1, \cdots, N_s \\ 1 & \text{if } i = N_s + 1. \end{cases} \tag{3.48}$$

The new state change vectors are defined such that the firing of a reaction of the unaugmented system i.e, with index $j = 1, \cdots, N_r$ does not change $W_{N_s+1}(t)$. At the same time, the firing of the extra reaction only changes $W_{N_s+1}(t)$, but has no influence on other states.

The time evolution of the augmented system can be described as

$$W(t) = W(0) + \sum_{j=1}^{N_r+1} \upsilon'_j \cdot \mathcal{P}_j \left(\int_0^t a_j \left(Y(s), Z(s) \right) \, ds \right). \tag{3.49}$$

For the reaction indexed $j = 1, \cdots, N_r$ of the augmented system, the reaction propensities are the same as in the unaugmented or original system. Now, the question is how does one design the reaction propensity of the extra reaction $(a_{N_r+1}(Y(s), Z(s)))$? Let $B(t)$ be the stochastic upper bound of the sum of reaction propensities of the unaugmented system such that

$$a_0(t) = \sum_{j=1}^{N_r} a_j \left(Y(t), Z(t) \right) \leq B(t) \ , \ t \geq 0 \tag{3.50}$$

and assign the reaction propensity of the extra reaction according to

$$a_{N_r+1}(t) = B(t) - a_0(t). \tag{3.51}$$

By construction it follows that the sum of reaction propensities of the augmented system is $B(t)$ i.e,

$$B(t) = \sum_{j=1}^{N_r+1} a_j \left(Y(t), Z(t) \right). \tag{3.52}$$

The EXTRANDE algorithm requires selecting $B(t)$ such that it is constant in between firings. Generally, a user selects a look-ahead time horizon L and the upper bound is computed such that

$$B(t) = B(t + \tau) \geq a_0(t + \tau) \text{ where } 0 < \tau \leq L, \tag{3.53}$$

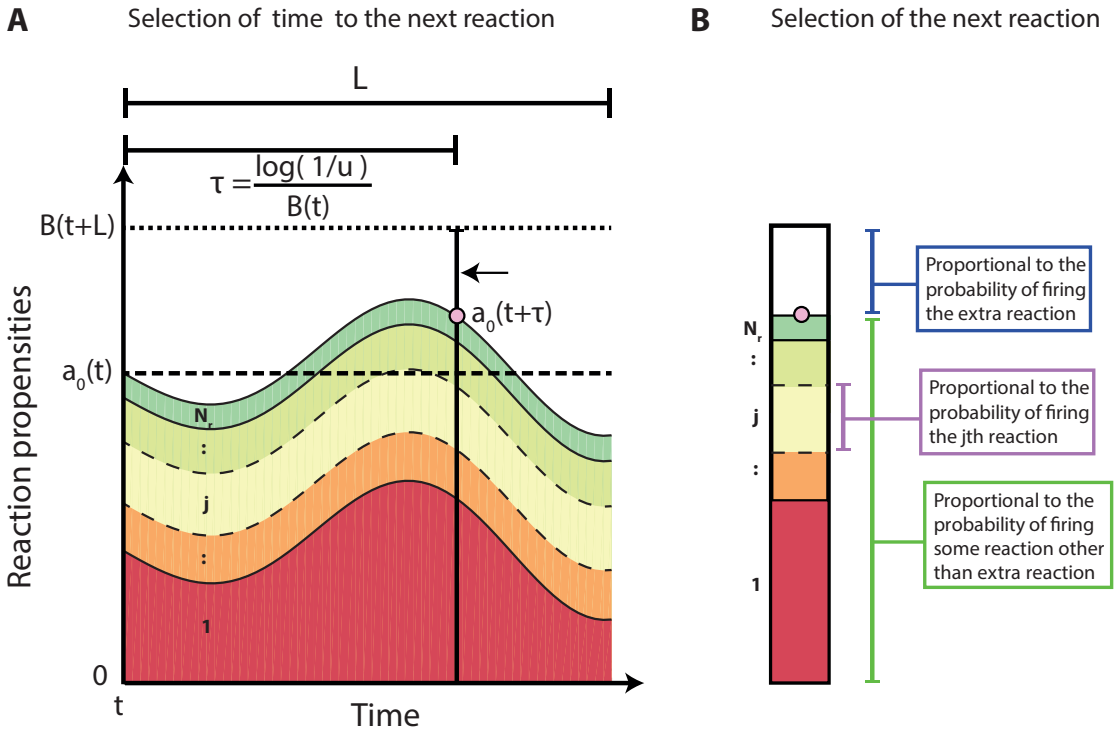

Figure 3.1: **Schematic depiction of steps in EXTRANDE for time-variant reaction propensities:** **A** : Selection of time to the next reaction for an augmented system at time t. Different colored areas depict the time evolution of reaction propensities $a_j(Y(t+s), Z(t+s))$, where $j = 1 \cdots N_r$ and $0 < s \leq L$ assuming no reaction fires in time interval $[t, t+L]$. The white region below the thin dashed horizontal line (marking the upper bound $B(t)$) represents the difference $B(t) - a_0(t+s)$ where $0 < s \leq L$. The thick black dashed horizontal line marks the sum of propensities of the unaugmented system at time t i.e, $a_0(t)$. For a look-ahead time horizon L, an upper bound is computed such that $B(t) = B(t+s) \geq a_0(t+s)$, where $0 < s \leq L$. The time to next reaction (τ) is sampled from an exponential distribution with intensity $B(t)$. The vertical solid line marks a randomly generated putative time for the next reaction ($t+\tau$) and the purple dot denotes the corresponding sum of reaction propensities ($a_0(t+\tau)$) at that time. **B**: Selection of the next reaction to fire. The stacked bar illustrates the sum of reaction propensities ($a_0(t+\tau)$) and individual reaction propensities ($a_j(t+\tau)$). The white area on the top is proportional to the probability of firing the extra reaction, whereas the colored area below is proportional to the probability of firing some reaction other than the extra reaction. Each colored area belongs to the particular reaction propensity ($a_j(t+\tau)$) and is proportional to the probability that the particular reaction fires next.

holds. This means that the computed sum of propensities for the augmented system is greater than the sum of propensities of unaugmented system from time t to $t+L$ assuming no stochastic reaction fires during this interval. Secondly, it is guaranteed that the augmented system has a constant sum of propensities between two firings. Hence, the time to the next reaction firing given that the augmented system is in state w at time t is an exponential random variable with intensity $B(t)$:

$$p(\tau|w;t) = B(t) \cdot \exp(-B(t) \cdot \tau) \tag{3.54}$$

and can be sampled as shown below

$$\tau = \frac{1}{B(t)} \cdot \log\left(\frac{1}{u}\right) \text{ where } u \sim \mathcal{U}(0,1). \tag{3.55}$$

Similarly, from the counting process theory [107], the probability that the next reaction is R_j

is given by:

$$p(j|\tau, w; t) = \frac{a_j(Y(t+\tau), Z(t+\tau))}{B(t)}. \tag{3.56}$$

From this, it follows that the probability of the extra reaction to fire is :

$$p(N_r + 1|\tau, w; t) = \frac{a_{N_r+1}(Y(t+\tau), Z(t+\tau))}{B(t)} = \frac{B(t) - a_0(t)}{B(t)}. \tag{3.57}$$

When an extra reaction is fired, the time of the system is updated from t to $t + \tau$ without changing the number of species i.e, $Y(t) = Y(t + \tau)$, whereas all other reactions change the number of species. If a randomly generated τ is bigger than look-ahead time horizon L, the time is updated $t = t + L$ without changing the state of unaugmented system. Thus, an ensemble of trajectories of the original system can be generated, by taking in account the time-variant reaction propensities. Figure 3.1 schematically depicts the two steps of EXTRANDE algorithm.

3.6 Summary

Biochemical reaction networks can be interpreted as chemical systems. In a microscopic level, the changes in chemical system is discrete and stochastic. This is captured by the definition of the reaction propensity function, which is regarded as the fundamental premise. The chemical master system follows directly from the fundamental premise. It describes the time-evolution of probability of being at a particular state and completely characterizes the statistic of the chemical system. Though theoretically elegant the chemical master equation can rarely be solved, as it suffers from the curse of dimensionality. This can be circumvented by using Monte Carlo techniques such as stochastic simulation algorithm to generate an ensemble of numerical realizations of the chemical system in exact accordance with the chemical master equation. When the thermodynamic limit is reached, the chemical system can be approximated as a continuous deterministic process represented by ODEs.

In addition to the chemical systems behaving stochastically and deterministically, there are coupled chemical systems. Such systems have a subset of their reactions behaving stochastically and another subset behaving deterministically. They can be dealt with a hybrid stochastic-deterministic approach. The hybrid approach encounters issues such as partitioning of a system and time-variant reaction propensities. Though the chemical master equation can account for the time-variant propensities, approximations need to be pursued to tackle the curse of dimensionality. Also, the time-variant reaction propensities necessitate modifications in stochastic simulation algorithms, regarding the generation of the time to next reaction. The integral-based stochastic simulation algorithm uses numerical integration methods, whereas rejection-based stochastic simulation algorithm employing thinning or rejection techniques to generate the time to next reaction.

CHAPTER 4

Methods for model building

A clinical trial seeks to understand dose-response relationships and can be conceptually divided into two parts. The first part aims to understand **pharmacokinetics** (PK) which study 'what does the body do to the drug?' [108]. The main goal of pharmacokinetics is to describe drug concentration time profiles in blood and relevant tissues under a particular dosage regimen. The second part, **pharmacodynamics** (PD), studies 'what does the drug do to the body or disease?' [108]. Pharmacodynamics relates the drug response(effects) to the concentration of the drug.

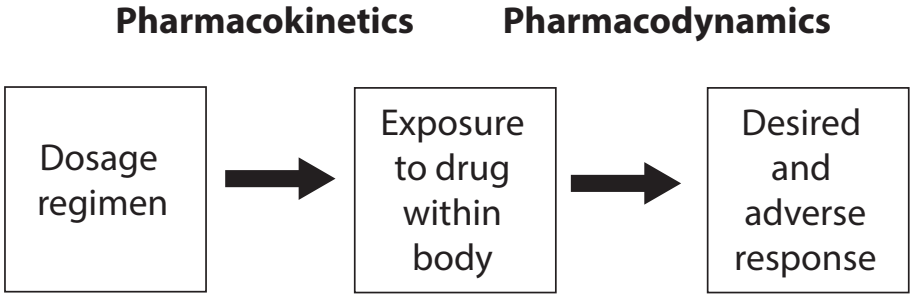

Figure 4.1: **Schematic view of pharmacokinetics and pharmacodynamics:** Pharmacokinetics relate the dosage to the drug exposure (for example drug concentration in plasma), whereas pharmacodynamics characterize the relationship between the drug exposure and response. Adapted from the book by Rowland et al. [108].

Modelling and simulation are vital steps in a PK-PD study. Previously, we dealt with simulation methods for chemical systems. Here, we proceed by providing a brief general introduction on inverse problems (model building) and subsequently discuss modelling approaches used in pharmacokinetics and pharmacodynamics.

4.1 Inverse problem/model building

Modelling characterizes data by analysing its systematic and error components [109]. Mathematically, modelling is an inverse or a backward problem, as it seeks to infer a model and its parameterization from the observed data. Once a model has been developed, it can be used to answer 'what if' questions [109]. This process is known as simulation. Mathematically, simulation is a forward problem and it involves generating 'data'(prediction) from a model.

Broadly speaking, a model can be classified into two categories: empirical models and mechanistic models [109]. Empirical models require few assumptions and are useful when little is known about the system under investigation from which the observed data are obtained. Though

empirical models can be used to characterize the data, caution should be taken for extrapolation using empirical models. In contrast, mechanistic models are built based on known principles of the underlying system, which demands more assumptions. This confers a benefit to the mechanistic models, such that they are suited for prediction and extrapolation purposes. For the PK-PD analysis of our system of interest, we will focus on mechanistic models. Roughly speaking, modelling requires solving the following two problems:

- Given a data set and assuming that a model is known, a modeller needs to identify the parameters of the model that best describes the data (**parameter identification**).
- Given a set of competing models and their parameterization, select the best model that describes the data (**model selection**).

4.1.1 Parameter identification

Assume that we have a dataset $\{(y_1, x_1), \cdots (y_N, x_N)\}$, where x_i and y_i are the i$^{\text{th}}$ **predictor variables** and the i$^{\text{th}}$ **response variable** respectively. Let f be the function representing a model and the term θ be its parameters or 'set of parameters'. A simple way to describe a response variable is to break it down as a sum of parts described by the model $f(\theta, x_i)$ and the residual error ε_i as shown below:

$$y_i = f(\theta, x_i) + \varepsilon_i. \tag{4.1}$$

A modeller seeks to infer the value of the unknown parameters (θ), which best describe the data. Next, we will give a brief overview of methods for parameter identification, namely ℓ_p minimization and maximum likelihood methods.

4.1.1.1 ℓ_p-norm minimization and least square method

Under the ℓ_p-norm minimization criterion method, the best-fit estimate of the unknown parameters θ is described as the estimate that minimizes the ℓ_p-norm distance between vectors of response variables and the model prediction [110]. Mathematically, we can write the best estimate of a weighted ℓ_p-norm as

$$\theta^* = \underset{\theta \in \Theta}{\operatorname{argmin}} \left(\sum_{i=1}^{N} \left(\frac{|y_i - f(\theta, x_i)|}{w_i} \right)^p \right)^{1/p} \tag{4.2}$$

where $1 \leq p \leq \infty$ and w_i is a positive constant known as the weight associated with the i$^{\text{th}}$ observation.

In biological applications, the ℓ_2 norm minimization is widely used, where the best estimate is the estimate that minimizes the square root of sum of squares of residual errors as shown below:

$$\theta^* = \underset{\theta \in \Theta}{\operatorname{argmin}} \left(\sum_{i=1}^{N} \left(\frac{y_i - f(\theta, x_i)}{w_i} \right)^2 \right)^{1/2}. \tag{4.3}$$

The best estimate from a ℓ_2 minimization is equivalent to the estimate obtained by the minimization of sum of squares of weighted errors i.e,

$$\theta^* = \underset{\theta \in \Theta}{\operatorname{argmin}} \left(\sum_{i=1}^{N} \left(\frac{y_i - f(\theta, x_i)}{w_i} \right)^2 \right)^{1/2} = \underset{\theta \in \Theta}{\operatorname{argmin}} \sum_{i=1}^{N} \left(\frac{y_i - f(\theta, x_i)}{w_i} \right)^2. \tag{4.4}$$

This method of minimization is known as the least square method, first proposed by Gauss [111].

Intuitively, reducing some ℓ_p-norm distance between the vectors of response variables and the model prediction makes sense. However, the ℓ_p-norm minimization method is agnostic to the information regarding the residual errors i.e. does not explicitly state assumptions on the distribution of response variables or residual errors [112]. The question arises whether the selection of ℓ_p-norm can be better guided by the information on the distribution of response variables or residual errors. For instance, when the residual errors are from a long-tailed distribution such as a symmetric exponential function ($\exp(-|\varepsilon|)$), the ℓ_1 minimization has been shown to be more diserable. Similarly, when errors are due to rounding off the last digit, the parameter identification can be interpreted as an ℓ_∞ minimization problem [110].

Following this line of thought, next we will present the maximum likelihood method for the parameter identification problem which explicitly makes use of the information regarding the statistics of residual errors or distributions of observed response variables. In particular, we will focus on normal distributed residual errors due to their wide applications and importance in biology.

4.1.1.2 Maximum likelihood method

The central idea behind the maximum likelihood method popularized by Fischer [113] is to choose the model parameter that makes the observed data most likely. The first step in the maximum likelihood method is to define the likelihood function as a function of the model parameters given the observed data. For the discrete random variable, the likelihood can be interpreted as the probability of the observed data given the model parameters. For the continuous random variable, the likelihood is described using its probability density function [114] [I]. The likelihood function is defined as

$$\mathcal{L}(\theta|\mathbf{y}) := p(\mathbf{y}|\theta) \tag{4.5}$$

where $p(\mathbf{y}|\theta)$ is the probability density function of the multidimensional vector of response variables $\mathbf{y}$ given model parameters (θ). Under the independence assumption, the likelihood of parameter θ given all the response variables $\mathbf{y} = (y_1, \cdots y_N)$ is given by the product

$$\mathcal{L}(\theta|\mathbf{y}) = \prod_{i=1}^{N} \mathcal{L}(\theta|y_i). \tag{4.6}$$

This highlights the fact that the likelihood of all observed response variables is the joint probability density function. Let us assume that the residual errors are independent and normally distributed as shown below:

$$\varepsilon_i \sim \mathcal{N}(0, \sigma_i^2) \tag{4.7}$$

where σ_i represents the standard deviation for the i$^{\text{th}}$ residual error. This is equivalent to the following statement:

$$y_i \sim \mathcal{N}(f(\theta, x_i), \sigma_i^2). \tag{4.8}$$

i.e. the response variable y_i is normally distributed with a mean equal to the model prediction $f(\theta, x_i)$ and with a standard deviation of σ_i. Thus, the likelihood for the response variable y_i can be written as follows:

$$\mathcal{L}(\theta|y_i) := p(y_i|\theta) = \frac{1}{\sigma_i \cdot \sqrt{2 \cdot \pi}} \cdot \exp\left(-\frac{1}{2} \cdot \left(\frac{y_i - f(\theta, x_i)}{\sigma_i}\right)^2\right) \tag{4.9}$$

which uses the equation for the probability density function of a normal distribution.

[I] Unless otherwise stated, we assume the data to be continuous random variables.

Instead of the maximization of the likelihood, the maximization of the logarithm of likelihood (log-likelihood) is performed since it is more convenient to handle. The log-likelihood function is

$$\begin{aligned}\log \mathcal{L}(\theta|\mathbf{y}) &= \log\left(\prod_{i=1}^{N} \mathcal{L}(\theta|y_i)\right), \\ &= \sum_{i=1}^{N} \log\left(\mathcal{L}(\theta|y_i)\right),\end{aligned}$$

Substituting Eqn (4.9) above and further simplification results in the following equation:

$$\log \mathcal{L}(\theta|\mathbf{y}) = -\sum_{i=1}^{N} \log\left(\sigma_i \cdot \sqrt{2\cdot\pi}\right) - \frac{1}{2}\cdot\sum_{i=1}^{N}\left(\frac{y_i - f(\theta, x_i)}{\sigma_i}\right)^2. \tag{4.10}$$

The best-fit estimate or maximum likelihood estimate is achieved by maximizing above Eqn 4.10. Simplication steps are shown below

$$\begin{aligned}\theta^* &= \underset{\theta\in\Theta}{\operatorname{argmax}} \log \mathcal{L}(\theta|y), \\ &= \underset{\theta\in\Theta}{\operatorname{argmin}} -\log \mathcal{L}(\theta|y), \\ &= \underset{\theta\in\Theta}{\operatorname{argmin}} \left(\sum_{i=1}^{N} \log\left(\sigma_i \cdot \sqrt{2\cdot\pi}\right) + \frac{1}{2}\cdot\sum_{i=1}^{N}\left(\frac{y_i - f(\theta, x_i)}{\sigma_i}\right)^2\right), \\ &= \underset{\theta\in\Theta}{\operatorname{argmin}} \left(2\cdot\sum_{i=1}^{N} \log\left(\sigma_i \cdot \sqrt{2\cdot\pi}\right) + \sum_{i=1}^{N}\left(\frac{y_i - f(\theta, x_i)}{\sigma_i}\right)^2\right).\end{aligned} \tag{4.11}$$

Under the assumption that σ_i is independent of the model prediction $f(\theta, x_i)$, which is usually the case [115], the first summand is constant and can be removed. This gives the following:

$$\theta^* = \underset{\theta\in\Theta}{\operatorname{argmax}} \log \mathcal{L}(\theta|y) = \underset{\theta\in\Theta}{\operatorname{argmin}} \left(\sum_{i=1}^{N}\left(\frac{y_i - f(\theta, x_i)}{\sigma_i}\right)^2\right). \tag{4.12}$$

Hence, under the assumption that residual errors are independent and are from a normal distribution, the estimate of the maximimum likelihood method is equivalent to that of the least square method or ℓ_2 norm minization [109]. Mathematically,

$$\boxed{\theta^* = \underset{\theta\in\Theta}{\operatorname{argmax}} \log \mathcal{L}(\theta|y) = \underset{\theta\in\Theta}{\operatorname{argmin}} \sum_{i=1}^{N}\left(\frac{y_i - f(\theta, x_i)}{\sigma_i}\right)^2}. \tag{4.13}$$

Often rather than directly maximizing the likelihood function, equivalent weighted least squares can be constructed. For some frequent error types, equivalent weighted least squares are listed below ([116]):

(i) When all residual errors are independent and from the same distribution (i.e. $\forall i, \sigma_i = \sigma$) also known as *constant additive error*, the maximum likelihood estimate is identical to the best estimate from minimization of the sum of unweighted squared errors i.e,

$$\theta^* = \underset{\theta\in\Theta}{\operatorname{argmax}} \log \mathcal{L}(\theta|y) = \underset{\theta\in\Theta}{\operatorname{argmin}} \sum_{i=1}^{N} (y_i - f(\theta, x_i))^2. \tag{4.14}$$

(ii) Similarly, when residual errors are independent and are proportional to the prediction i.e. $\forall i, \sigma_i = f(\theta, x_i) \cdot \sigma$ also known as *proportional error*, the maximum likelihood estimate is obtained by using the following least square minimization [116]:

$$\theta^* = \underset{\theta \in \Theta}{\operatorname{argmax}} \log \mathcal{L}(\theta|y) = \underset{\theta \in \Theta}{\operatorname{argmin}} \sum_{i=1}^{N} \left(\frac{y_i - f(\theta, x_i)}{f(\theta, x_i)/f_{gm}} \right)^2, \tag{4.15}$$

where

$$f_{gm} = \left(\prod_{i=1}^{N} |f(\theta, x_i)| \right)^{1/N}.$$

(iii) When residual errors are exponential; this means

$$y_i = f(\theta, x_i) \cdot \exp(\varepsilon), \quad \varepsilon \sim \mathcal{N}(0, \sigma^2), \tag{4.16}$$

the maximum likelihood estimate can be achieved by the following weighted least squares minimization

$$\theta^* = \underset{\theta \in \Theta}{\operatorname{argmax}} \log \mathcal{L}(\theta|y) = \underset{\theta \in \Theta}{\operatorname{argmin}} \sum_{i=1}^{N} (\log(y_i) - \log(f(\theta, x_i)))^2. \tag{4.17}$$

To reiterate, the maximum likelihood method is statistically more refined than the ℓ_p-norm minimization method, which does not explicitly state its statistical assumptions. However, often a maximum likelihood problem can be simplified to an equivalent ℓ_p-norm minimization problem.

4.1.2 Model selection

A modeller faces the problem of selecting a model from a set of candidate models that best approximates the reality given the data at hand. The candidate models vary in their complexity, which is reflected in the number of parameters required by a model [117, 118]. Generally, a more complex model tends to better fit the data than a simpler one [109]. Here, it should be emphasized that *the task of the modeller is to better approximate the reality rather than to better fit the data.* It has been observed that increasing the model complexity improves the goodness of fit of the model, however, beyond a certain threshold its generalizability decreases [109] (see Figure 4.2). Hence, unnecessary complexity should be avoided. This is also advocated by Occam's razor or principle of parsimony [117].

To rephrase, models with few parameters do not sufficiently capture the reality, which leads to underfitting, whereas models with many parameters capture spurious trends. Thus, a model selection problem calls for a proper trade-off between underfitting and overfitting [117]. Next, we will introduce a selection criterion known as Akaike Information Criteria (AIC), which takes these considerations into account.

4.1.2.1 Akaike information criteria

Given m candidate models describing the observed data at hand, let $f_1, \cdots, f_m$ be functions and $n_1, \cdots, n_m$ be the number of parameters of those models. The Akaike Information criteria (AIC) for the i^{th} model is

$$\mathrm{AIC}_i = -2 \cdot \log \mathcal{L}_i + 2 \cdot n_i \tag{4.18}$$

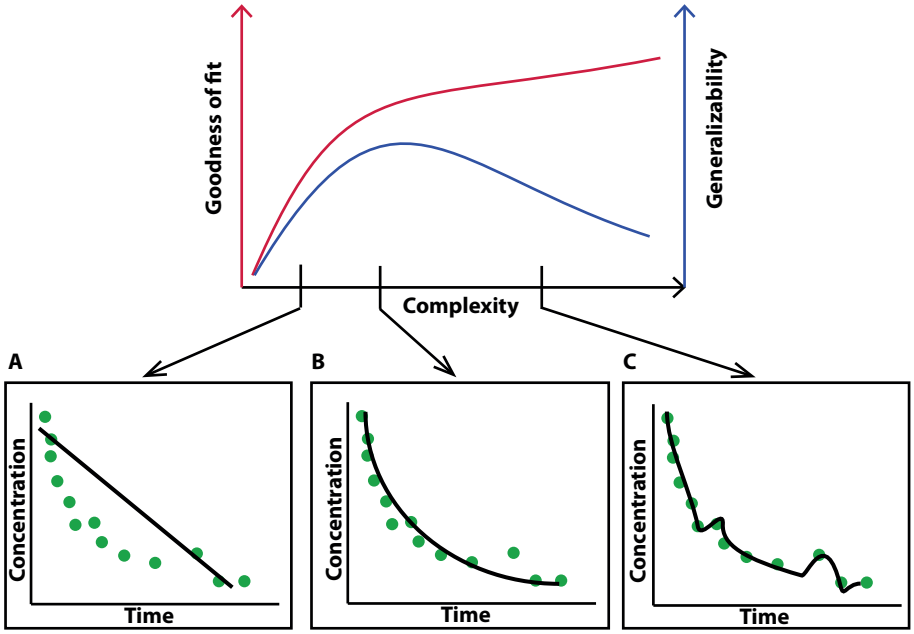

Figure 4.2: **Relationship between goodness of fit and generalizability vs. model complexity:** The figure illustrates schematically that increasing the model complexity improves the goodness of fit. On the otherhand, the generalizability of the model increases with increasing model complexity upto a certain threshold, after which it decreases. The three figures at the bottom exemplify scenarios of underfitting, good fitting and overfitting. In panel A, the model complexity is less than required to explain the observed data. In panel C, the model complexity is more than justified by the data. In panel B, there is good balance between complexity and goodness of fit. Adapted from the book by Bonate et al. [109].

which consists of the maximum likelihood for the i$^{\text{th}}$ model ($\mathcal{L}_i$) and the number of parameters n_i. Roughly speaking, AIC quantifies the quality of data-fitting by a model and at the same time penalize its complexity. AIC is based on Kullback-Leiber information and represents a distance between the reality and the approximation by the model.

For each candidate model, AIC values are computed and the candidate model with the minimum AIC is selected as the best model. Conceptually, this selection means that a candidate model is selected with the least distance to the reality given the data at hand [119].

The individual AIC values are not interpretable and should be seen in comparison to AIC values of other candidate models. AIC values can be used to compute metrics with more intuitive interpretation. The metric is known as Akaike weight of model, which is defined as [109, 119]:

$$w(\text{AIC}_i) = \frac{\exp\left(-\frac{1}{2}\cdot(\text{AIC}_i - \text{AIC}_{\text{min}})\right)}{\sum_{k=1}^{m}\exp\left(-\frac{1}{2}\cdot(\text{AIC}_k - \text{AIC}_{\text{min}})\right)} \tag{4.19}$$

where AIC_{min} is the minimum of all the AIC values i.e.

$$\text{AIC}_{\text{min}} = \min\{\text{AIC}_1, \cdots, \text{AIC}_m\}\,. \tag{4.20}$$

The Akaike weight of a model can be interpreted as the probability that the model is correct given the set of candidate models and the observed data [119]. The weight provides the strength of evidence in favour of- or against a particular model. Note that the best model among the candidate models still might fail to adequately describe the data [120].

When the data size N is relatively small in comparison to the number of parameters n, the use of AIC may favour complex models [117]. To circumvent this, generally when $N/n < 40$ corrected AIC should be used. The corrected AIC is computed as follows:

$$c\text{AIC} = -2 \cdot \log \mathcal{L}f + 2 \cdot n + 2 \cdot \frac{n \cdot (n+1)}{N - n - 1}. \tag{4.21}$$

In addition to AIC, Bayesian Information Criterion (BIC) is widely used. The analytical expression for BIC is similar to that of AIC, however, the two criteria differ in their underlying assumptions. BIC assumes the true model is in the set of candidate models, whereas AIC does not make such assumption [119][II]. Besides information criteria, visual predictive checks and cross validation techniques should be applied whenever possible.

4.2 Model building in pharmacokinetics and pharmacodynamics

A PK-PD study is performed with a cohort of individuals sampled from a population of interest and for each individual quantities of interest are measured regularly. The response variables vary from one another, which necessitates quantification of their variability and understanding of sources of variation. This is commonly known as the 'population approach'. Next, we will describe prevalent methods for population approaches in pharmacokinetics and pharmacodynamics [III].

Let us assume that there are N_I individuals in the cohort of the study. For each individual in the cohort, quantities of interest are sampled regularly. Let $N_{i,J}$ represent the number of observations for i$^{\text{th}}$ individual. Let $y_{i,j}$ represents the j$^{\text{th}}$ response variable of the i$^{\text{th}}$ individual. Usually, the response variables are continuous variables which are observed at discrete time points. Examples of response variables in pharmacokinetics study are drug concentrations in blood plasma or in relevant tissues or cells. In pharmacodynamics studies, examples are viral load in plasma of HIV-1 infected persons or some other clinical endpoints.

Let $\mathbf{y}_i$ be the vector of response variables belonging to the i$^{\text{th}}$ individual. [IV] Mathematically,

$$\mathbf{y}_i = \begin{pmatrix} y_{i,1} \\ \cdots \\ y_{i,j} \\ \cdots \\ y_{i,N_{i,J}} \end{pmatrix} \in \mathbb{R}^{N_{i,J}} \tag{4.22}$$

Similarly, let $\mathbf{x}_{i,j}$ denote the j$^{\text{th}}$ predictor variable of the i$^{\text{th}}$ individual. For instance, the time point associated with the j$^{\text{th}}$ measurement denoted by $t_{i,j}$ is a predictor variable. Other examples include details of the dosing regimen, such as the dosing amount of a drug and time points of dosing. Let $\mathbf{Dose}_i$ and $\mathbf{T}_i$ be vectors representing the sequence of dosing amounts administered and the corresponding time points for the i$^{\text{th}}$ individual respectively:

$$\mathbf{Dose}_i = \begin{pmatrix} \text{Dose}_{i,1} \\ \cdots \\ \cdots \\ \text{Dose}_{i,N_{i,D}} \end{pmatrix} \quad \text{and} \quad \mathbf{T}_i = \begin{pmatrix} \mathcal{T}_{i,1} \\ \cdots \\ \cdots \\ \mathcal{T}_{i,N_{i,D}} \end{pmatrix}$$

[II] Besides AIC and BIC, other information criteria exist such as Takeuchi's Information Criterion (TIC) and Widely Applicable Information Criterion (WAIC) and might be more suitable for certain cases [120].

[III] The modelling approaches in pharmacokinetics and pharmacodynamics are in part adapted from Ette et al. [121].

[IV] Obviously, there can be more than one response variable, such that $y_{i,j}$ is a vector instead of a scalar variable and correspondingly $\mathbf{y}$ is a matrix instead of a vector. In such a case, one can introduce $y_{i,j,k}$ where k denotes the index of the response variable. For simplicity, we assume that there is only one response variable, which implies that $y_{i,j}$ is a scalar.

where $N_{i,D}$ is the number of doses administered to the i$^{\text{th}}$ individual. Besides these variables, measurements characteristic to the individual such as age, total body weight and height can also influence the response variables. These variables are called covariates. In general, covariates are assumed to be constant for the time horizon of the experiment. Let $\mathbf{C}_i$ be the vector of $N_{i,C}$ covariates belonging to the i$^{\text{th}}$ individual:

$$\mathbf{C}_i = \begin{pmatrix} C_{i,1} \\ \cdots \\ \cdots \\ C_{i,N_{i,C}} \end{pmatrix}$$

Let $\mathbf{x}_{i,j}$ be represented as a vector, which contains all the measured predictor variables that might influence the response variable $y_{i,j}$. Mathematically,

$$\mathbf{x}_{i,j} = \left(t_{i,j}, \mathbf{Dose}_i^\top, \mathbf{T}_i^\top, \mathbf{C}_i^\top\right).$$

and correspondingly $\mathbf{x}_i$ is a matrix of predictor variables belonging to the i$^{\text{th}}$ individual:

$$\mathbf{x}_i = \begin{pmatrix} \mathbf{x}_{i,1} \\ \cdots \\ \mathbf{x}_{i,j} \\ \cdots \\ \mathbf{x}_{i,N_I} \end{pmatrix}. \tag{4.23}$$

Next, we present various population approaches used in PK-PD studies.

4.2.1 Naive averaging approach

Usually in preclinical and clinical pharmacokinetics studies, the dosing regimen as well as sampling schedules are identical for all individuals. It means that for each sampling time, there are a number of response variables available from different individuals. Analysis of such data can be performed by naive averaging, which consists of the following steps:

(i) Compute the average value for each sampling time.

$$\bar{y}_{\bullet,j} = \frac{1}{N_I} \cdot \sum_{i=1}^{N_I} y_{i,j} \tag{4.24}$$

where $\bar{y}_{\bullet,j}$ is the average j$^{\text{th}}$ response variable across all individuals.

(ii) Perform the modelling exercise on the profile of the average response variable.

Implicitly, this approach assumes that the average- or typical response profile belongs to a typical (hypothetical) individual. As convention, the average response variable can be separated as shown below

$$\bar{y}_{\bullet,j} = f(\mathbf{x}_{\bullet,j}, \theta) + \varepsilon_{\bullet,j} \tag{4.25}$$

where $f(\mathbf{x}_{\bullet,j}, \theta)$ is the j$^{\text{th}}$ prediction and $\varepsilon_{\bullet,j}$ is the corresponding error term. The model parameter θ is interpreted as a typical- or mean parameter. Interestingly, assuming a typical individual imposes that the predictor variable $\mathbf{x}_{\bullet,j}$ is also typical. This has no effect on dosing regimens and sampling time points, since they are identical for all individuals. However, the covariates are implicitly

assumed to be typical. If ordinary least squares is applied, the following objective function is minimized:

$$\mathrm{OF}_{\mathrm{NA}}(\theta) := \sum_{j=1}^{N_{i,J}} \left(y_{\bullet,j} - f(\mathbf{x}_{\bullet,j}, \theta)\right)^2 \tag{4.26}$$

The advantage of this approach is its simplicity. However, there are several drawbacks of this approach. The smoothing effect of averaging can lead to loss of individual peculiarities. For example, the averaging can render secondary peaks in the plasma concentration time profile inconspicuous, if the secondary peaks occur at different time points. Thus, the approach may lead to a misinformed model. For instance, averaging the monoexponential profiles from two individuals with significantly different half-lives may produce a curve exhibiting an apparent biexponential decay. Thus, a correct model with monoexponetial decay may be discarded in favour of an incorrect model with biexponential decay. Furthermore, the approach is sensitive to outliers, since averaging is strongly affected by outliers.

Secondly, the approach attributes an average response profile to a typical individual, which might not be true due to nonlinearity of model functions. Furthermore, the approach does not provide the study of variability of the parameters and also does not allow discerning the influence of variability of covariates on responses.

4.2.2 Naive pooled data approach

The naive pooled data approach is more general than the naive averaging approach. It assumes that all data arises from one unique individual [122] and the response variable can be written as

$$y_{i,j} = f(\mathbf{x}_{i,j}, \theta) + \varepsilon_{i,j} \tag{4.27}$$

where θ is the model parameter belonging to the unique individual. If an ordinary least square method is applied to infer the parameters, then the following objective function is minimized

$$\mathrm{OF}_{\mathrm{NP}}(\theta) := \sum_{i=1}^{N_I} \left(\sum_{j=1}^{N_{i,J}} \left(y_{i,j} - f(\mathbf{x}_{i,j}, \theta)\right)^2 \right) \tag{4.28}$$

where N_I represents the total number of individuals and $N_{i,J}$ denotes the total number of observations for the i^{th} individual. $f(\mathbf{x}_{i,j}, \theta)$ is the model prediction with θ for the j^{th} time point and i^{th} individual. Unlike the naive averaging approach, the naive pooling approach does not require an identical sampling schedule for all individuals. The drawbacks of the naive pooling approach are similar to the naive averaging approach.

4.2.3 Two-stage approach

Both naive averaging- and naive pooling approaches focus on the average behaviour of the cohort neglecting the measurement of deviation from the mean (dispersion). The standard two-stage approach delivers both. The first step is to perform a model and parameter inference for each individual profile. The response variable can be written as

$$y_{i,j} = f(\mathbf{x}_{i,j}, \theta_i) + \varepsilon_{i,j} \tag{4.29}$$

where θ_i is the model parameter specific to the i^{th} individual. The modelling exercise requires performing N_I separate model fittings, one for each individual. The objective function for the i^{th}

individual, if the ordinary least square method is applied, is given by

$$\mathrm{OF_{TS}}(\theta_i) := \sum_{j=1}^{N_{i,J}} \Big(y_{i,j} - f(\mathbf{x}_{i,j}, \theta_i)\Big)^2 \tag{4.30}$$

The second step involves obtaining statistical measures from the parameter of individuals. The mean and dispersion of parameters are computed as shown below

$$\bar{\theta} = \frac{1}{N_I} \cdot \sum_{i=1}^{N_I} \theta_i \quad \text{and} \quad \Psi = \frac{1}{N_I} \cdot \sum_{i=1}^{N_I} \Big(\theta_i - \bar{\theta}\Big) \cdot \Big(\theta_i - \bar{\theta}\Big)^\top, \tag{4.31}$$

where θ_i is the parameter estimated for the i^{th} individual.

Though simple and straightforward, the method has several drawbacks. For each individual, a model fitting is performed on its data neglecting what has been learned from the model fitting from other individuals. This becomes unsatisfactory in case of imbalanced data [123]. For instance, if there is a mix of dense and sparse data for individuals. The parameter estimation performs satisfactorily for individuals with a dense data situation and fails for individuals with a sparse data situation rendering the estimation of statistical measures difficult [122, 124]. Moreover, the approach is known to be biased and usually overestimates the variance [125]. These problems can be overcome by a statistically more rigorous method known as nonlinear mixed-effects approach [126].

4.2.4 Nonlinear mixed-effects approach

Nonlinear mixed-effect approaches or hierarchical modelling approaches are currently the state of art in the population study of PK and PD [127]. In comparison to the two-stage approach, the nonlinear mixed-effect approach is parsimonious in terms of parameters and statistically more rigorous. Unlike the two-stage approach, the model fitting is performed on the data of all individuals simultaneously instead of one at a time. This confers benefit to the nonlinear mixed-effect approach, when sampling is sparse for some individuals in the data-sets (imbalanced data) [109, 123, 126]. The knowledge gained from individuals with denser sampling helps to overcome the problem of sparsity in other individuals [127].

The term ‘nonlinear’ in the nomenclature of the approach refers to the characteristic of the model function, which denotes that the response variable is nonlinearly dependent on its model parameters [109]. The term ‘mixed-effects’ comes from statistical modelling and it refers to incorporation of ‘fixed effects’ and ‘random effects’. Fixed effects are parameters associated with an entire population of interest or with certain repeatable levels of experimental factors. Random effects are associated with an individual sampled randomly from the population of interest.

The nonlinear mixed-effects approach can be separated into three components, namely structural, covariate and stochastic submodels [128]. The structural submodel consists of a function governing the temporal relationship between the response variables and predictor variables. The covariate submodel describes the influence of covariates on the model parameter of the structural submodel. The stochastic submodel describes the statistics of model parameters and errors. This includes intra- and inter-individual variations of model parameters.

In general, the nonlinear mixed-effects in PK-PD studies is modelled in a two-level hierarchy with individual and population levels [129]. At the individual level, we have

$$\begin{aligned} y_{i,j} &= f(\mathbf{x}_{i,j}, \theta_i) + \varepsilon_{i,j}, \quad j = 1, \cdots N_{i,J} \\ \mathbf{y}_i &= f(\mathbf{x}_i, \theta_i) + \varepsilon_i. \quad \text{in vector form} \end{aligned} \tag{4.32}$$

The function f is also known as a structural submodel. The residual error or intra-individual error is assumed to come from a multivariate normal distribution

$$\varepsilon_i \sim \mathcal{N}(0, \Sigma). \tag{4.33}$$

where Σ is covariance matrix. For simplicity, here we assume that the intra-individual errors are homoscedastic, independent and identically distributed for all individuals i.e,

$$\varepsilon_{i,j} \sim \mathcal{N}(0, \sigma^2) \quad \text{and in vector form} \quad \varepsilon_i \sim \mathcal{N}(0, \mathbf{Id} \cdot \sigma^2). \tag{4.34}$$

The intra-individual error is part of the stochastic submodel.

At the population level, we assume that model parameters come from a particular distribution. A simple formulation of individual model parameters is shown as below:

$$\theta_i = \theta_{pop} + \Delta_i \tag{4.35}$$

where θ_{pop} is the mean population parameter. Usually Δ_i is assumed to come from a multivariate normal distribution such that

$$\Delta_i \sim \mathcal{N}(0, \Psi) \tag{4.36}$$

where Ψ is the covariance matrix. Equivalently, we can write

$$\theta_i \sim \mathcal{N}(\theta_{pop}, \Psi) \tag{4.37}$$

The covariate submodel considers the influence of individual's covariates on response variables. This is performed such that the individuals' model parameters are influenced by their covariates as below:

$$\theta_i = f_c(\theta_{pop}, \mathbf{C}_i, \phi) + \Delta_i \tag{4.38}$$

where f_c is the covariate function which takes the population parameter θ_{pop}, the vector of covariates $\mathbf{C}_i$ and a parameter vector ϕ. Correspondingly, the model parameters of the individual can be written as:

$$\theta_i \sim \mathcal{N}(f_c(\theta_{pop}, \mathbf{C}_i, \phi), \Psi). \tag{4.39}$$

The statistical submodel describing the inter-individual variation (distribution of the individual model parameter θ_i) is also the part of the stochastic submodel.

For the given data set, the nonlinear mixed-effect modelling aims at finding the unknown parameters, which is the set $\left\{\theta_{pop}, \Psi, \Sigma\right\}$ or $\left\{\theta_{pop}, \phi, \Psi, \Sigma\right\}$ when a covariate submodel is considered. To determine the maximum likelihood estimate, let us look at the likelihood function for the nonlinear mixed-effect modelling for all observed response variables, also known as population likelihood function: [V]

$$\begin{aligned} \mathcal{L}(\theta_{pop}, \Psi, \Sigma|\mathbf{y}) &= p(\mathbf{y}|\theta_{pop}, \Psi, \Sigma), \\ &= \prod_{i=1}^{N_I} p(\mathbf{y}_i|\theta_{pop}, \Psi, \Sigma), \\ &= \prod_{i=1}^{N_I} \mathcal{L}(\theta_{pop}, \Psi, \Sigma|\mathbf{y}_i) \end{aligned} \tag{4.40}$$

[V] For simplicity, hitherto we ignore the covariate submodel.

which is the joint probability density function and, as shown above, it can be written as the product of individual likelihood functions. The individual likelihood function can be further separated as shown below[VI]

$$\begin{aligned}
\mathcal{L}(\theta_{pop}, \Psi, \Sigma|\mathbf{y}_i) = p(\mathbf{y}_i|\theta_{pop}, \Psi, \Sigma) &= \int p(\mathbf{y}_i, \theta_i|\theta_{pop}, \Psi, \Sigma)\, d\theta_i, \\
&= \int p(\mathbf{y}_i|\theta_i, \theta_{pop}, \Psi, \Sigma) \cdot p(\theta_i|\theta_{pop}, \Psi, \Sigma)\, d\theta_i, \\
&= \int p(\mathbf{y}_i|\theta_i, \Sigma) \cdot p(\theta_i|\theta_{pop}, \Psi)\, d\theta_i, \\
&= \int \underbrace{\mathcal{L}(\theta_i, \Sigma|\mathbf{y}_i)}_{\text{individual level}} \cdot \underbrace{p(\theta_i|\theta_{pop}, \Psi)}_{\text{population level}}\, d\theta_i, \qquad (4.41)
\end{aligned}$$

where the likelihood $\mathcal{L}(\theta_i, \Sigma|\mathbf{y}_i)$ denotes the individual nonlinear regression likelihood. As previously described in Subsection 4.1.1.2, the maximum likelihood estimate is obtained by maximizing the log likelihood function. The maximization problem for the nonlinear mixed-effect modelling is

$$(\theta^*_{pop}, \Psi^*, \Sigma^*) = \underset{(\theta_{pop}, \Psi, \Sigma)}{\operatorname{argmax}} \log \mathcal{L}(\theta_{pop}, \Psi, \Sigma|\mathbf{y}) \qquad (4.42)$$

where $(\theta^*_{pop}, \Psi^*, \Sigma^*)$ is the maximum likelihood estimate and the log likelihood function is

$$\log \mathcal{L}(\theta_{pop}, \Psi, \Sigma|\mathbf{y}) = \sum_{i=1}^{N_I} \log \int \mathcal{L}(\theta_i, \Sigma|\mathbf{y}_i) \cdot p(\theta_i|\theta_{pop}, \Psi)\, d\theta_i. \qquad (4.43)$$

However, the above maximization problem cannot be solved analytically since the integral in the log likelihood function cannot be solved analytically. Hence, various methods have been developed to circumvent this problem. Methods to solve the nonlinear mixed-effect modelling can be broadly classified into two categories, namely based on the exact likelihood and based on the approximate likelihood [131].

The exact likelihood methods, such as the expectation-maximization (EM), uses numerical integral algorithms, however, it is in general infeasible except for simple cases [131]. In contrast stochastic approximation expectation-maximization (SAEM) utilizes Monte Carlo techniques to approximate the integral in the individual likelihood function (see Eqn (4.41))[VII]. The software MONOLIX uses SAEM for NLME [112].

On the other hand, the approximate likelihood methods maximize an approximation of the original likelihood function instead of maximizing the exact likelihood function. One way to approximate the exact likelihood function is by Laplace approximation [132]. Laplace approximation entails approximating the integral using Taylor expansion. The popular software NONMEM uses the Laplacian Method, first order conditional expectation (FOCE) and first order (FO) methods to solve nonlinear mixed-effect modelling problems, which are based on approximate likelihood [132] obtained from Laplace approximation. Similarly, the linear mixed-effects approximation method suggested by Lindstrom and Bates [133] approximates the exact likelihood by using Taylor expansion of the model function around the conditional modes instead of the conditional expected value of the random effects [134, 135]. This method is default in the 'nlmefit' function in Matlab [136].

[VI] The derivation are from A5 module lecture note of PharMetrX Graduate Program [130].

[VII] Note that Monte Carlo techniques are inherently not exact. The term 'exact' refers to the use to the original likelihood function without approximation.

Usually, a modeller needs to perform parameter identifications for a number of candidate nonlinear mixed-effects models, which vary from each other regarding the structural-, the covariate- and the stochastic submodel. The model selection should be performed on the set of candidate nonlinear mixed-effect models based on information criteria such as AIC as discussed earlier in Subsection 4.1.2.

4.3 Summary

In this chapter, we briefly presented a general introduction to model building which is also known as inverse problems in mathematics literature. Broadly speaking, the inverse problem requires solving a parameter identification and a model selection problem. We discussed the ℓ_p minimization and maximum likelihood methods for parameter identification. The introduction is far from being exhaustive and various important methodologies like 'maximum a posteriori' and 'bayesian inference' have not been discussed. The readers are suggested to consult relevant literature.

It is noteworthy to reiterate that model building should be performed to better approximate the reality rather than to better fit the data. This requires a balance between the model complexity and its generality. To this end, a modeller should use information criteria, visual predictive checks and cross validation techniques.

Subsequently, we discussed various population approaches used in the model building process in pharmacokinetics and pharmacodynamics. Though naive averaging and naive pooling are simple to use, they have several disadvantages. They describe the central tendency of data, however, they ignore the variability in parameters and suffer from the smoothening effect. The two-stage approach and nonlinear mixed-effect modelling overcome drawbacks faced by naive approaches, with nonlinear mixed-effect modelling being parsimonious and superior to the two-stage approach.

CHAPTER 5

Pharmacokinetic and pharmacodynamic models

In the following, we will deal with the pharmacokinetic and pharmacodynamic (PK-PD) model development of four antiretroviral drugs;(i) tenofovir disoproxil fumarate (TDF), (ii) emtricitabine (FTC), (iii)lamivudine (3TC) belonging to the class of nucleoside reverse transcriptase inhibitors (NRTI) and (iv) dolutegravir (DTG) belonging to integrase inhibitor class (InI). All of them are administered orally. For each drug, we employed methods for model building (see Chapter 4) suitable for the available data [I].

Box. 5.1: Pharmacokinetic subprocesses

The pharmacokinetics of a drug can be broken down into sub-processes, which are absorption, distribution, metabolism and excretion of the drug, also known as ADME in a short form [137]. A brief description of the sub-processes drugs is given as below:

- Absorption: Generally, a drug needs to be absorbed in the bloodstream in order to reach its target-site. This process of movement of drug from its site of administration into the bloodstream is known as absorption. This is influenced by the *route of administration* of the drug [138]. Broadly speaking, the administration of drug can be classified into two categories, namely extravascular (oral, intramuscular, subcutaneous etc. [139]) and intravascular administration (intravenous and intraarterial). For all extravascularly administered drugs, absorption process plays a very important role and the systemically available fraction [139], also termed *bioavailability* is crucial.
- Distribution: Distribution is the movement of the drug through the body. This is determined by the blood flow in and out of tissues and properties of the drug such as hydrophilicity, lipophilicity, molecular size, protein binding etc [138].
- Metabolism: It is the process of biotransformation of the drug. The primary metabolising organs are in order of relevance are liver, kidney, lung, small intestine, skin and blood-brain barrier [139].
- Excretion: It is the process of removal of the drug from the body. The major route of excretion are renal, bile, intestinal and pulmonary excretion.

Often, the metabolism and excretion are collectively referred as elimination. Similarly, the distribution, metabolism and excretion of a drug are collectively called disposition [139].

[I] This section is based on articles [23, 26, 84].

5.1 Tenofovir (TFV), Emtricitabine (FTC), Lamivudine(3TC)

For orally administered drugs, the formulation that is administered might be different from the active form of the drug, which exerts the pharmacodynamic effects. Drugs that are inactive in their administrated form are called 'prodrugs'. Prodrug formulations are optimized to maximize the bioavailability (see Box 5.1). Upon absorption from the alimentary canal, the drug circulates in the blood and can be measured in the blood plasma.

Lamividine and emtricitabine are structurally related and both are deoxycytosine (dC) analogs [140]. Their prodrugs are identical to their major circulating forms. After uptake in target-cells, the drug becomes tri-phosphorylated by intracellular kinases to form 3TC-TP and FTC-TP respectively, which exert the antiviral effect [140].

Tenofovir disoproxil fumarate is a prodrug analog of a monophosphorylated deoxyadenosine (dAMP) [141] that carries a chemical mask to improve absorption through the alimentary canal [142]. After absorption, the chemical mask is removed in the liver to form tenofovir (TFV), which is the major circulating form. Upon uptake by cells, TFV is consecutively phosphorylated twice to form TFV-DP, which competes with endogenous deoxyadenosine triphosphate (dATP) for an incorporation into a nascent viral DNA during the reverse transcription [142]. Table 5.1 shows the prodrug, major circulating form, steps of intracellular modifications and active moieties of lamivudine, emtricitabine and tenofovir disoproxil fumarate respectively.

Prodrug	Circulating Agent	Intracellular Modification	Active Moiety
3TC	3TC	3TC → 3TC-MP → 3TC-DP → 3TC-TP	3TC-TP
FTC	FTC	FTC → FTC-MP → FTC-DP → FTC-TP	FTC-TP
TDF	TFV	TFV → TFV-MP → TFV-DP	TFV-DP

Table 5.1: **Modification to active moiety:** Prodrug, major circulating form, steps of intracellular modifcations and active agents of lamivudine, emtricitabine and tenofovir disoproxil fumarate.

5.1.1 Clinical data

Tenofovir disoproxil fumarate

Plasma pharmacokinetic data for TFV were extracted from Droste et al. [143], Chittick et al. [144] and Barditch-Crovo et al. [145], whereas the intracellular TFV-DP concentration data were available from Hawkins et al. [146]. Viral load data for dosage regimen 75mg QD[II], 150mg QD, 300mg QD and 600mg QD TDF monotherapy over 28 days are from Barditch-Crovo et al. [145].

Emtricitabine

Plasma pharmacokinetic data were extracted from clinical studies FTC-106 [147], FTC-101 [147, 148] and FTC-303 [147], Blum et al. [149], Zong et al. [150] and Kearney et al. [151]. All studies reported average FTC plasma profiles over a 24 hour time course at plateau phase for 200mg QD FTC. All studies were conducted in uninfected volunteers except for FTC-101 and FTC-303. FTC-101 also reports plasma FTC concentrations for 25mg BID[III], 100mg QD, 100mg BID, 200mg QD and 200mg BID over a time period of 24 hours, which were utilized for cross-validation of the plasma PK model. Jackson et al. [152] reported the intracellular decay of FTC-TP in PBMCs

[II] QD means 'once daily' dosing and is abbreviated from 'quaque die' (Latin).
[III] BID means 'twice daily' dosing and is abbreviated from 'bis in die' (Latin).

after cessation of Atripla (FTC + TDF + efavirenz single tablet formulation) over a period of 228 hours, and FTC-106 [147] reported the intracellular decay after cessation of 200mg FTC QD monotherapy over a period of 120 hours. FTC-101 [148] reported FTC-TP concentrations in PBMCs (peripheral blood mononuclear cells) after 1 and 4 hours on day 12 for 25mg BID, 100mg QD, 100mg BID, 200mg QD and 200mg BID monotherapy and viral load kinetics for the same regimens over a time period of 14 days. Furthermore, FTC-102 [153] also reported viral dynamics over 12 days, when FTC monotherapy with either 25mg QD, 100mg QD or 200mg QD was administered over a total period of 10 days. We cross-validated the pharmacodynamic predictions using the data set (FTC-102).

Lamivudine

Moore et al. [154] reported plasma- and intracellular pharmacokinetics time profiles in PBMC after oral administration of 150mg and 300mg BID for 10 HIV-1 infected individuals. In the study, the respective regimen is administered for 14 days and pharmacokinetic measurements are taken over a total period of 36 hours after the last dose. The viral load kinetics following 3TC 150mg BID monotherapy were measured over a total duration of 12 days after 10 days of monotherapy in the FTC-102 study [153].

5.1.2 Outline of the model

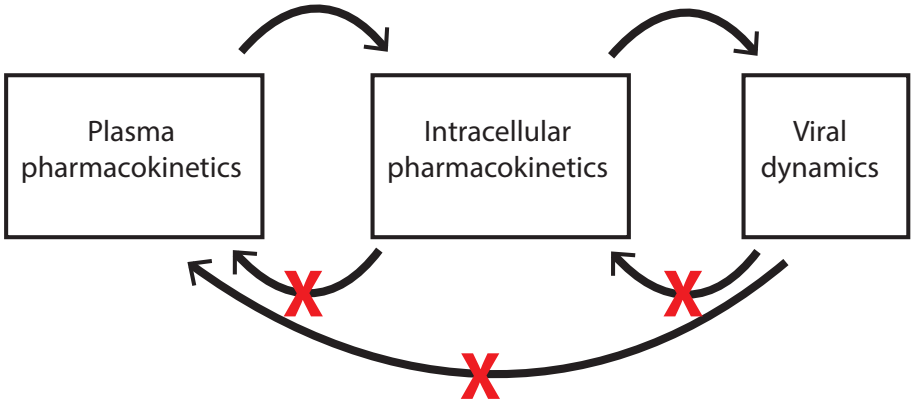

Figure 5.1: **Schematic depiction of step-wise PK-PD model building process:** The plasma pharmacokinetic model provides an input to the intracellular pharmacokinetic model. The intracellular pharmacokinetics affect the pharmacodynamics (viral dynamics). The intracellular pharmacokinetics do not affect the plasma pharmacokinetics. This assumption is justified by the negligible amount of NRTIs in target-cells in comparison to the plasma. The viral dynamics influence neither plasma nor intracellular pharmacokinetics.

The pharmacokinetic and pharmacodynamic (PK-PD) models for all three NRTIs were built in a step-wise fashion, which is also depicted in Figure 5.1. The asynchronous and nonlinear relationship between the plasma pharmacokinetics and target-site pharmacokinetics i.e. intracellular pharmacokinetics for NRTI [155, 156] necessitates building models for both plasma and intracellular pharmacokinetics to accurately capture drug's effect on viral dynamics. For each NRTI, we firstly develop a plasma pharmacokinetics model of the pre-dominant circulating agent independent of its intracellular pharmacokinetics. This step neglects any mass-influx from the target-cell to the blood plasma compartment. However, this is justified because the total volume of PBMCs, which is the target-cell surrogate marker, is very small ($1 \cdot 10^{-6}$ L [157, 158]) in comparison to the

plasma volume (≈ 3.5 L) and consequently the amount of NRTIs in the target cellular compartment is negligible compared to the amount in plasma compartment.

The next step involves building a model for intracellular pharmacokinetics that takes the plasma PK as input. Upon a cellular uptake, NRTIs undergo subsequent phosphorylations to form their tri-phosphates - NRTI-TP (see Table 5.1). The detailed concentration time profiles of intermediate phorphorylated forms are usually not available. Hence, as often practiced in pharmacometrics, we lumped a number of intermediate steps involved in the conversion of the dominant circulating form to active intracellular moiety into a single step. Finally, the composite pharmacokinetics model is coupled to the previously described HIV-1 dynamics model [83, 85] (see Subsection 2.5.2). The unknown coupling parameter in the effect model is inferred by fitting to clinically observed viral load profiles. We assume that viral dynamics neither affect plasma nor intracellular pharmacokinetics. We used various methods of model building (see Chapter 4) suitable to the available data. Whenever possible model predictions were cross-validated on data sets not used for parameter estimation. Visual predictive checks, goodness-of-fit and Akaike information criteria guided the model selection.

Pharmacokinetic Model

The plasma concentration time profiles of the dominant circulating agents (TFV, FTC, 3TC) were all best described by a two compartment model:

$$\frac{\mathrm{d}}{\mathrm{d}t}Z_0(t) = -k_a \cdot Z_0(t) \tag{5.1}$$

$$\frac{\mathrm{d}}{\mathrm{d}t}Z_1(t) = \frac{F_{\mathrm{bio}} \cdot k_a \cdot Z_0(t)}{V_c} - Z_1(t) \cdot k_e - k_{12} \cdot Z_1(t) + k_{21} \cdot Z_2(t) \tag{5.2}$$

$$\frac{\mathrm{d}}{\mathrm{d}t}Z_2(t) = k_{12} \cdot Z_1(t) - k_{21} \cdot Z_2(t) \tag{5.3}$$

where Z_0, Z_1 and Z_2 represent the amount of prodrug in the dosing compartment, the concentration of the dominant circulating agent in the central compartment (= blood plasma) and the apparent concentrations in the peripheral compartment respectively. F_{bio} denotes the oral bioavailability and V_c represents the volume of the central compartment. The terms k_a and k_e denote the absorption and elimination rate constant for the central compartment. Similarly, k_{12} and k_{21} are the influx and the apparent outflux rate constants to/from the peripheral compartment respectively. The amount of drug in the dosing compartment is updated in an impulse manner as shown below

$$Z_0(t) = Z_0(t) + \mathrm{Dose}(k) \tag{5.4}$$

when the time t coincides with the k^{th} dosing time. The elimination of the active intracellular moiety (3TC-TP, FTC-TP or TFV-DP) was assumed to be of the first order in all cases. The cellular uptake of the major circulating agents and its intracellular phosphorylation into the active moiety are best described by Michaelis-Menten kinetics in all cases:

$$\frac{\mathrm{d}}{\mathrm{d}t}D(t) = \frac{\mathrm{d}}{\mathrm{d}t}Z_3(t) = \frac{V_{\max} \cdot Z_1(t)}{k_m + Z_1(t)} - k_{\mathrm{out}} \cdot Z_3(t) \tag{5.5}$$

where $V_{\max}$ is the maximum velocity and k_m the Michaelis-Menten constant for the uptake and intracellular anabolism. Z_3 denotes the intracellular concentration of active drug moieties, which we also denote by $D(t)$ for ease of notation[IV]. Figure 5.2A depicts the schematic of pharmcokinetic models for NRTIs.

[IV] Henceforth, we denote the concentration of active moiety at the target-site by $D(t)$

PK-PD Linker model

The HIV-1 dynamics model [83, 85] presented in Chapter 2 can take mechanistic effects of all currently available antivirals on HIV dynamics into account. The model can be used to estimate the effect of NRTIs on viral dynamics and provide an IC_{50} estimate that relates to the inhibition of a target-process. Previously, the authors [83] have shown that the antiviral effect of NRTIs translates into a reduction of the rate of successful cell infection $\beta_{T/M}$ and a proportional increment in the clearance of virus due to an unsuccessful infection event $CL_{T/M}$:

$$\beta_{T/M}(t) = \beta_{T/M}(\varnothing) \cdot (1 - \eta_{RTI}(t)) \tag{5.6}$$

and

$$CL_{T/M}(t) = \left(\frac{1}{\rho_{rev,\varnothing}} - (1 - \eta_{RTI}(t)) \right) \cdot \beta_{T/M}(\varnothing) \tag{5.7}$$

where $(1 - \eta_{RTI}(t))$ denotes the residual infection modelled in terms of the standard Emax function with slope parameter 1 [87], which is

$$(1 - \eta_{RTI}(t)) = \frac{IC_{50}}{IC_{50} + D_{RTI}(t)}. \tag{5.8}$$

In the equation above, $D_{RTI}(t)$ denotes the intracellular NRTI-TP concentration within target-cells. The IC_{50} was then estimated by minimizing the squared residual error between model-predicted and observed viral decay data from the respective studies, while all other parameters were fixed, as detailed in Duwal et al. [23]. Figure 5.2B illustrates the viral dynamics model and the influence of NRTI-TPs on the viral dynamics model.

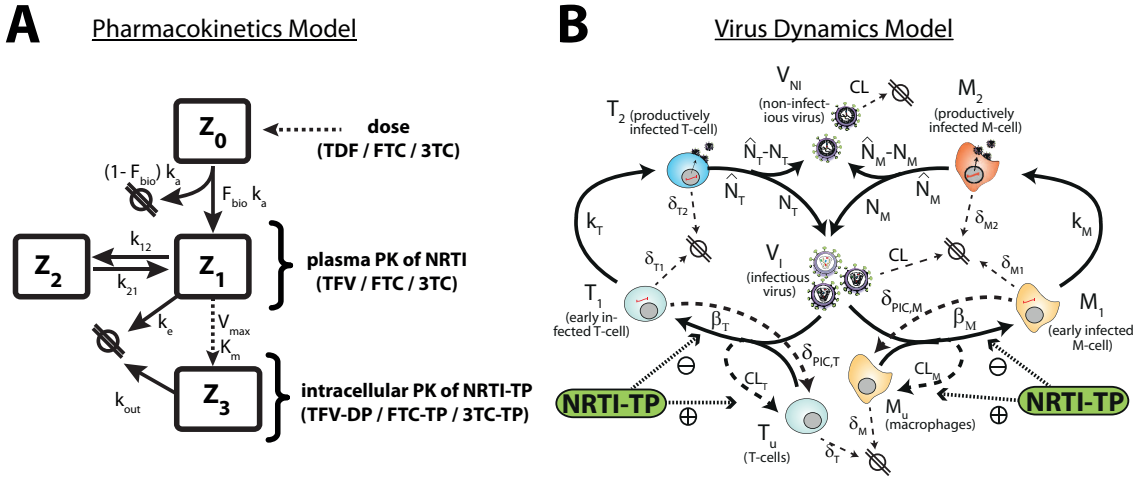

Figure 5.2: **Plasma and intracellular pharmacokinetics models for TDF, FTC and 3TC and model of viral dynamics.** **A**: The plasma pharmacokinetics of the dominant circulating agent is best described by a two compartment model. The intracellular pharmacokinetics of the active moiety is linked with the plasma pharmacokinetics, where the intracellular uptake and modification are described by the Michaelis-Menten equation and the elimination is of the first order. **B**: The viral dynamics model comprises T-cells, macrophages at various stages of infection and free viruses (non-infectious and infectious). The antiviral effects of NRTI-TP can be modelled as an inhibition of the rate of successful cell infection and a proportional increase in unsuccessful infection events. For details see Subsection 2.5.2. Adapted from Duwal et al. [84]

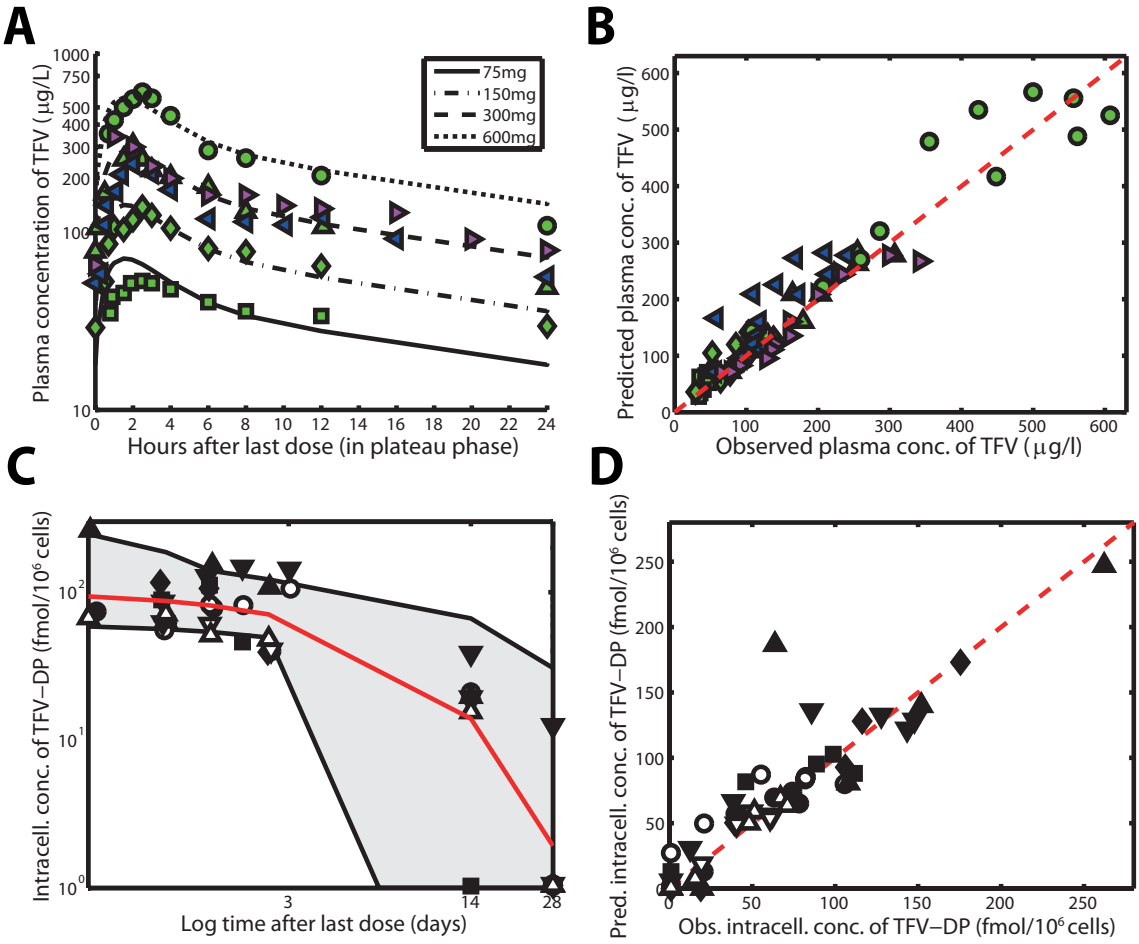

Figure 5.3: **Model prediction vs. available clinical data for TDF pharmacokinetics.** **A**: Predicted pharmacokinetics of TFV after once daily 75-, 150-, 300- and 600mg oral TDF (lines) together with data from various studies [143–145] (markers). **B**: Goodness-of-fit plot for the plasma pharmacokinetics of TFV with data from 3 clinical studies and 4 different dosing schemes [143–145]. The dashed red line indicates the line of unity, whereas the green squares, -diamonds, triangles and filled dots represent the observed TFV concentrations in Barditch-Crovo et al. [145] following 75-, 150-, 300- or 600mg once daily administration of TDF. The blue left-pointing triangles and the magenta right-pointing triangles represent observed TFV concentrations after 300mg once daily oral administration from Chittick et al. [144] and Droste et al. [143] respectively. **C**: Predicted pharmacokinetics of intracellular TFV-DP after stopping of 300mg once daily oral TDF dosing (lines) together with data from Hawkins et al. [146] (markers). **D**: Goodness-of-fit plot for intracellular TFV-DP. The up- and downward pointing filled and open triangles, open- and filled circles, filled squares and filled diamonds indicate intracellular TFV-DP pharmacokinetics after stopping 300mg once daily oral TDF dosing in 8 different individuals from Hawkins et al. [146]. Reproduced from Duwal et al. [84].

5.1.3 Tenofovir pharmacokinetic-pharmacodynamic model

For TDF, the plasma pharmacokinetics model is fitted to a pooled data set with average plasma pharmacokinetics from different studies with 300 mg QD dosage regimen (see Subsection 4.2.2). The model was cross-validated using data of dosage regimen 75 mg, 150 mg and 600 mg QD. The intracellular concentration profiles of eight patients from a drug-cessation study are available from Hawkins et al [146]. The data is appropriate to estimate the intracellular elimination constant. The two-stage approach (see Subsection 4.2.3) is applied, where the elimination constant of TFV-DP

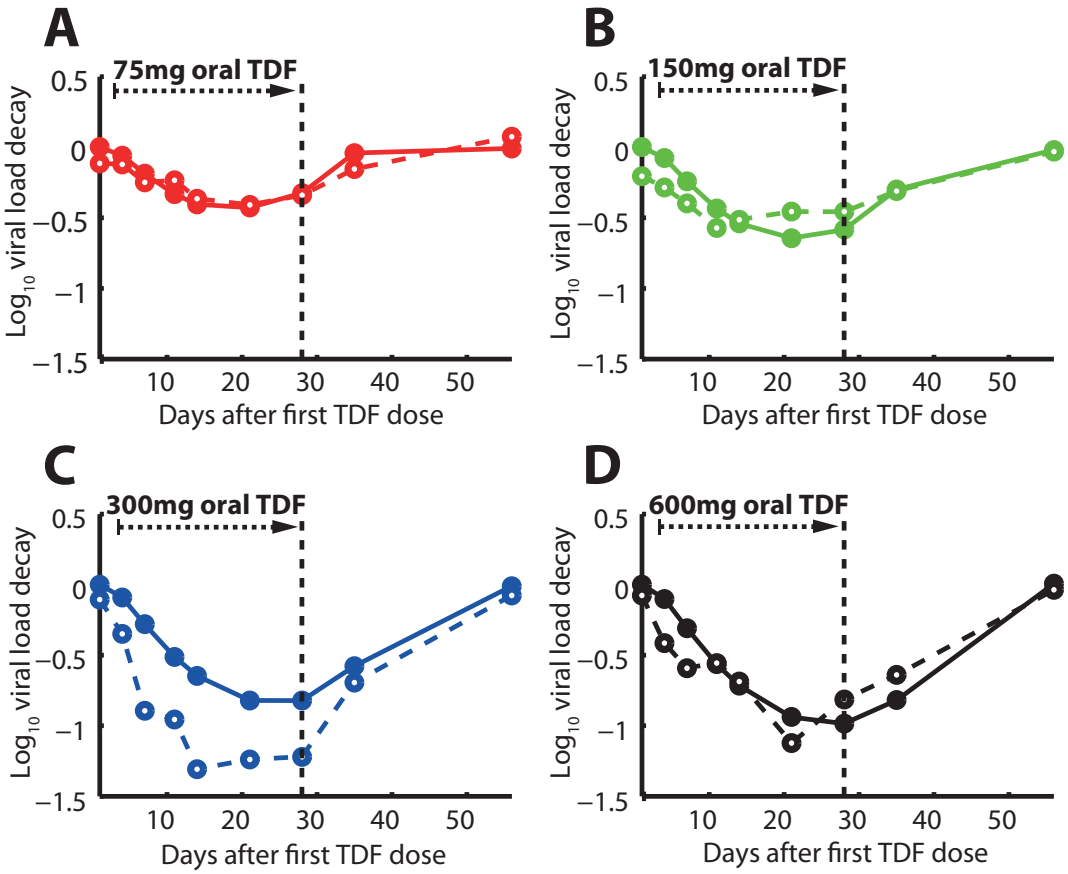

Figure 5.4: **Model prediction vs. clinical data for TDF pharmacodynamics.** The viral load $\log_{10}$ data are from a TDF mono-therapy study [145], where once daily regimen is administered for 28 days and discontinued afterward. Black dashed vertical lines indicate the cessation of TDF dosing. Solid lines represent predicted median viral dynamics using the coupled PK-PD model, whereas dashed lines represent the observed $\log_{10}$ change in viral load [145] with respect to the baseline. **A:** Once daily 75mg TDF dosing. **B:** Once daily 150mg TDF dosing. **C:** Once daily 300mg TDF dosing. **D:** Once daily 600mg TDF dosing. Reproduced from Duwal et al. [84].

in PBMCs are estimated for each individual and then the statistics of these parameters were computed. Figure 5.3 compares the model prediction and observation for the plasma and intracellular pharmacokinetics.

The intracellular pharmacokinetics of TFV-DP lag behind the plasma pharmacokinetics of TFV with $t_{\max}$ = 13 hours for TFV-DP and $t_{\max}$ = 1.57 for TFV at steady state. The terminal half-life is prolonged for TFV-DP (terminal half-life 125 hours) in contrast to TFV (terminal half-life 19 hours). The IC_{50} was estimated to be 0.17 μM (5% – 95% percentile range 0.15 – 0.18), which corresponds to 29.78 fmol/10^6 cells, assuming an average cell volume of 180 fL [157]. Figure 5.4 compares the observed and model-predicted change in viral load with respect to the baseline.

The estimated plasma pharmacokinetic parameters are similar to the parameters reported by Baheti et al. [159]. Madrasi et al. [160] employed and validated the plasma pharmacokinetics model with clinical observations from MTN-001 study [161]. Moreover, the authors [160] presented an extensive mechanistic intracellular pharmacokinetics model based on the nonlinear relation reported in our work.

5.1.4 Emtricitabine pharmacokinetic-pharmacodynamic model

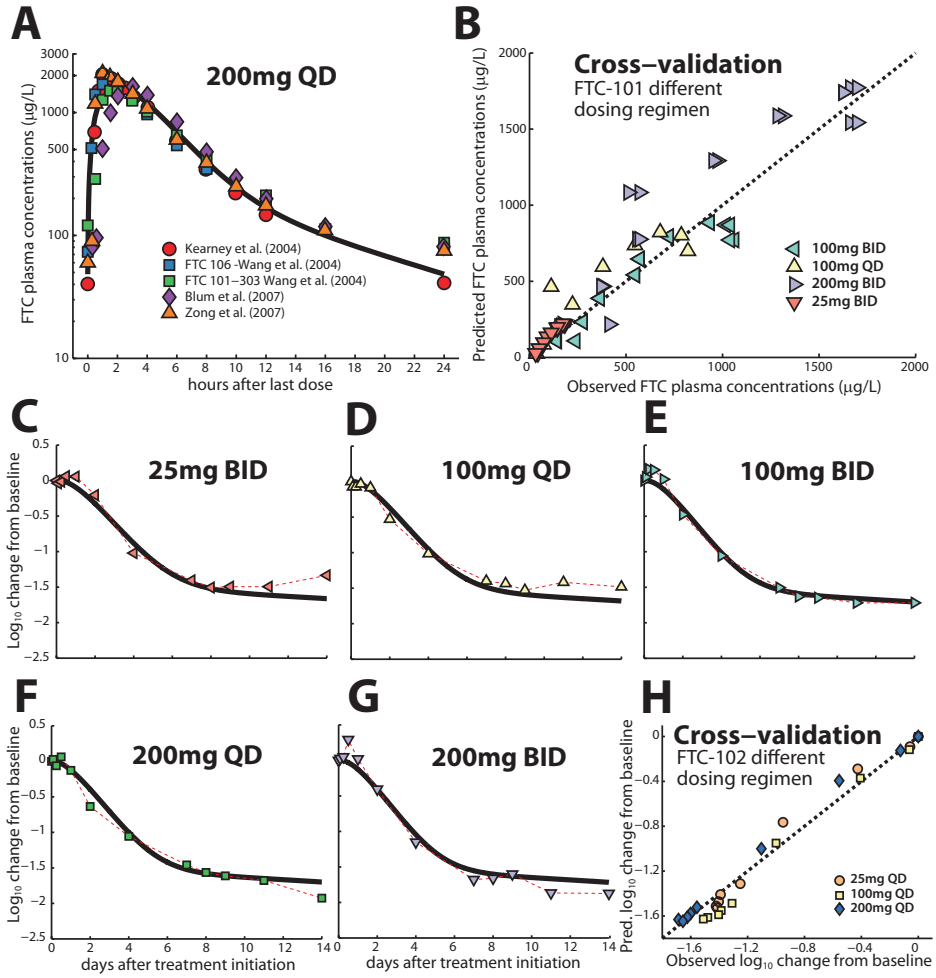

Figure 5.5: **Model prediction vs. clinical data for FTC pharmacokinetics and -dynamics. A:** Average FTC concentrations time profiles in the blood plasma over a time course of 24 hours after administration of 200mg QD in the plateau phase. Differently coloured markers report data from different studies [147, 149–151] and the solid black line depicts the model predictions. **B:** Model predictions for 25mg BID, 100mg QD, 100mg BID, and 200mg BID were cross-validated against average concentrations from [148] for the same dosing regimens. **C-G:** Median viral dynamics ($\log_{10}$ change in HIV RNA/mL) after administration of 25mg BID, 100mg QD, 100mg BID, 200mg QD and 200mg BID FTC monotherapy for 14 days. Differently coloured markers connected by thin red dashed lines indicate data from [148], while the solid black lines represent model predictions for the respective dosing regimen. **H:** Cross-validation of model predicted viral dynamics with data from FTC-102 (25, 100 and 200mg FTC QD monotherapy given for 10 days) [153]. Reproduced from Duwal et al. [23].

Due to the absence of individual pharmacokinetic profiles for FTC in the blood plasma, a non-linear mixed-effects approach was not applied. We conducted a naive pooled data approach (see Subsection 4.2.2), where a model was fitted to the pooled data set with average plasma pharmacokinetic profiles from different studies. Briefly, the best model describing plasma pharmacokinetics was a two compartment model and it is fitted to data from various independent studies testing 200mg QD [147–151], as illustrated in Figure 5.5A.

As can be seen in Figure 5.5A, FTC is rapidly taken up ($t_{\max}$ = 1.9 hours) and eliminated

moderately fast (terminal half-life = 11.2 hours). The average FTC concentration time profiles in distinct studies are very similar and are unaffected by whether FTC is given in combination, or alone and whether individuals were infected or not. We cross-validated the fitted model against the data from [148] with various dosing regimen, which we had not used for the model development. One can see in Figure 5.5B that model predictions are in line with the independent data set.

The intracellular FTC-TP data is sparse, and we employed a two step approach. Details can be found in the supplementary text of Duwal et al. [23]. In brief, we first estimated the elimination constant of FTC-TP from PBMCs. The derived elimination constant was then fixed, and we assessed different cellular uptake and phosphorylation dynamics (linear vs. nonlinear), arriving at a nonlinear model for the uptake and phosphorylation of FTC to FTC-TP. We observed that the intracellular FTC-TP concentrations are not synchronized with the plasma pharmacokinetics. The intracellular decay of FTC-TP is much slower (terminal half-life of 39 hours) than the decay of FTC in the blood plasma. Moreover, the uptake is delayed ($t_{\max} \approx 10$ hours for QD and 7 hours for BID) in comparison to the circulating drug in the blood plasma. This indicates that both the uptake and phosphorylation process, as well as the elimination from the cells are rate limiting.

We used the developed PK model and estimated the IC_{50} from the viral dynamics following 14 days monotherapy with various dosing regimens, see Figure 5.5C-G. The IC_{50} is estimated to be 1.02 μM (5% − 95% percentile range: 0.74 − 1.35), which corresponds to 182.89 fmol/10^6 cells assuming an average volume of 180 fL [157]. Finally, we cross-validated model predictions with an independent data set [153], which assessed viral dynamics after 10 days monotherapy for various dosing regimens (see Figure 5.5H).

A two compartment model has been previously used by others [162, 163] to describe the plasma pharmacokinetics of FTC. The estimated absorption rate constant k_a is 0.54 close to the value reported by [162] (0.53hours^{-1}). The estimated apparent clearance CL/F_{bio} (19.28 vs. 15.1 L/hour in [162]) and terminal plasma elimination half-life (11.2 hours vs. 10 hours in [142, 164, 165]) are also very similar. The plasma AUC_{0-24} (area under the curve) for 200mg FTC QD is also in line with previous reports (10371 vs. 8000-11300 $\mu g\cdot$ hour/L in [147, 152]). To our knowledge, no FTC-TP intracellular pharmacokinetics model had been published to date, however it had been speculated that the kinetics may be similar to 3TC-TP [140, 164]. The intracellular derivatives of FTC are FTC-MP, FTC-DP, FTC-TP and FTC-DP choline [166, 167]. Due to the lack of data, we only focused on FTC-TP, which exerts the antiviral effect. Wang et al. [147] have reported a nonlinear increase of intracellular FTC-TP intracellular when the dose of FTC was linearly increased, suggesting saturation of intracellular FTC uptake and anabolism in agreement with the Michaelis-Menten uptake for the intracellular active moiety in the presented model. The estimates of intracellular half-life of FTC-TP are generally in line with the literature, which report 30–39 hours hours in PBMCs [142, 156].

5.1.5 Lamivudine pharmacokinetic-pharmacodynamic model

The availability of individual pharmacokinetic profiles for 3TC in the blood plasma and 3TC-TP in peripheral blood mononuclear cells (PBMCs) allowed us to use the nonlinear mixed-effects approach (see Subsection 4.2.4) to infer pharmacokinetic parameters. The final model for plasma pharmacokinetics has a random effect on parameters k_e and k_{21} and a proportional error submodel, while the intracellular submodel has a random effect on parameter $V_{\max}$ and an exponential error submodel. Figure 5.6 A-D and Figure 5.4 show that both plasma- and intracellular pharmacokinetics for 150mg BID and 300mg BID are well captured by the model. The plasma pharmacokinetics are characterized by a rapid uptake ($t_{\max}$ = 1.56 hours) and a moderately fast elimination (terminal half-life = 14.15 hours). The overall inter-patient variation in the pharmacokinetic profiles is

relatively small. In contrast, intracellular pharmacokinetics of 3TC-TP are characterized by large inter-individual variation. Moreover, intracellular pharmacokinetics are not synchronised with the plasma pharmacokinetics, evident by differences in their half-life (intracellular half-life 22 hours vs. plasma half-life 14.15) and $t_{\max}$ (intracellular $t_{\max} \approx 8$ hours for QD and 6 hours for BID vs. plasma $t_{\max}$ 1.56 hours). This indicates that both the uptake and phosphorylation process, as well as the elimination from the cells are rate limiting.

The 3TC pharmacokinetics model is coupled with the viral dynamics. A single parameter IC_{50} is estimated from the viral load decay data [153]. As can be seen in Figure 5.6E, the predicted profiles (solid black lines) match the data (blue dots) satisfactorily. The IC_{50} is estimated to be 0.74 μM (5% – 95% percentile range: 0.47 – 1.07), which corresponds to 132.28 fmol/10^6 cells, assuming an average cell volume of 180 fL [157].

The model developed for 3TC plasma pharmacokinetics agrees with previous studies [168–170], which all report that a two compartment model best describes the data. However, the parameters of the model cannot be directly compared with previous studies: Studies [154, 169] fail to report the kinetic micro-parameters for their models and [170] use an unphysiologic absorption model (zero order), which likely affects remaining parameter estimates. However, a comparison can be made in terms of macro-parameters: The terminal plasma half-life was 14.2 hours in our study, which is slightly longer than previously reported (6-12 hours [142, 154, 171, 172]). The mean apparent volume of distribution (V_{dss}/F_{bio}) of 143L is close to the previously reported value of 151L [173] and the mean apparent clearance $V_c/F_{\text{bio}} \cdot k_e = \text{CL}/F_{\text{bio}}$ was 23L, in range with the range of reported values (20-25 L) [174]. The plasma AUC_{0-24} values for 150mg 3TC QD and 300mg 3TC QD were 6103 and 12206 μg $\cdot$ h/L respectively, which is slightly higher than corresponding values reported in [175] (4473 and 8354 μg $\cdot$ h/L).

Zhou et al. [170] developed a detailed intracellular pharmacokinetics model including 3TC-MP, 3TC-DP, 3TC-DP choline and 3TC-TP. They showed that the conversion from the intracellular 3TC to 3TC-MP was rate limiting and that the intracellular activation cascade is saturable. Although the presented model for intracellular pharmacokinetics is much less detailed, it reflects the same findings: the intracellular 3TC-TP concentrations are nonlinearly related to extracellular 3TC and their kinetics are asynchronous. In terms of macro-parameters, we estimate an intracellular 3TC-TP half-life of 22 hours, in line with the literature (10.5-22hours [142, 156]). However, as previously described, the utilized data seems to report lower levels of 3TC-TP than observed elsewhere [176, 177]. Consequently, our model may underestimate the 3TC-TP exposure (AUC_{0-24} = 16319 and 24291 vs. 44000 and 59500 fmol $\cdot$ h/10^6 cells [177] for 150mg and 300mg QD respectively), which also may result in a slight over-prediction of the potency of 3TC-TP (see Figure 5.6). Pharmacokinetic parameters of the final models are presented in Table 5.2.

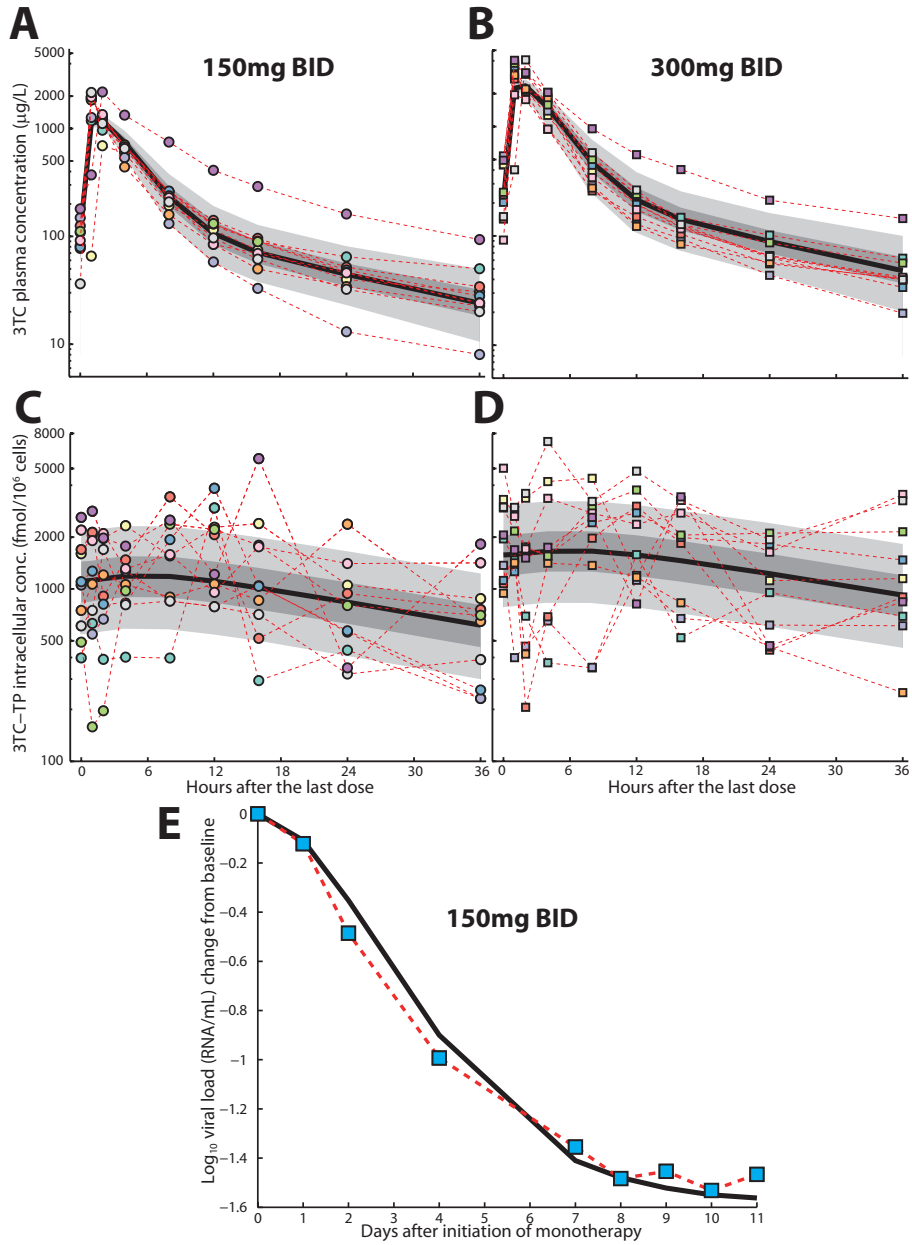

Figure 5.6: **Model prediction vs. clinical data for 3TC and 3TC-TP pharmacokinetics and -dynamics. A-B:** Concentrations time profiles of 3TC in the blood plasma of 10 HIV-1 infected individuals (differently coloured markers, connected by thin red dashed lines) for 150mg BID (panel **A**) and 300mg BID (panel **B**) respectively. The solid black lines represent the predicted median plasma pharmacokinetics profile for the respective regimens and the light- and dark grey regions encompass the 5% and 95% percentiles and the quartile ranges of predictions from the developed nonlinear mixed-effects model. The percentiles represent the model-predicted concentration ranges for 1000 virtual patients using the final model. Each parameter vector (virtual individual) was drawn from a log-normal distribution with a variance corresponding to the inter-individual variability. **C-D:** Concentrations time profiles of 3TC-TP in peripheral mononuclear cells (PBMCs) for the same 10 individuals after administration of 150mg BID (panel **C**) and 300mg BID (panel **D**). The solid black lines represent the predicted median intracellular 3TC-TP pharmacokinetics for the respective regimens and the light- and dark grey regions encompass the 5% and 95% percentiles and the quartile ranges of predictions from the nonlinear mixed-effects model. **E:** Predicted (solid black line) vs. observed average (blue markers connected by the red dashed line) viral load decay from baseline after administration of 150mg BID monotherapy for 10 days. Reproduced from Duwal et al. [23].

Param.	3TC	FTC	TDF	Unit
F_{bio}	0.86[†]	0.93[#]	0.32[*]	-
k_a	0.945[§]	0.542	1[‡]	1/h
V_c	61.252	43.823	110.31	1/h
k_{12}	0.0605	0.113	0.2926	1/h
k_{21}	0.0594	0.082	0.1537	1/h
$V_{\max}$	0.5819	0.6191	0.0032	μM· 1/h
k_m	3.3977	0.9464	0.1020	μM
k_{out}	0.0315	0.0176	0.006	1/h
IC_{50}	0.74	1.02	0.17	μM

Table 5.2: **Estimated pharmacokinetic and pharmacodynamic parameters.** [†]fixed value taken from Yuen et al. [173]. [#]fixed value taken from Modrzejewski et al. [165]. [*]fixed value from Barditch-Crovo et al. [145]. [§]fixed value taken from Linnankoski et al. [178]. [‡]fixed value from Gagnieu et al. [179]. Reproduced from Duwal et al. [23].

5.2 Dolutegravir (DTG)

Dolutegravir (DTG) is a second generation integrase inhibitor developed by ViiV healthcare and approved by FDA (Food and drug agency) on 2013 [180]. DTG has an excellent tolerability and minimal toxicity. Furthermore, it has a high barrier to resistance and has limited cross-resistance to other integrase inhibitors (raltegravir and elvitegravir) [181][V].

5.2.1 Clinical data

We used dolutegravir plasma pharmacokinetics data from two clinical studies. The first study assessed 50mg QD dolutegravir administered to 17 healthy volunteers for 10 days and serial blood sampling performed up to 216 hours after the final dose [182]. The second study was performed in 39 HIV-infected patients on 50 mg QD dolutegravir, who were previously on efavirenz-based therapy with a stable viral load of less than 40 copies/mL. Random, single blood samples were drawn over the 24 hour dosing interval 1, 2, 3 and 4 weeks after the switch to DTG [183]. Median (range) age, weight and BMI of all individuals were 47 years (26-68), 76 kg (51-105) and 26 kg/m^2 [183]. In summary, a total of 354 plasma concentration measurements from 56 individuals were available to build the population pharmacokinetic model for DTG. Healthy volunteers contributed rich PK profiles with a total of 270 samples taken between 0 hours (pre-dose) and 216 hours after a final DTG dose. In addition, eighty-four measurements, randomly drawn between 1-25.75 hours post-dose were available from HIV patients week 1, 2, 3 and 4 weeks post-efavirenz switch.

5.2.2 Outline of the model

We use nonlinear mixed-effects modelling techniques to derive a pharmacokinetic model that accurately captures the observed pharmacokinetic variability within- and across different patients. All data are fitted simultaneously and the first-order estimation (FOCE-I) method of NONMEM (v.7.3, ICON plc, Dublin, Ireland), interfaced with Pirana (v.2.9.0 [184]) is used for the parameter inference. Different structural submodels and inclusion of various covariates are tested according to the criteria stated in the book by Bonate [109].

[V]This section is based on Duwal et al. [26].

Unlike for NRTIs, the major circulating agent and the intracellular active moiety of DTG are identical [185]. Linking DTG plasma pharmacokinetics directly with the pharmacodynamics requires that the plasma pharmacokinetics is linearly and synchronously related to intracellular active moiety. The requirement is fulfilled for DTG. In the next Chapter, we will provide more details.

Due to the lack of the viral dynamics data for DTG monotherapy the IC_{50} cannot estimated using classical PK-PD approach. However, *ex vivo* data (single round infectivity cell assay) can be used to infer the IC_{50} [87], which we will present in the next chapter. The plasma pharmacokinetics can be directly linked with viral dynamics model using the EMAX model as presented in Chapter 2. The drug inhibits the integrase activity, which is modelled by:

$$k_{\mathrm{T/M}}(t) = (1 - \eta_{\mathrm{InI}}(t)) \cdot k_{\mathrm{T/M}}(\varnothing) \tag{5.9}$$

where

$$(1 - \eta_{\mathrm{InI}}(t)) = \frac{\mathrm{IC}_{50}^{m}}{\mathrm{IC}_{50}^{m} + (D_{\mathrm{InI}}(t))^{m}}. \tag{5.10}$$

where IC_{50} is the total (unbound plus bound) plasma concentration inhibiting the integrase activity by 50 %, $D_{\mathrm{InI}}(t)$ is the total plasma concentration of DTG and m is the hill coefficient of DTG.

5.2.3 Dolutegravir pharmacokinetic model

The final pharmacokinetic model of DTG is a two-compartment model with an oral absorption:

$$\frac{\mathrm{d}}{\mathrm{d}t}Z_0 = -k_a \cdot Z_0 \tag{5.11}$$

$$\frac{\mathrm{d}}{\mathrm{d}t}D = \frac{\mathrm{d}}{\mathrm{d}t}Z_1 = \frac{k_a \cdot Z_0}{V_c/F_{\mathrm{bio}}} - \frac{\mathrm{CL}/F_{\mathrm{bio}}}{V_c/F_{\mathrm{bio}}} \cdot Z_1 - \frac{Q/F_{\mathrm{bio}}}{V_c/F_{\mathrm{bio}}} \cdot Z_1 + \frac{Q/F_{\mathrm{bio}}}{V_p/F_{\mathrm{bio}}} \cdot Z_2 \tag{5.12}$$

$$\frac{\mathrm{d}}{\mathrm{d}t}Z_2 = \frac{Q/F_{\mathrm{bio}}}{V_c/F_{\mathrm{bio}}} \cdot Z_1 - \frac{Q/F_{\mathrm{bio}}}{V_p/F_{\mathrm{bio}}} \cdot Z_2, \tag{5.13}$$

where Z_0, Z_1 and Z_2 denote the amount of drug in the dosing compartment and the concentration of dolutegravir in the central compartment and peripheral compartment respectively. The variable of interest is the concentration in the blood plasma (central compartment), i.e. $D = Z_1$. Dosing events are updated in an impulse manner as shown below

$$Z_0(t) = Z_0(t) + \mathrm{Dose}(k), \tag{5.14}$$

whenever the simulation time t coincided with the dosing event time $\mathcal{T}_k$. In the equations above, k_a and $\mathrm{CL}/F_{\mathrm{bio}}$ denote the uptake and bioavailability-adjusted drug clearance respectively. The term V_c/F_{bio} and V_p/F_{bio} are the bioavailability-adjusted volume of the central and peripheral compartment. The term Q/F_{bio} is the intercompartmental clearance rate adjusted for bioavailability. Notice that the ODEs for the two compartment model are identical to the two compartment model presented for NRTIs previously. The difference is that here they are expressed in terms of macro parameters instead of micro parameters.

Following multivariate analysis, allometric scaling (centered around 70kg) of weight was considered as a fixed effect in the model. Different values of apparent oral clearance ($\mathrm{CL}/F_{\mathrm{bio}}$) were estimated for DTG alone in healthy volunteers and in patients following 1, 2, 3 and 4 weeks after the treatment switch. A combined proportional-additive error submodel described the residual variability in healthy volunteers, whereas a proportional error submodel was sufficient for HIV-infected patients. All parameter estimates for healthy volunteers are displayed in Table 5.3. The

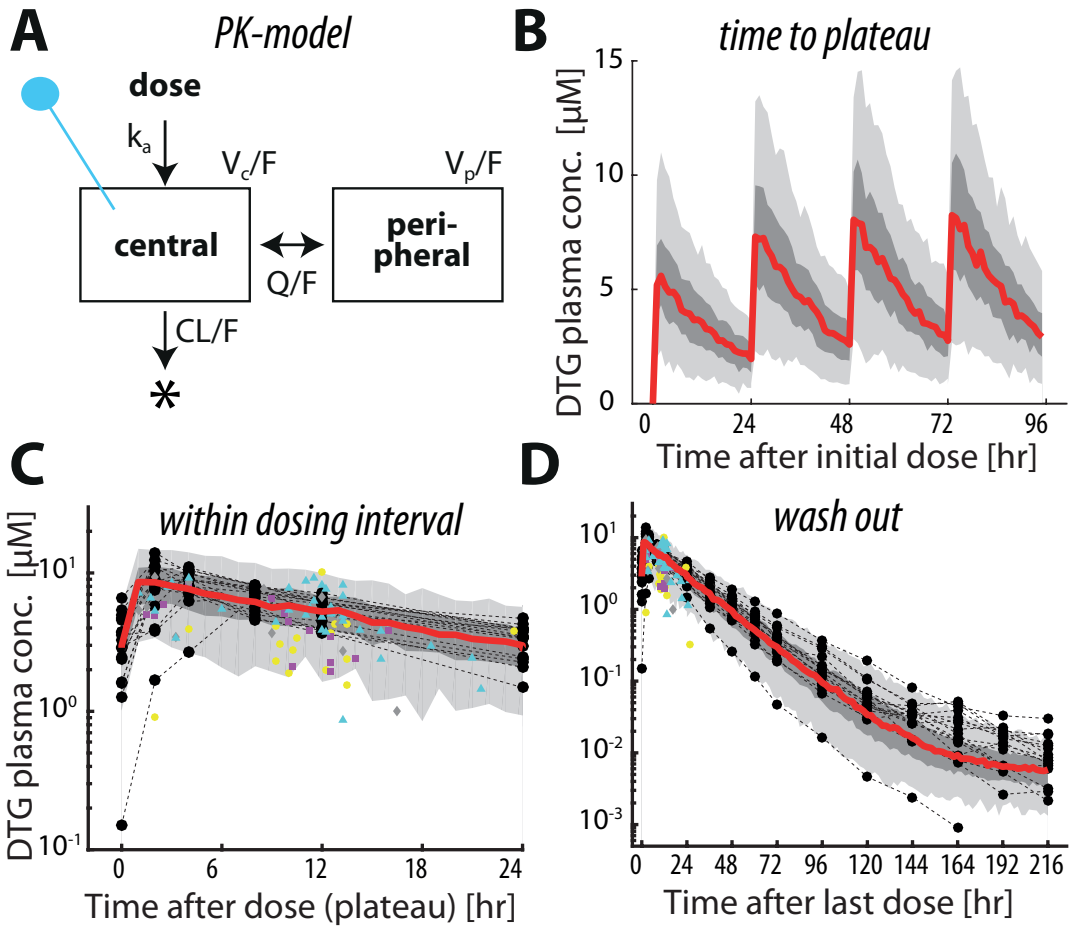

Figure 5.7: **Population pharmacokinetics of dolutegravir (DTG). A:** Pharmacokinetic model. Concentrations within the central compartment with bioavailability-adjusted volume V_c/F correspond to measured plasma concentrations of DTG (indicated by the blue pin). Parameters k_a, Q/F_{bio} and CL/F_{bio} denote the uptake and bioavailability-adjusted inter-compartmental and drug clearance rate respectively and V_p/F_{bio} denotes the bioavailability adjusted volume of the peripheral compartment. **B:** Predicted plasma concentration time profiles of dolutegravir (DTG) for the first four days after initiation of a once daily 50mg oral regimen ($N = 300$ virtual patients). The red line depicts the median predicted concentrations, whereas the dark- and light grey areas present the quartile range and the 5–95% range respectively. Predicted (red line, grey areas) and measured plasma concentrations during 24h after drug intake in steady state (panel **C**) and after cessation of drug intake (panel **D**). Black circles and thin dashed lines represent DTG plasma concentration profiles in healthy volunteers (n = 17 concentration time profiles, 270 data points in total), whereas yellow circles, purple squares, grey diamonds and cyan triangles are DTG plasma concentration measurements in HIV patients (n = 39) observed 1, 2, 3 and 4 weeks after switching from efavirenz-based therapy to dolutegravir. Altogether, 354 plasma concentration measurements from 56 individuals are depicted. Reproduced from Duwal et al. [26].

model was used to generate PK parameters of virtual patients'in populations, whose PK-profiles are summarized in Figure 5.7B–D alongside observed DTG concentrations, Figure 5.7C–D. As one can see in Figure 5.7B, DTG is quickly taken up after oral administration and maximal concentrations are achieved after $t_{\text{max}} = 1.58$ hours (population 5-95% range: 1.53–1.63). Pharmacokinetics reach a plateau phase after about 4 doses. During the plateau phase, pre-dose minimum and maximum concentrations were $C_{\text{min}} = 2918$nM (1916–4336) and $C_{\text{max}} = 8471$nM (6353–11331)

parameter	value	unit	CV [%]
V_p/F_{bio}	0.73	L	-
Q/F_{bio}	0.0082	L/h	-
CL/F_{bio}	0.85	L/h	16.9
V_c/F_{bio}	17.7	L	16.4

Table 5.3: **Pharmacokinetic parameter estimates.** The table displays the estimated pharmacokinetic parameter estimates for healthy individuals. Interindividual variability (random effects) was included on drug clearance CL/F_{bio} and the volume of distribution V_c/F_{bio}. These parameters were log-normal distributed with coefficient of variation [%] $CV = 100 \cdot \sqrt{\exp(\sigma^2) - 1}$, where σ^2 is the variance of the associated normal distribution. A covariance of $11.3\% = 100 \cdot \sqrt{\exp(\sigma^2_{x,y}) - 1}$ between $x = \text{CL}/F_{\text{bio}}$ and $y = V_c/F_{\text{bio}}$ was estimated. The absorption rate constant was fixed [186] to 2.24h^{-1}. Residual variability was described by a combined proportional-additive model for healthy volunteers [σ =0.213 (37.2%) and $\widetilde{\sigma}$ =0.0019 mg/L (40.9%), respectively] and a proportional error model for HIV-infected patients [σ =0.402 (24.2 %)]. Reproduced from Duwal et al. [26].

for 50mg oral DTG. The plasma half-life of the DTG was 14.5h (5-95% range: 13.5–15.9).

5.3 Summary

In this chapter, we used various methods for model building discussed in Chapter 4 for the pharmacokinetics and pharmacodynamics. For TDF, FTC and 3TC, we built a plasma pharmacokinetic model of the major dominant circulating agent, which is dynamically linked with the model of intracellular pharmacokinetics. The plasma pharmacokinetics are best described by two compartment models respectively, whereas the intracellular pharmacokinetics is characterized by a nonlinear uptake and the first order elimination. The pharmacokinetics model is linked with the viral dynamics model. For DTG, we described a detailed nonlinear mixed-effects model for plasma pharmacokinetics. The plasma pharmacokinetics is best described by two compartment model. Due to the lack of the viral load data, the pharmacokinetics is not linked with pharmacodynamics.

CHAPTER 6

In vitro and *ex vivo* drug potencies

Understanding and predicting dose-response relationships requires building pharmacokinetic- pharmacodynamic models. As seen in Chapter 2, IC_{50} is an important parameter linking the two. We refer to IC_{50} as the *in vivo* (target-process) drug potency, which determines how strongly a particular concentration of a drug inhibits the target-process. The IC_{50} can be estimated using a PK-PD approach as in the previous chapter, illustrated for TDF, FTC and 3TC. We refer to this approach as 'top-down', as it utilizes clinical data and may lack mechanistic insight. A problem with the top-down approach is that the necessary clinical data is notoriously difficult and expensive to obtain. Moreover, in a number of scenarios clinical trials cannot be performed due to ethical reasons.

On the other hand, a number of *in vitro* and *ex vivo* experiments can be conducted under controlled conditions. The 'bottom-up' approach builds on these *in vitro* and *ex vivo* experiments to gain vital insights. Obviously, bottom-up models that can mechanistically translate *in vitro* parameters to *in vivo* parameters or parameters of clinical relevancy are desirable, but usually not available. Translation of *in vitro* or *ex vivo* parameters involves critical tasks, such as the integration of dynamic processes that may occur on various time scales [187], and validation of proposed processes/mechanisms.

In this chapter, we briefly recapitulate a bottom-up translation model based on the molecular mechanism of action of NRTIs [24]. The model describes viral DNA polymerization process, a crucial step in reverse transcription which is inhibited by NRTIs. We compare IC_{50} predictions from the 'bottom up' model with those from the top-down approach in order to validate the bottom-up model. For other antivirals, we provide a way to adjust their IC_{50}s determined in *ex vivo* single-round infectivity assays [87] for *in vivo* use.

6.1 A bottom-up model for NRTIs

NRTI are analogs of endogenous 2'-deoxy-nucleosides or nucleotides [141]. After an intracellular uptake they undergo sequential phosphorylation by host cell kinases and phosphotransferases to form analogs of naturally occurring deoxynucleoside triphosphate (dNTP) (see Figure 6.1 panel A). They compete with their natural counterparts for the integration in nascent viral DNA during HIV reverse transcription. If they become integrated, due to absence of the necessary chemical group to attach the next incoming nucleotide unlike their natural counterparts (see Figure 6.1 panel B), they bring the RNA/DNA polymerization to a halt, until they are excised [I].

[I] This section is based on Duwal et al. [23]. For further details on the model based on molecular mechanism of action for NRTIs, see von Kleist et al. [24]

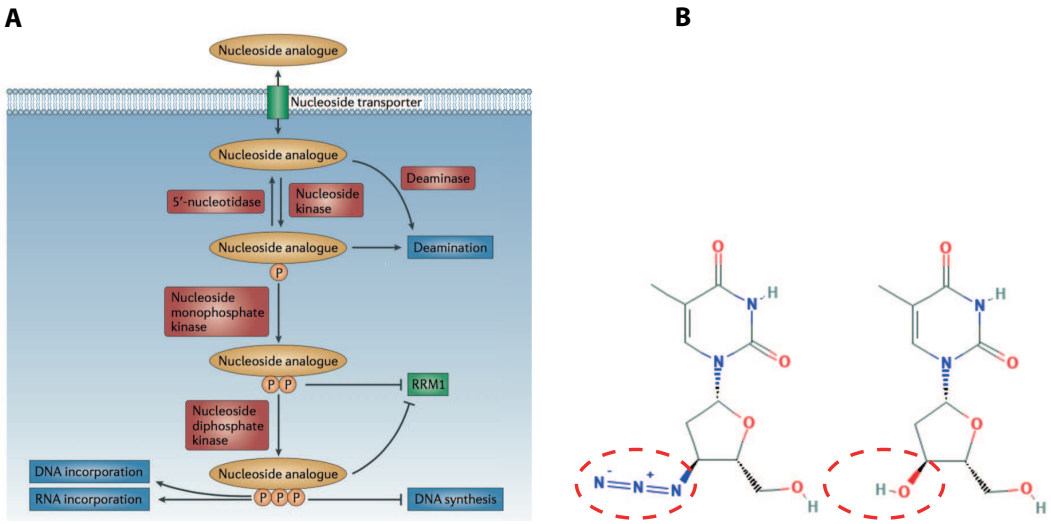

Figure 6.1: **Nucleoside reverse transcriptase inhibitor: A:** Intracellular modification (sequential phosphorylation) of nucleoside reverse transcriptase inhibitor. Extracted from Jordheim et al. [188]. **B:** Chemical structure of zidovudine and its natural occurring analog deoxythymidine. Adapted from Pubchem database [189, 190].

6.1.1 Molecular mechanism of action

The bottom-up model requires various kinetic parameters for the incorporation and removal of NRTI-TP and dNTP respectively, as well as typical concentrations of dNTPs in HIV-1 target cells. These parameters are available from various enzymatic assays. The kinetic parameters can be derived from pre-steady state kinetic *in vitro* experiments and are compiled in von Kleist et al. [24]. Concentrations of endogenous dNTPs in HIV-1 target cells can be measured *ex vivo* and are compiled in e.g. [191].

The residual polymerase activity in the presence of activated (tri-phosphorylated) nucleoside analogs ($1 - \epsilon(D_{\mathrm{RTI}})$) is expressed as [24]:

$$1 - \epsilon(D_{\mathrm{RTI}}) = \frac{\mathcal{T}_{0\to \mathrm{N}}(\varnothing)}{\mathcal{T}_{0\to \mathrm{N}}(D_{\mathrm{RTI}})}, \tag{6.1}$$

where $\mathcal{T}_{0\to \mathrm{N}}(\varnothing)$ and $\mathcal{T}_{0\to \mathrm{N}}(D_{\mathrm{RTI}})$ denote the expected time to finalize DNA polymerization mediated by the viral reverse transcriptase in the absence of drugs ($\varnothing$) and in the presence of nucleoside analog triphosphates (D_{RTI}) respectively.

The dose response curve for Eqn (6.1) has the shape of the standard Emax-model with slope coefficient 1 (see [24]), which is in line with observations by Shen et al. [87] for this inhibitor class. If the virus does not succeed to reverse-transcribe its genome in time, the virus will eventually be cleared intracellularly. The bottom-up model allows us to assess the relative probability that reverse transcription finishes in the presence of NRTIs, before the virus is cleared. This parameter can be compared to the ones derived from the top-down approach. The derivations can be found in von Kleist et al. [24]. We get the following relation

$$1 - \eta(D_{\mathrm{RTI}}) = \frac{1}{\rho_{rev,\varnothing} + \frac{1-\rho_{rev,\varnothing}}{1-\epsilon(D_{\mathrm{RTI}})}}, \tag{6.2}$$

with $1 - \eta(D_{\mathrm{RTI}}) = \rho_{rev,D_{\mathrm{RTI}}}/\rho_{rev,\varnothing}$, where $\rho_{rev,D_{\mathrm{RTI}}}$ denotes the probability that the reverse transcription is completed in the presence of inhibitors D_{RTI}. Similarly, $\rho_{rev,\varnothing} = 0.5$ [192] is the

probability that the reverse transcription is completed in the absence of inhibitors. After substituting the standard Emax model and solving for the respective IC_{50}, one obtains the following relation

$$IC_{50} = \frac{IC_{50,poly}}{1 - \rho_{rev,\varnothing}}. \tag{6.3}$$

where $IC_{50,poly}$ denotes the concentration that reduces reverse transcriptase mediated DNA polymerization by 50 % with respect to the absence of the drug. On the other hand, IC_{50} denotes the target-process drug potency which corresponds to the IC_{50} value from the top-down approach (see Subsection2.5.2).

6.1.2 Comparison of bottom-up model and top-down model

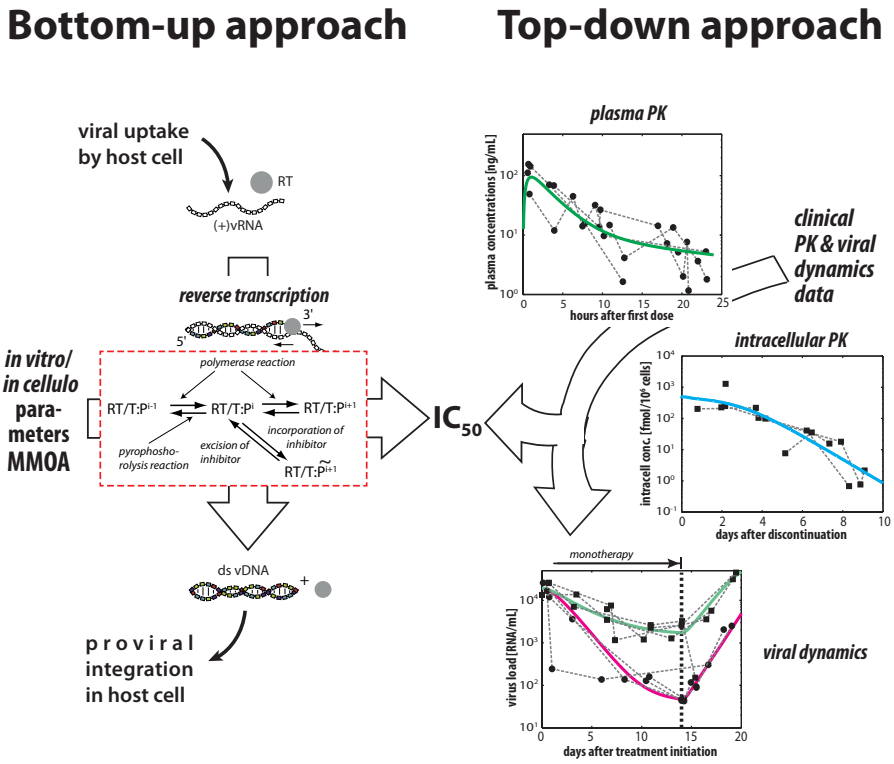

Figure 6.2: **Schematic of the two approaches to infer *in vivo* target-process potency for NRTIs.** We use two modelling strategies to infer target-process potency IC_{50}s . In the bottom-up approach (left) we explicitly model inhibition of reverse transcription by NRTI-TP and take *in vitro* kinetic parameters, as well as *ex vivo* physiological parameters as input. The central box depicts the types of reactions that occur during RT-induced DNA polymerization. A reverse transcriptase bound template:primer complex RT/T:P^i can undergo four basic reactions: (i) The primer may be shortened by one nucleotide during the exonuclease reaction RT/T:$P^i \rightarrow$ RT/T:P^{i-1}. (ii) The primer may be extended by one base during the polymerase reaction RT/T:$P^i \rightarrow$ RT/T:P^{i+1}, (iii) the NRTI-TP may be incorporated and the primer blocked RT/T:$P^i \rightarrow$ RT/T:$\tilde{P}^{i+1}$. In addition (iv) an incorporated NRTI may be excised from the blocked primer RT/T:$\tilde{P}^{i+1} \rightarrow$RT/T:$P^i$. In the top-down approach (right) we use pharmacokinetic (PK) data (plasma NRTI and intracellular NRTI-TP concentrations) to successively build and validate a composite PK model that links oral prodrug administration to intracellularly active NRTI-TP. The composite PK model is then linked to an established HIV-1 dynamics model [83, 85] and used to predict clinically observed, mono-therapy induced viral dynamics via fitting an Emax model. Reproduced from Duwal et al. [23].

Figure 6.2 schematically illustrates the top-down (PK-PD) and bottom-up (molecular mechanism of action) approaches for NRTIs. Both approaches can be used to infer the *in vivo* drug potency (IC_{50}). Next, we compare IC_{50} estimations from the bottom-up approach with those from top-down approaches. For bottom-up approach, we estimated inhibition of DNA-based polymerization in the wild type HIV-1 RT enzyme for 5000 nucleotide long heteromeric random sequences containing equal proportions of adenosine, cytosine, guanine and thymidine for lamivudine triphosphate (3TC-TP), emtricitabine triphosphate (FTC-TP) and tenofovir diphosphate (TFV-DP) with parameters stated in [24] (Table S1) and [191] (Table 2) for resting $CD4^+$ T-cells, which are the main HIV-1 target compartment. The leftmost panel in Figure 6.3 panel A shows the predicted % residual infection of resting $CD4^+$ T-cells. As can be seen, TFV-DP appears most potent in resting $CD4^+$ T-cells with an estimated IC_{50} value of 0.1μM ($\approx$ 18fmol/10^6cells), followed by FTC-TP (0.82 μM; $\approx$ 146fmol/10^6cells) and 3TC-TP (1.72 μM; $\approx$ 302fmol/10^6cells), which are similarly potent.

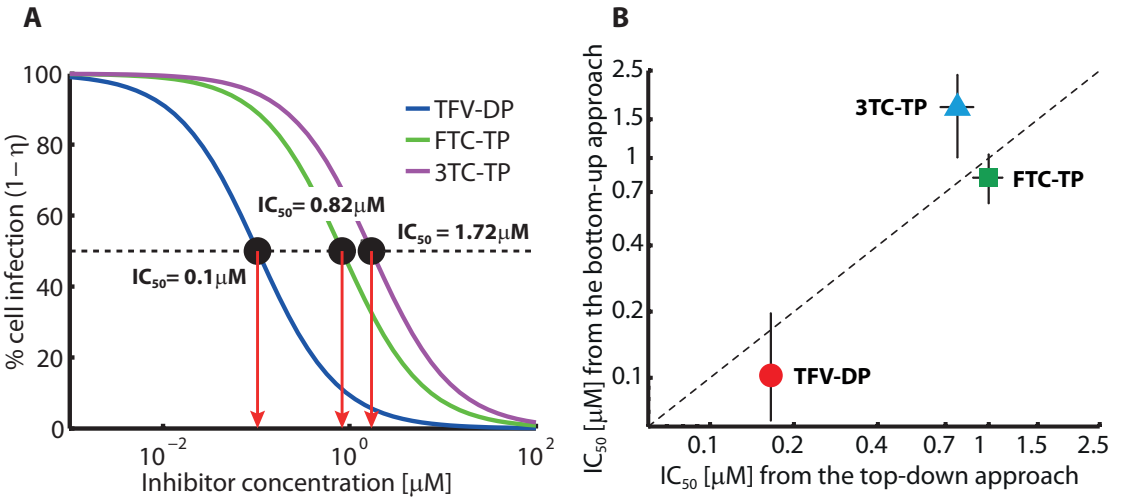

Figure 6.3: **Estimation of IC_{50} using a bottom-up model and comparison with top-down (PK-PD) estimates. A**: Relationship between the NRTI-TP intracellular concentration in μM and the inhibition of $CD4^+$ T-cell infection by HIV-1 in the bottom-up model. Blue-line: concentration vs. response for TFV-DP, green line : FTC-TP and magneta line: 3TC-TP. The black-dashed horizontal line marks 50 % inhibition and the red downward pointing arrows mark the IC_{50}s. **B**: The blue triangle, green square and red circle denote the respective median IC_{50} estimates for 3TC-TP, FTC-TP and TFV-DP. The dashed black diagonal line represents the line of unity. IC_{50} values from the bottom-up model are indicated on the y-axis for the respective drugs. Vertical error bars represent values contained by the 25-75th percentiles derived by recomputing estimates from 500 bootstrap resampled kinetic micro-parameters from the respective literature sources. Horizontal error bar represents the 25-75th percentiles of the corresponding IC_{50} estimates obtained from the top-down approach. Statistical properties of the top-down estimates were derived by recomputing estimates for each of the 500 bootstrap samples of the viral dynamics data used for IC_{50} calculation using the top-down approach. Reproduced from Duwal et al. [23].

Figure 6.3 panel B compares the IC_{50} predictions from the bottom-up vs. the top-down approaches for all analysed NRTIs. The horizontal error bars represent the predicted IC_{50} values contained by the 25-75th percentiles from the top-down approach whereas the vertical error bars represent the corresponding IC_{50} estimates from the bottom-up approach. Qualitatively both approaches estimate a TFV-DP > FTC-TP $\approx$ 3TC-TP ranking with regard to target-potency. Quantitatively, the top-down approach under-predicts the 50% inhibitory concentrations for 3TC-TP in comparison with the bottom-up approach (2.3 fold difference, discussed below), whereas for

TFV-DP it is slightly over-predicted (< 2 fold difference). For FTC-TP, the agreement is excellent. With the exception of 3TC-TP, this indicates that the predictions from the two different approaches are in good agreement and that the bottom-up approach may be used to infer the clinical efficacy of NRTIs.

In our specific case, we achieve an overall very good agreement between estimates of *in vivo* potency. This apparent discrepancy may be largely attributed to the top-down approach: The predicted IC_{50} from the top-down approach is highly dependent on the quality and statistical reliability of the clinical data. For NRTIs, pharmacokinetic profiles of intracellular active components are notoriously difficult to measure, sparse and noisy. Some of this difficulty may be contributed to differences in the preparation of PBMC samples and their potential contamination with red blood cells [193]. Along these lines, we utilized clinical data that reports lower concentrations of 3TC-TP than e.g. [176] and [175] (compare Figure 5.6C-D [150 and 300mg BID] in Chapter 5 with Figure 2 of Else et al. [175] [150 and 300mg QD]). Consequently, our top-down model might predict a greater potency of 3TC-TP (smaller IC_{50} value) than if we had fitted our model to the data of Else et al. [175], who report higher 3TC-TP concentrations.

Another limitation of the top-down approach is that in order to ensure parameter identifiability some interdependent parameters have to be fixed. In our case parameters related to viral kinetics were fixed to literature values in order to enable the estimation of the respective IC_{50} values. Obviously, viral dynamics may exert some variability in different populations, which we could not be fully accounted for.

6.2 Determining drug potency for other antiviral classes

Unlike NRTIs, for all other antiretrovirals drugs the dominant circulating agent in plasma corresponds to the active moiety and does not need to undergo chemical modification for activation. Obviously, their concentrations in the target site determine their effects. For RTI, InI and PI, the target site is located intracellularly, whereas for CRA, the target site is the cell surface. However, it should be noted that not all drug molecules are available to exert antivirals effects, since a fraction of these are bound to proteins and lipids. This is particularly true for lipophylic drugs. According to the first statement of free drug hypothesis [194] (see Box 6.1), only the free unbound concentration at the target-site exerts the pharmacological effect [195, 196].

The second key concept of the free drug hypothesis states that in dynamical equilibrium, the unbound drug concentrations are identical on both sides of the cellular membrane. Under this assumption, the unbound plasma concentration of antivirals corresponds to the unbound intracellular concentration. In fact, all analysed NNRTIs, InIs and PIs, except for raltegravir (RAL), are highly lipophilic, enabling the *unbound* drug to rapidly cross cellular membranes, generating an equilibrium between the *unbound* drug on either side of the cellular membrane [197]. Even for the weakly lipophilic compound raltegravir, intracellular concentrations are proportional to plasma concentrations by a factor precisely resembling their unbound moiety [198, 199], strongly arguing for the validity of the free drug hypothesis for all analysed drugs. Note that for NRTIs, the free drug hypothesis is not valid, since the dominant circulating agents are subjected to active transport and intracellular modifications, which are saturable processes. Secondly, for NRTIs the active moiety is strongly charged, such that passive diffusion across membrane is unlikely [160].

An important pharmacological parameter is the fraction unbound in plasma f_u. Various methods can be used to determine the fraction unbound in plasma such as ultracentrifugation, ultrafiltration and equilibrium dialysis [196]. To summarize, for all antivirals except NRTIs, their unbound plasma concentrations closely reflect their target site concentrations and hence, the plasma pharmacokinetics can be directly linked to pharmacodynamics or viral dynamics obviating the need to

explicitly model intracellular concentration.

Box. 6.1: Free Drug hypothesis

In vivo, a major fraction of drug molecules binds reversibly to proteins and lipids in blood plasma and in tissues and the remaining fraction is free or unbound [194]. The free drug molecules can diffuse from blood to other tissues across biomembranes and interact with the therapeutic targets. The two key concepts of the hypothesis are that (i) the unbound or free drug concentration at the site of action exerts the pharmacological activity and (ii) in equilibrium the unbound concentrations are identical on both sides of any biomembrane. In equilibrium

$$D_{\text{plasma, unbound}} = D_{\text{tissue, unbound}}$$

where $D_{\text{plasma, unbound}}$ and $D_{\text{tissue, unbound}}$ denote unbound plasma and tissue drug concentrations respectively. It should be emphasized that the total concentrations are not identical across the biomembrane, i.e.,

$$D_{\text{plasma, total}} \neq D_{\text{tissue, total}}$$

where $D_{\text{plasma, total}}$ and $D_{\text{tissue, total}}$ are total plasma and tissue drug concentrations. In plasma, drug molecules bind to plasma proteins. The most relevant plasma protein are albumin and α_1-acidic glycoproteins. The extent of plasma protein binding is closely related to the physiochemical properties of drugs such as lipophilicity, polarity, molecular size, degree of ionization etc.
It should be noted that not all drugs obey the free drug hypothesis. Examples include drugs with very low passive permeability (charged or polar compounds), drugs undergoing active transport in or out the target-site tissues and drugs with poorly perfused target-site tissue.

In order to link plasma pharmacokinetics to pharmacodynamics, the *in vivo* drug potency parameter IC_{50} is required. The drug potency parameter IC_{50} can be inferred from *ex vivo* experiment such as a single-round infectivity assay [87] (see Figure 6.4). The virus is incubated with HIV susceptible cells along with drug at a particular concentration. If a virus infects the cell, the cell produces the green fluorescent protein, which can be detected by flow cytometry. This allows to measure the drug efficacy as the percentage of cells producing green fluorescent protein with respect to the absence of drug.

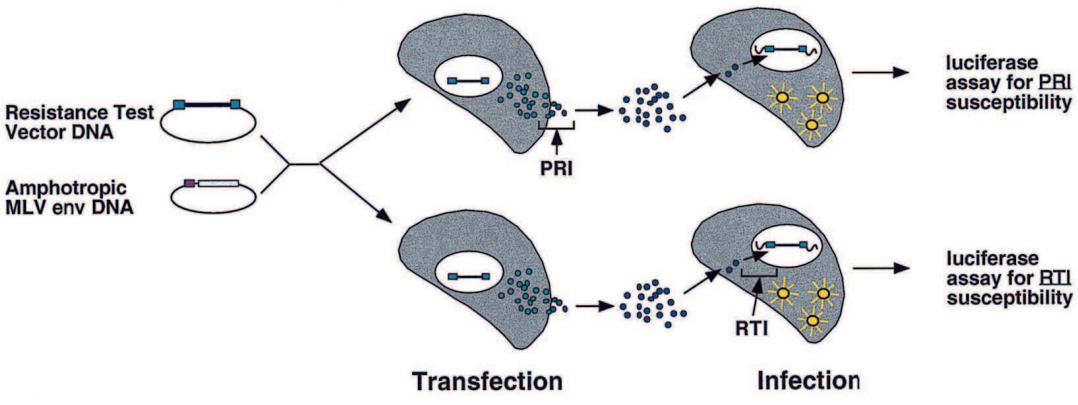

Figure 6.4: **Schematic illustration of single-round infectivity assay:** The pseudotyped viruses are generated by transfecting HEK293T cells with green fluorescent protein tagged, envelope-defective HIV-1 vector along with a plasmid that expresses amphotrophic murine Leukemia virus [200]. Shen et al. [87] modified the assay by replacing amphotrophic murine leukemia virus with an HIV-1 CXCR4 envelope expression vector. After the transfection, the virus particles are harvested and are incubated with healthy $CD4^+$ cells. The successful infection of $CD4^+$ cells is measured by the luciferase activity. Extracted from Petropoulos et al. [200]).

However, the *ex vivo* drug potency determined in the assay is not identical to the *in vivo* parameter, since the *unbound* fraction $f_{u,\text{assay}}$ in the assay is different to the physiological *unbound* fraction f_u in plasma. This is attributed to the fact that the cells in the assays are not incubated in 100 % human plasma. Thus, $\text{IC}_{50,\text{assay}}$ determined need to be adjusted. In Appendix B, we derive equation

$$\text{IC}_{50} = \text{IC}_{50,\text{assay}} \cdot \frac{2}{f_u + 1}, \tag{6.4}$$

where IC_{50} denotes the total concentration (unbound and bound) in plasma that inhibits 50 % of target process. $\text{IC}_{50,\text{assay}}$ is the total concentration (unbound and bound) determined in the single-round infectivity assay that inhibits 50 % of the target process. The term f_u represents the unbound fraction of the drug in plasma. The derivation is based on the free drug hypothesis. Table B.1 in Appendix B enlists adjusted IC_{50} from the single-round infectivity assay for various antivirals utilizing Eqn (6.4) and drug specific protein binding parameter.

6.3 Summary

To understand how *in vitro* and *ex vivo* repeatable insights translate into clinical outcomes is of great value, because this allows to optimize therapy and to assess particular treatment scenarios before they are tested in human. While integration of pre-clinical knowledge and data with clinical pharmacology is desirable, it is often a challenging task.

In this chapter, we briefly provided the main idea behind the bottom-up model for NRTIs [24]. For NRTIs, the free drug hypothesis cannot be used, as the formation of intracellular active moiety requires saturable active transport process and intracellular modifications [156,201]. This makes it particularly difficult to determine the potency of NRTIs experimentally: In a phenotypic assay (e.g. single-round infectivity assay [200, 202]), it may be insufficient to relate the compounds potency to the concentrations added to the medium surrounding the cells, unless the relation between NRTIs and intracellular NRTI-TP is known for the analysed cell type. This possibly explains the discrepancy between the quantitative results from different phenotypic assays [203].

We used top-down models to test the validity of the bottom-up model for NRTIs. The predictions from the bottom-up model showed remarkable agreement with the predictions obtained from the top-down models (see Figure 6.3), arguing for the validity of the mechanistic assumptions regarding the molecular mechanism of action of NRTIs. Noteworthy, this argues that *in vitro* parameters can be translated into measures of clinical efficacy using the bottom-up model. This can be extremely valuable, since many experiments cannot be conducted in the *clinic*. The bottom-up model can be used to infer the potency of various NRTIs in inhibiting e.g. mutant viruses (using e.g. parameters stated in von Kleist et al. [24]).

All other antivirals besides NRTIs exhibit physiochemical properties arguing for validity of the free drug hypothesis. We provided a way to correct the IC_{50} determined in the *ex vivo* experiments for *in vivo* use and the corrected IC_{50}s are reported.

CHAPTER 7

Viral extinction and infection probabilities

In this chapter, we deal with methods to quantify the viral extinction probabilities and reciprocally the infection probabilities influenced by antivirals employing methods discussed in Chapter 3. We begin by simplifying the detailed viral replication cycle model described in Chapter 2. Then, we proceed by distinguishing between scenarios where reaction propensities of the viral dynamics are time-invariant and time-variant (see Section 3.5.2). Time-invariant reaction propensities arise when the active moiety concentration at the target-site remains constant resulting in a time-constant target-process inhibition. In general, the active moiety concentration at the target-site does not remain constant. Correspondingly, the target-process inhibition is time-varying and reaction propensities of the viral dynamics are time-variant (time-inhomogeneous Markov Jump Process) [I].

7.1 A simplified viral dynamics model for the early infection phase

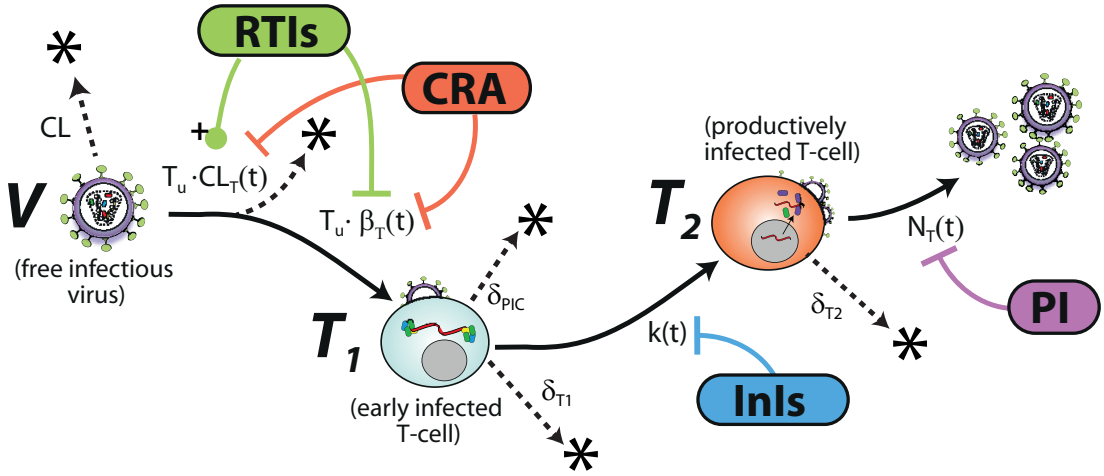

Figure 7.1: **Schematic of the simplified HIV dynamics model and mechanism of action by treatment-approved drug classes:** CRA: Co-receptor antagonist, RTI: reverse transcriptase inhibitor, InI: Integrase inhibitor, PI: Protease inhibitor. Reproduced from Duwal et al. [27].

[I] This chapter is based on articles [25–27]

Whether or not an infection occurs is determined very shortly after a viral challenge. For instance, if an infection has occurred, the eclipse phase lasts for roughly 10 days (see Chapter 2 Section 2.3) after which viremia grows exponentially. Hence, for the aforementioned purpose, it suffices that the viral dynamics model adequately describes the viral dynamics shortly after a challenge and it might not need the complexity of the detailed model that captures long-time viral dynamics behaviours such as three decay phases. Motivated by this insight, we pursue a simplification of the detailed viral dynamics model.

Ping et al. [204] studied phenotypic and genotypic variations of HIV-1 in a large number of acute and early infected subjects and reported that the transmitted or founder viruses are exclusively T-cell tropic in agreement with other studies [205–207]. In similar lines, Isaacmen-Beck et al. [208] reported that the transmission does not enhance macrophage-cell tropism. The preferential infection of T-cell in comparison to slow replicating cells like macrophages during early infection can be explained by the necessity to maintain high basic reproductive number R_0 in order to establish the infection [209].

Following these insights, we simplified the original model [83] and its extension [85] by focussing on T-cells, which are the primary target of virus during the early infection. We only implicitly considered latent infected cells and macrophages. Similar simplifications have been previously used by other studies [77, 210–213]. The simplified model is schematically depicted in Figure 7.1. The term $\mathrm{T_{u,SS}}$ denotes the steady state level of uninfected T-cells prior to a virus challenge and is given by following ratio:

$$\mathrm{T_{u,SS}} = \frac{\lambda_\mathrm{T}}{\delta_\mathrm{T}}. \tag{7.1}$$

During the onset of infection, the number of viruses are relatively low and the number of uninfected T-cells is fairly unaffected by virus dynamics [210, 214]. Thus, during simulations, we consider the number of uninfected T-cells to be constant as described by equation (7.1), and in line with related approaches [215].

The terms $\delta_{\mathrm{T}_1} < \delta_{\mathrm{T}_2}$ denote the rates of clearance of T_1 and T_2 cells respectively and $\delta_{\mathrm{PIC,T}}$ denotes the rate of intracellular destruction of the pre-integration complex. Other than these events, the dynamics of the stochastic viral replication model after the virus challenge are defined by six reactions. In absence of antivirals $\varnothing$, we have

R_1. Clearance of free virus $V \rightarrow *$

$$a_1(\mathrm{V}(t), \varnothing) = \left(\mathrm{CL} + \mathrm{CL_T} \cdot \mathrm{T_{u,SS}}\right) \cdot V(t) \tag{7.2}$$

R_2. Clearance of an early infected cell $\mathrm{T}_1 \rightarrow *$

$$a_2(\mathrm{T}_1(t), \varnothing) = \left(\delta_{\mathrm{PIC,T}} + \delta_{\mathrm{T}_1}\right) \cdot \mathrm{T}_1(t) \tag{7.3}$$

R_3. Clearance of a late infected cell $\mathrm{T}_2 \rightarrow *$

$$a_3(\mathrm{T}_2(t), \varnothing) = \delta_{\mathrm{T}_2} \cdot \mathrm{T}_2(t) \tag{7.4}$$

R_4. Infection of a susceptible cell $V \rightarrow \mathrm{T}_1$

$$a_4(V(t), \varnothing) = \beta_\mathrm{T} \cdot \mathrm{T_{u,SS}} \cdot \mathrm{V}(t) \tag{7.5}$$

R_5. Proviral integration $\mathrm{T}_1 \rightarrow \mathrm{T}_2$

$$a_5(\mathrm{T}_1(t), \varnothing) = k_\mathrm{T} \cdot \mathrm{T}_1(t) \tag{7.6}$$

R_6. Production of virus $T_2 \rightarrow V + T_2$

$$a_6(T_2(t), \varnothing) = N_T \cdot T_2(t), \tag{7.7}$$

with $CL_T = \left(\frac{1}{\rho_{rev,\varnothing}} - 1\right) \cdot \beta_T$ in R_1 where $\rho_{rev,\varnothing} = 0.5$ denotes the probability to successfully complete reverse transcription in the absence of inhibitors [192,216]. The parameters of the simplified viral dynamics model can be found in Table A.1. Note that in the first reaction we assumed that the target-cell population changes only marginally during the initial steps of the infection and was thus approximated by its steady state value $T_{u,SS}$ (see Eqn (7.1)). Therefore, both the clearance of free virus and the clearance of virus by unsuccessful infection can be subsumed into the expression for a_1.

7.2 Time-constant target-process inhibition

Here, we utilize the simplified viral dynamics described in Section 7.1, which is sufficient to describe the stochastic behaviour shortly after a viral exposure. Let $Y(t)$ be a state vector consisting of all viral compartments i.e, number of free viruses, early and late infected cells at time t as shown below:

$$Y(t) = \begin{bmatrix} V \\ T_1 \\ T_2 \end{bmatrix}, \tag{7.8}$$

where V, T_1 and T_2 are the number of viruses, early and late infected T cells at time t respectively. Let y_0 denote an initial state vector i.e, $Y(0) = y_0$. We are interested in the extinction probability or reciprocally the infection probability for any given initial state. Mathematically, the extinction probability is defined as

$$\mathcal{E}(y_0, \bullet) := \mathbb{P}\left(Y(t) = \begin{bmatrix} 0 \\ 0 \\ 0 \end{bmatrix} \,\middle|\, y_0 = \begin{bmatrix} V \\ T_1 \\ T_2 \end{bmatrix}; \bullet \right) \tag{7.9}$$

for $t \rightarrow \infty$ under some drug condition $\bullet$. In other words, the extinction probability is the probability that a stochastic trajectory starting at y_0 eventually reaches the absorbing state $[0, 0, 0]^\top$. Obviously, the infection probability is the complement of the extinction probability, hence,

$$\mathcal{I}(y_0, \bullet) = 1 - \mathcal{E}(y_0, \bullet). \tag{7.10}$$

Next, we will assume a time-constant drug inhibition i.e.,

$$\eta_{\mathcal{K}}(t) = \text{const.}, \quad \text{where} \quad \text{const.} \in [0, 1], t \geq 0$$

and employ branching processes techniques to compute the virus extinction probability analytically [217]. Firstly, the assumption of a time-constant drug inhibition permits the computation of the infection probability in an absence of a drug. The assumption is exactly valid, since the drug inhibition is constant in the absence of drug ($\eta_{\mathcal{K}}(t) = 0$).

The concentration of an active moiety for a dosing regimen varies over time and corresponding the resulting target-process inhibition on the viral life cycle also varies. Hence, predicting the stochastic behaviour of a viral dynamics trajectory shortly after exposure needs to account for the time-varying target process inhibition. However, usually a detailed concentration time-profile may not be easily available. Instead the range of concentration over a time period may be available. Assuming the minimum concentration is maintained for the relevant time horizon, the lower range

of the infection or extinction probabilities for the dosing regimen can be computed. Similarly, the maximum concentration can be used to infer the upper range of the probabilities.

We use $\bullet = \varnothing$ to denote the absence of any drug, whereas $\bullet = D_{\mathcal{K}}$ denotes some constant drug concentration belonging to the drug class $\mathcal{K}$. For ease of notation, we will replace $\mathcal{E}(y_0, \bullet)$ with $\mathcal{E}(y_0)$, since the results are valid as long as the target-process inhibition is constant throughout the process.

When the drug pharmacokinetics is assumed to be constant $Z(t) = \text{const.}$ or changes insignificantly $Z(t) \approx \text{const.}$, the hybrid stochastic-deterministic system $X(t)$ can be reduced to the stochastic system $Y(t)$. For the ease of notation, we introduce the unit vectors $\widehat{\mathrm{V}}$, $\widehat{\mathrm{T}}_1$ and $\widehat{\mathrm{T}}_2$ which denotes the states where only one infected compartment is present (either virus, early or late infected cells)

$$\widehat{\mathrm{V}} = \begin{bmatrix}1\\0\\0\end{bmatrix}, \ \widehat{\mathrm{T}}_1 = \begin{bmatrix}0\\1\\0\end{bmatrix}, \ \widehat{\mathrm{T}}_2 = \begin{bmatrix}0\\0\\1\end{bmatrix}. \tag{7.11}$$

Any state of the system can be expressed as a linear combination of these unit vectors, e.g. $5 \cdot \widehat{\mathrm{V}} \oplus 3 \cdot \widehat{\mathrm{T}}_1 \oplus 2 \cdot \widehat{\mathrm{T}}_2$ denotes the state, where we have 5 viruses, 3 early infected cells and 2 late infected cells. Similarly, the zero vector ($[0, 0, 0]^\top$ is denoted by $\mathbf{0}$.

7.2.1 Viral dynamics as a Markov jump process

The viral replication cycle can be interpreted as a Markov jump process [II]. For the sake of simplicity, the state $Y(t_n)$ at time t_n is denoted by y_n and without loss of generality, y_0 and y_1 denote the initial- and the next state respectively.

Here, we introduce a term 'single path' or 'unit transition' for the sake of clarity. A single path or a unit transition is closely related to the next firing reaction in the context of the stochastic approach for chemical systems. For example, consider a single virus in the host at time 0. For some time to next reaction τ, let the next reaction firing for the illustration purpose be the clearance of the virus (R_1). In this case, the single path or the unit transition is denoted by $\widehat{\mathrm{V}} \to *$ which refers to the virus being cleared. The probability of the path is equivalent to the probability that the associated reaction fires next:

$$\mathbb{P}(y_1 = \mathbf{0} | y_0 = \widehat{\mathrm{V}}) = p(j = 1 | \tau, \widehat{\mathrm{V}}; 0), \tag{7.12}$$

where $j = 1$ denotes the index of the reaction which clears the virus. Thus, we can write

$$\mathbb{P}(y_1 = \mathbf{0} | y_0 = \widehat{\mathrm{V}}) = \frac{a_1}{a_1 + a_4} = \frac{\mathrm{CL} + \mathrm{CL_T} \cdot \mathrm{T_{u,SS}}}{\mathrm{CL} + \mathrm{CL_T} \cdot \mathrm{T_{u,SS}} + \beta_{\mathrm{T}} \cdot \mathrm{T_{u,SS}}}. \tag{7.13}$$

where $\mathrm{CL_T}$ and β_{T} denote the rate constants of virus intracellular clearance and infection respectively. Similarly, the probability of the path ($\widehat{\mathrm{V}} \to \widehat{\mathrm{T}}_1$) is given by:

$$\mathbb{P}(y_1 = \widehat{\mathrm{T}}_1 | y_0 = \widehat{\mathrm{V}}) = \frac{a_4}{a_1 + a_4}. \tag{7.14}$$

Notice that these unit transition probabilities are time-invariant due to the assumption of a time-constant target-process inhibition.

Any composite path can be described by these unit transition probabilities. For instance, the probability of a composite path such as $\widehat{\mathrm{V}} \to \widehat{\mathrm{T}}_1 \to \widehat{\mathrm{T}}_2$ can be broken into the corresponding probabilities of a single paths as shown below (for further details see Appendix C):

$$\mathbb{P}(y_2 = \widehat{\mathrm{T}}_2 | y_0 = \widehat{\mathrm{V}}) = \mathbb{P}(y_2 = \widehat{\mathrm{T}}_2 | y_0 = \widehat{\mathrm{T}}_1) \cdot \mathbb{P}(y_1 = \widehat{\mathrm{T}}_1 | y_0 = \widehat{\mathrm{V}}). \tag{7.15}$$

[II] For our purpose, we constructed the embedded Markov chain model [217] from the continuous-time Markov jump process model of the viral replication cycle.

7.2.2 Closed-form solutions

Under the assumption of statistical independence(assuming that the competition for target-cells is negligible during the onset of infection), the probability that n infectious viruses within a target-cell environment go extinct is given by [III]

$$\mathcal{E}(y_0 = n \cdot \widehat{\mathrm{V}}) = (\mathcal{E}(y_0 = \widehat{\mathrm{V}}))^n. \tag{7.16}$$

The extinction event can be interpreted as a high-dimensional analog to the classic gambler's ruin problem first solved by pascal [218]. The term $\mathcal{E}$ can be written as [219]

$$\begin{aligned} \mathcal{E}(y_0 = \widehat{\mathrm{V}}) &= \sum_{i=0}^{\infty} \mathbb{P}(y_r = i \cdot \widehat{\mathrm{V}} | y_0 = \widehat{\mathrm{V}}) \cdot \mathcal{E}(y_r = i \cdot \widehat{\mathrm{V}}), \\ &= \sum_{i=0}^{\infty} \mathbb{P}(y_r = i \cdot \widehat{\mathrm{V}} | y_0 = \widehat{\mathrm{V}}) \cdot \mathcal{E}(y_r = \widehat{\mathrm{V}})^i \end{aligned} \tag{7.17}$$

where $\mathcal{E}(y_r = i \cdot \widehat{\mathrm{V}})$ denotes the probability of a virus extinction when i viruses were produced in the first replication cycle and where we used Eqn (7.16) in the second equality. In words, the extinction probability for a single virus is given by the probability that i viruses are produced in a single replication cycle r, $\mathbb{P}(y_r = i \cdot \widehat{\mathrm{V}} | y_0 = \widehat{\mathrm{V}})$, and that all of these viruses eventually go extinct, considering all possible values of i. Herein, we assumed statistical independence, i.e. $\mathcal{E}(y_r = i \cdot \widehat{\mathrm{V}}) = \mathcal{E}(y_r = \widehat{\mathrm{V}})^i$. The extinction probability for parent- and progeny virus remain identical, since the reaction rates do not change when the inhibition and uninfected target-cell cells remain constant, hence the equality $\mathcal{E}(y_0 = \widehat{\mathrm{V}}) = \mathcal{E}(y_r = \widehat{\mathrm{V}})$ holds.

In Appendix C, we simplified Eqn (7.17) by breaking down it into its respective single path probabilities, which are ratios of reaction propensities. The algebraic simplification results in a quadratic equation with the unknown variable being the extinction probability for a single virus $\mathcal{E}(y_0 = \widehat{\mathrm{V}})$. Hence, two solutions exist and the extinction probability is given by the minimum of the two solutions as shown below:

$$\mathcal{E}(y_0 = \widehat{\mathrm{V}}) = \min\left(1, \frac{a_1}{a_1 + a_4} + \frac{a_4}{a_1 + a_4} \cdot \frac{a_2}{a_2 + a_5} + \frac{a_3}{a_6}\right). \tag{7.18}$$

Reciprocally, the infection probability is given by :

$$\mathcal{I}(y_0 = \widehat{\mathrm{V}}) = \max\left(0, 1 - \frac{a_1}{a_1 + a_4} - \frac{a_4}{a_1 + a_4} \cdot \frac{a_2}{a_2 + a_5} - \frac{a_3}{a_6}\right). \tag{7.19}$$

[III] Here, we used $\mathcal{E}(y_0 = n \cdot \widehat{\mathrm{V}})$ instead of explicitly denoting an absence of drug (i.e. $\mathcal{E}(y_0 = n \cdot \widehat{\mathrm{V}}, \varnothing)$ or a constant drug concentration $\mathcal{E}(y_0 = n \cdot \widehat{\mathrm{V}}, D_{\mathcal{K}})$, as the derivation onward is valid for both cases.

7.2.3 Relation to the reproductive number

Box. 7.1: Reproductive number (R_0)

The concept of the basic reproductive number R_0 is extensively used in population ecology (study of spread or dynamics of species and their interaction with the environment), epidemiology (study of spread and distribution of a disease in a population) and in the study of within-host pathogen dynamics. In population ecology, the basic reproductive number R_0 is defined as the average number of offspring an individual has during its entire life-time. Similarly, in context of epidemiology, it refers to the average number of secondary infections produced by an infected individual during his or her entire infectious period [220, 221].
R_0 is an important parameter that indicates the transmissibility of an infection and the potential for a species to spread in the population. For an infection, R_0 determines whether a pathogen can persist or perish in such a population. For an infection with $R_0 < 1$, which means that on average each infectious individual infects less than one other individual and implies that the infection will die out. On the other hand, if $R_0 > 1$, the infection or pathogen may be able to spread in the population [220, 221].

Here, we are interested in R_0 in the context of *within-host infection*. Let R_0 denote the average number of viruses produced from a single founder virus [220] in a replication cycle. Mathematically, R_0 can be written as follows

$$R_0 = \sum_{i=1}^{\infty} \mathbb{P}(y_r = i \cdot \widehat{\mathrm{V}} | y_0 = \widehat{\mathrm{V}}) \cdot i, \tag{7.20}$$

and the algebraic simplification (shown in Appendix C) leads to the following expression:

$$R_0 = \frac{a_4}{a_1 + a_4} \cdot \frac{a_5}{a_2 + a_5} \cdot \frac{a_6}{a_3}. \tag{7.21}$$

Note that the number of viruses being produced from a single founder virus is likely bimodal. This implies that in the majority of cases a single founder virus will not manage to produce any progeny, however, those viruses that produce progeny will produce vast amounts of viral offspring. The extinction and infection probabilities for a single virus inoculum can be expressed in terms of R_0 as given below:

$$\mathcal{E}(y_0 = \widehat{\mathrm{V}}) = \min\left(1, 1 - \frac{a_4}{a_1 + a_4} \cdot \frac{a_5}{a_2 + a_5} \cdot \left(1 - \frac{1}{R_0}\right)\right) \tag{7.22}$$

and

$$\begin{aligned} \mathcal{I}(y_0 = \widehat{\mathrm{V}}) &= 1 - \mathcal{E}(y_0 = \widehat{\mathrm{V}}), \\ &= \max\left(0, \frac{a_4}{a_1 + a_4} \cdot \frac{a_5}{a_2 + a_5} \cdot \left(1 - \frac{1}{R_0}\right)\right). \end{aligned} \tag{7.23}$$

Other compartments

Until now, we have derived a closed-form solution for the extinction probability conditioned that a single virus reaches the target-cell compartment. Similarly, we can derive the extinction probability given a single early- or late infected cell T_1 and T_2 respectively. Let the term $\mathcal{E}(y_0 = \widehat{\mathrm{T}}_1)$

and $\mathcal{E}(y_0 = \widehat{\mathrm{T}}_2)$ be the respective extinction probabilities for a single T_1 or T_2 cell.

$$\mathcal{E}(y_0 = \widehat{\mathrm{T}}_1) = \min\left(1, 1 - \frac{a_5}{a_2 + a_5} \cdot \left(1 - \frac{1}{R_0}\right)\right) \tag{7.24}$$

$$\Leftrightarrow \mathcal{I}(y_0 = \widehat{\mathrm{T}}_1) = \max\left(0, \frac{a_5}{a_2 + a_5} \cdot \left(1 - \frac{1}{R_0}\right)\right) \tag{7.25}$$

and

$$\mathcal{E}(y_0 = \widehat{\mathrm{T}}_2) = \min\left(1, \frac{1}{R_0}\right), \tag{7.26}$$

$$\Leftrightarrow \mathcal{I}(y_0 = \widehat{\mathrm{T}}_2) = \max\left(0, 1 - \frac{1}{R_0}\right) \tag{7.27}$$

Under the assumption of statistical independence, the extinction probability of any given combination of free virus V, early-stage infected cell T_1 and late-stage infected cell T_2 can then be computed as

$$\mathcal{E}\left(y_0 = \begin{bmatrix} \mathrm{V} \\ \mathrm{T}_1 \\ \mathrm{T}_2 \end{bmatrix}\right) = \left(\mathcal{E}(y_0 = \widehat{\mathrm{V}})\right)^{\mathrm{V}} \cdot \left(\mathcal{E}(y_0 = \widehat{\mathrm{T}}_1)\right)^{\mathrm{T}_1} \cdot \left(\mathcal{E}(y_0 = \widehat{\mathrm{T}}_2)\right)^{\mathrm{T}_2} \tag{7.28}$$

Using the parameters in Table A.1 , the extinction probabilities in the absence of drug are computed: $\mathcal{E}(y_0 = \widehat{\mathrm{V}}, \varnothing) = 0.9018$, $\mathcal{E}(y_0 = \widehat{\mathrm{T}}_1, \varnothing) = 0.5212$ and $\mathcal{E}(y_0 = \widehat{\mathrm{T}}_2, \varnothing) = 0.0150$. Reciprocally, the infection probabilities are: $\mathcal{I}(y_0 = \widehat{\mathrm{V}}, \varnothing) = 0.0982$, $\mathcal{I}(y_0 = \widehat{\mathrm{T}}_1, \varnothing) = 0.4788$ and $\mathcal{I}(y_0 = \widehat{\mathrm{T}}_2, \varnothing) = 0.985$.

7.3 Time-varying target-process inhibition

We derived closed-form solutions for extinction probabilities for the time-constant target-site drug concentration (time-invariant reaction propensities). In general, target-site drug concentrations are time-varying and correspondingly the reaction propensities of viral dynamics are time-variant. Figure 7.2 schematically depicts stochastic viral dynamics under deterministic pharmacokinetics arising in the context of PrEP. Closed form solutions for extinction probabilities are not possible for the time-varying target-site drug concentration. Thus, we have to employ algorithms discussed in the hybrid stochastic-deterministic approach (see Chapter 3). In the following, we tailored the algorithms (CME and SSA) to quantify the extinction probability or reciprocally the infection probability for time-varying target-site drug concentrations (time-variant reaction propensities).

7.3.1 Reduced-state viral dynamics model and the chemical master equation

Solving a full state CME suffers from the curse of dimensionality. To circumvent this, we propose a reduced-state model for viral dynamics model as an approximation. This relies on the key observation that reaching the T_2 stage is critical in order to establish an infection. Previously, we observed that in absence of drug the infection probability is very high once the viral dynamics has advanced to T_2. $\mathcal{I}(\widehat{\mathrm{T}}_2, \varnothing)$ is roughly 10 fold of $\mathcal{I}(\widehat{\mathrm{V}}, \varnothing)$ and twice $\mathcal{I}(\widehat{\mathrm{T}}_1, \varnothing)$ (compare $\mathcal{I}(\widehat{\mathrm{T}}_2, \varnothing) = 0.9850$ vs. $\mathcal{I}(\widehat{\mathrm{V}}, \varnothing) = 0.0982$ and $\mathcal{I}(\widehat{\mathrm{T}}_2, \varnothing) = 0.9850$ vs. $\mathcal{I}(\widehat{\mathrm{T}}_1, \varnothing) = 0.4788$). These comparisons highlight that establishing a systemic infection is a *boom or bust process*, either there is no offspring (bust) or T_2 stage is reached producing a large number of offspring (boom) making

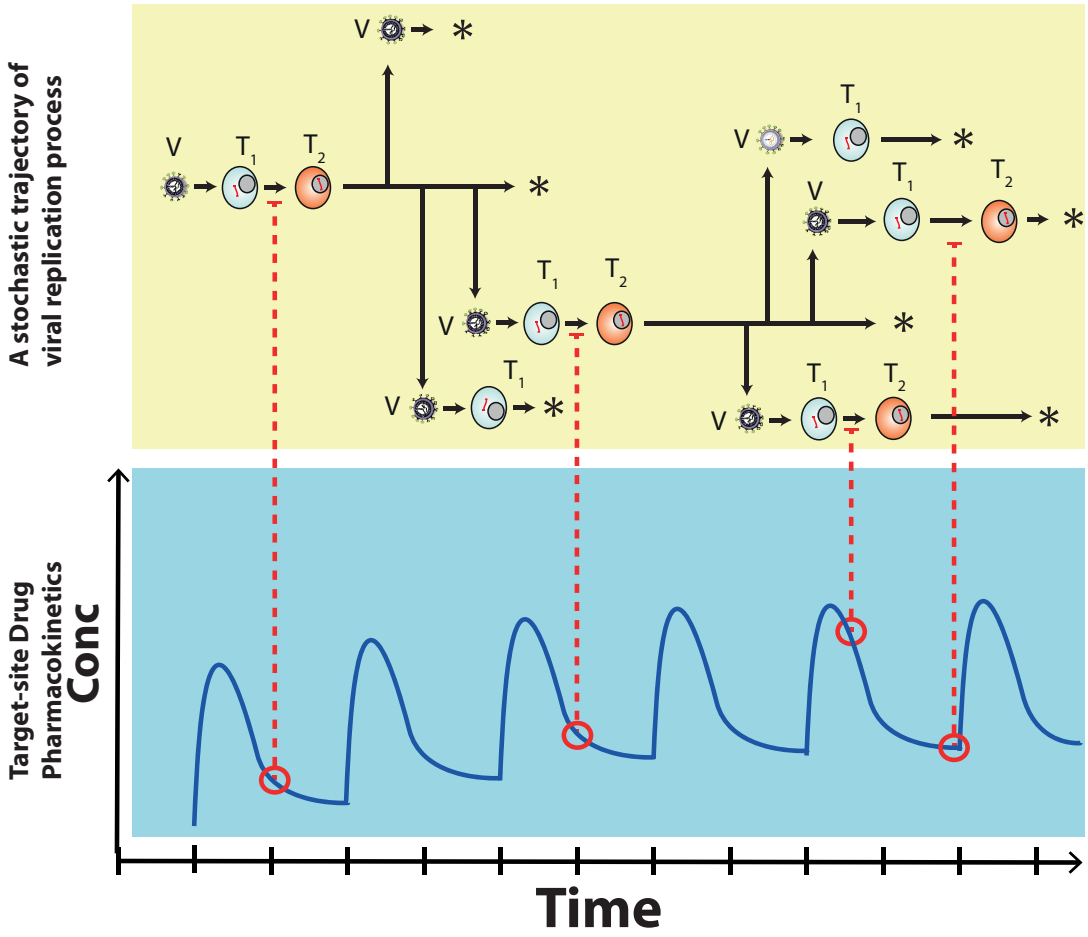

Figure 7.2: **Schematic depiction showing the target-site drug pharmacokinetics time profile (an extrinsic process) affecting the intrinsic stochastic dynamics of viral replication cycle:** The bottom most panel depicts an exemplary target-site pharmacokinetic time profile for an integrase inhibitor after multiple oral doses. The topmost panel illustrates an exemplary stochastic trajectory starting with a single virus under the influence of drug pharmacokinetics.

extinction very unlikely. The transitions in the viral replication cycle before T_2 is reached are bottle-necking in nature.

Obviously, the question arises how reaching T_2 determines whether or not a systemic infection establishes *in presence of a drug*. To that end, let us look at the probability that a single virus fails to produce any progeny until the end of the first replication cycle under some influence of drug. We denote this probability $\mathcal{E}_R(\widehat{V})$:

$$\mathcal{E}_R(\widehat{V}) = \frac{a_1}{a_1 + a_4} + \frac{a_4}{a_1 + a_4} \cdot \frac{a_2}{a_2 + a_5} + \frac{a_4}{a_1 + a_4} \cdot \frac{a_5}{a_2 + a_5} \cdot \frac{a_3}{a_3 + a_6}. \tag{7.29}$$

The above equation is the summation of probability that a virus is cleared before reaching T_1, probability that T_1 is reached but cleared before advancing to T_2 and the probability that T_2 is reached but cleared before producing any progeny (see Eqn (C.7) and Eqn (C.8)). Note that the complement of this probability is the probability that a virus reaches T_2 and produces some offspring.

Next, we computed the relative difference between the extinction probability and the probability that a virus fails to produce any single progeny at the end of the first replication cycle.

Mathematically, we computed

$$\text{Relative difference} = \frac{\mathcal{E}(\widehat{\mathrm{V}}) - \mathcal{E}_R(\widehat{\mathrm{V}})}{\mathcal{E}(\widehat{\mathrm{V}})}. \tag{7.30}$$

Figure 7.3 panel A depicts the relative difference with increasing target-process inhibition for all drug classes given a single virus. Interestingly, for CRA, RTI and InI, the relative error is less than 0.2 % and is constant for a wide range of target-process inhibition. Whereas for PI, the relative difference increases (up to 10 %) with increasing target-process inhibition. This highlights that the completion of the first replication cycle is crucial in establishing the infection. Also, we see that the probability that a virus fails to produce any progeny at the end of first replication cycle ($\mathcal{E}_R(\widehat{\mathrm{V}})$) serves as a good proxy for the extinction probability of a single virus ($\mathcal{E}(\widehat{\mathrm{V}})$) for drug classes CRA, RTI and InI. However, $\mathcal{E}_R(\widehat{\mathrm{V}})$ does not approximate $\mathcal{E}(\widehat{\mathrm{V}})$ for PI. Furthermore, we plotted the relative difference vs. target-process inhibition for all drug classes, when a recipient is challenged with 100 viruses in Panel B of Figure 7.3. Mathematically, the relative difference is given by

$$\text{Relative difference} = \frac{\mathcal{E}(100 \cdot \widehat{\mathrm{V}}) - \mathcal{E}_R(100 \cdot \widehat{\mathrm{V}})}{\mathcal{E}(100 \cdot \widehat{\mathrm{V}})}. \tag{7.31}$$

Figure 7.3 panel B shows that the relative difference is strongly magnified for all drug classes as a consequence of exposure to multiple viruses. Hence, the suggested approximation for extinction probability works only for CRA, RTI and InI given an exposure with a low number of viruses.

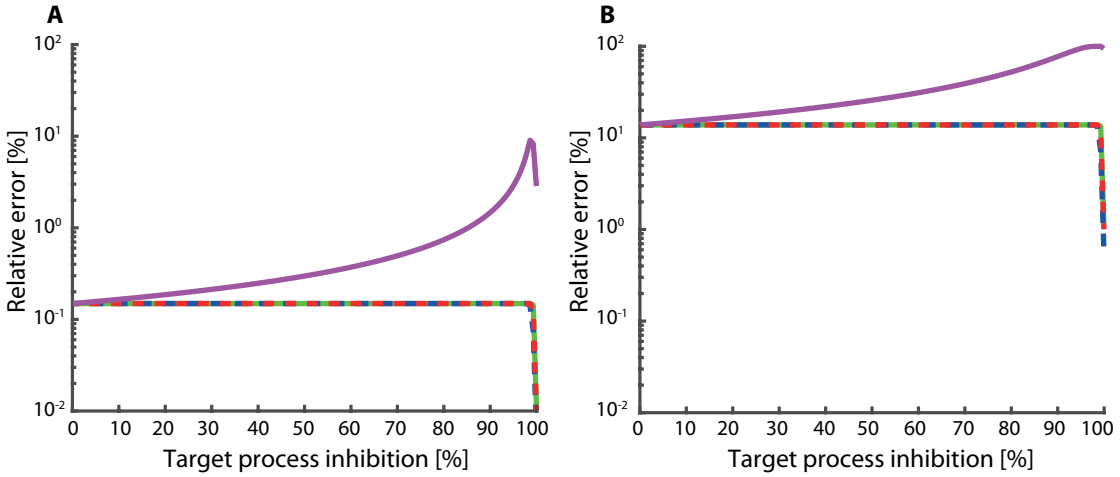

Figure 7.3: **Relative error due to an approximation of the viral extinction probability for various drug classes with a varying target-process inhibition:** The approximation utilizes the probability that a virus fails to complete its first replication round as a proxy for the extinction probability. **A:** Relative error of the approximation for a single virus **B:** Relative error of the approximation for 100 viruses. The dashed green, red, blue and solid purple lines belong to RTI, CRA, InI and PI respectively.

We propose an approximation for CME based on the insight that the probability that a virus fails to produce any progeny in the first replication round serves as a good approximation for the extinction probability. Instead of considering all the possible states, we only consider states relevant in the first replication cycle and introduce a virtual state 'Pro' (proliferation state). The proliferation state Pro denotes that the first replication cycle has been completed (see Figure 7.4). [IV]

[IV] Note that the introduction of the 'proliferation' state requires an extra dimension in the state vector and the state

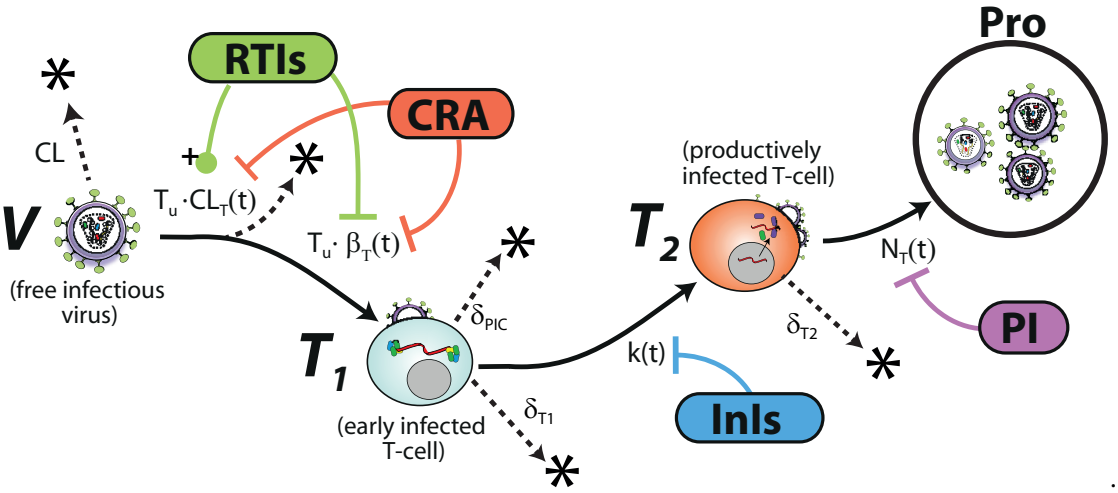

Figure 7.4: **reduced-state viral dynamics model:** The reduced-state viral dynamics model for the CME constitutes a virtual state Pro. The state Pro denotes that the first replication cycle has been completed. The proposed approximation is based on the insight that the probability that a virus fails to produce any progeny in the first replication round serves as a good approximation for the extinction probability. Adapted from Duwal et al. [27].

We make use of the stochastic transition function, which we introduce in Chapter 3. Here, we have

$$\mathbf{p}(t, Y(t_0), Y(t)) := \mathbb{P}(Y(t) = y | Y(t_0) = \widehat{\mathrm{V}}; \mathcal{D}), \tag{7.32}$$

which is the probability that the stochastic process is in state y at time t given that the process started at t_0 with a single virus $\widehat{\mathrm{V}}$ under a some time-varying drug concentration trajectory $\mathcal{D}$.

For ease of readability, we use a short notation $\mathbf{p}(t, Y(t))$ where we leave the initial state vector $\widehat{\mathrm{V}}$ from the notation. The corresponding CME can be written as follows:

$$\begin{aligned}
\frac{\mathrm{d}}{\mathrm{d}t}\mathbf{p}(t, \widehat{\mathrm{V}}) &= -\left(\mathrm{CL} + \mathrm{CL_T}(t) \cdot \mathrm{T_{u,SS}} + \beta_\mathrm{T}(t) \cdot \mathrm{T_{u,SS}}\right) \cdot \mathbf{p}(t, \widehat{\mathrm{V}}), && (7.33)\\
\frac{\mathrm{d}}{\mathrm{d}t}\mathbf{p}(t, \widehat{\mathrm{T}}_1) &= \beta_\mathrm{T}(t) \cdot \mathrm{T_{u,SS}} \cdot \mathbf{p}(t, \widehat{\mathrm{V}}) - \left(\delta_{\mathrm{PIC,T}} + \delta_{\mathrm{T}_1} + k_\mathrm{T}\right) \cdot \mathbf{p}(t, \widehat{\mathrm{T}}_1), && (7.34)\\
\frac{\mathrm{d}}{\mathrm{d}t}\mathbf{p}(t, \widehat{\mathrm{T}}_2) &= k_\mathrm{T} \cdot \mathbf{p}(t, \widehat{\mathrm{T}}_1) - \left(\delta_{\mathrm{T}_2} + \widehat{N}\right) \cdot \mathbf{p}(t, \widehat{\mathrm{T}}_2), && (7.35)\\
\frac{\mathrm{d}}{\mathrm{d}t}\mathbf{p}(t, \mathrm{Pro}) &= \widehat{N} \cdot \mathbf{p}(t, \widehat{\mathrm{T}}_2). && (7.36)
\end{aligned}$$

At t_0, the simulation is started with $\mathbf{p}(t_0, \widehat{\mathrm{V}}) = 1$. For $t \to \infty$, the probabilities of states $\widehat{\mathrm{V}}, \widehat{\mathrm{T}}_1, \widehat{\mathrm{T}}_2$ decay to zero and the stationary values of the probability of being in the state Pro is achieved. The extinction probability can be approximated as shown below:

$$\mathcal{E}(\widehat{\mathrm{V}}, \mathcal{D}) \approx 1 - \mathbf{p}(\infty, \mathrm{Pro}). \tag{7.37}$$

Under the statistical independence assumption, the extinction of n viruses can be approximated as shown below:

$$\mathcal{E}(n \cdot \widehat{\mathrm{V}}, \mathcal{D}) \approx (1 - \mathbf{p}(\infty, \mathrm{Pro}))^n. \tag{7.38}$$

vectors need to be redefined accordingly. For example, the state vector $\widehat{\mathrm{V}}$ should be $[1, 0, 0, 0]^\top$ with the last entry for the proliferation state instead of $[1, 0, 0]^\top$. Here, we implicitly assume such extension.

Notice that this approximation using the reduced-state CME, instead of full-state CME, inherits the same weakness as the approximation of the infection probability by the probability to complete the first replication cycle. Thus, as mentioned previously, this approximation is only good for drug classes CRA, RTI and InI and not for PI. Secondly, the relative error scales up with an increase in the number of viruses.

This reduced-state CME assumes that the extinction is very unlikely once the first replication cycle is completed. However, this might not hold in case of drug with high efficacy ($\eta > 90\%$). Thus, using the reduced-state CME is only suggested for drug classes CRA, RTI and InI when their instantaneous target-process inhibition is under 90% for the time horizon of interest and for a relatively low number of initial viruses.

7.3.2 Adaptation of stochastic simulation algorithms

Next, we discuss the adaptation of stochastic simulation algorithms for the purpose of quantification of extinction and infection probabilities for time-varying drug concentrations.

7.3.2.1 EXTRANDE and upper bound of reaction propensities

EXTRANDE requires the selection of two parameters (i) a look-ahead time horizon L and (ii) a way to compute the upper bound $B(t)$ for the sum of reaction propensities valid for the entire look-ahead time horizon. Here, we adapt EXTRANDE for simulating the dynamics of viral extinction/infection by proposing an upper bound that does not require a manual choice of a so called look-ahead time horizon L.

In Subsection 2.5.2, we introduced a term $\eta_{\mathcal{K}}$ denoting the efficacy of an antiretroviral belonging to the drug class $\mathcal{K} \in \{\text{CRA, RTI, InI, PI}\}$ described by an Emax equation.

Reverse transcriptase inhibitors. Since $\eta_{\text{RTI}} \in [0, 1]$ and from Eqn (2.2), Eqn (2.3) and Eqn (2.4) it can easily be shown that

$$a_1(V(t), D_{\text{RTI}}(t)) + a_4(V(t), D_{\text{RTI}}(t)) = a_1(V(t), \varnothing) + a_4(V(t), \varnothing) \tag{7.39}$$

and therefore

$$a_0(Y(t), D_{\text{RTI}}(t)) = a_0(Y(t), \varnothing), \tag{7.40}$$

where $a_0 = \sum_k a_k$ is the sum of reaction propensities. It also follows that

$$a_0(Y(t+s), D_{\text{RTI}}(t+s)) = a_0(Y(t), \varnothing) \tag{7.41}$$

where $0 \leq s \leq \tau$ denotes any time interval *before* a stochastic reaction has fired. Consequently, the sum of reaction propensities does not change for RTIs and we can choose $B = a_0(Y(t))$. Interestingly, there will be no rejection steps in this case.

Other inhibitor classes. Co-reception antagonists (CRA) decrease reaction propensity a_1 and a_4, InIs decrease a_5 and PIs reduce a_6 respectively by a factor $(1 - \eta_{\mathcal{K}}) \in [0, 1]$, which implies

$$a_0(Y(t), D_{\mathcal{K}}(t)) \leq a_0(Y(t), \varnothing), \tag{7.42}$$

and consequently

$$a_0(Y(t+s), D_{\mathcal{K}}(t+s)) \leq a_0(Y(t), \varnothing). \tag{7.43}$$

for any time interval $0 \leq s \leq \tau$ *before* a stochastic reaction has fired. Therefore, we can always choose $B = a_0(Y(t), \varnothing)$ as an upper bound to meet condition (3.50) without the requirement to select a look-up time horizon L.

7.3.2.2 Stopping criteria for stochastic simulation algorithm

Using stochastic simulation algorithms to assess the PrEP/PEP efficacy requires classification of stochastic trajectories of the viral dynamics as an extinction or an infection event. For the simplified viral dynamics model, the null state is an unstable fixed point and also an absorbing state, i.e. when trajectories hit this state, the virus is eliminated, and we can stop the simulation. To stop the simulation when trajectories move away from the extinction state is not a straightforward choice. *We are interested to determine how or when to stop a trajectory that moves away from the extinction state, in other words when to classify a trajectory as an infection trajectory.*

One may set arbitrary thresholds $[\mathrm{V}(t) = \mathrm{const}_0, \mathrm{T}_1(t) = \mathrm{const}_1, \mathrm{T}_2(t) = \mathrm{const}_2]^\top$ and assume that an infection occurred when a trajectory exceeds these thresholds. While too small thresholds misleadingly overestimate the number of infection events, large thresholds increase the run-time of the simulations considerably. Furthermore, there is no control of the numerical error made, i.e. the probability to falsely classify a trajectory as an infection event.

Below, we present a method to rigorously classify stochastic trajectories as infection events, incorporating a user-defined error tolerance (probability to falsely classify a trajectory as an infection event). This can be used as the stopping criteria for a stochastic simulation using the integral-based stochastic simulation algorithm and EXTRANDE.

Extinction simplex

Previously, we presented a closed form solution for computing the extinction probability for any particular state of the virus dynamics system, under the assumption that the drug effect η is constant. Under the assumption of statistical independence, the extinction probability for any state of the system $y = [\mathrm{V}, \mathrm{T}_1, \mathrm{T}_2]^\top$ is given by:

$$\mathcal{E}\left(y = \begin{bmatrix} \mathrm{V} \\ \mathrm{T}_1 \\ \mathrm{T}_2 \end{bmatrix}, D_{\mathcal{K}}\right) = \left(\mathcal{E}(\widehat{\mathrm{V}}, D_{\mathcal{K}})\right)^{\mathrm{V}} \cdot \left(\mathcal{E}(\widehat{\mathrm{T}}_1, D_{\mathcal{K}})\right)^{\mathrm{T}_1} \cdot \left(\mathcal{E}(\widehat{\mathrm{T}}_2, D_{\mathcal{K}})\right)^{\mathrm{T}_2}. \tag{7.44}$$

Let us consider a term $\varepsilon \in (0, 1]$. We can divide the state space of viral dynamics $y \in \mathbb{N}_0^3$ into two sets: The first set contains all the states where the extinction probability exceeds ε (which we will refer as *extinction simplex* or *extinction polyhedron*). Mathematically, for any state in this extinction simplex, the following should be valid

$$\varepsilon \leq \mathcal{E}(y, D_{\mathcal{K}}), \tag{7.45}$$

whereas in the second set, the extinction probabilities of states are smaller than ε:

$$\varepsilon > \mathcal{E}(y, D_{\mathcal{K}}). \tag{7.46}$$

Taking the logarithm on both sides of Eqn (7.45), we get

$$\begin{aligned} \log_{10}(\varepsilon) &\leq \log_{10}(\mathcal{E}(y, D_{\mathcal{K}})) \\ &= \mathrm{V} \cdot \log_{10}(\mathcal{E}(\widehat{\mathrm{V}}, D_{\mathcal{K}})) + \mathrm{T}_1 \cdot \log_{10}(\mathcal{E}(\widehat{\mathrm{T}}_1, D_{\mathcal{K}})) + \mathrm{T}_2 \cdot \log_{10}(\mathcal{E}(\widehat{\mathrm{T}}_2, D_{\mathcal{K}})). \end{aligned} \tag{7.47}$$

For any state in the extinction simplex, this should be valid. Given a user-defined threshold $\varepsilon \ll 1$ we therefore only consider stochastic states within the *extinction simplex*, e.g. states y for which

$$\mathcal{E}(y, D_{\mathcal{K}}) \geq \varepsilon \tag{7.48}$$

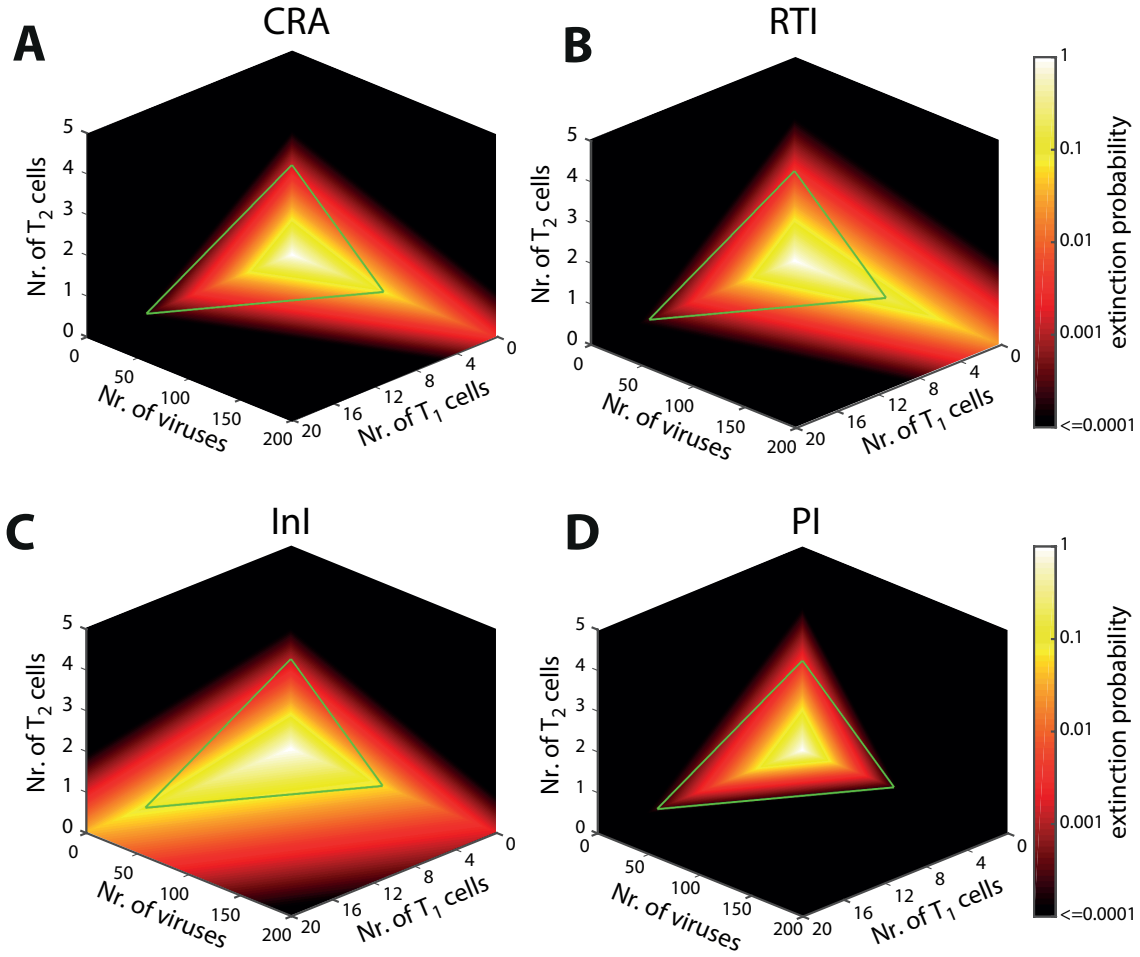

Figure 7.5: **Extinction simplices for all drug classes for a target inhibition of 80 %. A:** CRA **B:** RTI **C:** InI **D:** PI. The three dimensions are the number of free viruses, early-infected T cells (T_1) and late-stage infected T cells (T_2). The colour varies from bright yellow denoting certain extinction, to black denoting an extinction probability less than 0.0001. The region enclosed by green lines is the extinction simplex in the absence of antivirals with a threshold of 0.0001.

is true. Figure 7.5 displays the extinction simplices belonging to different drug classes assuming a respective target inhibition of 80 %. The colour varies from bright yellow denoting certain extinction, to black denoting an extinction probability less than 0.0001.

For a constant target-site antiviral concentration the stopping criteria for the stochastic simulation algorithm could be determined using the extinction simplex; Whenever a trajectory leaves the simplex, an infection is encountered, i.e. the simulation is stopped whenever

$$\mathcal{E}(Y(t), D_{\mathcal{K}}(t)) < \varepsilon$$

and the realization is classified as an infection event. This criterion guarantees that the probability to falsely classify a trajectory as an infection event is smaller than ε. However, for the fixed target-site concentrations, we already derived closed form solutions, making simulations unnecessary.

We will next incorporate the above derived stopping criteria to utilize them in the case of time-varying drug efficacy. Note that there is a positive relationship between the size of the extinction simplex and the drug efficacy η, this means for the more efficient (potent) drug, the extinction simplex is larger.

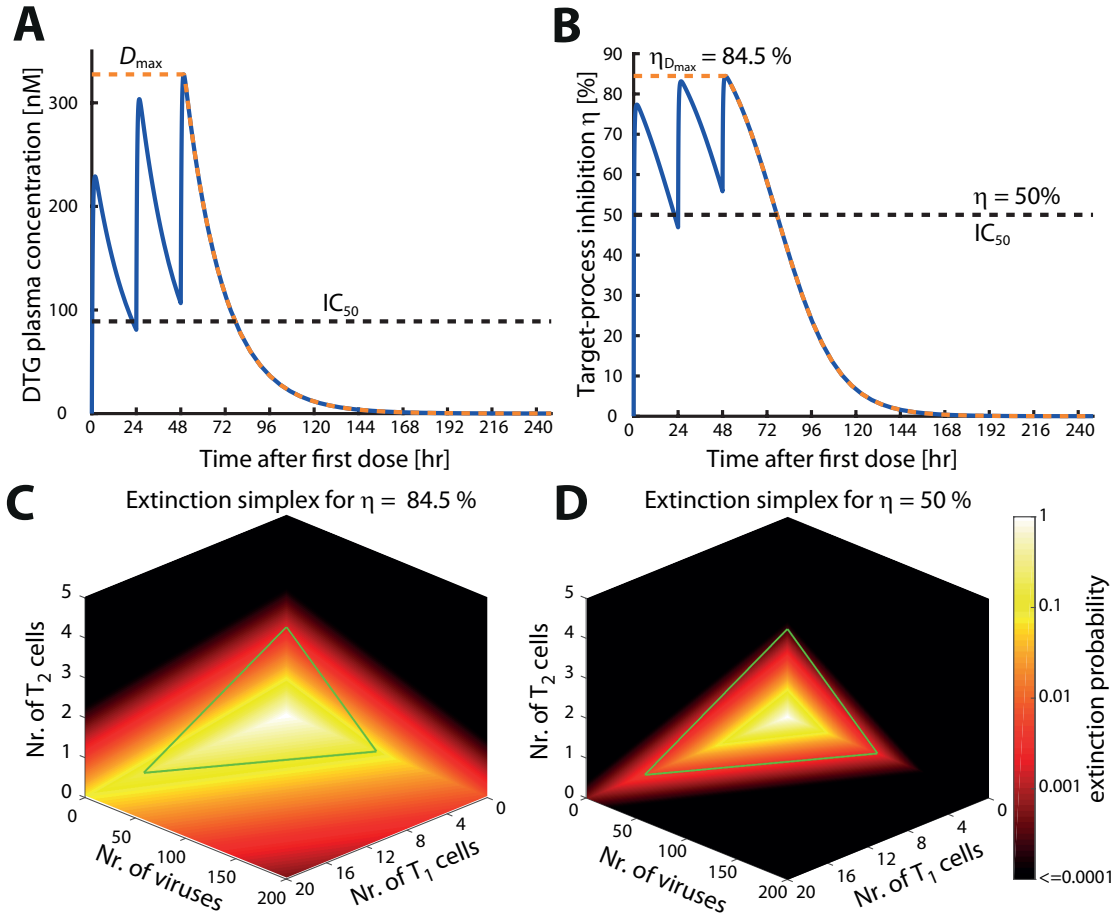

Figure 7.6: **Adaptation of extinction simplex based on antiviral pharmacokinetics:** **A**: Exemplary dolutegravir (DTG) pharmacokinetics for 3days of 2mg oral DTG once daily. The blue line represents DTG plasma concentrations. The dashed orange line represents the function $D_{max}(t)$, which for a particular t returns the maximum DTG concentration achieved in any future time i.e $D_{max}(t) = \max(D(s))$ where $s \in [t, \infty)$. The black horizontal dashed line marks the IC_{50} for DTG [222]. **B**: Instantaneous target-process inhibition (blue line) corresponding to the concentration-time profile in **A**. The orange line is the target-process efficacy profile for $D_{max}(t)$. The black horizontal dashed line marks $\eta = 50\%$. **C**: Extinction simplex corresponding to $\eta = 84.5\%$. **D**: The extinction simplex corresponding to $\eta = 50\%$. Panels **C** and **D** show the state space with three dimensions corresponding to number of free viruses, early-infected T cells (T_1) and late-stage infected T cells (T_2). The colour varies from bright yellow denoting certain extinction, to black denoting an extinction probability less than 0.0001. The region enclosed by green lines is the extinction simplex in absence of antivirals. Reproduced from Duwal et al. [26]

Therefore, a simple way is to pre-compute the maximum achievable target-site concentration of an antiviral for a particular dosing regimen, i.e.

$$D_{max} = \max_{t \in [0,\infty]} D_{\mathcal{K}}(t) \tag{7.49}$$

and to define an *extinction simplex* using D_{max}, i.e. to stop the trajectories and count an infection event if, for some state $Y(t)$,

$$\mathcal{E}(Y(t), D_{max}) < \varepsilon, \tag{7.50}$$

which guarantees that the probability to falsely classify a trajectory as an infection event is smaller than ε. However, due to the relationship between the size of the *extinction simplex* and the drug

efficacy η, the simplex might be large and therefore simulations may take a long time until they can be regarded as infection events. In order to further improve the run-time of simulations, instead of a fixed extinction simplex one can use the maximum antiviral concentration reachable in any future time $[t, \infty]$:

$$D_{max}(t) = \max_{u \in [t,\infty]} D_{\mathcal{K}}(t). \tag{7.51}$$

Figure 7.6 illustrates the adaptation of the *extinction simplex* in the EXTRANDE algorithm for a typical pharmacokinetics profile achieved during a short course PrEP with dolutegravir (once daily for 3 days with 2 mg DTG - Panel A). The blue line represents DTG plasma concentration, whereas the dashed orange line marks the $D_{max}(t)$. The black horizontal dashed line marks the IC_{50} for DTG. The panel B shows the target inhibition corresponding to the PK profile in panel A and $D_{max}(t)$. Panel C and D display the extinction simplices corresponding to $D_{max}(t)$ and IC_{50} respectively. Note that the size of the extinction simplex shrinks as the drug concentration tapers after the last dosing and consequently reaches the size of extinction simplex without any drug. Particularly during short-course PrEP and PEP simulations, this guarantees that the algorithm will stop in reasonable CPU time.

Infection of long-lived cells as a stopping criterion

It has previously been shown that long lived- and latently infected cells are a major barrier to the elimination of HIV and that they may be established early in infection [223–225]. This reservoir has been attributed to infected macrophages [51, 79] and latently infected T-cells with very long half-lives [226–228]. If any of these compartments become infected after viral exposure, infection may be considered irreversible. During simulations we considered two parameters, $p_{M|a_4} = 1.25 \cdot 10^{-4}$ and $p_{L|a_5} = 8 \cdot 10^{-6}$ to assess whether a long-lived cell (e.g. macrophage) had been infected or whether a latently infected cell emerged. These parameter choices accurately reproduce viral decay kinetics during antiretroviral combination therapy, as shown in articles [83,85] and recapture estimated reservoir sizes during chronic infection [223, 229]. I.e., during simulations, whenever reaction R_4, or R_5 fires, it is assessed whether a long lived- or latently infected cell emerged.

For our purpose, we adapted the EXTRANDE algorithm by introducing an intuitive upper bound for the sum of reaction propensities and stopping criteria. Similarly, we adapted the integral-based SSA algorithm by using stopping criteria. The pseudo-codes of the adapted algorithm are provided in Appendix D. Figure 7.7 demonstrates two trajectories using the adapted EXTRANDE for illustration purposes. We simulated a chronic PrEP with 2 mg of oral DTG with a low adherence for a 3 month duration. The left panels belong to a simulation which led to an infection. Panel A shows the instantaneous target-process inhibition time profiles due to the drug pharmacokinetics, whereas Panel B shows the stochastic time profiles of three viral compartments namely V, T_1 and T_2. The right panels belong to the simulation leading to a viral extinction. Panel C and D depict the instantaneous target-process inhibition profiles and trajectories of viral compartment respectively.

In theory, both stochastic simulation algorithms are exact. However, the EXTRANDE algorithm is preferential to integral-based SSA since the integral-based SSA might suffer from numerical errors in integral steps. Additionally, the integral-based SSA is in general inefficient due to computationally time consuming integral steps. It should be noted that if the upper bound of the sum of reaction propensities for EXTRANDE is not stringent enough, there might be a large number of extra reactions rendering EXTRANDE inefficient. To test whether or not the adapted EXTRANDE is more efficient than the adapted integral-based SSA, we ran simulations for various scenarios comparing the performance of both algorithms (see Appendix D). For all the test scenarios, EXTRANDE was indeed faster than the integral-based SSA. The performance of the

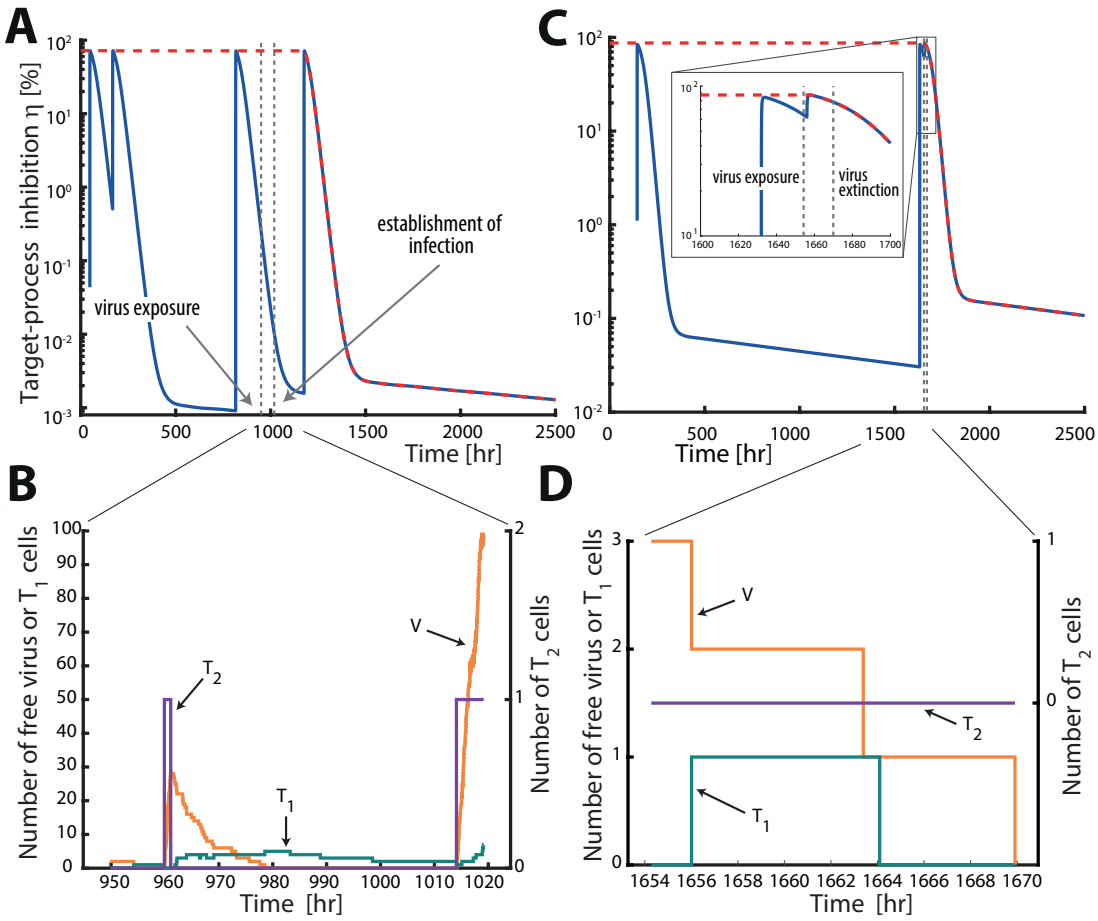

Figure 7.7: **Trajectories for time-varying drug effects.** The left panels show an example of an infection event, whereas the right panels show an example of viral extinction for chronic PrEP with 2mg DTG and 5% adherence. Panels **A** and **C** depict the instantaneous target-process inhibition profiles and panels **B** and **D** depict the corresponding viral trajectories using the adapted EXTRANDE algorithm. Viral exposure occurs randomly during a 3 month period and is sampled from the transmitted virus distribution as in the article [25]. **A and C:** The blue lines depict the instantaneous target-process inhibition profiles $\eta_D(t)$. The dashed red line denotes the maximum target-process inhibition $\eta_{D_{max}}(t)$. The leftmost grey vertical dashed lines mark the time of viral exposure, whereas the rightmost lines mark the time point of either establishment of infection (panel **A**) or virus extinction (panel **C**). **B and D:** Stochastic trajectories of viral compartments (orange: free viruses, green: early-infected cells T_1, purple: late-infected T_2 cells) for the time after virus exposure and before virus infection/extinction. Stochastic simulations are stopped in panel **B** when the trajectories leave the extinction simplex and because of virus extinction in panel **D**. Reproduced from Duwal et al. [26].

integral-based SSA deteriorated strongly in comparison to EXTRANDE for simulations involving a large number of reaction firings. This is usually the case with infection trajectories.

7.4 Summary

In this chapter, we derived closed-form solutions for extinction and infection probabilities for various viral compartment (V, T_1 and T_2) for a time-constant target-site drug concentration. For time-varying target-site drug concentration, the extinction and infection probabilities in general

may not have closed-form solutions and require numerical methods such as solving an CME and simulating SSA.

Solving the underlying CME is in general not possible due to the curse of dimensionality. We proposed a reduced-state viral dynamics model which circumvents the need to consider all possible states. This approximation is based on a key insight from the analysis of time-constant target-site drug concentration that the extinction is unlikely once T_2 stage is reached. This approximation performs satisfactorily for CRA, RTI and InI and for a challenge with a low number of viruses, however, there are a number of limitations. Hence, we explored stochastic simulation algorithms. For the EXTRANDE algorithm, we introduced an intuitive upper bound for the sum of reaction propensities that does not require manual selection of look-ahead time horizon.

Stopping simulations for trajectories leading to the extinction is straightforward, as all viral compartments are zero. This is not case with simulations for infection related trajectories. Arbitrary stopping criteria either lead to unnecessary increments in computation or inaccurate estimation of infection probability. We tackle the problem by designing stopping criteria that obviate unnecessary computation and at the same time limit the probability that a trajectory is wrongly classified as an infection. A trajectory is stopped and classified as an infection when it moves out of the extinction simplex. This guarantees that the extinction is very unlikely, and the extinction probability of the trajectory is less than the user-defined threshold. The size of the extinction simplex changes dynamically based on the drug pharmacokinetics. In addition to being less prone to numerical error, the adapted EXTRANDE is also more efficient than the adapted integral-based SSA.

CHAPTER 8

Viral exposure model

In Chapter 7, we presented methods to quantify viral infection and extinction probabilities within a host, which requires that the target-cell compartment has been reached by virus or viruses. However, the question arises how many viruses reach the target-cell compartment per coitus and what are factors that affect the quantity of transmitted viruses? In this chapter, we proceed by presenting various crucial insights regarding the HIV-1 transmission and present a novel statistical model for a viral exposure taking those insights into account.

8.1 Statistical model of viral exposure per coitus

HIV transmission during coitus is a complex process, in which viruses need to overcome a number of physical and immunologic barriers. For instance, a virus needs to reach the genital tract of the donor, penetrate the mucosal barrier of the recipient and migrate to the environment conducive for replication to establish a systemic infection [19]. The transmission process is inefficient which is reflected in the low transmission probability per coitus. In fact, more than 99 % of unprotected sex acts with an infected person fail to cause an infection [230]. Hence, HIV transmission is stochastic in nature and is characterized by several bottlenecks [19, 209]. Next, we discuss briefly some important observations regarding HIV transmission.

Since HIV is a sexually transmitted disease, the transmission risk is associated with genital viral concentrations [231, 232]. The plasma viral load of the donor correlates strongly with genital viral concentrations [233–236]. In the Rakai study [237] conducted in Uganda, the plasma viral load of the donor was identified as the most dominant factor that determines HIV transmission from a donor to a recipient during a coitus (see Box. 8.1 for a brief summary on the Rakai study [237]). Other studies also support the observation [14, 238]. The insight that controlling the viral load in donors reduces their infectiousness formed the basis for the prevention strategy known as treatment-as-prevention.

On the recipient side, an important observation was made by Keele et al. [239]. The authors found evidence that HIV infection is established by a very low number of viruses, usually a single founder virus (see Box 8.2 for a brief description of the article). A number of follow-up studies corroborated the observation [206, 240, 241]. The finding indicates that a low number of transmitted viruses reach the conducive environment in the recipient owing to the severe bottleneck. This aligns with the stochastic and inefficient nature of the transmission.

The transmission probability per coitus is also affected by the modes of transmission. A number of studies have observed that the transmission probability per coitus in men who have sex with men is higher than in heterosexuals [230, 242]. Interestingly, Keele et al. [239] and Li et al. [206] have reported the number of transmitter or founder viruses in a homosexual transmission is in

general larger than in a heterosexual transmission. This suggests that the bottleneck in case of a homosexual exposure is comparatively less severe allowing more viruses to be transmitted. This aligns with the knowledge that the rectal mucosa is more susceptible to traumatic tears than the cervovaginal mucosa [243].

A number of empirical models have been developed which link the viral load in donors to the transmission risk, for example Wilson et al. [244] and Duwal et al. [15]. Similarly, Chakraborty et al. [232] presented a model linking genital HIV concentrations to the transmission probability per coitus. However, these models cannot be used to assess effects of antiretroviral intake by the recipient, since these models do not link the donor viremia to the number of transmitted viruses in the recipient.

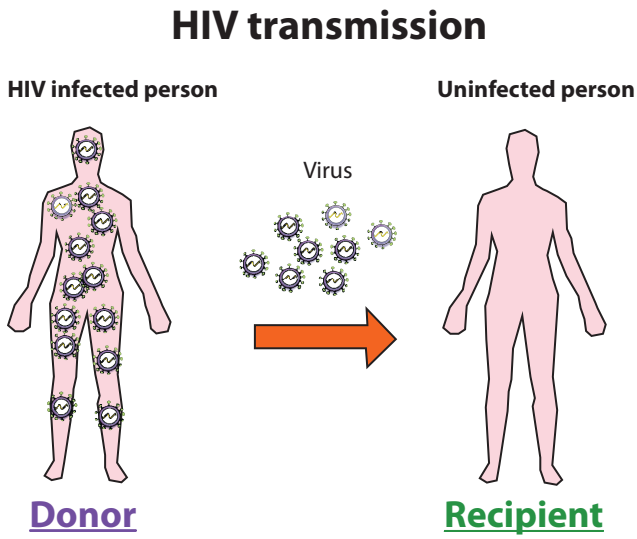

Figure 8.1: **Illustration showing HIV transmission from an infected donor to an uninfected recipient**

Box. 8.1: Viral load and transmission risk per coitus (Rakai study).

The Rakai study [237] was conducted in rural Uganda, where 415 serodiscordant couples were prospectively followed for a period of up to 30 months. A serodiscordant couple refers to a couple where one partner is HIV-1 positive and the other partner is HIV-1 negative. The HIV-1 negative partner in such relationship is exposed to a high risk of contracting HIV-1 from the HIV-1 infected partner. The couples in the study were in a stable heterosexual relationship.
The couples participated in a routine follow up every 10 months, where individuals were interviewed and various samples such as blood and urine were taken. The uninfected partners were tested for HIV-1 seroconversion using immunoassays. The seroconversion means that the sero status of the person has changed from negative for HIV-1 to positive, confirming that HIV-1 infection has taken place. The viral loads from the blood samples of the infected partners were retrospectively determined to infer the viral load at the time of transmission.
The infected partner did not receive any antiretrovirals, because antiretrovirals were not available in rural Uganda at the time of the study. Furthermore, they reported each ten-fold increment in the viral load was associated with 2.45 fold increase in the transmission-risk of HIV-1 per coitus [237, 244]. The value of fold increase is in line with the recent study by Hughes et al. [238] which reports a value of 2.9.

In order to avoid confusion, we define a few terminologies. We refer to unprotected sex acts between an infected person (donor) and an uninfected person (recipient) as **viral exposures**. Dur-

ing a viral exposure, it might be that viruses reach the mucus membrane of the recipient, but it is not guaranteed that they reach the target-cell compartment. **Viral challenges** denote viral exposures, where the target-cell compartment is reached by a virus or a number of viruses. The initial number of transmitted viruses (viruses reaching the target-cell compartment) is called **inoculum**. A founder virus is a transmitted virus that manages to establish the systemic infection. We also distinguish between an infection event and a transmission event. We denote an infection event as an intra-host process that refers to the establishment of the systemic infection in the recipient. In contrast, we define a transmission event as an inter-host event. Precisely, transmissions are viral exposures leading to a successful infection of the recipient. In summary, *all transmissions are viral challenges, all viral challenges are viral exposures, but the inverse statement is not valid.*

8.1.1 Mean transmission probabilities

The mean transmission probability per coitus is a weighted average transmission probability over all potential donors and their respective viral loads at the time of contact:

$$\mathbb{P}(\text{trans}) = \sum_{k=0}^{\infty} \mathbb{P}(\text{VL} = k) \cdot \mathbb{P}(\text{trans}|\text{VL} = k) \tag{8.1}$$

where the term $\mathbb{P}(\text{VL} = k)$ is the probability that a donor has a viral load k and the term $\mathbb{P}(\text{trans}|\text{VL} = k)$ is the transmission probability per coitus conditioned that a donor has viral load k. Further, the transmission probability per coitus conditioned that a donor has viral load k can be broken down as shown below

$$\mathbb{P}(\text{trans}|\text{VL} = k) = \left(\sum_{n=0}^{\infty} \mathbb{P}(y_0 = n \cdot \widehat{\text{V}}|\text{VL} = k) \cdot \mathcal{I}(y_0 = n \cdot \widehat{\text{V}}, \varnothing) \right), \tag{8.2}$$

where $\mathbb{P}(y_0 = n \cdot \widehat{\text{V}}|\text{VL} = k)$ denotes the probability that n viruses reach the target-compartment in a recipient given that the donor has viral load k. The term $\mathcal{I}(y_0 = n \cdot \widehat{\text{V}})$ denotes the infection probability given n viruses reach the target-compartment in the recipient. Substituting Eqn (8.2) in Eqn (8.1), we can rewrite the mean transmission probability as given below:

$$\mathbb{P}(\text{trans}) = \sum_{k=0}^{\infty} \underbrace{\mathbb{P}(\text{VL} = k)}_{\text{1. part}} \cdot \left(\underbrace{\sum_{n=0}^{\infty} \mathbb{P}(y_0 = n \cdot \widehat{\text{V}}|\text{VL} = k)}_{\text{2. part}} \cdot \underbrace{\mathcal{I}(y_0 = n \cdot \widehat{\text{V}}, \varnothing)}_{\text{3. part}} \right). \tag{8.3}$$

The above equation of mean transmission probability consists of three parts. The first part captures the viral load information of donors, whereas the third part captures the infection dynamics in recipients. The second part is a function that links the viral load in donors to the number of transmitted viruses.

Previously, we have dealt with the derivation of a closed-form solution for the infection probability in recipients (see Eqn (7.19)). Next, we will discuss the computation of probabilities $\mathbb{P}(\text{VL} = k)$ and $\mathbb{P}(y_0 = n \cdot \widehat{\text{V}}|\text{VL} = k)$.

8.1.2 Viral load distribution in donors

The viral load in untreated HIV-1 infected individuals is log-normally distributed [237, 245], i.e. $k \sim \log \mathcal{N}(\mu, \sigma^2)$. In order to infer the distribution of viral loads in treatment naive potential HIV-1

donors, we analysed viral load data from recently infected treatment-naive individuals (German HIV-1 sero-converter study and acute sero-converters, N = 1213) [246, 247]. Since viral transmission occurs preferentially shortly after infection [247], this particular population will provide a good source of relevant information regarding the viral load distribution at the time of transmission. Figure 8.2 panel A shows the histogram of $\log_{10}$ transformed viral load data with a superimposed red line representing the probability of viral load assuming a normal distribution with mean $\mu = 4.51$ and standard deviation $\sigma = 0.98$. This is in good agreement with reports from the Rakai study [237] ($\mu = 4.02$ and $\sigma = 0.85$).

Box. 8.2: A pioneer study identifying and characterizing early transmitted virus.

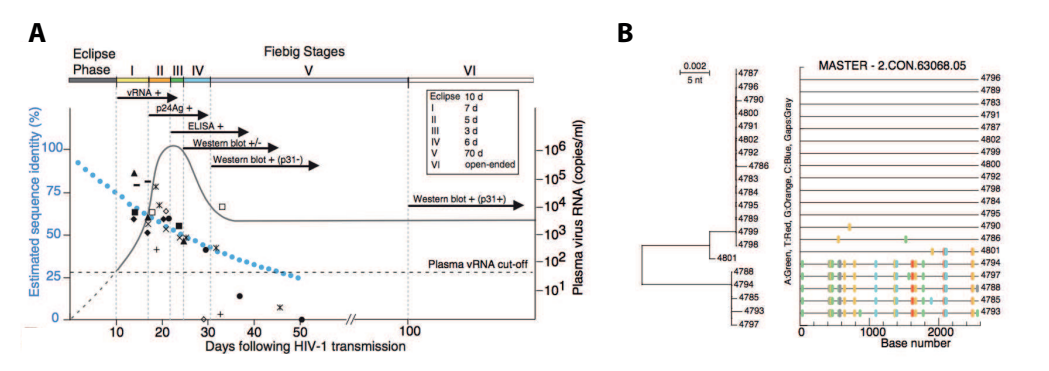

Identification of early founder viruses using envelope sequences of acutely infected individuals : A: The progression of HIV-1 env sequence diversity with advancement of Fiebig stage. Blue dots depict the predicted env sequence identity in percent after a viral transmission by the mathematical model presented in Keele et al. [239]. Various black symbols denote sequentially measured env sequence identity in 10 individuals, each symbol representing an individual. **B:** A phylogenetic tree from neighbor-joining and a highlighter analysis of env sequences of a subject at Fiebig stage II with evidence of infection by two viruses. Sequence 4801 resulted from a recombination. Extracted from Keele et al. [239].

Keele et al. [239] constructed a mathematical model for HIV-1 sequence diversification within a host shortly after infection. The mathematical model assumes that initially an individual founder virus replicates exponentially exhibiting a poisson distributed number of mutations in its sequence and a star-like phylogeny. These assumptions are valid for the viral sequence diversification within a host shortly after the infection before selection pressure by the immune system initiates. Using the model the authors analysed 3,449 complete env sequences from 102 subjects at various Fiebig stages of acute HIV-1 infection. The sequences were analysed by using neighbor-joining phylogenetic tree and sequence highlighter that allows tracing the common ancestry between sequences based on individual nucleotide polymorphisms.

The phylogeny construction of env sequences from an individual coalesced to a single or few most recent common ancestor sequences at the time of viral transmission. *The analysis showed that 78 acutely infected person out of 102 were infected by a single founder virus (a single consensus sequence), whereas the rest were infected by two and five viruses (few consensus sequences). Furthermore, they noted that men who have sex with men (MSM) are more likely to be infected by more than one virus strain from their HIV-infected partner than the heterosexuals.*

These observations have been corroborated by recent similar studies conducted by Li et al. [206] and Abraham et al [240]. Both studies reported that the number of founder viruses is very low and most of times there is a single founder virus. Li et al [206] applied the approach to HIV-1 env sequence in a cohort of acutely infected men who have sex with men and observed that a high proportion of them has been infected by more than one virus. Of note, though men who have sex with men are twice as much likely to be infected by more than one virus than the heterosexuals, yet large proportion are infected by a single founder virus [206].

This enables us to devise a function, which computes the probability of a viral load k in a potential donor,

$$\mathbb{P}(\text{VL} = k) = G(k, \mu, \sigma) = \int_{i=k}^{<k+1} g(i, \mu, \sigma). \tag{8.4}$$

where $g(i, \mu, \sigma)$ is the probability density function for a log normal distribution with parameters μ and σ.

8.1.3 Transmitted viruses distribution, donor's viral load and transmission modes

We assume that the number of viruses transmitted and reaching a target-cell environment n is related to the virus load in the donor k through a binomial distribution with success rate s (probability of successfully transmitting a donor virus to the recipient).

$$n \sim \mathcal{B}(h(k), s), \tag{8.5}$$

where $h(k)$ is some function of the viral load k in the donor. We propose a power function for $h(k)$ such that

$$h(k) = \lceil k^m \rceil \tag{8.6}$$

where m is an exponent of the viral load k in the donor and $\lceil \bullet \rceil$ is a next integer function. The rationale behind the selection of a power function for $h(k)$ is explained later. The probability of transmitting n viruses to the recipient when the viral load in the donor is k is then:

$$\mathbb{P}(y_0 = n \cdot \widehat{\text{V}} | \text{VL} = k) = \begin{pmatrix} \lceil k^m \rceil \\ n \end{pmatrix} \cdot s^n \cdot (1 - s)^{(\lceil k^m \rceil - n)}. \tag{8.7}$$

Algebraic simplification using Eqn (8.7) in Eqn (8.2) reveals the following equation :

$$\mathbb{P}(\text{trans} | \text{VL} = k) = 1 - (1 - s \cdot \mathcal{I}(\widehat{\text{V}}, \varnothing))^{\lceil k^m \rceil}. \tag{8.8}$$

Using a Taylor approximation, we can rewrite the above equation as shown below :

$$\mathbb{P}(\text{trans} | \text{VL} = k) \approx \mathcal{I}(\widehat{\text{V}}, \varnothing) \cdot s \cdot \lceil k^m \rceil. \tag{8.9}$$

Note that this approximation is only valid where $\mathcal{I}(\widehat{\text{V}}, \varnothing) \cdot s \cdot f(k) \ll 1$. Taking the logarithm on both sides of Eqn (8.9), we get

$$\begin{aligned} \log_{10}(\mathbb{P}(\text{trans} | \text{VL} = k)) &\approx \log_{10}(s \cdot \mathcal{I}(\widehat{\text{V}}, \varnothing) \cdot \lceil k^m \rceil), \\ &= \log_{10}(s) + \log_{10}(\mathcal{I}(\widehat{\text{V}}, \varnothing)) + \log_{10}(\lceil k^m \rceil), \\ &\approx \log_{10}(s) + \log_{10}(\mathcal{I}(\widehat{\text{V}}, \varnothing)) + m \cdot \log_{10}(k). \end{aligned} \tag{8.10}$$

This shows that the relation between the logarithm of the transmission probability per coitus and the corresponding viral load in logarithm is approximately linear with a slope m and an intercept $\log_{10}(s) + \log_{10}(\mathcal{I}(\widehat{\text{V}}, \varnothing))$. This linear relationship is in agreement with previous reports by a number of authors [237, 238]. Further, the slope parameter m can be inferred from these studies. We used the value reported from the Rakai studies [244], which is $\log_{10}(2.45)$. Hence, the proposal of power function for $h(k)$ is well justified and allows the simplification as shown in Eqn (8.10).

Substituting Eqn (8.8) and Eqn (8.4) in Eqn (8.3), the mean transmission probability per coitus can be rewritten as

$$\begin{aligned}\mathbb{P}(\text{trans}) &= \sum_{k=0}^{\infty} \mathbb{P}(\text{VL}=k)\cdot\left(\sum_{n=0}^{\infty}\mathbb{P}(y_0 = n\cdot\widehat{\text{V}}|\text{VL}=k)\cdot\mathcal{I}(y_0 = n\cdot\widehat{\text{V}},\varnothing)\right),\\ &= \sum_{k=0}^{\infty} G(k,\mu,\sigma)\cdot\left(1-(1-s\cdot\mathcal{I}(y_0=\widehat{\text{V}},\varnothing))^{\lceil k^m\rceil}\right). \qquad (8.11)\end{aligned}$$

In the above equation, as previously described, we inferred the parameters μ and σ from the German HIV-1 sero-converter study. The slope parameter m is taken from the Rakai study [244]. In Chapter 7, we previously presented the computation of the infection probability for a single transmitted virus. The mean transmission probabilities $\mathbb{P}(\text{trans})$ for different transmission modes are taken from literature: 0.03 for homosexual transmission and 0.003 [230, 248] for heterosexual transmission [242]. The success rate s is then estimated by fixing all known parameters described above using the least square method. The success rates s are estimated to be 3.7×10^{-3} and 3.6×10^{-4} for homosexual and heterosexual transmission respectively.

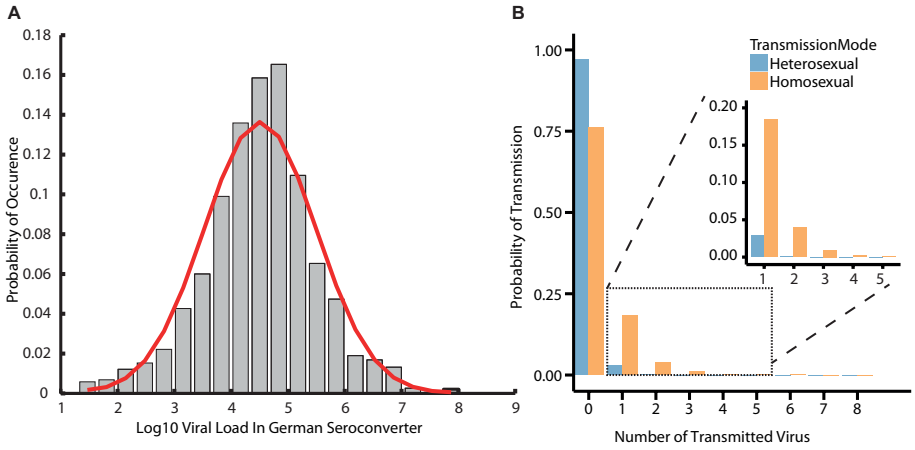

Figure 8.2: **Viral load distribution in potential donor and predicted transmitted viruses distribution in the recipient**. **A** : Viral load distribution ($\log_{10}$ scale) in a representative donor population (German Sero-converter study). The mean and standard deviation of $\log_{10}$ viral load is 4.51 and 0.98 in good agreement with Quinn et al. [237] **B** : Predicted transmitted viruses distribution in recipients for heterosexual and homosexual transmission modes using the virus exposure model. The blue and orange bars belong to heterosexual and homosexual transmission mode. Reproduced from Duwal et al. [25].

Using the viral exposure model presented above, we predicted the distribution of transmitted viruses for different transmission modes displayed in panel B of Figure 8.2. Note that in the majority of cases no virus reaches a target-cell compartment and when the viral transmission occurs, a low number of virus 1 to 5 are transmitted. If virus reached a target-cell compartment, it was a single virus in more than 77 % of cases in homosexuals and 96 % of cases in heterosexuals. This is in good agreement with studies [206, 239, 240] reporting a low number of founder viruses. The analysis conducted by Keele et al [239] in heterosexuals and homosexuals reported that in 76 % of infection cases, there was only a single founder virus. The low number of transmitted or founder viruses indicates stringent physiological bottlenecks for viral transmission [209, 249]. Secondly, one can see that the number of transmitted viruses is larger during homosexual transmission in comparison to heterosexual transmission. This aligns with the observation of higher number of founder viruses in homosexual transmission than in heterosexual transmission [206, 239].

8.2 Summary

In this chapter, we presented a statistical model of virus exposure per coitus, which links the viral load in a donor to the number of transmitted viruses in a recipient. The model can distinguish between the homosexual and heterosexual transmission modes, and in the future, it can easily be calibrated for the intravenous transmission mode (for intravenous drug users). The prediction of a low number of transmitted viruses is in line with other studies [206, 239, 240]. In contrast to the existing approaches [244], the model has the advantage which allows us to simultaneously analyse the effect of treatment-as-prevention and chemo-prophylaxis on reducing HIV-1 transmission.

CHAPTER 9

Prophylactic utility of various antivirals

In this chapter, we begin by recapitulating the various modules of the framework. We present insights and results regarding the prophylactic utility of various antivirals obtained by using the framework[I].

9.1 Multiscale systems pharmacology framework

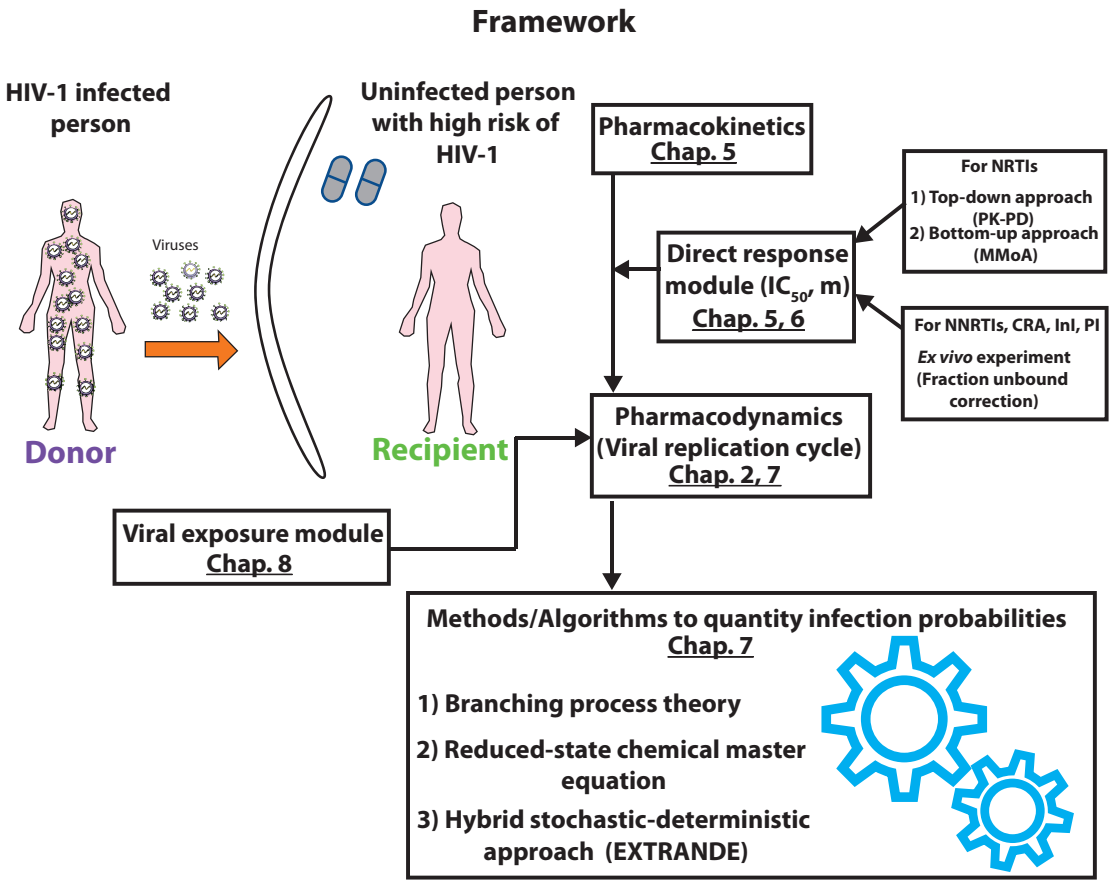

Figure 9.1: **Scheme of the multiscale systems pharmacology framework for PrEP and PEP**

[I]The results of this chapter are based on the articles [25–27]

In order to predict the prophylactic utility of various antivirals, it is necessary to account for processes occurring at various scales, which we have dealt with in Chapter 2, 5, 6, 8. On the other hand, tailored algorithms are required to quantify the infection probability as described in Chapter 7. Combining all of these modules and algorithms, we can build a flexible modular framework (see Figure 9.1), which integrates processes mechanistically to predict the prophylactic utility of various antivirals. The various modules and algorithms used in the pipeline are briefly described below:

Pharmacodynamics module: In Section 7.1, we simplified the detailed viral replication cycle model from Subsection 2.5.2. The simplified viral replication cycle model sufficiently captures the early infection dynamics. The model allows for the mechanistic integration of antiviral effects of all drug classes.

Pharmacokinetics module: The pharmacokinetic module can be used to specify pharmacokinetic properties of antivirals of interest. Note that the model should include the pharmacokinetics of the active moiety at the target-site. One can use a detailed compartmental pharmacokinetic model. In Chapter 5, we presented plasma and intracellular pharmacokinetic models for TDF, FTC, 3TC. For NRTIs, the plasma concentration is nonlinearly and asynchrously linked with the intracellular concentration of their active moieties. Thus, the intracellular concentrations of active moieties need to be captured. We also presented a plasma pharmacokinetic model for DTG. Owing to the free drug hypothesis, it is sufficient to link the plasma pharmacokinetics with pharmacodynamics without explicitly modelling the intracellular pharmacokinetics. We employed various model building methods (see Chapter 4) suitable for the available data. Usually, such compartmental model is not readily available for all antivirals due to the lack of data. However, maximum and minimum concentrations (peak and trough concentrations) and half-lives are easily available. These pharmacokinetic parameters can also be used in the framework. Obviously, the predictions based on these parameters are limited, compared to a detailed pharmacokinetics model.

Direct response module: The direct response module links the pharmacokinetics with pharmacodynamics using the *in vivo* drug potency parameter IC_{50}. IC_{50} can be estimated from the viral load decay data for a particular dosing regimen (top-down approach). However, such data are difficult to obtain and are very noisy. For some scenarios, clinical trials might be unethical, limiting the possibility of inferring the IC_{50}. Hence, translation of *in vitro* and *ex vivo* parameters to *in vivo/clinical* parameters is desirable.

In Chapter 6, we presented the main idea behind the bottom-up model based on the molecular mechanism of action of NRTIs and compared its prediction with that from the top-down approach. The bottom-up approach satisfactorily allows the translation of *in vitro* parameters to the *in vivo* drug potency parameter IC_{50}. For NRTIs, this is important as the free drug hypothesis is not valid for them.

For all other antivirals, the free drug hypothesis is valid and the IC_{50} can be inferred from an *ex vivo* single-round infectivity assay. However, a correction is required for translation to *in vivo* use, due to differences in *ex vivo* and *in vivo* settings. In Chapter 6, we provided a way to adjust the *ex vivo* drug potency to *in vivo* (target-process) drug potency (also see Appendix B).

Viral exposure module: The viral exposure module presented in Chapter 8 links the viremia of an infected person (donor) to the distribution of transmitted viruses in an uninfected person (recipient) per coitus. Moreover, the model can distinguish between heterosexual and homosexual transmission modes.

Methods/Algorithms to quantify infection probabilities: In Chapter 7, we presented various methods and algorithms to quantify infection probabilities. We derived closed-form equations for the constant target-process inhibition (time-invariant propensities) utilizing the theory of branching processes.

For the general case i.e., the time-varying drug efficacy (time-variant propensities), we explored various algorithms. We presented a reduced-state model for the chemical master equation, which approximates the infection probability. Furthermore, for our purpose we optimized integral-based and rejection-based stochastic simulation algorithms (SSA) by introducing dynamical stopping criteria. In contrast to the reduced-state CME approach, these algorithms are exact. The integral-based SSA is more inefficient than rejection-based SSA (EXTRANDE) due to computationally intense integral steps.

9.2 Prophylactic efficacy

The presented modelling framework predicts the infection probability by mechanistically integrating various essential processes. In order to assess, screen and optimize antivirals for PrEP, it is crucial to define measures of efficacy.

Let us define the prophylactic efficacy for a given initial state vector y_0 and a particular prophylactic scheme $\mathcal{S}$ as

$$\varphi(y_0, \mathcal{S}) = 1 - \frac{\mathcal{I}(y_0, \mathcal{S})}{\mathcal{I}(y_0, \varnothing)}. \tag{9.1}$$

The prophylactic efficacy $\varphi(y_0, \mathcal{S})$ refers to the reduction in the infection probability for a given initial state vector y_0 by a drug administration scheme, relative to the infection probability in the absence of any drug. Note that the initial state vector does not necessarily mean only viruses but can also refer to any possible combination of viruses and infected cells within a recipient.

Owing to the low transmission probability per coitus, in a large number of exposures, viruses fail to reach the target-cell compartment. Hence, we can define the prophylactic efficacy in context of viral challenge (exposure with non-zero transmitted viruses) as

$$\begin{aligned} \psi(\mathcal{S}) &= \sum_{n=1}^{\infty} \frac{\mathbb{P}(y_0 = n \cdot \widehat{\mathrm{V}})}{1 - \mathbb{P}(y_0 = \mathbf{0})} \cdot \varphi(y_0 = n \cdot \widehat{\mathrm{V}}, \mathcal{S}) \\ &= \sum_{n=1}^{\infty} \frac{\mathbb{P}(y_0 = n \cdot \widehat{\mathrm{V}})}{1 - \mathbb{P}(y_0 = \mathbf{0})} \cdot \left(1 - \frac{\mathcal{I}(y_0 = n \cdot \widehat{\mathrm{V}}, \mathcal{S})}{\mathcal{I}(y_0 = n \cdot \widehat{\mathrm{V}}, \varnothing)}\right). \end{aligned} \tag{9.2}$$

We refer this to as *prophylactic efficacy per viral challenge*. Note that the factor $\mathbb{P}(y_0 = n \cdot \widehat{\mathrm{V}})/(1 - \mathbb{P}(y_0 = \mathbf{0}))$ denotes the probability that there are n number of transmitted viruses per exposure given n being bigger than 0. In other words, $\psi(\mathcal{S})$ is *the expected reduction in the infection probability per viral challenge* with respect to the absence of drug.

In a trial it is not possible to differentiate between exposures in which virus does not reach the target-cell compartment and those where virus reaches the target-cell compartment (viral challenges). Accordingly, another possible measure of prophylactic efficacy can be defined by considering the *expected reduction in the transmission probability per exposure*:

$$\begin{aligned} \text{Reduction in the transmission probability per exposure} &= 1 - \frac{\mathbb{P}(\text{trans}, \mathcal{S})}{\mathbb{P}(\text{trans}, \varnothing)} \\ &= 1 - \frac{\sum_{n=0}^{\infty} \mathbb{P}(y_0 = n \cdot \widehat{\mathrm{V}}) \cdot \mathcal{I}(y_0 = n \cdot \widehat{\mathrm{V}}, \mathcal{S})}{\sum_{n=0}^{\infty} \mathbb{P}(y_0 = n \cdot \widehat{\mathrm{V}}) \cdot \mathcal{I}(y_0 = n \cdot \widehat{\mathrm{V}}, \varnothing)}. \end{aligned} \tag{9.3}$$

Eqn (9.2) for prophylactic efficacy per viral challenge ($\psi(\mathcal{S})$) is, in fact, the mean of ratios, whereas Eqn (9.3) is the ratio of means. Interestingly, in our modelling pipeline these two measures of

prophylactic efficacy were found to be almost identical. Hence,

$$\psi(\mathcal{S}) \approx 1 - \frac{\mathbb{P}(\text{trans}, \mathcal{S})}{\mathbb{P}(\text{trans}, \varnothing)} \tag{9.4}$$

and for our purpose the prophylactic efficacy per exposure and prophylactic efficacy per viral challenge are interchangeable [II].

9.2.1 Dependency on the inhibited stage in the viral replication cycle.

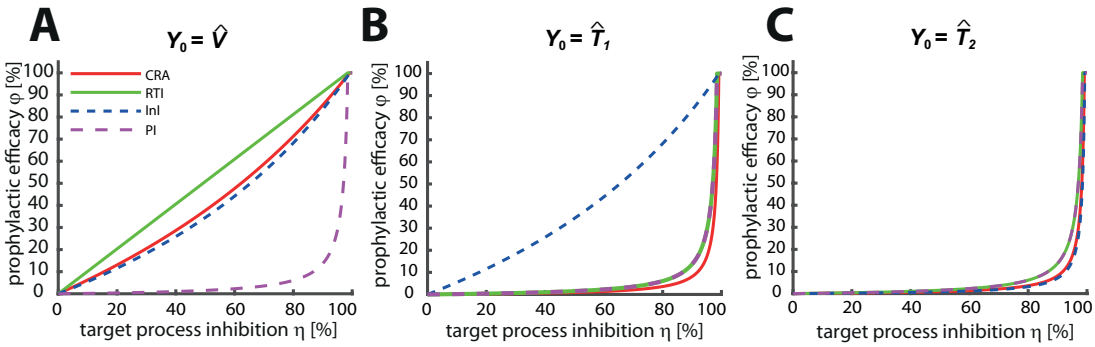

Figure 9.2: **Relation of prophylactic efficacy φ and target-process inhibition.** The relation between target-process inhibition η and prophylactic efficacy φ (reduction in infection) is shown for different drug classes utilizing the viral model depicted in Fig. 7.1 with parameters stated in Table A.1. Panel **A:** Relation between η and φ when a single virus $y_0 = \widehat{\mathrm{V}}$ reached a target-cell compartment of the recipient. Panel **B and C:** Relation between η and φ when a single early infected cell $y_0 = \widehat{\mathrm{T}}_1$ or (panel **C**) a late infected T-cell $y_0 = \widehat{\mathrm{T}}_2$ are present in the target-cell compartment. Solid red lines: CRAs (Co-receptor antagonists), solid green line: RTIs (reverse transcriptase inhibitors), dashed blue line: InI (integrase inhibitors), dashed purple line: PIs (protease inhibitors). Reproduced from Duwal et al. [27].

While HIV transmission typically occurs after the target-cell compartment is reached by viruses, it is insightful to study the prophylactic efficacy of distinct drug classes in the hypothetical case when infected cells were present in the exposed individual. A realistic example for this scenario is post-exposure prophylaxis (PEP): During PEP, drugs are taken shortly *after* a virus exposure and initial viral replication steps may have taken place generating early- or late infected cells.

Figure 9.2 shows the relations between the prophylactic efficacy and target-process inhibition for various drug classes and for different initial state vectors, namely when a free virus, a T_1-cell or a T_2-cell is present. For a single virus $y_0 = \widehat{\mathrm{V}}$, target-process inhibition of RTI directly translates to the prophylactic efficacy. The translation of the target-process inhibition to the prophylactic efficacy for CRA, InI and PI deviates strongly from identity in aforementioned order (see Figure 9.2 A). As can be seen in Figure 9.2B–C, the prophylactic efficacy of all drugs profoundly deteriorates compared to their target-process inhibition, i.e. only very effective (in terms of η) drugs may prevent systemic infection once cells become infected in the exposed individual. An exception is integrase inhibitors: Their prophylactic efficacy φ is moderately less than their direct effect η (panel B) if only early infected cells T_1 (before proviral integration) are present. Thus, while the prophylactic efficacy of all other drug classes is profoundly less than their direct effects once infected cells emerged, integrase inhibitors may still potently prevent infection.

[II] Of cautionary note, the mean of ratios and ratio of means are in general not equal.

9.2.2 Drug-class specific relation between concentration and prophylactic efficacy

Next, we derive closed-form equations for the prophylactic efficacy for various drug classes. This allows us to obtain the concentration-prophylactic curve. The concentration-prophylactic curve is motivated by concentration-effect or dose-response curve analysis in pharmacological studies. The equations for RTI, CRA and InI, after a viral challenge with a single virus $\widehat{\mathrm{V}}$, are given below

$$\varphi(\widehat{\mathrm{V}}, D_{\mathrm{CRA}}) = \frac{R_0(\varnothing)}{R_0(\varnothing)-1} \cdot \frac{D_{\mathrm{CRA}}^m}{\mathrm{IC}_{50}^m\left(\frac{1}{\nu}\right) + D_{\mathrm{CRA}}^m} \approx \frac{D_{\mathrm{CRA}}^m}{\mathrm{EC}_{50}^m + D_{\mathrm{CRA}}^m}, \tag{9.5}$$

$$\varphi(\widehat{\mathrm{V}}, D_{\mathrm{RTI}}) = \frac{R_0(\varnothing)}{R_0(\varnothing)-1} \cdot \frac{D_{\mathrm{RTI}}^m}{\mathrm{IC}_{50}^m + D_{\mathrm{RTI}}^m} \approx \frac{D_{\mathrm{RTI}}^m}{\mathrm{EC}_{50}^m + D_{\mathrm{RTI}}^m}, \tag{9.6}$$

$$\varphi(\widehat{\mathrm{V}}, D_{\mathrm{InI}}) = \frac{R_0(\varnothing)}{R_0(\varnothing)-1} \cdot \frac{D_{\mathrm{InI}}^m}{\mathrm{IC}_{50}^m\left(\frac{1}{\vartheta}\right) + D_{\mathrm{InI}}^m} \approx \frac{D_{\mathrm{InI}}^m}{\mathrm{EC}_{50}^m + D_{\mathrm{InI}}^m}, \tag{9.7}$$

where D denotes the total concentration of the drug in the relevant site, m is a slope parameter and IC_{50} denotes the drug concentration that inhibits the target-process (co-receptor binding, reverse transcription or proviral integration) by 50 percent. The parameters m and IC_{50} are drug-specific parameters as discussed in Chapter 2. $R_0(\varnothing)$ denotes the basic reproductive number in the absence of drugs, i.e. the average number of viruses produced from a single founder virus [220] in a single replication cycle when no antiviral is present ($R_0(\varnothing) \approx 67$ according to the utilized model). The parameter

$$\nu = \frac{\mathrm{CL} \cdot \rho_{\mathrm{rev},\varnothing}}{\mathrm{CL} \cdot \rho_{\mathrm{rev},\varnothing} + \beta_{\mathrm{T}} \cdot \mathrm{T}_{\mathrm{u,SS}}} < 1 \tag{9.8}$$

denotes the probability that the virus is eliminated before entering a host cell. Similarly, the parameter

$$\vartheta = \frac{\delta_{\mathrm{PIC,T}} + \delta_{\mathrm{T}_1}}{\delta_{\mathrm{PIC,T}} + \delta_{\mathrm{T}_1} + k_{\mathrm{T}}} < 1 \tag{9.9}$$

denote the probability that essential virus components get cleared intracellularly after the reverse transcription and before the genome integration in the absence of drugs. For any realistic model, $R_0(\varnothing) \gg 1$ and hence the left-side scaling factor in eqs. (9.5)–(9.7) will be close to one i.e., $R_0(\varnothing)/(R_0(\varnothing)-1) \approx 1$. The overall shape of the concentration-prophylactic curve for co-receptor antagonists (CRAs), reverse transcriptase inhibitors (RTIs) and integrase inhibitors (InIs) is a classical Emax equation, which is the equation of choice for evaluating concentration-effect relations. The parameter EC_{50} denotes the total concentration of the drug in the relevant site that decreases the infection probability by 50 %.

For protease inhibitors (PIs), we derive a power function to describe their prophylactic efficacy:

$$\varphi(\widehat{\mathrm{V}}, D_{\mathrm{PI}}) = \frac{1}{R_0(\varnothing)-1} \cdot \frac{D_{\mathrm{RTI}}^m}{\mathrm{IC}_{50}^m} = G \cdot \frac{D_{\mathrm{RTI}}^m}{\mathrm{IC}_{50}^m} \qquad \text{for} \quad 0 \le \varphi \le 1 \tag{9.10}$$

where $G \ll 1$ is a constant. Moreover, for any realistic $R_0(\mathrm{V}, \varnothing) \gg 3$, their total concentrations have to exceed their IC_{50} to decrease the probability of infection by at least 50%. Figure 9.3 depicts the concentration-prophylactic curve of all drug classes assuming challenges with a single virus and 100 viruses.

9.2.3 Translation of target-process drug potency to prophylactic potency

Let EC_x denote the total concentration of the drug in the relevant site that decreases the infection probability by a single transmitted virus by x %. Algebraic simplifications of Eqn (9.5)–Eqn (9.7)

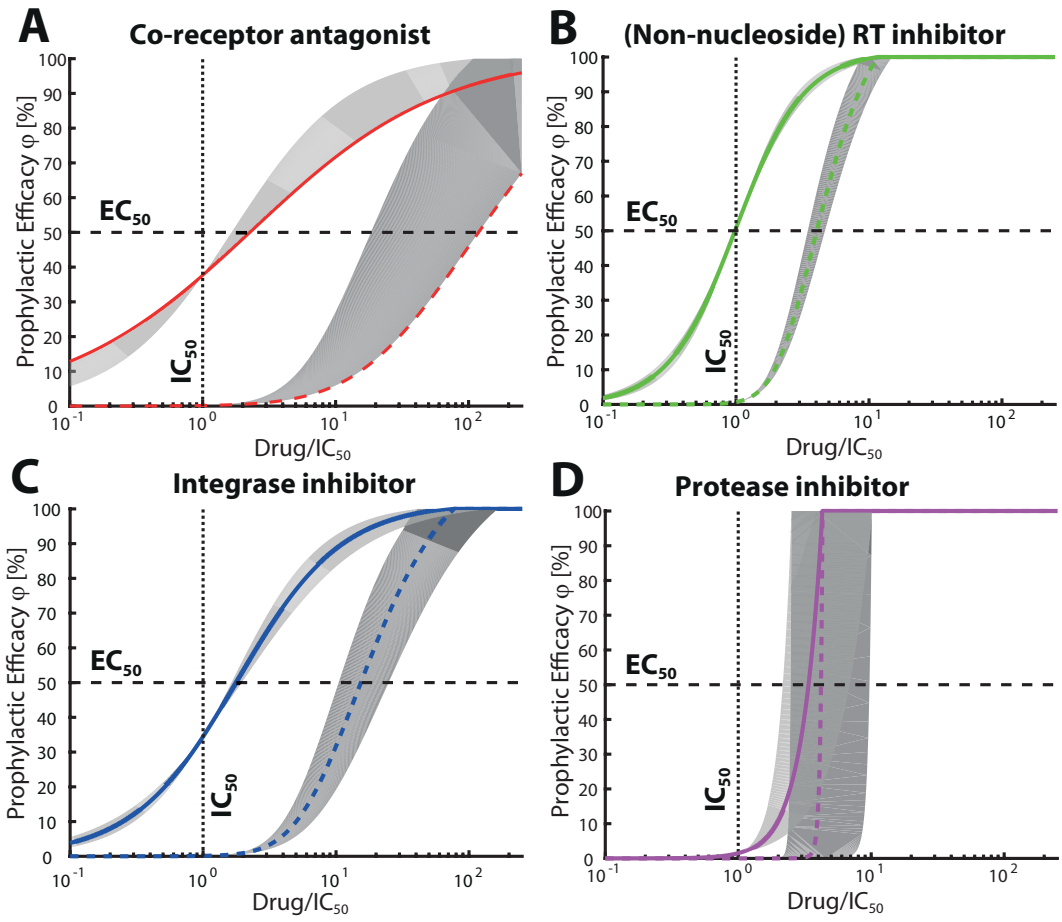

Figure 9.3: **Shape of the concentration-prophylactic efficacy curve.** coloured lines depict the concentration-prophylactic curve for an average drug class-specific slope parameter $\bar{m}$ in Eqn (2.2). Solid coloured line for an inoculum of one virus $y_0 = \widehat{V}$ and dashed coloured line for an inoculum of $y_0 = 100 \cdot \widehat{V}$. Shaded areas indicate the concentration-prophylactic curve for the smallest $m_{\min}$ and largest class-specific slope parameter $m_{\max}$ for the respective drug class as indicated in Table B.1. **A:** Co-receptor antagonists. Currently only one co-receptor antagonist, maraviroc, is approved. We use $\bar{m} = m_{\min} = 0.61$ and also plot $m_{\max} = 1$ as a reference. **B:** Non-nucleoside reverse transcriptase inhibitors (NNRTIs); $\bar{m} = 1.71$, $m_{\min} = 1.55$ and $m_{\max} = 1.92$. The overall shape for NRTI is also EMAX. **C:** Integrase inhibitors, $\bar{m} = 1.12$, $m_{\min} = 0.95$ and $m_{\max} = 1.3$. **D:** Protease inhibitors; $\bar{m} = 2.87$, $m_{\min} = 1.81$ and $m_{\max} = 4.53$. Utilized virus dynamics parameters are stated in Table A.1. Reproduced from Duwal et al. [27].

give us the following relation for CRA, RTI and InI:

$$\mathrm{EC}_x = \mathrm{IC}_{50} \cdot \left(\mathcal{F} \cdot \frac{x}{100 \cdot C - x} \right)^{1/m}, \tag{9.11}$$

where the term $\mathcal{F} \geq 1$ is a drug-class specific factor as shown below :

$$\mathcal{F} = \begin{cases} \frac{1}{\nu} & \text{for CRA} \\ 1, & \text{for RTI} \\ \frac{1}{\vartheta}, & \text{for InI} \end{cases} \tag{9.12}$$

and

$$C := \frac{R_0(\varnothing)}{R_0(\varnothing) - 1} \approx 1. \tag{9.13}$$

Similarly, for PI utilizing Eqn (9.10) we obtain the following relation:

$$\mathrm{EC}_x = \mathrm{IC}_{50} \cdot \left(\mathcal{G} \cdot \frac{x}{100}\right)^{1/m} \tag{9.14}$$

where $\mathcal{G} := R_0(\varnothing) - 1$.

EC_{50} and EC_{90} can be used to analyse the prophylactic utility of an antiviral *in vivo*. Notably, for RTIs, we have $\mathrm{EC}_{50} \approx \mathrm{IC}_{50}$ i.e., the target-process drug potency (IC_{50}) directly translates into the prophylactic potencyEC_{50} of the drug. For CRAs and InIs, we observe $\mathrm{EC}_{50} > \mathrm{IC}_{50}$, i.e. compared to their target-process drug potency, they are less potent in preventing infection. This is largely due to the respective factors $\vartheta^{-1}, \nu^{-1} > 1$, compare Figure 9.3A–C. Consequently, for CRAs and InIs, higher concentrations are required to prevent infection than suggested by target-process drug potency. PIs exhibits a switch-like behaviour as seen in Figure 9.3D.

In case of exposure to a single virus particle $\widehat{\mathrm{V}}$, the slope parameters of the prophylactic efficacy coincide with the slope parameter for the respective drug target-process inhibition m (Eqn (2.2)), stated in Table B.1. Importantly, when exposure to multiple viruses occurs, the concentration-prophylactic curve is no longer an Emax equation for any inhibitor class, Figure 9.3A–C. Furthermore, the EC_{50} value and the slope parameter exceed their corresponding *in vitro* measurable values m and IC_{50}.

Similarly, in the case of exposure to multiple viruses, the slope parameter and EC_{50} of PIs also increase, making the prophylactic efficacy of PIs strongly a switch-like as can be seen in Figure 9.3D. This switch-like behaviour makes the prophylactic use of PIs vulnerable to non-adherence, as well as general variations in concentrations (e.g. pharmacokinetics, inter-individual variability), as the prophylactic efficacy with these inhibitors may alternate between zero- or complete protection.

Note that we define parameters EC_{50} and EC_{90} considering a viral challenge with a single virus. Accordingly, EC_{50} is defined as the total drug concentration at the target-site that reduces prophylactic efficacy $\varphi(\widehat{\mathrm{V}}, \mathcal{S})$ by 50 %. Obviously, it would make more sense to define these terms for the prophylactic efficacy per challenge ($\psi(\mathcal{S})$), where the transmitted viruses are sampled from the distribution as presented in the viral exposure model, rather than for the prophylactic efficacy per challenge with a single virus ($\varphi(\widehat{\mathrm{V}}, \mathcal{S})$). As previously mentioned, in the majority of challenges, there is only a single transmitted virus (more than 96 % in heterosexual- and 77 % in homosexual challenges, see Chapter 8), which indicates that the $\varphi(\widehat{\mathrm{V}}, \mathcal{S})$ closely approximates $\psi(\mathcal{S})$ [III]. Here, the rationale for preferring $\varphi(\widehat{\mathrm{V}}, \mathcal{S})$ over $\psi(\mathcal{S})$ in computing EC_x is that it results in a closed-form equation that allows us to easily discern various factors affecting the prophylactic efficacy.

9.3 Prophylactic efficacy of NRTIs

We consider the following NRTIs currently used for treatment against HIV-1: tenofovir disoproxil fumarate (TDF), emtricitabine (FTC), lamivudine (3TC), zidovudine (AZT), stavudine (D4T) and abacavir (ABC). We built a detailed pharmacokinetic-pharmacodynamic model using population approaches for TDF, FTC and 3TC, which are presented in Chapter 5. For NRTIs, we approximated the viral extinction probability ($\mathcal{E}$) by using the probability that viruses are completely cleared in the first replication round ($\mathcal{E}_R$). As discussed previously (see Chapter 7 Subsection 7.3.1), this approximation works satisfactorily for NRTIs.

[III] In the article [27], EC_{50} and EC_{90} after a challenge with a single virus $\widehat{\mathrm{V}}$ and with viruses sampled from the transmitted viruses distribution are compared. The relative difference between the corresponding values is less than 2.5 % (not shown here)

9.3.1 Concentration-prophylactic efficacy curves for treatment-approved NRTIs

We obtained the range of intracellular concentrations of the active moieties for the aforementioned NRTIs after chronic dosing with their respective standard of care from various literature [23, 142, 146, 147, 152, 160, 170, 175, 250–254]. We used the MMOA model to compute the IC_{50} associated with the target-process inhibition for different NRTIs. Utilizing the modelling framework, we assess the concentration-prophylactic curve (ψ, Eqn (9.2)) for AZT, TDF, 3TC, FTC, D4T and ABC. The curves are shown in Figure 9.4A and allow for the first assessment of the suitability of these drugs for repurposing as PrEP compounds. Note that the solid lines and the background shading in Figure 9.4A show the prophylactic efficacy ψ and inter-quartile ranges at clinically relevant concentrations. We predict that AZT can prevent 14–53% infections at clinically relevant concentrations, followed by TDF (24–89%), D4T (55–95%), ABC (73–84%), 3TC (64–96%) and FTC (92–99%).

We further assessed the prophylactic efficacy of TDF, FTC and 3TC when drug-resistant viral strains are transmitted [255]. Resistance to FTC and 3TC is associated with the M184V mutation, whereas resistance to TDF is associated with the K65R mutation [256, 257]. Inhibition of the mutant viruses can be assessed in the MMOA model. Furthermore, the MMOA model allows for the assessment the fitness costs associated with these mutations. The predicted prophylactic efficacy of TDF, FTC and 3TC against wildtype (WT), and mutant viruses (M184V, K65R and M184V/K65R) is shown in Figure 9.4B-D. We assessed the percentage of infections prevented by prophylaxis after exposure to the mutant virus relative to the wildtype virus in the absence of drugs, i.e.:

$$\psi(\mathcal{S}) = \sum_{n=1}^{\infty} \frac{\mathbb{P}(y_0 = n \cdot \widehat{\mathrm{V}})}{1 - \mathbb{P}(y_0 = \mathbf{0})} \cdot \left(1 - \frac{\mathcal{I}_{mut}(y_0 = n \cdot \widehat{\mathrm{V}}, \mathcal{S})}{\mathcal{I}_{wt}(y_0 = n \cdot \widehat{\mathrm{V}}, \varnothing)}\right) \tag{9.15}$$

where 'mut' denotes the mutant virus (M184V, K65R or M184V/K65R) and 'wt' denotes the wild type virus. Thus, both the effect of the drugs, as well as inherent fitness costs are simultaneously evaluated, allowing to assess whether PrEP fosters the transmission of resistant viruses (this is the case whenever mutant transmission is more effective; i.e. whenever the dashed line is below the solid line in Figure 9.4B-D). Our analysis shows that the K65R mutation may decrease the PrEP efficacy of TDF, whereas the M184V-containing virus is very susceptible to TDF. The M184V/K65R double mutant is almost as susceptible as the wildtype, but it has a profound fitness deficit. In the case of FTC, both the M184V and K65R mutation, as well as the double mutant diminish its PrEP efficacy from 92–99% (wildtype) to 72–92 % (K65R) and 47–71% (M184V). In the case of 3TC, mutations K65R, M184V and the double mutant gradually diminish its efficacy down to complete resistance (in case of the double mutant). At low drug concentrations, the fitness defect of the resistant viruses causes their reduced transmission ($\approx$ 37–54% less likely to be transmitted than the wild type in the absence of drugs).

9.3.2 PrEP on demand with TDF, FTC and 3TC

Next, the prophylactic efficacy of TDF, FTC and 3TC alone, or in combination was analysed, when PrEP is initiated shortly before a challenge (PrEP on demand), similar to the IPERGAY protocol [258]. In the protocol, individuals initiate PrEP up to 24 hours before a viral challenge with a double-dose and then take two more pills on day 1 and 2. Evaluated pill sizes are 200mg for FTC or 300mg for 3TC and TDF. We simulated the population-average plasma and intracellular pharmacokinetics for TFV, FTC and 3TC, respectively TFV-DP, FTC-TP and 3TC-TP [23, 84] (see Chapter 5). We used the reduced-state CME to assess the infection probability (see Subsection 7.3.1).

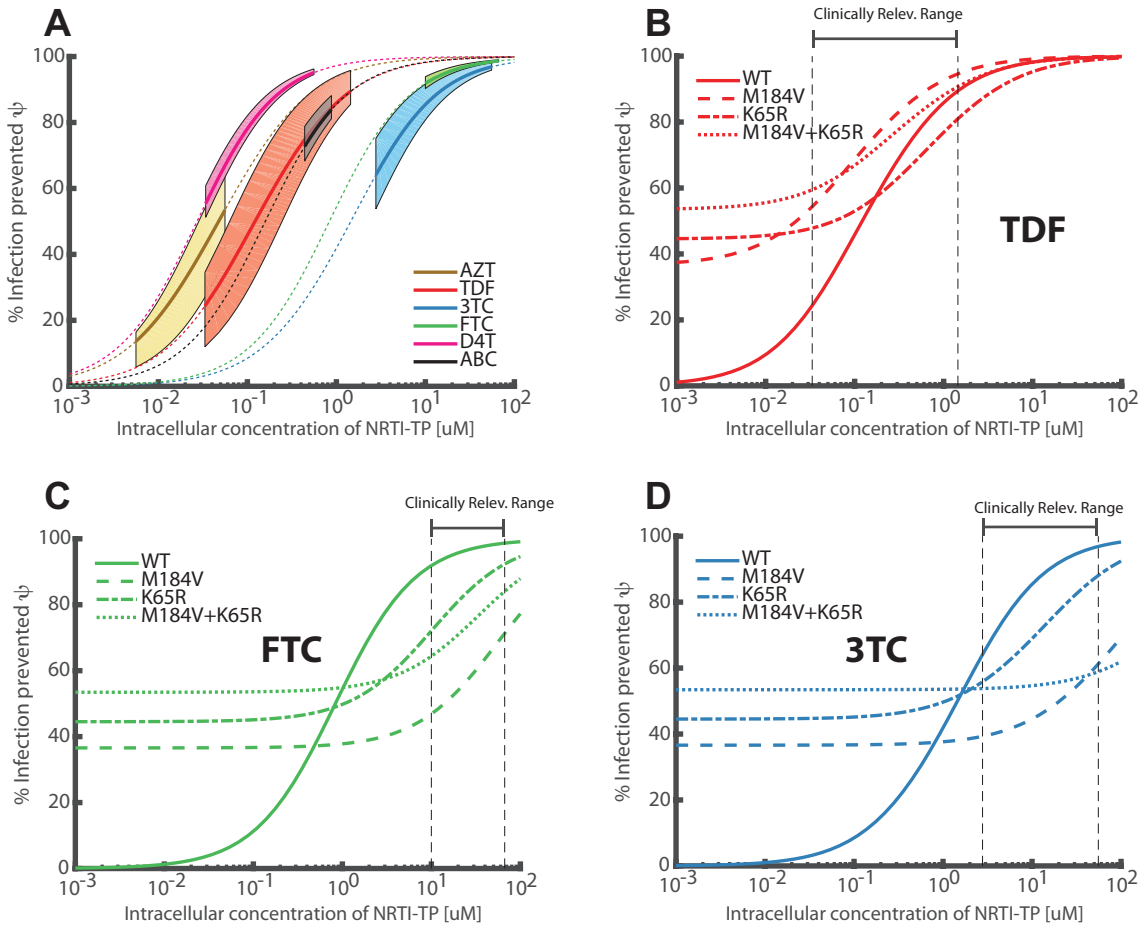

Figure 9.4: **Target-cell NRTI-TP concentration vs. prophylactic efficacy in wild type and mutant viruses ψ. A:** Mean prophylactic efficacies per viral challenge (Eqn (9.2)) are illustrated by the dotted lines. Solid thick lines mark the prophylactic profile at clinically relevant ranges for the respective drugs. Shaded areas indicate the corresponding IQR of the efficacy estimate, taking variability in microscopic parameters and virus exposure into account. **B-D:** Mean efficacies ψ of TDF, FTC and 3TC against the wild type virus are highlighted by solid lines. Efficacies against mutant viruses combine both drug effects and inherent fitness defects of the mutants. The relative reduction in infection with the mutant virus in the presence of drug vs. the wild type virus in the absence of drugs is evaluated (dashed line: M184V, dash-dotted line: K65R, dotted line M184V/K65R double mutant). Vertical black dashed lines indicate the clinically relevant drug concentrations range after chronic therapy. Reproduced from Duwal et al. [25].

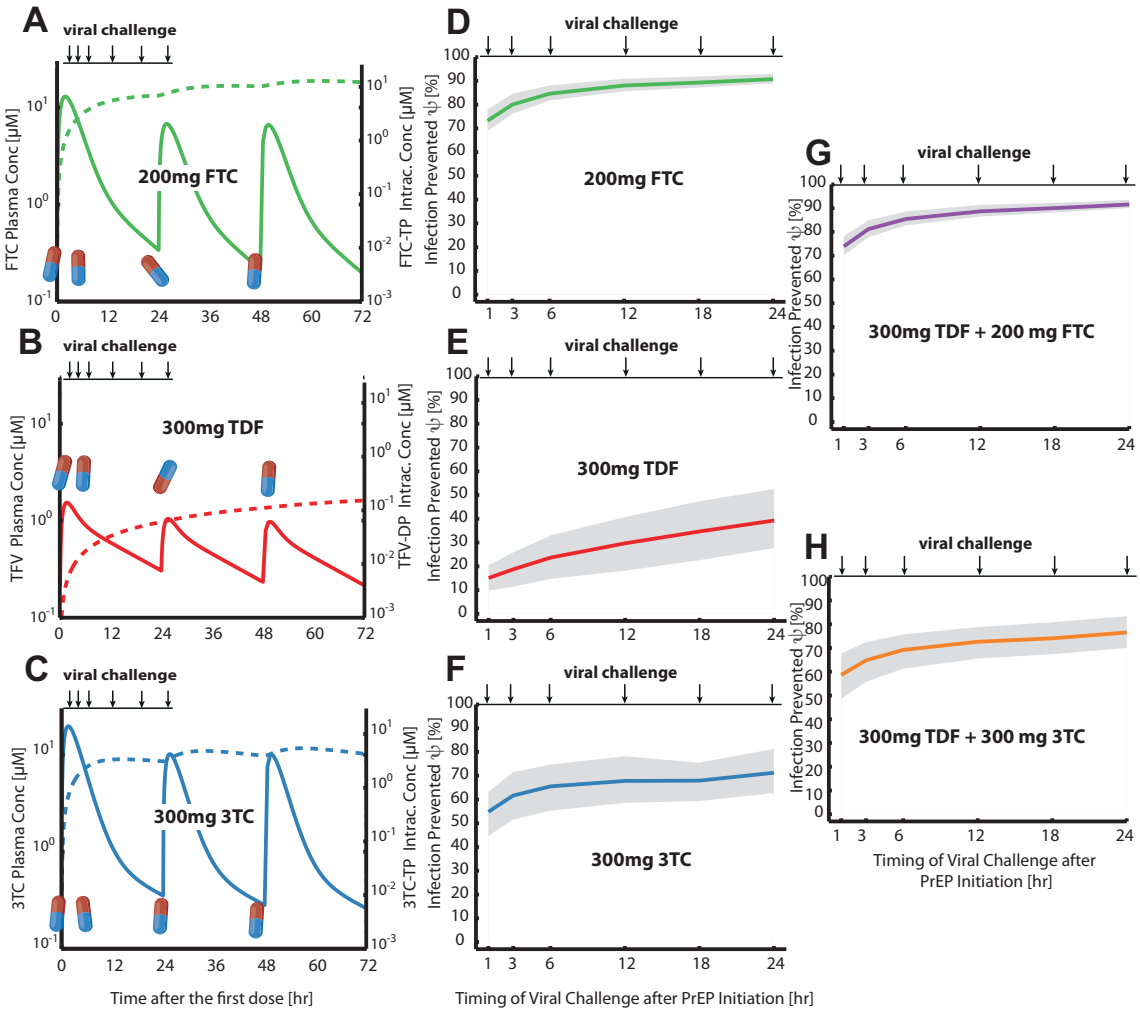

Figure 9.5: **Efficacy ψ of PrEP on demand against infection following viral challenges in homosexuals within 24hours after PrEP initiation. A-C:** Pharmacokinetic profiles during PrEP on demand for the circulating NRTI prodrug (solid lines) and the intracellular, active NRTI-TP moiety (dashed lines). FTC oral dose was 400mg at 0hours, followed by 200mg at 24 and 48hours (panel A), while TDF or 3TC dosage was 600mg at 0hours, followed by 300mg at 24 and 48hours respectively. **D-F:** Infections averted for PrEP on demand when viral challenge occurred either 1, 3, 6, 12, 18 or 24hours after PrEP initiation with either FTC (panel D), TDF (panel E) or 3TC (panel F). Solid lines indicate the mean % infections averted (see Eqn (9.2)), while shaded areas indicate interquartile ranges of this estimate, taking variability in microscopic parameters in MMoA model and virus exposure during homosexual intercourse into account. **G-H:** Infections averted for combinations of TDF+FTC (panel G) and TDF+3TC (panel H), taken on demand (double doses at day 0, followed by single doses at day 1 and 2). Combination predictions assumed that no significant pharmacokinetic interactions occur. Reproduced from Duwal [25].

One can see in Figure 9.5A-C that intracellular concentrations (dashed lines) quickly increase to almost steady state levels for FTC-TP and 3TC-TP after $\approx$ 6–12 hours, but not for TFV-DP, arguing that TFV-DP may not reach protective levels when applied on demand. For a challenge occurring either 1, 3, 6, 12, 18 or 24 hours after PrEP initiation, Figure 9.5D-F show the prophylactic efficacy ψ of the different drugs used alone. All tested drugs are more efficient at preventing infection, if the viral challenge occurs late with respect to PrEP initiation. FTC is the most efficacious, preventing 73–90% of potential infections, followed by 3TC (55–71%). TFV is observed to

poorly prevent an infection when taken on demand, only preventing 15–40% of potential infections after virus exposure. The observation corroborates the hypothesis that protective TFV-DP levels may build up too slowly in the intracellular compartment to provide sufficient protection [259]. The combination of FTC and TDF resembles the efficacy profile of FTC alone (see Figure 9.5G), whereas the efficacy of the combination 3TC and TDF is slightly elevated (59–77%), in comparison to 3TC alone.

9.3.3 Efficacy after PrEP discontinuation with TDF, FTC and 3TC

The prophylactic efficacy of TDF, FTC and 3TC, alone or in combination, during chronic PrEP and after its discontinuation is assessed based on population-average pharmacokinetics after oral administration of 200mg FTC or 300mg TDF or 300mg 3TC daily, or combinations thereof. The prophylactic efficacy profiles are computed using Eqn (9.2). The results are depicted in Figure 9.6A-E. Daily administration of FTC, TDF and 3TC for 30 days prior to a viral challenge lead to a prophylactic efficacy ψ of $\approx$ 95, 74 and 75% respectively. After discontinuation, FTC, TDF and 3TC remain $\geq$ 50% effective for about 7, 10 and 2 days respectively; the prophylactic efficacy of 3TC declined most rapidly. The combination FTC+TDF and 3TC+TDF prevent $\approx$ 96% and 87% of infections respectively after 30 days of daily administration. Both combinations remain $\geq$ 50% effective for about 10 days after discontinuation. Figure 9.6F-G show the efficacy of the combination, with the efficacy of the single drugs superimposed. Figure 9.6 indicates that the prophylactic efficacy of tenofovir is retained after the discontinuation of the combination and thus makes the regimen robust to poor adherence.

9.4 Prophylactic efficacy of antivirals other than NRTIs

Currently, a number of antivirals are under investigation for PrEP repurposing [18]. In this section, we assessed the utility of treatment-approved antivirals other than NRTIs for prophylaxis.

9.4.1 Concentration-prophylactic efficacy curves for antivirals except NRTIs

We utilized drug-specific pharmacodynamic and pharmacokinetic parameters (Table B.1) to parameterize Eqn (2.2) and to predict the prophylactic efficacy of treatment approved CRAs, non-nucleoside reverse transcriptase inhibitors (NNRTIs), InIs and PIs at clinically relevant concentration ranges. As for NRTIs, we sampled the number of viruses transmitted and reaching a target-cell compartment using the viral exposure module from a previously parameterized model (see Chapter 8). For each antiviral, the range of total concentrations after chronic administration of a standard dose is obtained from literature (see Table B.1).

Figure 9.7 depicts the concentration-prophylactic curves for all antivirals except NRTIs. The prophylactic efficacy per challenge (ψ) due to peak (D_{peak}) and trough concentrations (D_{trough}) are marked by thick black lines and downward pointing arrows respectively. A desirable property of an antiviral for prophylactic use is its pharmacologically forgiveness. Pharmacologic forgiveness refers to the property where the efficacy does not deteriorate strongly, despite a couple of missed doses. To preferentially select pharmacologically forgiving antivirals, we used the trough concentration after two consecutive missed doses D_{low} for the computation of prophylactic efficacy. The trough concentration after two consecutive missed doses was computed as shown below

$$D_{low} = D_{trough} \cdot \exp(-2 \cdot 24 \cdot k_e), \tag{9.16}$$

where D_{trough} is the trough concentration in the plateau phase and k_e is the first order elimination rate which can be computed as $k_e = \log(2)/t_{1/2}$ (half-lives are reported in Table B.1). The range

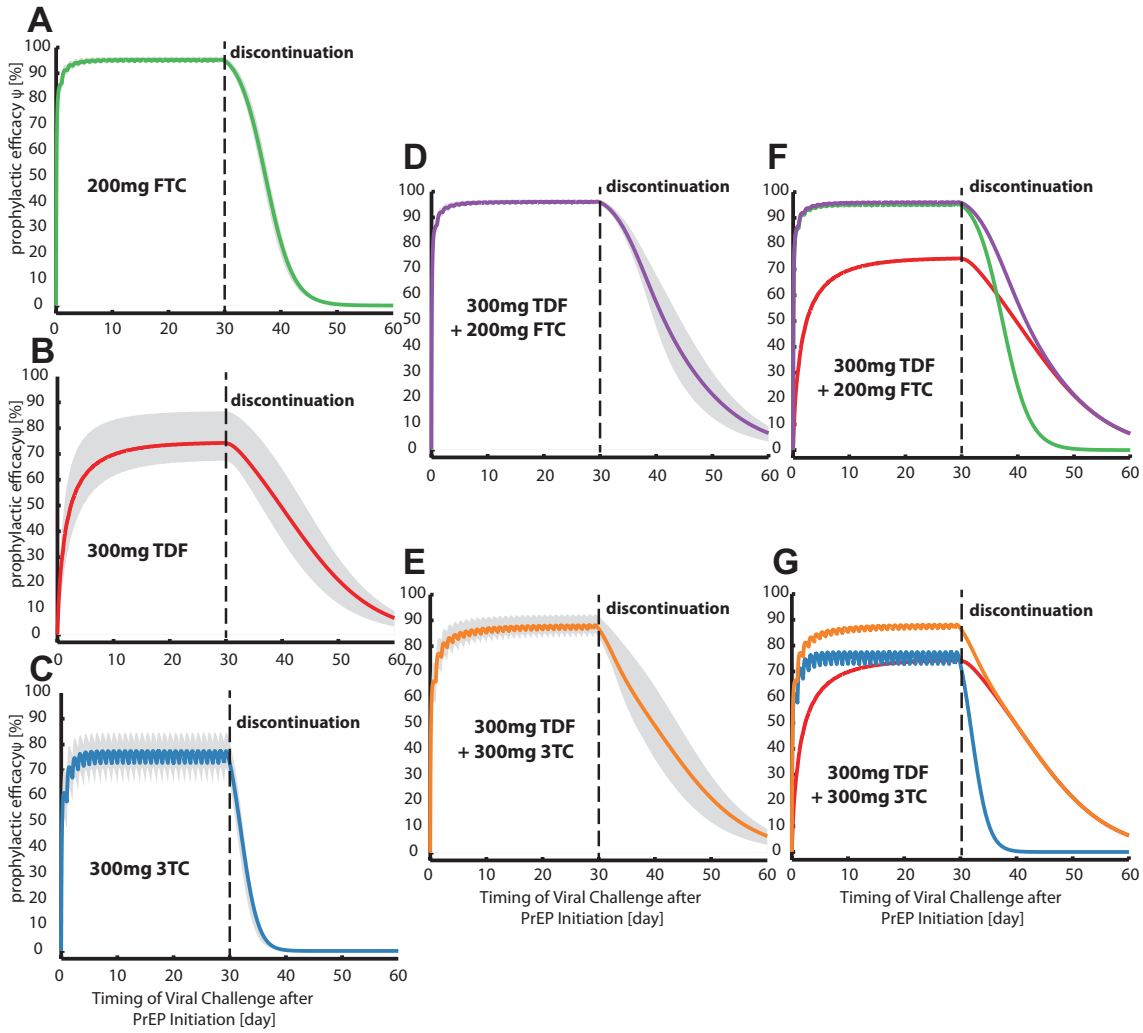

Figure 9.6: **Prophylactic efficacy per challenge ψ (homosexual transmission mode) occurring within 30 days of PrEP or after its discontinuation. A-E:** Mean prophylactic efficacy profiles (see Eqn (9.2)) when either oral doses of 200mg FTC (panel A), 300mg TDF (panel B), 300mg 3TC (panel C), 300mg TDF+200mg FTC (panel D), 300mg TDF+300mg 3TC (panel E) were administered daily for 30 days and discontinued thereafter are illustrated by solid lines. Mean prophylactic efficacy profiles for drug combinations TDF+FTC (panel D) and TDF+3TC (panel E). Shaded areas indicate interquartile ranges of this estimate, taking variability in microscopic parameters (module II) and virus exposure during homosexual intercourse (viral exposure module, Figure 8.2B) into account. **F:** The mean prophylactic efficacy for the combination 300mg TDF + 200mg FTC (violet solid line) is shown together with the mean prophylactic efficacy profiles for the single drugs FTC (green) and TDF (red). **G:** The mean prophylactic efficacy profile for the combination 300mg TDF + 300mg 3TC (yellow solid line) is shown together with the mean prophylactic efficacy profiles for the single drugs 3TC (blue) and TDF (red). Combination predictions assumed that no significant pharmacokinetic interactions occur. Reproduced from Duwal et al. [25].

of prophylactic efficacy per challenge $(\psi(D_{low}), \psi(D_{peak}))$ are listed in the Table 9.1. Figure 9.7 allows for an initial screen of the utility of the various drugs for oral PrEP. Table 9.1 lists EC_{50}, EC_{90} computed from the corrected IC_{50} as shown in Table B.1 using Eqn (9.11) for CRA, RTI and InI and Eqn (9.14) for PI.

Most analysed drugs, except for maraviroc (MVC), raltegravir (RAL), elvitegravir (EVG) and nelfinavir (NFV), potently prevent infection at concentrations ranges typically encountered

in fully adherent individuals during treatment (range between minimum- to maximum concentration, $[D_{trough}; D_{peak}]$). Since the lack of adherence to the dosing regimen is a major problem, we consider a lower bound concentration that would arise if the drug had not been taken for three days prior to exposure D_{low} (thin dashed vertical line in Figure 9.7). This emphasizes a 'pharmacokinetic safety margin' in case of poor adherence.

Numerical values for the computed maximum prophylactic efficacy and the efficacy at the lower bound concentrations are presented in Table 9.1 alongside with estimated EC_{50} and EC_{90} values. Our simulations indicate a residual risk of infection for most analysed drugs. Notably, most protease inhibitors may confer anything from none to absolute protection within relevant concentration ranges, $[D_{low}; D_{peak}]$, which highlights a severe limitation to their PrEP use in the context of poor adherence or pharmacokinetic (intra-/inter individual) variability. An exception is darunavir (DRV), which is predicted to be almost fully protective for the entire concentration range.

	prophylactic efficacy ψ [%]				$EC_{50}(\widehat{V})$	$EC_{90}(\widehat{V})$
drug	$\psi(D_{peak})$		$\psi(D_{low})$		[nM]	[nM]
MVC*	96.10	(74.11;100)	50.12	(18.63;85.42)	11.45	349.63
EFV	100	(100;100)	100	(100;100)	10.55	36.23
NVP	100	(100;100)	100	(100;100)	114.06	438.06
DLV	100	(100;100)	3.38	(0.88;10.19)	329.50	1254.58
ETR	100	(100;100)	100	(100;100)	8.45	26.75
RPV*	100	(100;100)	100	(99.02;100)	7.61	22.55
RAL*	100	(100;100)	8.15	(6.32;10.23)	45.40	302.36
DTG*	100	(99.03;100)	72.12	(57.77;84.85)	145.18	722.23
EVG	94.61	(89.02;97.97)	6.96	(3.66;12.49)	108.66	976.25
ATV	100	(100;100)	0.08	(0.04;0.15)	87.44	108.79
APV	100	(100;100)	0.01	(0.01;0.03)	1394.96	1848
DRV*	100	(100;100)	100	(100;100)	118.32	139.24
IDV	100	(100;100)	0	(0;0)	280.80	319.71
LPV	100	(100;100)	0	(0;0)	389.69	519.09
NFV	100	(64.01;100)	0	(0;0)	2253.66	3118.34
SQV	100	(100;100)	0	(0;0)	227.29	266.66
TPV	100	(100;100)	0	(0;0.02)	1944.89	2458.09

Table 9.1: **Prophylactic efficacy and sensitivity to incomplete adherence.** The table shows the prophylactic efficacy (% reduction in infection probability per challenge) of all investigated drugs at their respective maximum achievable drug concentrations after chronic oral administration of the standard regimen and its efficacy at a concentration level that would be reached if the last dose had been taken least three days prior to virus exposure $D_{low} = D_{trough} \cdot \exp(-2 \cdot 24 \cdot k_e)$, with $k_e = \ln(2)/t_{1/2}$ and halflifes $t_{1/2}$ reported in Table B.1. The 5-95% range of these estimates are shown in brackets and consider uncertainty in pharmacodynamic parameters IC_{50}, m and variability in virus exposure after homosexual contact, according to Duwal et al. [25]. The last two columns show the EC_{50} and EC_{90} in the case when an individual was exposed to a single virus $\widehat{V}$. MVC -maraviroc, EFV -efavirenz, NVP -nevirapine, DLV -delavirdine, ETR -etravirine, RPV -rilpivirine, RAL -raltegravir, EVG -elvitegravir, DTG -dolutegravir, ATV -atazanavir, APV -amprenavir, DRV -darunavir, IDV -indinavir, LPV -lopinavir, NFV -nelfinavir, SQV -saquinavir, TPV -tipranavir. * currently investigated for PrEP. Reproduced from Duwal et al. [27].

The NNRTIs efavirenz (EFV), nevirapine (NVP), etravirine (ETR) and rilpivirine (RPV) are observed to be extremely potent: These drugs prevent infection, even when three consecutive days doses were missed, Table 9.1. The co-receptor antagonist maraviroc (MVC) and the integrase

inhibitor dolutegravir (DTG) retain some prophylactic efficacy (50 and 72% respectively) at lower bound concentrations D_{low}. The CRA maraviroc (MVC), the NNRTI rilpivirine (RPV) and the InI raltegravir (RAL) are currently investigated for use as PrEP compounds (long-acting injections of RPV and RAL; oral- or topical application of MVC). The predicted PrEP efficacy of these drugs would drop to 8% (RAL) and 50% (MVC) after missing three consecutive doses prior to a virus exposure. Notably, RPV remained 100% effective.

9.5 Prophylactic utility of oral dolutegravir

Next, we assessed the prophylactic utility of oral dolutegravir, because dolutegravir has an excellent safety profile and is currently investigated in a PrEP clinical trial [18]. The population pharmacokinetic model of DTG was discussed in Chapter 5. The prophylactic efficacy of various prevention strategies based on dolutegravir is assessed using EXTRANDE algorithm (see Chapter 7). Figure 9.8A shows the relation between the plasma concentration of DTG and its prophylactic efficacy after homosexual virus exposure. For these simulations, the number of viruses reaching a target-cell compartment after homosexual contact were sampled from the virus exposure module (Chapter 8). Within the concentration range, the median prophylactic efficacy for 2mg QD ranged from 43.6 to 75.7%. For 10mg QD, efficacies ranged from 87.1 to 97.5%, and for 50mg QD almost complete (99.5 to 100%) protection was attained. The estimated $EC_{50}(\widehat{V})$ and $EC_{90}(\widehat{V})$ were 145.18 and 722.23nM respectively.

9.5.1 Sensitivity to incomplete medication adherence

During pre-exposure prophylaxis, adherence to the regimen may be imperfect. Figure 9.8B displays the prophylactic efficacy of once daily 50mg, 10mg and 2mg oral dolutegravir, considering varying levels of adherence (25-, 50-, 75-, 95- and 100% of doses taken). Viral challenges were simulated to randomly take place during a 3 month interval with inoculum sizes drawn from the transmitted virus distribution [25] (see Chapter 8). The mean predicted prophylactic efficacies for 50mg with 25-, 50-, 75-, 95- and 100% adherence were 60 %, 85.54%, 96.63% , 98.88% and 99.36%, respectively. Interestingly, the prophylactic efficacy of 50mg oral DTG becomes saturated, and exceeds 95%, if at least 75% of the pills were taken. Conversely, 2mg and 10mg oral dolutegravir allow for considerable residual infection events and 2mg oral dolutegravir efficacy increases almost linear with increasing adherence levels.

9.5.2 PrEP on demand with DTG

We simulated PrEP on demand using DTG with a dosing scheme similar to the IPERGAY protocol [258]: An individual at risk initiates PrEP a few hours before a viral exposure and takes two consecutive doses 24 and 48hours after the first dose. Figure 9.8C displays the predicted prophylactic efficacy of DTG when taken on demand. The mean prophylactic efficacies for 50mg varied between 78.63–83.93% depending on the timing of the first dose with respect to viral exposure. For 10mg, it was 64.49–73.01% and for 2mg it was 36.86–46.34%. The prophylactic efficacy decreased with a lowering of dose. An increment in the time difference between the initiation of PrEP on demand and viral exposure causes a reduction in the prophylactic efficacy. This trend is opposite to the trend for PrEP on demand with Truvada [25]. A reason for this is the rapid uptake of systemic DTG (compare Figure 9.8B), whereas the Truvada's active moieties tenofovir diphosphate (TFV-DP) and emtricitabine triphosphate (FTC-TP) require intracellular phosphorylation

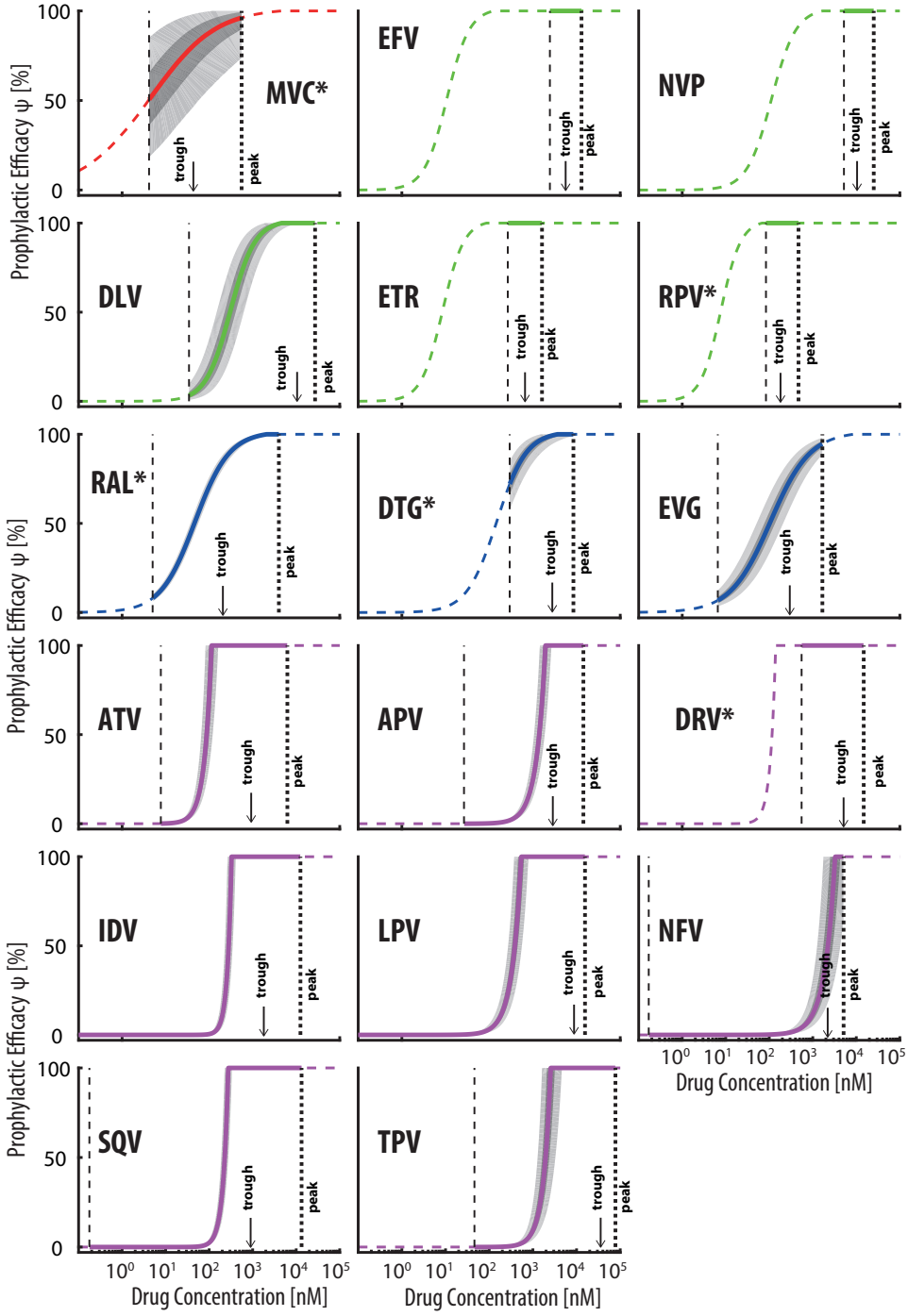

Figure 9.7: **Drug specific prophylactic efficacy.** Solid and dashed coloured lines depict the concentration-prophylactic curve for the individual drugs. The solid lines represent the concentration-prophylactic curves and light and dark grey areas indicate the quartile ranges and 5-95% ranges of the concentration-prophylactic curve, considering uncertainty in pharmacodynamic parameters (Table B.1) and the distribution of viral inoculum sizes after homosexual exposure to HIV [25]. Maximum clinically achievable concentrations D_{max} for chronic oral administration of the standard dosing regimen and a lower bound concentration D_{low} that would be achieved if the last dose had been taken three days prior to virus exposure are marked by thick and thin vertical black dashed lines respectively. For IDV, LPV, NFV and SQV D_{low} falls below the range of the x-axis. Downward pointing arrows indicate minimum (pre-dose) concentrations achieved for standard regimen in *adherent* individuals as reported in [87,260,261]. * - Recently or currently tested for PrEP. Reproduced from Duwal et al. [27].

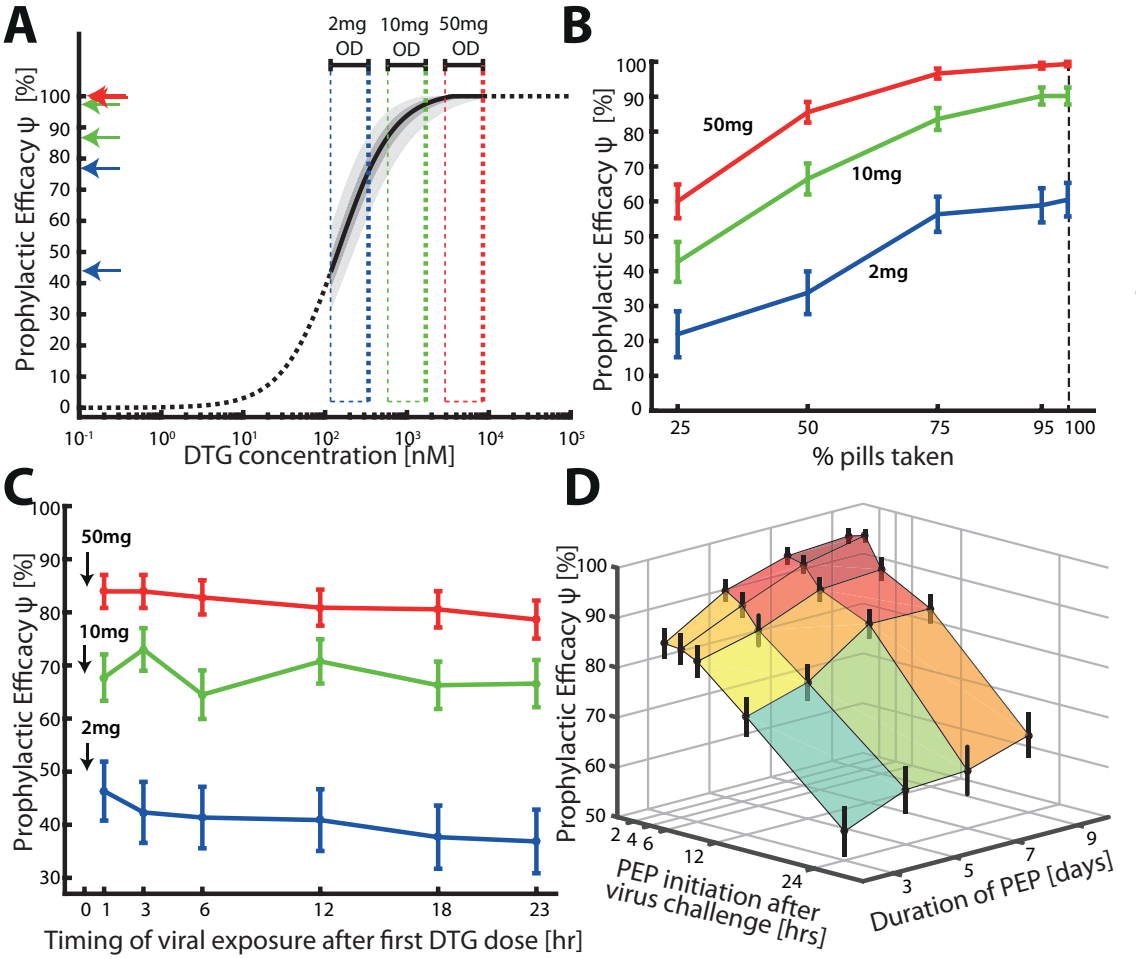

Figure 9.8: **Prophylactic efficacy of different DTG regimen. A:** Prophylactic utility of chronically administered oral DTG regimen (homosexual contact [25]). The red-, green and blue dashed boxes mark the considered concentration ranges of DTG [$C_{\min}$ (pre-dose), $C_{\max}$] achieved with 50, 10 and 2mg once daily (OD) oral dosing. The left pointing arrows at the y-axis mark the respective prophylactic efficacy ranges. **B:** Prophylactic efficacy of chronically administered oral DTG regimen with varying adherence levels. The red-, green- and blue lines denote mean prophylactic efficacy for a 50mg, 10mg and 2mg oral DTG regimen. Error bars depict the 5–95% confidence bounds for the ensemble estimate, computed using Greenwoods formula. **C:** Prophylactic efficacy of DTG for PrEP on demand. Only three doses of oral DTG were ingested at 0, 24 and 48 hours. Homosexual viral exposure occurred within the first dosing interval at either 1, 3, 6, 12, 18 or 23 hours after initiating PrEP on demand. The red, green and blue lines represent the mean prophylactic efficacy for PrEP on demand using 50-, 10 or 2mg OD respectively, where error bars denote the 5–95% confidence bounds for the ensemble estimate, computed using Greenwoods formula. **D:** Prophylactic efficacy for post exposure prophylaxis (PEP) with 50mg DTG for various durations of PEP (y-axis; 3, 5, 7 and 9 days) and delayed initiation of PEP after homosexual viral exposure (x-axis; 2, 4 , 6 , 12 and 24 hours). Error bars mark the 5-95% range computed using Greenwoods formula. Reproduced from Duwal et al. [27].

after cellular uptake of the parent compound. This delays the time until maximal concentrations are achieved at the target-site [23, 84].

9.5.3 Post-exposure prophylaxis (PEP) with DTG

Here, we assessed the efficacy of 50mg oral DTG in preventing infection when taken as post-exposure prophylaxis (PEP). We varied durations of PEP and the timing of PEP initiation after virus exposure (see Figure 9.8D). Figure 9.8D indicates that 50mg oral DTG can effectively prevent infection (> 80%) when initiated shortly (within 6 hours) after exposure and when continued for as long as possible. One can see in Figure 9.8D that the efficacy starts to drop when PEP is initiated later than 6 hours and when it is shorter than 7 days. Our simulations also suggest that initiating the prophylaxis earlier has a more pronounced effect than prolonging PEP, arguing for the immediate start of PEP in case of known or suspected HIV exposure.

9.5.4 Comparison with Truvada (TDF+FTC)

Our analysis shows that once daily PrEP with Truvada provides ≈ 96% protection in fully adherent individuals (see Section 9.3.3). Due to difficulties in quantifying PrEP adherence clinically [262], a surrogate measure is often used, which is based on the percentage of individuals with detectable drug. In apparently highly-adherent individuals, clinical efficacy estimates of Truvada were 86-100% in the IPERGAY study [263], 58-96% in the PROUD study [264] and 96% in the Partners PrEP OLE study. In comparison, we predicted almost complete (99-100%) protection with 50mg QD DTG. The VOICE [265] and FEM-PrEP [266] studies indicated that Truvada may not prevent infection in poorly adherent individuals, i.e. if ≈ 30% of individuals had detectable drug. In contrast, we estimated about 60% protection with 25% adherence to once daily 50mg DTG and over 85% protection if at least half the pills were taken. For PrEP on demand with Truvada, we estimated that about 74–92% infections can be averted, depending on the time of viral exposure relative to the initiation of Truvada dosing [25]. The corresponding efficacy estimate in the IPERGAY trial was 86% [258], in line with our work. Our analysis shows that PrEP on demand with 50mg DTG is non-inferior to Truvada, providing 78.63–83.93% protection. While PEP with Truvada is not recommended due to the slow intracellular accumulation of pharmacologically active NRTI-triphosphates, PEP with 50mg DTG can prevent about 80% infections when initiated no later than 6 hours post exposure. In summary, our simulations indicate that prophylaxis with 50mg DTG is non-inferior to Truvada and that it may outperform Truvada in the case of poor adherence. Furthermore, DTG may outperform Truvada in the case of the post-exposure prophylaxis.

9.6 Clinical trials and prophylactic efficacy

Until now, we predicted the prophylactic utility of various antivirals by means of the prophylactic efficacy per challenge ψ. However, in a clinical trial an uninfected person may be repeatedly challenged. In this section, we discuss a measure of PrEP efficacy that involve repeated viral challenges similar to clinical trials. This is helpful as it delineates various confounding factors that affect estimate of PrEP efficacy in a clinical trial.

Clinical trial efficacy

A clinical trial consists typically of two arms, –a treatment arm and a placebo arm–, which are followed for the trials' duration. At the end of the trial, based on the incidence rates in two arms, the efficacy of the intervention is computed, e.g. [13, 231, 258, 264]:

$$\omega = 1 - \frac{\text{Incidence rate in the treatment arm}}{\text{Incidence rate in placebo arm}} \tag{9.17}$$

The clinical trial efficacy can be interpreted as the reduction in the expected number of infected individuals in the treatment arm with respect to the expected number of infected individuals in the placebo arm. In Appendix E, we derived the following:

$$\omega \approx 1 - \frac{1 - (1 - \mathbb{P}(\text{trans}, \mathcal{S}))^{T \cdot N_{c,\mathcal{S}}}}{1 - (1 - \mathbb{P}(\text{trans}, \varnothing))^{T \cdot N_{c,\varnothing}}} \tag{9.18}$$

where T is the trial duration in months, which is usually identical for both arms. $N_{c,\mathcal{S}}$ and $N_{c,\varnothing}$ are numbers of virus exposures per month in the treatment- and placebo arm respectively.

9.6.1 Trial duration, transmission modes and risk compensation

In order to compute the effects of trial duration, mode of transmission and risk compensation on clinical trial efficacy estimates, we predicted clinical trial outcomes by stochastic simulations. Stochastic simulations were motivated by the well-known Gillespie Algorithm [95]. Parameterizations for the simulations (Figure 9.9 below) are largely based on data provided in the IPERGAY study [258, 267]: Around 7 condom-less anal sex acts per month per study participant with different sexual partners among MSM were reported in the IPERGAY study [267]. The HIV-1 prevalence in a similar MSM group was reported to be around 17 % [268]. Hence, the average number of exposures (risky sex acts performed by a recipient) per month was fixed to 1.19 (7×0.17). We consider the same risk behaviour in both arms i.e. $N_{c.\varnothing} = N_{c,\mathcal{S}} = 1.19$. The prophylactic efficacy per exposure of the PrEP treatment ψ was set to 80%. The average infection probabilities per exposure $\mathbb{P}(\text{trans}, \varnothing)$ for homosexual- and heterosexual transmission are assumed to be 0.03 and 0.003 respectively [230, 242, 248].

Figure 9.9 shows Kaplan-Meier estimates of the proportion of infected individuals during the course of the simulated clinical trial in the untreated and placebo (panel **A**) and the PrEP-treated arm (panel **B**) respectively. The clinical trial simulation had 400 individuals (200 in each arm) belonging to homosexual vs. heterosexual risk groups. The solid yellow and blue lines indicate the computed proportions using the analytical formula. Panel **C** of Figure 9.9 depicts the clinical trial efficacy estimate ω computed from the analytical Eqn (9.18) for the homosexual (yellow), and the heterosexual target group (blue). It can be seen that the clinical trial efficacy estimates ω decrease with increasing trial duration, relative to the actual PrEP efficacy per exposure (dashed horizontal line). In particular, this bias is much stronger for the homosexual target group. The homosexual target group differs from the heterosexual target group in the simulations with respect to the transmission probability $\mathbb{P}(\text{trans}, \varnothing)$, which is 10-times larger than for the heterosexual target group. The analysis highlights that PrEP efficacy estimate ω is difficult to evaluate when its value is low. Specifically, in the PrEP treated arm almost no individual becomes infected after an average follow-up time of $\approx$ 12 month. Thus, an estimate of the incidence rate would be highly unreliable. The analysis recommends conducting a trial with a long-as-possible follow-up to ensure statistical certainty in the incidence rate.

Risk compensation

Table 9.2 depicts the results of a simulated clinical trial with untreated and PrEP-treated arms in homosexual target groups for different levels of risk compensation and follow-up durations (T = 6, 12, 18, 24 and 36 months). We considered the PrEP strategy with the prophylactic efficacy per exposure of ψ =70, 80 and 90% respectively. For each efficacy, 0, 10 and 20% risk compensation (additional percentage of risky sex acts in the treated arm compared to the untreated and placebo arm) were assessed. For all cases, the clinical efficacy estimate ω is lower than the PrEP efficacy

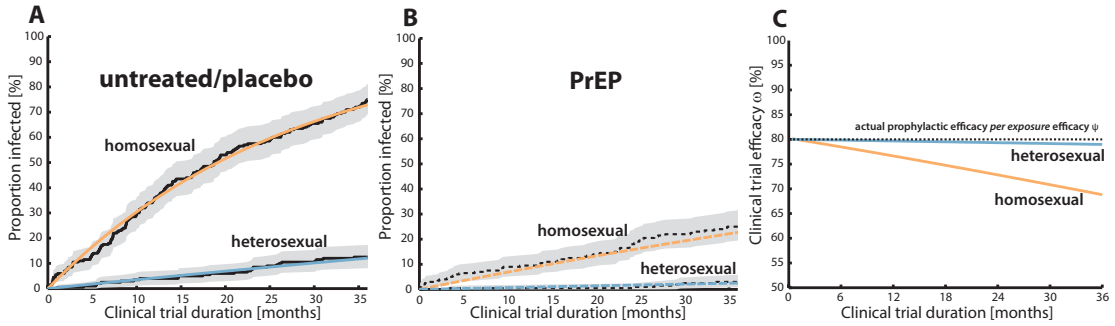

Figure 9.9: **Simulated PrEP clinical trials for homosexual- and heterosexual transmission modes. A:** Proportion of infected individuals in the placebo arm. The yellow and blue solid lines represent the proportion of infected individuals in the homosexual and heterosexual transmission groups. The solid black lines represent the Kaplan-Meier estimate of a stochastic simulation with 200 individuals. The gray area marks the region between the upper and lower bounds of the Kaplan-Meier estimate. The transmission probability *per coitus* in the absence of any drug ($\mathbb{P}(\text{trans}, \varnothing)$) for homosexual and heterosexual transmission were fixed to 3% and 0.3 % respectively. **B:** Proportion of infected individuals in the treated arm with prophylactic efficacy of ψ =80% *per coitus*. The yellow and blue dashes lines denote the homosexual- and heterosexual target group. The black dash lines denote the Kaplan-Meier estimate and the gray region denotes the area between the upper and lower bound of the Kaplan-Meier estimate for a stochastic simulation with 200 individuals. **C:** The trial efficacies ω for the homosexual group(yellow) and heterosexual group(blue) are compared. The horizontal black dashed line marks the actual prophylactic efficacy of PrEP per viral challenge ψ. Reproduced from Duwal et al. [25].

per exposure ψ and it decreases with increasing follow-up time. The decrease is more pronounced when the PrEP efficacy *per exposure* ψ is low. At 36 months of follow-up, without risk compensation, the clinical trial efficacy estimate ω underestimated the actual PrEP efficacy *per exposure* ψ by 14, 11 and 7% respectively for ψ = 70, 80 and 90%. This underestimation becomes even more pronounced when risk compensation occurs.

In summary, our simulations point to a profound limitation in estimating and comparing PrEP efficacy per exposure from incidence rates in clinical trials: On the one hand, a clinical trial has to be long enough to provide a statistically reasonable estimate of the incidence rate (a considerable number of individuals have to become infected). On the other hand, the longer the trial, the more confounded will the efficacy estimate ω be in relation to the actual PrEP efficacy $\psi(\mathcal{S})$ (see Table 9.2). For this reason, we provide the following formula which allows us to convert clinical efficacy estimates ω into unbiased PrEP efficacies *per exposure* $\psi(\mathcal{S})$, which can be compared between different studies (see Appendix E):

$$1 - \omega(\mathcal{S}) = \frac{1 - (1 - \mathbb{P}(\text{trans}, \varnothing) \cdot (1 - \psi(\mathcal{S})))^{T \cdot \mathrm{N}_{c,\mathcal{S}}}}{1 - (1 - \mathbb{P}(\text{trans}, \varnothing))^{T \cdot \mathrm{N}_{c,\varnothing}}}. \tag{9.19}$$

where the subscript $\mathcal{S}$ and $\varnothing$ denote the PrEP and untreated and placebo arm respectively.

9.7 Summary

In summary, we presented the framework and its modules, which can be used to assess the prophylactic efficacy of various antivirals. Using the framework, we derived the drug-class specific concentration-prophylactic efficacy curves. We observed that for all drug classes expect for the protease inhibitor, the concentration-prophylactic efficacy curves are approximately classical EMAX equation, whereas the curve for the protease inhibitor is a power function and exhibits

	Trial-based PrEP efficacy estimates ω								
Follow-up duration in months T	ψ = 70% risk compensation			ψ = 80% risk compensation			ψ = 90% risk compensation		
	0 %	10 %	20 %	0 %	10 %	20 %	0 %	10 %	20 %
6	68.01	64.93	61.86	78.48	76.38	74.28	89.14	88.06	86.99
12	65.66	62.46	59.30	76.65	74.42	72.21	88.09	86.93	85.77
18	63.26	59.96	56.73	74.76	72.41	70.09	86.99	85.73	84.49
24	60.83	57.44	54.14	72.82	70.35	67.92	85.84	84.49	83.15
36	55.93	52.39	48.99	68.81	66.11	63.48	83.42	81.88	80.36

Table 9.2: **Bias of clinical-trial efficacy estimates ω through risk compensation and follow-up duration.** Trial-based PrEP efficacy estimates ω (after repeated viral challenges) for different levels of risk compensation (reported as $100 \cdot (N_{c,\mathcal{S}} - N_{c,\varnothing}) / N_{c,\varnothing}$) and trial durations T were estimated using Eqn (9.18). The number of exposures per month $N_{c,\varnothing}$ in the untreated arm was set to 1.19. The transmission probability per exposure $\mathbb{P}(\text{trans}, \varnothing)$ was set to 3% and the prophylactic efficacies ψ were set to 70, 80 and 90% respectively. Reproduced from Duwal et al. [25].

a switch-like behavior. Furthermore, we provided formulas to translate the target-process drug potency to prophylactic potency i.e., for instance a conversion of IC_{50} to EC_{50}.

We used the framework to screen all the NRTIs. Besides TDF and FTC, 3TC and D4T also showed high prophylactic efficacy for their respective standard of care. The detailed pharmacokinetic models of TDF, FTC and 3TC are used to investigate various scenarios in detail. We observed that TFV-DP accumulation may be too slow for PrEP on demand, in agreement with Louissaint et al. [269]. All treatment-approved antivirals not belonging to NRTI are also screened for their PrEP utility. We predicted that the efavirenz (EFV), nevirapine (NVP), etravirine (ETR), rilpivirine (RPV) and darunavir (DRV) may fully prevent infection after oral application and in case of poor adherence. The drugs maraviroc (MVC) and dolutegravir (DTG) potently prevent infection but may allow for HIV transmission when individuals poorly adhere to the medication. Using the pharmacokinetic model of DTG, we analysed various roll-out schemes and found that it is non-inferior to truvada.

We highlighted that the clinical endpoint or clinical efficacy in a PrEP trial is confounded by various factors such as trial duration, transmission mode, risk compensation and risk behavior, rendering the comparison of clinical efficacies of two trials unreliable. We provide a formula to convert clinical efficacy $\omega(\mathcal{S})$ to prophylactic efficacy per challenge $\psi(\mathcal{S})$, which can be compared between different studies.

CHAPTER 10

Discussion

In this work, we presented a multiscale *systems pharmacology* framework that can be assembled in a building block manner to assess the prophylactic efficacy of antivirals. The framework integrates different relevant processes occurring at micro-, meso-, macro- and population-scale, such as drug-target interactions, antiviral pharmacokinetics, viral replication dynamics, a single viral challenge and multiple challenges in a clinical trial. We presented target-site pharmacokinetic models of several antivirals (TDF, FTC, 3TC and DTG) by employing various methods for model building. We coupled target-site pharmacokinetic models of antivirals with a well-established viral replication cycle models [83], which allows for the drug-class specific mechanistic integration of antivirals effects. A novel statistical viral exposure model was developed that encompasses insights from various studies linking the transmitted virus distribution with major factors determining the transmission risk.

The main algorithmic challenge considered in the work is the task of quantifying the infection probability after a viral challenge within a host in the context of antiviral pharmacokinetics. The antiviral pharmacokinetics was considered as a continuous-time continuous-state deterministic process, whereas the viral replication cycle was considered as a continuous-time discrete-state stochastic process which is influenced by pharmacokinetics. Thus, we needed to pursue a hybrid stochastic-deterministic approach. We distinguished between time-invariant- and time-variant reaction propensities in the viral replication cycle.

Time-invariant reaction propensities are valid for constant target-site antiviral concentrations. We constructed the embedded Markov process model of the viral replication cycle and employed the theory of branching processes to derive extinction and infection probabilities for time-invariant reaction propensities. For time-variant reaction propensities, the hybrid stochastic-deterministic approach is utilized. The deterministic pharmacokinetics can be solved by numerically integrating the corresponding ODE system. In theory, one can quantify the infection probabilities by using the chemical master equation that describes the stochastic viral replication cycle when it is coupled with pharmacokinetics. However, the chemical master equation cannot be solved due to the curse of dimensionality. To circumvent this problem, we presented a reduced-state CME, exploiting an important property of the viral replication cycle, namely that the probability to complete the first replication cycle closely approximates the infection probability. Although the reduced-state CME can be solved efficiently, it is only an approximation and can be applied only in a few cases.

Stochastic simulation algorithms based on Monte Carlo sampling can also be applied to circumvent the curse of dimensionality, and to empirically reconstruct $\mathbb{P}(X_t = x_i)$ from simulated trajectories. The challenge in doing so is the classification of a trajectory as an infection event. While there exists an unambiguous criterion for the classification of a trajectory as an extinction event, the analogous stopping criterion for an infection event is not straightforward to obtain. To

tackle this issue, we devised a stopping criterion based on a dynamically adapting extinction simplex that guarantees that the misclassification error is below the user-defined threshold and that the run-time is optimal.

In this work, we adapted the recently developed rejection-based SSA, namely EXTRANDE (extra reaction algorithm for networks in a dynamic environment) algorithm [28]. The algorithm requires a look-ahead time horizon to compute an upper bound for the sum of reaction propensities. The rejection-based SSA relies on extra reaction firings that do not change the state of the system but guarantees that the algorithm is numerically exact. At the same time, extra firings are devised in such a way that the computationally intense numerical integration step as in the integral-based SSA can be omitted. However, whether or not EXTRANDE is computationally more efficient than the integral-based SSA depends on the extent of computational overheads due to the look-ahead time horizon and the number of extra firings. We proposed an intuitive way to compute an upper bound of the sum of reaction propensities using an insight from the viral replication cycle model, which also removes the necessity for a look-ahead time horizon for our system of interest. The adapted EXTRANDE is run-time wise more efficient than the integral-based SSA method.

Another salient feature of the framework is that it captures drug-class specific effects of antivirals at various levels ranging from target-process inhibition, inhibition of target-cell infection and systemic infection, and finally long-term efficacy after multiple viral challenges akin to a clinical trial. It, therefore, provides a way to translate the effect from one level to another. Technically, the target-process drug potency (IC_{50}) can be determined from clinical trial data involving HIV-1 infected individuals under antiviral monotherapy, by employing a top-down approach (classical PK-PD). However, in addition to being costly and time-demanding, such trials generate sparse and noisy data and often cannot be conducted due to ethical reasons. On the other hand, pre-clinical *in vitro* and *ex vivo* experiments can be conducted in controlled conditions and are relatively inexpensive and less time-consuming. Hence, using *in vitro* and *ex vivo* parameters to determine the drug potency regarding target-process inhibition (IC_{50}) is desirable. However, it is difficult to accomplish this, due to the lack of an accurate model based on a mechanism of action and also due to a number of differences between *in vitro* and *ex vivo* experiment set-ups and *in vivo* or clinical trial set-ups.

A noteworthy contribution to bridge the gap is the model of the molecular mechanism of action for NRTIs developed by von Kleist et al. [24]. The model utilizes various *in vitro* parameters such as the binding affinity of NRTI-TPs and endogenous nucleotides to the viral enzyme, the maximum catalytic rate, intracellular concentrations of NRTI-TP and endogenous nucleotides etc., which can be used to compute IC_{50} for the target-process inhibition (reverse transcription). This is particularly important since the free drug hypothesis is not valid for NRTIs. We used the model to compute IC_{50}s for various NRTIs. For antivirals belonging to other drug classes, their potencies (IC_{50}) can be determined in single-round infectivity assays. However, due to difference in the plasma protein binding in the *ex vivo* assay and *in vivo*, a correction is required. We presented a way to correct the drug potency from the *ex vivo* assay for the *in vivo* case (IC_{50}).

Often, PrEP clinical trials are guided by target-process drug potency (IC_{50}s). For all drug classes except for RTI, we observed that the prophylactic drug potency (EC_{50}) is bigger than target-process drug potency IC_{50}. This implies that if PrEP clinical trials are designed using IC_{50} or IC_{90}, the prophylactic utility of antivirals is overestimated; that results in underperforming clinical trials. To make matters worse, IC_{50} from *in vitro* and *ex vivo* are used without proper translation and correction. In this work, we derived a formula to translate the target-process drug potency (IC_{50}) to the prophylactic drug potency (EC_{50} and EC_{90}). This can help to avoid unnecessary clinical trials, which waste not only money and time, but also risk causing individuals harm.

In a clinical trial, an uninfected individual is likely to encounter a number of viral challenges.

As a consequence, the clinical endpoint or efficacy (ω), which is the reduction in the number of infected individuals in the treatment arm with respect to the placebo arm, is confounded by a number of factors such as HIV-1 prevalence, risk behaviour, risk compensation, trial duration and transmission modes. Hence, comparing the clinical endpoints from different clinical trials is difficult due to differences in those factors. We provided a way to deconvolute the effects of various confounding factors on the clinical efficacy to compute the prophylactic efficacy per challenge (ψ), which is comparable across all clinical trials.

As mentioned earlier, the pharmacokinetic parameters and model can be integrated into the framework to assess the prophylactic utility of any antiviral. A detailed target-site pharmacokinetic model allows one to assess various PrEP roll-out schemes. Unfortunately, a detailed pharmacokinetic model is usually not available. Parameters such as trough and peak concentrations at target-site and drug half-lives are easily available. These pharmacokinetic parameters can be used for an initial screening and dose-finding based on the prophylactic efficacy. Here, it should be emphasized that the selection of an antiviral and a roll-out scheme for a prophylactic use requires careful considerations in addition to prophylactic efficacy, such as pill burden, pharmacological forgiveness, financial cost, toxicity, and interactions with other drugs and food.

Using the framework, we showed that FTC is more effective than TDF for PrEP, in contrast to the majority view. This is due to the fact that for FTC, higher concentrations with respect to its potency is achieved faster in target-cells than for TDF. However, TDF seems to be more pharmacologically forgiving owing to its long terminal half-life. Moreover, FTC's efficacy is strongly reduced by drug-resistant strains in comparison to TDF's efficacy [255]. These facts underscore the complementary roles of TDF and FTC in Truvada combination used for PrEP. The Partner PrEP study [270] compared the efficacy of TDF alone vs. TDF and FTC in combination, which is partly motivated by cost-effectiveness considerations. Our analysis discourages the use of TDF alone for PrEP. In addition, it shows that the drug combination 3TC and TDF may be an alternative to the combination of TDF and FTC. 3TC is interesting since it closely resembles FTC with a similar safety and efficacy profile but is cheaper than FTC and patent-expired [271].

Although MVC is stated to be used for PrEP, our analysis suggests that MVC may not be effective for PrEP, which is in line with results from the NEXT-PrEP (HPTN 069) phase II study [272]. This agrees with the reported lack of efficacy of MVC as a PrEP candidate in animals and human explant samples [273]. Our results suggest that the potency of any CRA, like MVC, against infection will always be less than its potency in preventing HIV replication ($EC_{50} > IC_{50}$, $EC_{90} > IC_{90}$).

In our screening, a number of protease inhibitors such as SQV, NFV and APV achieved high prophylactic efficacy. However, due to their short half-lives, they require inconvenient multiple doses per day to retain the efficacy (high pill burden) and are very sensitive to an imperfect adherence. DRV is the only protease inhibitor that remained effective despite incomplete adherence. DRV is currently in PrEP trial for topical use [18]. Notably, our screening shows a number of NNRTIs, such as EFV, NVP, RPV and ETR to be very interesting candidates for PrEP. NNRTIs exhibit long elimination half-lives (30-40h), and rapidly and durably achieve high concentrations with respect to their IC_{50} at target-site. NVP and EFV are patent-expired and are relatively cheap (US $ 0.1). NVP was shown to be effective in mother-to-child transmission [274, 275]. However, NVP has a very strong contraindication, which might disqualify it from use in uninfected individuals [71]. EFV is associated with adverse effects related to the central nervous system [71,276]. For EFV, reducing the dose amount for PrEP might be worth exploring, such that side-effects are prevented or reduced without compromising prophylactic efficacy. Another issue with EFV and NVP is the low barrier to viral resistance [277]. Resistant virus types are less fit than the wild type, and hence not readily transmitted. However, if the infection occurs despite EFV or NVP prophylaxis

treatment, for instance due to a low adherence, the virus is likely to develop resistance, thus reducing the treatment option for the infected person. RPV and ETR might be interesting too since they have a stronger barrier to resistance than EFV and NVP [278, 279]. At the same time, they have long half-lives similar to NVP and EFV and low side-effect profile. RPV is currently investigated as a long-acting formulation in HPTN076 using 1200mg injections every 2 months [280].

In our screening, DTG is the best among integrase inhibitors and it also exhibits an excellent safety profile. A detailed pharmacokinetic model of DTG was used to assess various PrEP scenarios. We found that oral 50mg DTG is non-inferior to Truvuda. A long-acting formulation of the integrase inhibitor carbotegravir, which is an analog of dolutegravir [281], is also currently being investigated for PrEP use in HPTN-083 [282]. The framework can be used for carbotegravir to address similar questions.

The framework utilizes target-site pharmacokinetic models of antivirals, which are either plasma or target-cell intracellular pharmacokinetics. Our model assumes that the systemic antiviral concentration corresponds to the concentration in the target-cell compartment. However, since viruses first reach the mucous membrane during a viral exposure, some questions arise: Are the drug concentrations at the site of mucosal exposure (e.g. cervix, rectum) more relevant than the plasma drug concentration [280, 283]? How are various processes at the site of mucosal exposure considered in the framework?

The framework does not take into account drug concentrations at the site of mucosal exposure, because these concentrations have not been validated as targets for successful prevention or treatment. For antivirals except for NRTIs, we utilized the unbound concentrations, in line with the broadly accepted free drug hypothesis. For drugs highly bound to plasma protein ($> 90\%$), their total concentrations at sites other than the plasma can be comparatively lower [283]. However, the unbound concentrations in plasma and various sites are found to be identical [284]. All analysed NNRTIs, InIs and PIs, except for raltegravir (RAL), exhibit strong lipophilicity, which enables the rapid exchange of unbound drug across cellular membranes, attaining an equilibrium between the unbound drug on either side of the cellular membrane [197]. Even for the weakly lipophilic compound raltegravir, evidence shows the validity of the free drug hypothesis [198, 199]. In contrast to other drug classes, the free drug hypothesis is not valid for NRTIs [23, 84, 155]. These antivirals require active uptake in cells and intracellular conversion into pharmacologically active triphosphates (NRTI-TP). Since the expression of transporters and intracellular enzymes is likely cell-specific, different cell types may contain vastly different concentrations of the pharmacologically active compound. It is, therefore, entirely unclear what relevance concentration measurements of NRTI-TPs in tissue homogenates [285] (containing HIV target- and non-target cells) from sites of viral exposure (e.g. cervix, rectum) have in terms of prophylaxis.

Our framework utilizes a viral exposure model that does not explicitly model the processes at the site of mucosal exposure. Instead, the processes are considered in a lumped fashion. The quantitative contribution of a number of physiological processes at the site of mucosal exposure (e.g. the cells involved, their residence duration at the local site of exposure and their capabilities to transduce virus through physiological barriers) are currently not fully resolved and difficult to measure in humans. However, evidence shows that the target-cell abundance at the local site of exposure is not sufficient to sustain the viral replication ($R_0 < 1$). Hence, to circumvent model- and parameter uncertainties, we presented a minimal and data-driven model, that subsumes all physiological barriers before viruses reach the target-cell compartment into a single bottlenecking process.

In line with the biological insight [207], our framework assumes that the target-cell compartment is decisive for establishing and shedding infection (in the compartment, a virus exhibits $R_0 > 1$). We also assumed that this compartment is well-perfused at the time scale of interest and

well-mixed. In the future, with more quantitative insights, these assumptions can be relaxed, and the target-cell compartment can be further refined. In a similar vein, the subsumed processes in viral exposure model can be modelled in detail. In particular, the processes at the mucosal site of exposure require more attention, as the topical application of antivirals is being considered [18].

In the future, the framework can be readily coupled to pharmacokinetic models/parameters of any novel antivirals (long-acting formulation and patent-expired or patent-protected) to assess their prophylactic utility, as soon as such models/parameters are available. As in treatment, various combinations of antivirals can be explored to increase the prophylactic efficacy and to reduce the development of the viral resistance. In this work, we studied the prophylactic utility of various antivirals for different sexual transmission modes. In the future, a similar analysis for the intravenous transmission mode (intravenous drug users) can be pursued, which is a major transmission mode in a number of countries [286]. Furthermore, the framework can be used to investigate the impact of treatment-as-prevention in conjunction with PrEP and to develop tailored deployment strategies that considers various contextual factors such as risk behaviour, HIV-1 prevalence, transmission mode and resource-availability. This is of particular importance, because these strategies are complementary to each other and are likely to act synergistically.

Deutsche Zusammenfassung

Die HIV-Epidemie ist nach wie vor ein globales Problem. Während die Suche nach einer Heilung und einem Impfstoff weitergeht, hat sich das Hauptaugenmerk auf antiretrovirale Präventionsstrategien zur Eindämmung der Epidemie gelegt. Eine solche Strategie ist die sogenannte Präexpositionsprophylaxe (PrEP), die kürzlich von UNAIDS als eine der fünf Säulen zur Prävention identifiziert wurde. Dabei ist Truvada das einzige für PrEP zugelassen Medikament. Obwohl der Einsatz von Truvada Erfolge gezeigt hat, bestehen einige Einschränkungen. Eine Reihe neuartiger Wirkstoffe und behandlungserprobter antiviraler Mittel, die noch nicht zur PrEP Behandlung eingesetzt werden, könnten diese Einschränkungen bewältigen.

Die große Aufgabe besteht darin, unter diesen Wirkstoffen potenzielle PrEP Kandidaten ausfindig zu machen und Einsatzstrategien zu entwickeln. Präklinische Experimente liefern hierbei nicht genügend Ergebnisse um ein Kandidaten-Screening vorzunehmen und klinische Studien sind ethisch problematisch und sehr kostspielig, da Tausende von Personen über mehrere Jahre hinweg beobachtet und untersucht werden müssen. Als Hilfestellung haben wir ein Systempharmakologie-Framework entwickelt, welches es ermöglicht, den prophylaktischen Nutzen von antiviralen Medikamenten zu bestimmen, Kandidaten zu priorisieren und Einsatzstrategien zu entwerfen. Um ein solches Framework zu entwickeln müssen verschiedene Modellierungs- und die Simulationensprobleme gelöst werden, da bei der PrEP komplexe Prozesse verschiedene Größenordnungen (Multiskala) involviert sind. Das Framework integriert flexibel Prozesse: (1) molekularen Interaktionen zwischen dem Medikament und den viralen Enzymen auf der Mikroskalenebene (2) antivirale Pharmakokinetik, Pharmakodynamik (viraler Replikationszyklus) auf den Mesoskalen- und Makroskalenebenen und (3) populationsebene Prozesse wie virale Exposition und die Infektionswahrscheinlichkeit nach vermehrter viralen Expositionen wie in klinischen Studien.

Eine der größten algorithmischen Herausforderungen, die in dieser Arbeit bewältigt wurde, ist die Quantifizierung der Infektionswahrscheinlichkeit. Wir haben mit Hilfe der Theorie des Verzweigungsprozesses die Formeln für eine zeitkonstante Wirkstoffkonzentration am Wirkort abgeleitet. Für die zeitvariable Wirkstoffkonzentration am Wirkort haben wir eine chemische Master-Gleichung mit reduziertem Zustand eingeführt und einen stochastischen Algorithmus (EXTRANDE) adaptiert, die das Problem der Dimensionalität der chemische Master-Gleichung umgehen.

Das Framework ermöglicht es präklinisches Wissen in Parameter klinischer Relevanz zu übersetzen. Dabei hilft es unnötige klinische Studien zu vermeiden, die nicht nur Geld und Zeit kosten, sondern auch das Risiko bergen, dass Menschen Schaden nehmen. Mithilfe dieses Frameworks haben wir alle bisherigen für die HIV-behandlung zugelassenen Medikamenten zum Präventionszweck überprüft. Wir haben die komplementären Rollen von Tenofovir Disoproxil Fumarate and Emtricitabine für PrEP erklärt. Darüber hinaus haben wir einige kostengünstige Alternative (Lamivudine, Nevirapine und Efavirenz) zu Truvada für eine weitere Überprüfung vorgeschlagen. Außerdem hat unsere Analyse gezeigt, dass Dolutegravir Truvada nicht unterlegen ist.

Selbständigkeitserklärung

Hiermit versichere ich, dass ich die von mir eingereichte Dissertation selbständig verfasst habe. Alle Hilfsmittel, wie Publikation, Bücher oder Webseiten, wurden in Literaturverzeichnis angegeben und Zitate aus fremden Arbeiten sind als solche gekennzeichnet. Diese Arbeit wurde in gleicher oder ähnlicher Form bisher in keinem anderen Promotionsverfahren eingereicht und auch nicht veröffentlicht.

Berlin, den 26. Juli 2018

Sulav Duwal

APPENDIX A: Viral dynamics parameters

Param.	Value	Ref.	Param.	Value	Ref.
λ_T	$2{\cdot}10^9$	[287]	λ_M	$6.9{\cdot}10^7$	[288]
δ_T, δ_{T_1}	0.02	[288]	δ_M, δ_{M_1}	0.0069	[288]
δ_{T_2}	1	[289]	δ_{M_2}	0.09	[83]
δ_{T_L}	10^{-4}	[290, 291]	ς	10^{-3}	[291]
$\delta_{PIC,T}$	0.35	[192, 292]	$\delta_{PIC,M}$	0.0035	[83]
k_T	0.35	[192]	k_M	0.07	[83]
$\beta_T(\varnothing)$	$8{\cdot}10^{-12}$	[82]	$\beta_M(\varnothing)$	10^{-14}	[83]
$\widehat{N}_T$	1000	[288]	$\widehat{N}_M$	100	[288]
CL(infected)	23	[289]	CL(naive)	2.3	[210, 212]
$b \cdot q \cdot \rho_{PR}$	0.67	[83]	ℓ	$8 \cdot 10^{-6}$	[291]
ρ_{rev}	0.5	[192]			

Table A.1: **Parameters used for the viral model.** All parameters refer to the absence of drug treatment ϕ. All parameters in units [1/day], except ρ_{rev} and $b \cdot q \cdot \rho_{PR}$ (unit less). $N_{T/M} = b \cdot q \cdot \rho_{PR} \cdot \widehat{N}_{T/M}$ [83]. Adapted from articles [83, 84, 88].

APPENDIX B: IC_{50} correction accounting protein binding

Here, we derive a formula to correct the IC_{50} determined in a single round infectivity assay for drug-classes other than NRTIs for *in vivo* use (target-process inhibition)[I].

The Emax model requires two parameters: a hill coefficient m and an 50% inhibitory concentration IC_{50}. These two parameters are usually measured *ex vivo* using single-round $CD4^+$ cell infection assays in 96-well plates supplemented with 50 % human serum for the majority of clinically utilized antivirals [87]. In these assays, the IC_{50} corresponds to the *total* (protein *bound* + *unbound*) concentration of the drug. According to the free drug hypothesis [194] that the available concentrations at the target-site correspond to their *unbound* moieties [195, 196]. For CRAs, the target-site is extracellular, while it is the intracellular space of the target-cells for NNRTIs, InIs and PIs. All analyzed NNRTIs, InIs and PIs displays physicochemical attributes that enable the *unbound* drug to rapidly cross cellular membranes, generating an equilibrium between the *unbound* drug on either side of the cellular membrane [197]. However, since the *unbound* fraction $f_{u,\text{assay}}$ in the assay is different to the physiological *unbound* fraction $f_{u,\text{plasma}}$, the measured IC_{50} value needs to be adjusted or scaled. This adjustment is particularly relevant to some highly protein bound drugs (> 90% protein bound, see [196] for an overview).

IC_{50} value correction for protein binding

The fraction of unbound drug $f_{u,\text{plasma}}$ in the blood plasma is given by

$$f_{u,\text{plasma}} = \frac{K_d}{K_d + [PR]} \tag{B.1}$$

where K_d denotes the dissociation constant of the drug from serum proteins and $[PR]$ denotes the concentration of serum proteins. The above equation can be reformulated to obtain

$$\frac{K_d}{[PR]} = \frac{f_{u,\text{plasma}}}{1 - f_{u,\text{plasma}}} \tag{B.2}$$

The single-round infectivity assay is supplemented with 50 % human serum. Thus, the Eqn (B.1) for the unbound fraction of drug in the assay $f_{u,assay}$ we have

$$f_{u,assay} = \frac{K_d}{K_d + [PR]/2}. \tag{B.3}$$

Using eqs (B.2)–(B.3) the relation between the unbound fraction in the assay $f_{u,assay}$ and the

[I]The derivations in this appendix can be found in the supplementary note of Duwal et al. [27].

plasma plasma $f_{u,\text{plasma}}$ is given by

$$\begin{aligned} f_{u,assay} &= \frac{K_d/[PR]}{K_d/[PR] + 1/2} \\ &= \frac{\dfrac{f_{u,\text{plasma}}}{1 - f_{u,\text{plasma}}}}{\dfrac{f_{u,\text{plasma}}}{1 - f_{u,\text{plasma}}} + \dfrac{1}{2}} \\ &= \frac{2 \cdot f_{u,\text{plasma}}}{f_{u,\text{plasma}} + 1}. \end{aligned} \tag{B.4}$$

The IC_{50} for the unbound drug concentrations is computed as [196]:

$$IC_{50}(\text{unbound}) = IC_{50}(\text{total}) \cdot f_u \tag{B.5}$$

From the equation above, we can derive the following

$$\begin{aligned} IC_{50}(\text{unbound}) &= IC_{50,plasma} \cdot f_{u,plasma} = IC_{50,assay} \cdot f_{u,assay} \\ &\Rightarrow IC_{50,plasma} = IC_{50,assay} \cdot \frac{f_{u,assay}}{f_{u,plasma}} \end{aligned} \tag{B.6}$$

Using Eqn (B.4) in Eqn (B.6), we derive

$$IC_{50,plasma} = IC_{50,assay} \cdot \frac{2}{f_{u,\text{plasma}} + 1} \tag{B.7}$$

which provides a way to translate the IC_{50} value from the single-round infectivity assays to the corresponding IC_{50} in human plasma. Note that in the main manuscript, we denoted $IC_{50,plasma}$ by IC_{50}. Table B.1 summarizes protein adjusted IC_{50}, hill coefficient m and fraction bound in blood plasma f_b of all analyzed antivirals.

Class	Name	IC_{50}	(CV)	m	(CV)	$C_{\min}$	$C_{\max}$	f_b	$t_{1/2}$
CRA	MVC	5.06	(290)	0.61	(27.9)	45	557	76$^\diamond$	14$^\diamond$
RTI	EFV	10.7	(16.7)	1.69	(4.73)	5630	12968	99.4 [293]	40$^\diamond$
RTI	NVP	116	(31.2)	1.55	(9.68)	10883	25153	60$^\diamond$	45$^\diamond$
RTI	DLV	336	(44.7)	1.56	(11.5)	10672	27134	98 [294]	5.8$^\diamond$
RTI	ETR	8.59	(16.3)	1.81	(12.7)	688	1617	99.9 [295]	35 [296]
RTI	RPV	7.73	(17.9)	1.92	(10.4)	177	470	99.1$^\diamond$	44.5$^\diamond$
InI	RAL	25.5	(12.1)	1.1	(4.55)	203	3996	83$^\diamond$	9$^\diamond$
InI	EVG	55.6	(43.8)	0.95	(4.21)	301	1661	99$^\diamond$	8.7$^\diamond$
InI	DTG	89.0	(25.3$^+$)	1.3	(15.4$^+$)	2918	8471	98.9$^\diamond$	14.5 [297]
PI	ATV	23.9	(11.8)	2.69	(10.4)	899	6264	86 [298]	7$^\diamond$
PI	APV	262	(12.6)	2.09	(6.70)	2870	14319	90$^\diamond$	7.1$^\diamond$
PI	DRV	45.0	(21.6)	3.61	(8.86)	5081	14783	95 [295]	15$^\diamond$
PI	IDV	130	(11.0)	4.53	(7.94)	1827	12508	60 [299]	1.8$^\diamond$
PI	LPV	70.9	(20.1)	2.05	(5.85)	8757	15602	99 [196]	2.5$^\flat$
PI	NFV	327	(26.8)	1.81	(12.7)	2285	5104	98$^\diamond$	3.5$^\diamond$
PI	SQV	88.0	(9.7)	3.68	(6.25)	897	13282	97 [300]	3.9 [301]
PI	TPV	483	(18.0)	2.51	(14.3)	35598	77585	99.9$^\diamond$	5$^\diamond$

Table B.1: **Pharmacodynamic and pharmacokinetic parameters.** IC_{50} [nM] and m [unit less] values are available from single turnover experiments in primary peripheral blood mononuclear cells supplemented with 50% human serum from Shen et al. [87], Laskey et al. [222] (DTG) and Jilek at al. [302] (MVC). Because some compounds are highly protein bound, IC_{50} values had to be adjusted for protein binding as outlined in the Supplementary Text S3. Indicated values are after protein adjustment. IC_{50} values are reported to be log normal distributed and m values to be normal distributed [87, 302] with respective coefficients of variation $CV = 100 \cdot \sigma/\mu$ [%]. Parameters $C_{\min}$ and $C_{\max}$ refer to the minimum and maximum concentrations in [nM] during chronic administration using the standard dosing regimen, taken from Shen et al. [87] except those for DTG [303], RPV [261] and MVC [260] (150mg twice daily). $t_{1/2}$ – half life of the drug in [hr], f_b – fraction of the drug bound to plasma proteins in [%]. $^+$These values were fixed to the typical parameter distributions observed for all other compounds. $^\diamond$Parameters were taken from Drug Bank when available [304], accession numbers: DB04835, DB00625, DB00238, DB00705, DB08864, DB06817, DB09101, DB08930, DB01072, DB00701, DB01264, DB00224, DB00220, DB00932 or $^\flat$PubChem [305], id: 92727. When parameters were not readily available in these databases, parameters were obtained from the indicated literature source. MVC -maraviroc, EFV -efavirenz, NVP -nevirapine, DLV -delavirine, ETR -etravirine, RPV -rilpivirine, RAL -raltegravir, EVG -elvitegravir, DTG -dolutegravir, ATV -atazanavir, APV -amprenavir, DRV -darunavir, IDV -indinavir, LPV -lopinavir, NFV -nelfinavir, SQV -saquinavir, TPV -tipranavir. Reproduced from Duwal et al. [27].

APPENDIX C: Derivation of extinction and infection probabilities

In this appendix, we present the derivation of the viral extinction and infection probabilities for time-invariant reaction propensities i.e., for a constant target-process inhibition [I].

Markov jump process

A virus can be cleared by immune system or due to an unsuccessful infection attempt. The probability of the path $\widehat{\mathrm{V}} \to *$ is given by

$$\mathbb{P}(y_1 = \mathbf{0} | y_0 = \widehat{\mathrm{V}}) = \frac{a_1}{a_1 + a_4} = \varrho. \tag{C.1}$$

where $\mathbf{0}$ denotes the extinction state $[0, 0, 0]^T$. Similarly, the probability of the path $(\widehat{\mathrm{V}} \to \widehat{\mathrm{T}}_1)$ is given by:

$$\mathbb{P}(y_1 = \widehat{\mathrm{T}}_1 | y_0 = \widehat{\mathrm{V}}) = \frac{a_4}{a_1 + a_4} = \zeta. \tag{C.2}$$

In analogy, we have

$$\mathbb{P}(y_1 = \mathbf{0} | y_0 = \widehat{\mathrm{T}}_1) = \frac{a_2}{a_2 + a_5} = \vartheta\,, \qquad \mathbb{P}(y_1 = \widehat{\mathrm{T}}_2 | y_0 = \widehat{\mathrm{T}}_1) = \frac{a_5}{a_2 + a_5} = \quad \xi \tag{C.3}$$

$$\mathbb{P}(y_1 = \mathbf{0} | y_0 = \widehat{\mathrm{T}}_2) = \frac{a_3}{a_3 + a_6} = \chi\,, \quad \mathbb{P}(y_1 = \widehat{\mathrm{V}} + \widehat{\mathrm{T}}_2 | y_0 = \widehat{\mathrm{T}}_2) = \frac{a_6}{a_3 + a_6} = \quad \gamma \tag{C.4}$$

where Eqn (C.1)–(C.4) define the entries of the transition matrix of the embedded Markov chain. From the conservation of probabilities, we have $\varrho + \zeta = 1$, $\vartheta + \xi = 1$ and $\gamma + \chi = 1$. From the drug-class specific target-process inhibition described in Eqn (7.2)–(7.7) (Chapter 7), it is evident that RTIs and CRAs affect the transition probability ϱ and ζ. Similarly, InIs affect ϑ and ξ and PIs affect γ and χ. Note that all paths of length one (one transition) can be expressed by Eqn. (C.1)–(C.4). For example the probability of the path $\begin{bmatrix} n \\ 0 \\ 1 \end{bmatrix} \to \begin{bmatrix} n+1 \\ 0 \\ 1 \end{bmatrix}$ is given by

$$\mathbb{P}(y_1 = (n+1) \cdot \widehat{\mathrm{V}} \oplus \widehat{\mathrm{T}}_2 \mid y_0 = n \cdot \widehat{\mathrm{V}} \oplus \widehat{\mathrm{T}}_2) \quad = \quad \frac{a_6}{a_3 + a_6} = \gamma \tag{C.5}$$

where $n \in \mathbb{Z}^+$. The probability of an arbitrary path, e.g. $\widehat{\mathrm{V}} \to \widehat{\mathrm{T}}_1 \to \widehat{\mathrm{T}}_2$ can be computed from Eqn. (C.1)–(C.4) applying the fundamental laws of probability

$$\mathbb{P}(y_2 = \widehat{\mathrm{T}}_2 | y_0 = \widehat{\mathrm{V}}) = \mathbb{P}(y_1 = \widehat{\mathrm{T}}_1 | y_0 = \widehat{\mathrm{V}}) \cdot \mathbb{P}(y_2 = \widehat{\mathrm{T}}_2 | y_1 = \widehat{\mathrm{T}}_1) = \zeta \cdot \xi \tag{C.6}$$

[I] The derivations in this appendix can be found in the supplementary note of Duwal et al. [27].

If multiple paths can lead to the particular state of interest, the probability is computed by summing over all possible paths. To demonstrate, let us consider the probability that the virus goes extinct in the first replication cycle $\mathbb{P}(y_r = \mathbf{0}|y_0 = \widehat{\mathrm{V}})$, i.e., starting from a single virus, we consider the paths $\widehat{\mathrm{V}} \to \mathbf{0}$, $\widehat{\mathrm{V}} \to \widehat{\mathrm{T}}_1 \to \mathbf{0}$ and $\widehat{\mathrm{V}} \to \widehat{\mathrm{T}}_1 \to \widehat{\mathrm{T}}_2 \to \mathbf{0}$ which is

$$\begin{aligned}\mathbb{P}(y_r = \mathbf{0}|y_0 = \widehat{\mathrm{V}}) &= \mathbb{P}(y_1 = \mathbf{0}|y_0 = \widehat{\mathrm{V}}) \\ &+ \mathbb{P}(y_2 = \mathbf{0}|y_1 = \widehat{\mathrm{T}}_1) \cdot \mathbb{P}(y_1 = \widehat{\mathrm{T}}_1|y_0 = \widehat{\mathrm{V}}) \\ &+ \mathbb{P}(y_3 = \mathbf{0}|y_2 = \widehat{\mathrm{T}}_2) \cdot \mathbb{P}(y_2 = \widehat{\mathrm{T}}_2|y_1 = \widehat{\mathrm{T}}_1) \cdot \mathbb{P}(y_1 = \widehat{\mathrm{T}}_1|y_0 = \widehat{\mathrm{V}}).\end{aligned}$$

Using the shorthand notation, we get

$$\mathbb{P}(y_r = \mathbf{0}|y_0 = \widehat{\mathrm{V}}) = \varrho + \zeta \cdot \vartheta + \zeta \cdot \xi \cdot \chi \tag{C.7}$$

and in terms of reaction propensities we have

$$\mathbb{P}(y_r = \mathbf{0}|y_0 = \widehat{\mathrm{V}}) = \frac{a_1}{a_1 + a_4} + \frac{a_4}{a_1 + a_4} \cdot \frac{a_2}{a_2 + a_5} + \frac{a_4}{a_1 + a_4} \cdot \frac{a_5}{a_2 + a_5} \cdot \frac{a_3}{a_3 + a_6}. \tag{C.8}$$

Next, we can compute the probability that $n > 0$ progeny viruses are produced in the first replication cycle, i.e., starting from a single virus, all paths that reach the late infected T-cell stage $\widehat{\mathrm{V}} \to \widehat{\mathrm{T}}_1 \to \widehat{\mathrm{T}}_2$, then R_6 (virus release) fire reaction(see Eqn (7.7) in Chapter 7) n times before finally reaction R_3 (clearance of late infected T-cell) occurs.

$$\begin{aligned}\mathbb{P}(y_r = n \cdot \widehat{\mathrm{V}}|y_0 = \widehat{\mathrm{V}}) &= \mathbb{P}(y_1 = \widehat{\mathrm{T}}_1|y_0 = \widehat{\mathrm{V}}) \times \\ &\quad \mathbb{P}(y_2 = \widehat{\mathrm{T}}_2|y_1 = \widehat{\mathrm{T}}_1) \times \\ &\quad \prod_{i=0}^{n-1} \mathbb{P}(y_{3+i} = \widehat{\mathrm{T}}_2 + (i+1) \cdot \widehat{\mathrm{V}} \mid y_{2+i} = \widehat{\mathrm{T}}_2 + i \cdot \widehat{\mathrm{V}}) \times \\ &\quad \mathbb{P}(y_{n+3} = n \cdot \widehat{\mathrm{V}}|y_{n+2} = \widehat{\mathrm{T}}_2 + n \cdot \widehat{\mathrm{V}})\end{aligned} \tag{C.9}$$

and in shorthand notation

$$\mathbb{P}(y_r = n \cdot \widehat{\mathrm{V}}|y_0 = \widehat{\mathrm{V}}) = \zeta \cdot \xi \cdot \gamma^n \cdot \chi. \tag{C.10}$$

Closed-form solution for the extinction probability

The probability that n infectious viruses within a target-cell environment go extinct is given by

$$\mathcal{E}(y_0 = n \cdot \widehat{\mathrm{V}}) = (\mathcal{E}(y_0 = \widehat{\mathrm{V}}))^n, \tag{C.11}$$

under the assumption of statistical independence (assuming that the competition for target cells is negligible during the onset of infection). The extinction probabilities for parent- and progeny virus remain identical since the reaction rates do not change when the target-process inhibition is constant. The term $\mathcal{E}$ can be written as

$$\begin{aligned}\mathcal{E}(y_0 = \widehat{\mathrm{V}}) &= \sum_{i=0}^{\infty} \mathbb{P}(y_r = i \cdot \widehat{\mathrm{V}}|y_0 = \widehat{\mathrm{V}}) \cdot \mathcal{E}(y_r = i \cdot \widehat{\mathrm{V}}) \\ &= \sum_{i=0}^{\infty} \mathbb{P}(y_r = i \cdot \widehat{\mathrm{V}}|y_0 = \widehat{\mathrm{V}}) \cdot \mathcal{E}(y_r = \widehat{\mathrm{V}})^i\end{aligned} \tag{C.12}$$

where $\mathcal{E}(y_r = i \cdot \widehat{\mathrm{V}})$ denotes the probability of virus extinction when i viruses were produced in the first replication cycle and where we used eqn. (C.11) in the second equality. Since we study the

eventual extinction ($t \to \infty$) and the entries of the transition matrix in our discrete-time process are constant, the equality $\mathcal{E}(y_0 = \widehat{\mathrm{V}}) = \mathcal{E}(y_r = \widehat{\mathrm{V}})$ holds. For brevity we will use $\theta = \mathcal{E}(y_0 = \widehat{\mathrm{V}})$ henceforth in the derivation below:

$$\begin{aligned}
\theta &= \sum_{i=0}^{\infty} \mathbb{P}(y_r = i \cdot \widehat{\mathrm{V}} | y_0 = \widehat{\mathrm{V}}) \cdot \theta^i, \\
&= \mathbb{P}(y_r = \mathbf{0} \cdot \widehat{\mathrm{V}} | y_0 = \widehat{\mathrm{V}}) \cdot \theta^0 + \sum_{i=1}^{\infty} \mathbb{P}(y_r = i \cdot \widehat{\mathrm{V}} | y_0 = \widehat{\mathrm{V}}) \cdot \theta^i, \\
&= (\varrho + \zeta \cdot \vartheta + \zeta \cdot \xi \cdot \chi) + \sum_{i=1}^{\infty} \zeta \cdot \xi \cdot \gamma^i \cdot \chi \cdot \theta^i, \quad \text{(using Eqn (C.7) and Eqn (C.10))} \\
&= \varrho + \zeta \cdot \vartheta + \zeta \cdot \xi \cdot \chi + \zeta \cdot \xi \cdot \chi \cdot \left(\sum_{i=1}^{\infty} \gamma^i \cdot \theta^i \right), \\
&= \varrho + \zeta \cdot \vartheta + \zeta \cdot \xi \cdot \chi \cdot \left(\sum_{i=0}^{\infty} \gamma^i \cdot \theta^i \right), \\
&= \varrho + \zeta \cdot \vartheta + \zeta \cdot \xi \cdot \chi \cdot \left(\frac{1}{1 - \gamma \cdot \theta} \right), \qquad \text{(C.13)}
\end{aligned}$$

where we used the solution of the geometric series, noticing that $\gamma \cdot \theta < 1$ as both terms γ and θ are probabilities. This shows that the extinction probability is the solution of the following quadratic problem:

$$\begin{aligned}
\gamma \cdot \theta^2 - (1 + (\varrho + \zeta \cdot \vartheta) \cdot \gamma) \cdot \theta + (\varrho + \zeta \cdot \vartheta + \zeta \cdot \xi \cdot \chi) &= 0 \\
\Rightarrow \theta^2 - \left(\frac{1 + (\varrho + \zeta \cdot \vartheta) \cdot \gamma}{\gamma} \right) \cdot \theta + \left(\frac{1 + (\varrho + \zeta \cdot \vartheta) \cdot \gamma}{\gamma} - 1 \right) &= 0
\end{aligned}$$

where we used $\varrho + \zeta = 1$, $\vartheta + \xi = 1$ and $\gamma + \chi = 1$ in the summand on the right side of the last equation. The possible solutions for θ of above quadratic problem are:

$$\theta_{1/2} = \frac{1}{2} \cdot \left(\left(\frac{1 + (\varrho + \zeta \cdot \vartheta) \cdot \gamma}{\gamma} \right) \pm \left(\frac{1 + (\varrho + \zeta \cdot \vartheta) \cdot \gamma}{\gamma} - 2 \right) \right). \qquad \text{(C.14)}$$

The first solution $\theta_1 = 1$ is trivial, i.e. extinction is certain $\mathcal{E}(y_0 = \widehat{\mathrm{V}}) = 1$, whereas the second solution

$$\theta_2 = \left(\frac{1 + (\varrho + \zeta \cdot \vartheta) \cdot \gamma}{\gamma} \right) - 1$$

provides some additional insights into the extinction probability. Rearranging the terms, we get:

$$\begin{aligned}
\theta_2 &= \tfrac{1}{\gamma} - 1 + (\varrho + \zeta \cdot \vartheta) \\
&= \tfrac{1-\gamma}{\gamma} + (\varrho + \zeta \cdot \vartheta) \\
&= \varrho + \zeta \cdot \vartheta + \tfrac{\chi}{\gamma} \qquad \text{(C.15)}
\end{aligned}$$

where we used $\gamma + \chi = 1$. The first part $(\varrho + \zeta \cdot \vartheta)$ is the probability that the viral replication cycle does not reach the late infected stage T_2 and the second part represents the odds of T_2 dying instead of producing virus progeny (the odds of R_3 firing rather than R_6; the inverse of the average number of viruses being produced once stage T_2 has been reached). We have

$$\chi / \gamma = a_3 / a_6 = \frac{\delta_{\mathrm{T}_2}}{\mathrm{N}_\mathrm{T}}$$

as introduced in Eqn. (C.4). It is evident from here, that both solutions for the extinction probability are valid and that

$$\mathcal{E}(y_0 = \widehat{\mathrm{V}}) = \theta = \min\left(1, (\varrho + \zeta \cdot \vartheta) + \frac{\chi}{\gamma}\right). \tag{C.16}$$

Relation to the reproductive number

The reproductive number R_0 denotes the average number of viruses produced from a single founder virus [220].

$$\begin{aligned} R_0 &= \sum_{i=1}^{\infty} \mathbb{P}(y_r = i \cdot \widehat{\mathrm{V}} | y_0 = \widehat{\mathrm{V}}) \cdot i, \\ &= \zeta \cdot \xi \cdot \chi \cdot \sum_{i=1}^{\infty} \gamma^i \cdot i, \\ &= \zeta \cdot \xi \cdot \chi \cdot \frac{\gamma}{(1-\gamma)^2}, \\ &= \frac{\zeta \cdot \xi \cdot \gamma}{\chi}, \\ &= \frac{a_4}{a_1 + a_4} \cdot \frac{a_5}{a_2 + a_5} \cdot \frac{a_6}{a_3}, \end{aligned}$$

where we used $(1 - \gamma) = \chi$ in the second last equation.

The infection probability for a single virus inoculum can be written as a function of R_0, i.e.

$$\begin{aligned} \mathcal{I}(y_0 = \widehat{\mathrm{V}}) &= 1 - \mathcal{E}(y_0 = \widehat{\mathrm{V}}) = \max\left(0, \zeta \cdot \xi \left(1 - \frac{1}{R_0}\right)\right), \\ &= \max\left(0, \frac{a_4}{a_1 + a_4} \cdot \frac{a_5}{a_2 + a_5}\left(1 - \frac{1}{R_0}\right)\right). \end{aligned} \tag{C.17}$$

The product $\zeta \cdot \xi$ denotes the bottlenecking process of reaching a productive compartment (productively infected cells).

Other compartments

Next, we derive the extinction probability given a single early- or late infected cell T_1 and T_2 respectively. Let the term $\mathcal{E}(y_0 = \widehat{\mathrm{T}}_1)$ and $\mathcal{E}(y_0 = \widehat{\mathrm{T}}_2)$ be the respective extinction probabilities for a single T_1 or T_2 cell. These probabilities relate to $\mathcal{E}(y_0 = \widehat{\mathrm{V}}) < 1$ as follows:

$$\begin{aligned} \mathcal{E}(y_0 = \widehat{\mathrm{T}}_1) &= \min\left(1, \vartheta + \xi \cdot \chi \cdot \left(\frac{1}{1 - \gamma \cdot \mathcal{E}(y_0 = \widehat{\mathrm{V}})}\right)\right), \\ &= \min\left(1, 1 - \xi \cdot \left(1 - \frac{1}{R_0}\right)\right), \\ &= \min\left(1, 1 - \frac{a_5}{a_2 + a_5} \cdot \left(1 - \frac{1}{R_0}\right)\right) \end{aligned} \tag{C.18}$$

$$\Leftrightarrow \mathcal{I}(y_0 = \widehat{\mathrm{T}}_1) = \max\left(0, \frac{a_5}{a_2 + a_5} \cdot \left(1 - \frac{1}{R_0}\right)\right) \tag{C.19}$$

and

$$\begin{aligned} \mathcal{E}(y_0 = \widehat{\mathrm{T}}_2) &= \min\left(1, \chi \cdot \left(\frac{1}{1 - \gamma \cdot \mathcal{E}(y_0 = \widehat{\mathrm{V}})}\right)\right), \\ &= \min\left(1, \frac{1}{R_0}\right), \qquad \text{(C.20)} \\ \Leftrightarrow \mathcal{I}(y_0 = \widehat{\mathrm{T}}_2) &= \max\left(0, 1 - \frac{1}{R_0}\right). \qquad \text{(C.21)} \end{aligned}$$

APPENDIX D: Pseudo-codes and performance of SSA

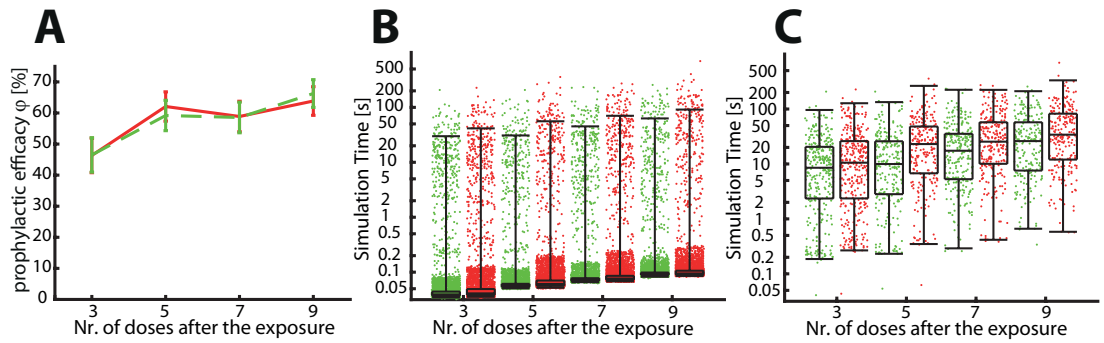

Figure D.1: **Results and performances comparison of SSA for PEP with DTG**. **A**: prophylactic efficacy for PEP strategy initiated 24 hours after a viral challenge where 3, 5, 7 and 9 daily doses of 50mg DTG are taken. **B**: Simulation run-time with EXTRANDE simulations (green) vs. an integral based method (red). **C**: Run-times of simulations where infection occurred. Median runtimes (sec) per infection simulation for EXTRANDE vs. the integral-based method were 8.524 vs. 10.548, 9.976 vs. 23.021, 17.402 vs. 25.454, 26.065 vs. 34.116 when 3, 5, 7 and 9 consecutive PEP doses are taken. Reproduced from Duwal et al. [26].

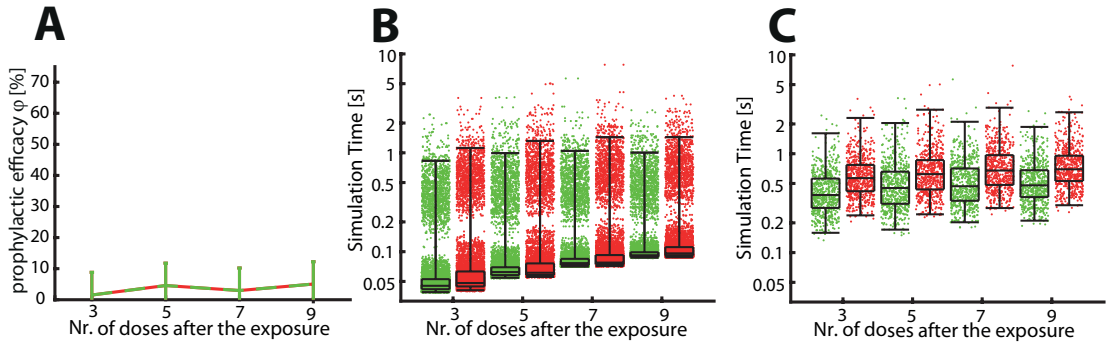

Figure D.2: **Results and performances comparison of SSA for PEP with TDF**. **A**: prophylactic efficacy for PEP strategies initiated 12 hours after a viral challenge where 3, 5, 7 and 9 daily doses (300mg TDF) are taken. **B**: Simulation run-time with EXTRANDE simulations (green) vs. an integral-based method (red). **C**: Runtimes for those simulations where infection occurred. Median runtimes (sec) per infection simulation for EXTRANDE vs. the integral based method were 0.382 vs. 0.566, 0.450 vs. 0.622, 0.469 vs. 0.676, 0.479 vs. 0.696 when 3, 5, 7 and 9 consecutive PEP doses are taken.

Precomputation :
Compute target-site pharmacokinetic profile D_s for $s \in [0, T]$
Compute $D_{max,s}$ profile for $s \in [0, T]$
Initialization :
$t = 0$ #Initial time of the system
$Y_t = Y_0$ #Initial state of the stochastic system
while *true* **do**
  #Determine the upper bound for the sum of reaction propensities
  $B = a_0(Y_t, \varnothing) = \sum_{k=1}^{|\mathcal{R}_S|} a_k(Y_t, \varnothing)$ #Sum of reaction propensities in absence of antivirals
  #Generate putative reaction time i.e $\tau \sim \text{Exp}(1/B)$:
  $u_1 \sim \mathcal{U}(0, 1)$ #Sample from a uniform distribution
  $\tau \leftarrow \frac{1}{B} \cdot \log\left(\frac{1}{u_1}\right)$ #Transformation to an exponential distribution
  $t \leftarrow t + \tau$ #Update time
  $a_0 \leftarrow \sum_{k=1}^{|\mathcal{R}_S|} a_k(Y_t, D_t)$ #Sum of all stochastic reaction propensities at time t
  $u_2 \sim \mathcal{U}(0, 1)$ #Sample from a uniform distribution
  if $a_0 \geq B \cdot u_2$ **then**
    #'Acceptance Step' - a reaction fires changing the state.
    #Choose the reaction, i.e.
    the smallest positive integer j such that $\sum_{k=1}^{j} a_k(Y_t, D_t) \geq B \cdot r_2$
    if *reaction* R_4 *or* R_5 *is chosen* **then**
      $u_3 \sim \mathcal{U}(0, 1)$
      if $u_3 \leq p_{M|a_4}$, *respectively* $u_3 \leq p_{L|a_5}$ **then**
        #a long lived/latently infected cell emerged.
        Stop the simulation
      end
    end
    $Y_t \leftarrow Y_t + v_j$ #Update the state of the system
    if $Y_t = \mathbf{0}$ **then**
      #Extinction event - the trajectory has reached the absorbing extinction state.
      Stop the simulation
    else
      #Compute the extinction probability of state Y_t and drug concentration $D_{max,t}$
      Compute D_{max} for the current time t
      if $\mathcal{E}(Y_t, D_{max,t}) < \varepsilon$ **then**
        #Infection event
        Stop the simulation
      else
        #The trajectory at time t is within the extinction simplex.
      end
    end
  else
    #'Rejection Step' - Extra reaction fires without changing the state.
  end
end

Algorithm 1: Adapted **Ext**ra **R**eaction **A**lgorithm for **N**etworks in **D**ynamic **E**nvironments (EXTRANDE). Reproduced from the supplementary note of Duwal et al. [26].

Y_0 #Initial state of the stochastic system
Precomputation :
Compute target-site pharmacokinetic profile D_s for $s \in [0, T]$
Compute $D_{max,s}$ profile for $s \in [0, T]$
Initialization :
$t = 0$ #Initial time of the system
$Y_t = Y_0$ #Initial state of the stochastic system
while *true* **do**
    #Generate the time to next reaction:
    $u_1 \sim \mathcal{U}(0, 1)$ #Sample from a uniform distribution
     #Transformation to an exponential distribution
    Solve the system of ODEs with initial value $A_{0,t} = 0$ at time t with

$$\frac{\mathrm{d}}{\mathrm{d}s} A_{0,s} = \sum_{k=1}^{|\mathcal{R}_S|} a_k(Y_s, D_s)$$

     until $s = t + \Delta t$ such that $A_{0,t+\Delta t} = u_1$
     #Time to the next reaction
    $\tau \leftarrow \Delta t$
    $t \leftarrow t + \tau$ #Update time
    #Choose the next reaction:
    $a_0 \leftarrow \sum_{k=1}^{|\mathcal{R}_S|} a_k(Y_t, D_t)$ #Sum of all stochastic reaction propensities at time t
    $u_2 \sim \mathcal{U}(0, 1)$ #Sample from a uniform distribution
    #Choose the reaction, i.e.
    the smallest positive integer j such that $\sum_{k=1}^{j} a_k(Y_t, D_t) \geq a_0 \cdot u_2$
    if *reaction* R_4 *or* R_5 *is chosen* **then**
        $u_3 \sim \mathcal{U}(0, 1)$
        if $u_3 \leq p_{M|a_4}$, *respectively* $u_3 \leq p_{L|a_5}$ **then**
            #a long lived/latently infected cell emerged.
            Stop the simulation
        end
    end
    $Y_t \leftarrow Y_t + v_j$ #Update the state of the system
    if $Y_t = \mathbf{0}$ **then**
        #Extinction event - the trajectory has reached the absorbing extinction state.
        Stop the simulation
    else
        #Compute the extinction probability of state Y_t and drug concentration $D_{max,t}$
        Compute D_{max} for the current time t
        if $\mathcal{E}(Y_t, D_{max,t}) < \varepsilon$ **then**
            #Infection event
            Stop the simulation
        else
            #The trajectory at time t is within the extinction simplex.
        end
    end
end

Algorithm 2: Adapted integral-based SSA [101] for estimating the infection/extinction probability for time-varying drug effects.

APPENDIX E: Clinical trial efficacy

A clinical trial consists typically of two arms: A treatment arm and a placebo arm, which are followed for the trials' duration[I]. At the end of the trial, reduction in the incidence rate in the treatment arm in comparison to the placebo arm is computed. Incidence rates is the number of infections or new cases within the trial duration divided by the follow-up time. The trial efficacy ω is measured as shown below [13, 231, 258, 264]:

$$\omega(\mathcal{S}) = 1 - \frac{\text{Incidence rate in the PrEP strategy arm}}{\text{Incidence rate in the placebo arm}}. \tag{E.1}$$

Let $\#\text{inf}_{\mathcal{S}}$ and $\#\text{inf}_{\varnothing}$ denote the number of infected individuals in the PrEP strategy- $\mathcal{S}$ and placebo $\varnothing$ arm respectively. Let $T_{F,\mathcal{S}}$ and $T_{F,\varnothing}$ denote the follow-up duration in person-years in the PrEP strategy- and placebo arm respectively. Let $n_{i,\varnothing}$ and $n_{i,\mathcal{S}}$ denote the number of individuals in the placebo- and in the strategy arm respectively. We can express the trial efficacy as given below

$$\omega(\mathcal{S}) = 1 - \left(\frac{\#\text{inf}_{\mathcal{S}}}{T_{F,\mathcal{S}}}\right) \cdot \left(\frac{\#\text{inf}_{\varnothing}}{T_{F,\varnothing}}\right)^{-1}. \tag{E.2}$$

Next, we will replace the number of infected individuals in trial arms by the expected number of infected persons in the trial. For a sufficiently large cohort, the number of infected persons will be approach the expected number owing to the law of large numbers. Typically, we have $T_{F,\mathcal{S}} \approx T_{F,\varnothing}$ in clinical trials. Hence, we can write

$$\omega(\mathcal{S}) = 1 - \left(\frac{\mathbb{E}_{\mathcal{S}}(\#\text{inf})}{T_{F,\mathcal{S}}}\right) \cdot \left(\frac{\mathbb{E}_{\varnothing}(\#\text{inf})}{T_{F,\varnothing}}\right)^{-1} \approx 1 - \frac{\mathbb{E}_{\mathcal{S}}(\#\text{inf})}{\mathbb{E}_{\varnothing}(\#\text{inf})}. \tag{E.3}$$

Let $\text{N}_{c,\varnothing}$ and $\text{N}_{c,\mathcal{S}}$ be the average number of viral exposures per month per individual in the placebo- and treatment arms respectively.

Given a trial duration of T months (note that $T_{F,\varnothing} \approx T_{F,\mathcal{S}}$), the expected number of infected individuals in the placebo- and treatment arm are $n_{i,\varnothing} \cdot \left(1 - (1 - \mathbb{P}(\text{trans}, \varnothing))^{T \cdot \text{N}_{c,\varnothing}}\right)$ and $n_{i,\mathcal{S}} \cdot \left(1 - (1 - \mathbb{P}(\text{trans}, \mathcal{S}))^{T \cdot \text{N}_{c,\mathcal{S}}}\right)$ respectively. Usually the number of individuals in both arms are also roughly the same size ($n_{i,\varnothing} \approx n_{i,\mathcal{S}}$). This allows us following simplification

$$\begin{aligned} \omega(\mathcal{S}) &\approx 1 - \frac{n_{i,\mathcal{S}} \cdot \left(1 - (1 - \mathbb{P}(\text{trans}, S))^{T \cdot \text{N}_S}\right)}{n_{i,\varnothing} \cdot \left(1 - (1 - \mathbb{P}(\text{trans}, \varnothing))^{T \cdot \text{N}_{\varnothing}}\right)}, \\ &\approx 1 - \frac{\left(1 - (1 - \mathbb{P}(\text{trans}, S))^{T \cdot \text{N}_S}\right)}{\left(1 - (1 - \mathbb{P}(\text{trans}, \varnothing))^{T \cdot \text{N}_{\varnothing}}\right)}. \end{aligned} \tag{E.4}$$

Rearranging Eqn (9.4) for the prophylactic efficacy per exposure, we get

$$\mathbb{P}(\text{trans}, S) = \mathbb{P}(\text{trans}, \varnothing) \cdot (1 - \psi(\mathcal{S})) \tag{E.5}$$

[I]The derivations in this appendix is based on the supplementary note 5 in the article [25].

where ψ is the prophylactic efficacy per exposure. Replacing the above Eqn (E.5) in Eqn (E.4), we get

$$1 - \omega(\mathcal{S}) = \frac{1 - (1 - \mathbb{P}(\text{trans}, \varnothing) \cdot (1 - \psi(\mathcal{S})))^{T \cdot \mathrm{N}_S}}{1 - (1 - \mathbb{P}(\text{trans}, \varnothing))^{T \cdot \mathrm{N}_\varnothing}}. \tag{E.6}$$

which shows the dependence of clinical trial efficacy ($\omega(\mathcal{S})$) on the duration of the clinical trial (T), the prophylactic efficacy of a strategy per exposure $\psi(\mathcal{S})$ and the number of unprotected sex acts with an infected individual (exposures) in the treatment arm $\mathrm{N}_{c,\mathcal{S}}$ and the placebo arm $\mathrm{N}_{c,\varnothing}$ respectively.

Eqn (E.6) can be used to assess the influence of **risk compensation** on the long-term efficacy, i.e. when the number of risky sex acts in the treatment arm is higher than in the placebo arm $\mathrm{N}_{c,\mathcal{S}} > \mathrm{N}_{c,\varnothing}$. Another important implication from Eqn (E.6) is the dependence of the trial efficacy on the trial duration. For instance, two trials using the same treatment PrEP strategy (i.e. same treatment efficacy ψ) evaluated over different trial durations (or alternatively evaluated in different risk groups) would result in different trial efficacy estimates. Thus, for an unbiased comparison, it is advisable to compute the treatment efficacy ψ from the clinical trial efficacy $\omega(\mathcal{S})$ estimate. Rearranging Eqn (E.6) gives the following relation to compute prophylactic efficacy per exposure of an intervention given the estimate of trial efficacy.

$$1 - \psi(\mathcal{S}) = \frac{1 - \sqrt[T \cdot \mathrm{N}_{c,\mathcal{S}}]{(1 - \mathbb{P}(\text{trans}, \varnothing))^{\mathrm{N}_{c,\varnothing} \cdot T} + \omega(\mathcal{S}) - \omega(\mathcal{S}) \cdot (1 - \mathbb{P}(\text{trans}, \varnothing))^{\mathrm{N}_{c,\varnothing} \cdot T}}}{\mathbb{P}(\text{trans}, \varnothing)}. \tag{E.7}$$

Let us hypothetically consider the case where there is exactly one exposure in both arms. In this case, we have

$$\mathrm{N}_{c,\varnothing} \cdot T = \mathrm{N}_{c,\mathcal{S}} \cdot T = 1$$

and the identity

$$1 - \psi(\mathcal{S}) = 1 - \omega(\mathcal{S})$$

which follows from Eqn (E.7). In all other cases, where $\mathrm{N}_{c,\mathcal{S}} \cdot T \geq \mathrm{N}_{c,\varnothing} \cdot T \geq 1$, we have $\omega(\mathcal{S}) \leq \psi(\mathcal{S})$, i.e. the trial efficacy may under predict the PrEP efficacy *per exposure* or stated inversely, the PrEP efficacy *per exposure* over predicts risk prevention following multiple viral challenges, and in the case of risk compensation.

Bibliography

[1] UNAIDS Global HIV Statistics. 2017 [accessed on 30-April-2018]. Available from: http://www.unaids.org/sites/default/files/media_asset/UNAIDS_FactSheet_en.pdf;.

[2] UNAIDS statistics on HIV-1 and AIDS. 2017 [accessed on 18-March-2018]. Available from: http://www.unaids.org/sites/default/files/media_asset/20170720_Data_book_2017_en//.pdf;.

[3] Palmisano L, Vella S. A brief history of antiretroviral therapy of HIV infection: success and challenges. Ann Ist Super Sanita. 2011;47(1):44–48.

[4] Trickey A, May MT, Vehreschild JJ, Obel N, Gill MJ, Crane HM, et al. Survival of HIV-positive patients starting antiretroviral therapy between 1996 and 2013: a collaborative analysis of cohort studies. Lancet HIV. 2017;4(8):e349–e356.

[5] Samji H, Cescon A, Hogg RS, Modur SP, Althoff KN, Buchacz K, et al. Closing the gap: increases in life expectancy among treated HIV-positive individuals in the United States and Canada. PloS One. 2013;8(12):e81355.

[6] Hartley O, Martins E, Scurci I. Preventing HIV transmission through blockade of CCR5: rationale, progress and perspectives. Swiss Med Wkly. 2018;148:w14580–w14580.

[7] UN Secretary-General. Uniting for universal access: towards zero new HIV infections, zero discrimination and zero AIDS-related deaths. 2011 [accessed on 18-March-2018]. Available from: http://files.unaids.org/en/media/unaids/contentassets/documents/document/2011/20110331_SG_report_en.pdf;.

[8] Rerks-Ngarm S, Pitisuttithum P, Nitayaphan S, Kaewkungwal J, Chiu J, Paris R, et al. Vaccination with ALVAC and AIDSVAX to prevent HIV-1 infection in Thailand. N Engl J Med. 2009;361(23):2209–2220.

[9] Rolland M, Edlefsen PT, Larsen BB, Tovanabutra S, Sanders-Buell E, Hertz T, et al. Increased HIV-1 vaccine efficacy against viruses with genetic signatures in Env V2. Nature. 2012;490(7420):417.

[10] Hütter G, Nowak D, Mossner M, Ganepola S, Müßig A, Allers K, et al. Long-term control of HIV by CCR5 Delta32/Delta32 stem-cell transplantation. New England Journal of Medicine. 2009;360(7):692–698.

[11] Liu C, Ma X, Liu B, Chen C, Zhang H. HIV-1 functional cure: will the dream come true? BMC Med. 2015;13(1):284.

[12] Allers K, Hütter G, Hofmann J, Loddenkemper C, Rieger K, Thiel E, et al. Evidence for the cure of HIV infection by CCR5Δ32/Δ32 stem cell transplantation. Blood. 2011;117(10):2791–2799.

[13] Cohen MS, Chen YQ, McCauley M, Gamble T, Hosseinipour MC, Kumarasamy N, et al. Prevention of HIV-1 infection with early antiretroviral therapy. N Engl J Med. 2011;365(6):493–505.

[14] Attia S, Egger M, Müller M, Zwahlen M, Low N. Sexual transmission of HIV according to viral load and antiretroviral therapy: systematic review and meta-analysis. AIDS. 2009;23(11):1397–1404.

[15] Duwal S, Winkelmann S, Schütte C, von Kleist M. Optimal Treatment Strategies in the Context of 'Treatment for Prevention' against HIV-1 in Resource-Poor Settings. PLoS Comput Biol. 2015;11(4):e1004200.

[16] Cohen J. Breakthrough of the year. HIV treatment as prevention. Science. 2011;334(6063):1628.

[17] Grant RM, Lama JR, Anderson PL, McMahan V, Liu AY, Vargas L, et al. Preexposure chemoprophylaxis for HIV prevention in men who have sex with men. N Engl J Med. 2010;363(27):2587–2599.

[18] AIDS Vaccine Advocacy Coalition. Pre-Exposure Prophylaxis (PrEP) by the Numbers. 2016 [Accessed 22-Oct-2017] Available from: http://www.avac.org/sites/default/files/resource-files/prep_BTN_aug2016.pdf;.

[19] Carlson JM, Schaefer M, Monaco DC, Batorsky R, Claiborne DT, Prince J, et al. HIV transmission. Selection bias at the heterosexual HIV-1 transmission bottleneck. Science. 2014;345(6193):1254031.

[20] Van Rompay KK. Evaluation of antiretrovirals in animal models of HIV infection. Antiviral Res. 2010;85(1):159–175.

[21] Hendrix CW. Exploring concentration response in HIV pre-exposure prophylaxis to optimize clinical care and trial design. Cell. 2013;155(3):515–518.

[22] Dezzutti CS. Animal and human mucosal tissue models to study HIV biomedical interventions: can we predict success? Journal of the International AIDS Society. 2015;18(1).

[23] Duwal S, von Kleist M. Top-down and bottom-up modeling in system pharmacology to understand clinical efficacy: An example with NRTIs of HIV-1. Eur J Pharm Sci. 2016;94:72–83. doi:10.1016/j.ejps.2016.01.016.

[24] von Kleist M, Metzner P, Marquet R, Schütte C. HIV-1 polymerase inhibition by nucleoside analogs: cellular- and kinetic parameters of efficacy, susceptibility and resistance selection. PLoS Comput Biol. 2012;8(1):e1002359.

[25] Duwal S, Sunkara V, von Kleist M. Multiscale Systems-Pharmacology Pipeline to Assess the Prophylactic Efficacy of NRTIs Against HIV-1. CPT Pharmacometrics Syst Pharmacol. 2016;5(7):377–387.

[26] Duwal S, Dickinson L, Khoo SH, von Kleist M. Hybrid stochastic framework predicts efficacy of prophylaxis against HIV: An example with different dolutegravir prophylaxis schemes. PLoS Comput Biol. 2018;14(6):e1006155.

[27] Duwal S, Dickinson L, Khoo SH, von Kleist M. Mechanistic framework predicts drug-class specific utility of antiretrovirals for HIV prophylaxis. 2018;.

[28] Voliotis M, Thomas P, Grima R, Bowsher CG. Stochastic simulation of biomolecular networks in dynamic environments. PLoS Comput Biol. 2016;12(6):e1004923.

[29] Montagnier L. A history of HIV discovery. Science. 2002;298(5599):1727–1728.

[30] Nowak M, May RM. Virus dynamics: mathematical principles of immunology and virology: mathematical principles of immunology and virology. Oxford University Press, UK; 2000.

[31] Hemelaar J. The origin and diversity of the HIV-1 pandemic. Trends Mol Med. 2012;18(3):182–192.

[32] Faria NR, Rambaut A, Suchard MA, Baele G, Bedford T, Ward MJ, et al. The early spread and epidemic ignition of HIV-1 in human populations. Science. 2014;346(6205):56–61.

[33] Aghokeng AF, Ayouba A, Mpoudi-Ngole E, Loul S, Liegeois F, Delaporte E, et al. Extensive survey on the prevalence and genetic diversity of SIVs in primate bushmeat provides insights into risks for potential new cross-species transmissions. Infect Genet Evol. 2010;10(3):386–396.

[34] Sharp PM, Hahn BH. Origins of HIV and the AIDS pandemic. Cold Spring Harb Perspect Med. 2011;1(1):a006841.

[35] Keele BF, Jones JH, Terio KA, Estes JD, Rudicell RS, Wilson ML, et al. Increased mortality and AIDS-like immunopathology in wild chimpanzees infected with SIVcpz. Nature. 2009;460(7254):515.

[36] Salemi M, de Oliveira T, Soares MA, Pybus O, Dumans AT, Vandamme AM, et al. Different epidemic potentials of the HIV-1B and C subtypes. J Mol Evol. 2005;60(5):598–605.

[37] Sauter D, Schindler M, Specht A, Landford WN, Münch J, Kim KA, et al. Tetherin-driven adaptation of Vpu and Nef function and the evolution of pandemic and nonpandemic HIV-1 strains. Cell Host Microbe. 2009;6(5):409–421.

[38] Gilbert MTP, Rambaut A, Wlasiuk G, Spira TJ, Pitchenik AE, Worobey M. The emergence of HIV/AIDS in the Americas and beyond. PNAS. 2007;104(47):18566–18570.

[39] Worobey M, Watts TD, McKay RA, Suchard MA, Granade T, Teuwen DE, et al. 1970s and "Patient 0" HIV-1 genomes illuminate early HIV/AIDS history in North America. Nature. 2016;539(7627):98.

[40] Wikimedia HIV Structure PNG [accessed on 18-March-2018] Available from: `https://en.wikipedia.org/wiki/File:HI-virion-structure_en.svg`;.

[41] Wikimedia HIV Genome PNG [accessed on 18-March-2018] Available from: `https://commons.wikimedia.org/wiki/File:HIV-genome.png`;.

[42] Sundquist WI, Kräusslich HG. HIV-1 assembly, budding, and maturation. Cold Spring Harb Perspect Med. 2012;2(7):a006924.

[43] Johnson SF, Telesnitsky A. Retroviral RNA dimerization and packaging: the what, how, when, where, and why. PLoS pathogens. 2010;6(10):e1001007.

[44] Moore MD, Hu WS. HIV-1 RNA dimerization: It takes two to tango. AIDS reviews. 2009;11(2):91.

[45] Kleiman L, Jones CP, Musier-Forsyth K. Formation of the tRNALys packaging complex in HIV-1. FEBS letters. 2010;584(2):359–365.

[46] Perilla JR, Schulten K. Physical properties of the HIV-1 capsid from all-atom molecular dynamics simulations. Nat Commun. 2017;8:15959.

[47] Watts JM, Dang KK, Gorelick RJ, Leonard CW, Bess Jr JW, Swanstrom R, et al. Architecture and secondary structure of an entire HIV-1 RNA genome. Nature. 2009;460(7256):711.

[48] von Kleist M. Combining pharmacology and mutational dynamics to understand and combat drug resistance in HIV. Doctoral Thesis. Hamilton Institute/National University of Ireland, Maynooth, Ireland. 2009;.

[49] Lazar DC, Morris KV, Saayman SM. The emerging role of long non-coding RNAs in HIV infection. Virus Res. 2016;212:114–126.

[50] Smyth RP, Smith MR, Jousset AC, Despons L, Laumond G, Decoville T, et al. In cell mutational interference mapping experiment (in cell MIME) identifies the 5' polyadenylation signal as a dual regulator of HIV-1 genomic RNA production and packaging. Nucleic Acids Res. 2018;.

[51] Stevenson M. HIV-1 pathogenesis. Nat Med. 2003;9:853–860.

[52] NIH HIV Life cycle Graphics[accessed on 18-March-2018] Available from: `https://www.niaid.nih.gov/diseases-conditions/hiv-replication-cycle`;.

[53] Freed EO. HIV-1 assembly, release and maturation. Nature Reviews Microbiology. 2015;13(8):484.

[54] Lusic M, Siliciano RF. Nuclear landscape of HIV-1 infection and integration. Nat Rev Microbiol. 2017;15(2):69.

[55] Bruner KM, Hosmane NN, Siliciano RF. Towards an HIV-1 cure: measuring the latent reservoir. Trends Microbiol. 2015;23(4):192–203.

[56] Archin NM, Sung JM, Garrido C, Soriano-Sarabia N, Margolis DM. Eradicating HIV-1 infection: seeking to clear a persistent pathogen. Nat Rev Microbiol. 2014;12(11):750.

[57] Simon V, Ho DD. HIV-1 dynamics in vivo: implications for therapy. Nat Rev Microbiol. 2003;1:181–190.

[58] McMichael AJ, Borrow P, Tomaras GD, Goonetilleke N, Haynes BF. The immune response during acute HIV-1 infection: clues for vaccine development. Nat Rev Microbiol. 2010;10(1):11.

[59] Fiebig EW, Wright DJ, Rawal BD, Garrett PE, Schumacher RT, Peddada L, et al. Dynamics of HIV viremia and antibody seroconversion in plasma donors: implications for diagnosis and staging of primary HIV infection. AIDS. 2003;17(13):1871–1879.

[60] De Clercq E. Anti-HIV drugs: 25 compounds approved within 25 years after the discovery of HIV. Int J Antimicrob Agents. 2009;33(4):307–320.

[61] Arts EJ, Hazuda DJ. HIV-1 antiretroviral drug therapy. Cold Spring Harb Perspect Med. 2012;2(4):a007161.

[62] Dean M, Carrington M, Winkler C, Huttley GA, Smith MW, Allikmets R, et al. Genetic restriction of HIV-1 infection and progression to AIDS by a deletion allele of the CKR5 structural gene. Science. 1996;273(5283):1856–1862.

[63] Liu R, Paxton WA, Choe S, Ceradini D, Martin SR, Horuk R, et al. Homozygous defect in HIV-1 coreceptor accounts for resistance of some multiply-exposed individuals to HIV-1 infection. Cell. 1996;86(3):367–377.

[64] Samson M, Libert F, Doranz BJ, Rucker J, Liesnard C, Farber CM, et al. Resistance to HIV-1 infection in caucasian individuals bearing mutant alleles of the CCR-5 chemokine receptor gene. Nature. 1996;382(6593):722.

[65] Palani A, Tagat JR. Discovery and development of small-molecule chemokine coreceptor CCR5 antagonists. J Med Chem. 2006;49(10):2851–2857.

[66] Wood A, Armour D. The discovery of the CCR5 receptor antagonist, UK-427,857, a new agent for the treatment of HIV infection and AIDS. Prog Med Chem. 2005;43:239–271.

[67] Briz V, Poveda E, Soriano V. HIV entry inhibitors: mechanisms of action and resistance pathways. J Antimicrob Chemother. 2006;57(4):619–627.

[68] Carter NJ, Keating GM. Maraviroc. Drugs. 2007;67(15):2277–2288.

[69] Dean L. Maraviroc Therapy and CCR5 Genotype. National Center for Biotechnology Information (US).2017 [Accessed on 30-April-2018]. Available from :https://www.ncbi.nlm.nih.gov/books/NBK279895/;.

[70] Matthews T, Salgo M, Greenberg M, Chung J, DeMasi R, Bolognesi D. Enfuvirtide: the first therapy to inhibit the entry of HIV-1 into host CD4 lymphocytes. Nat Rev Drug Discov. 2004;3(3):215.

[71] Warnke D, Barreto J, Temesgen Z. Antiretroviral drugs. The journal of clinical pharmacology. 2007;47(12):1570–1579.

[72] Kohlstaedt L, Wang J, Friedman J, Rice P, Steitz T. Crystal structure at 3.5 A resolution of HIV-1 reverse transcriptase complexed with an inhibitor. Science. 1992;256(5065):1783–1790.

[73] Tantillo C, Ding J, Jacobo-Molina A, Nanni RG, Boyer PL, Hughes SH, et al. Locations of anti-AIDS drug binding sites and resistance mutations in the three-dimensional structure of HIV-1 reverse transcriptase: implications for mechanisms of drug inhibition and resistance. J Mol Biol. 1994;243(3):369–387.

[74] Jegede O, Babu J, Di Santo R, McColl DJ, Weber J, Quinones-Mateu M. HIV type 1 integrase inhibitors: from basic research to clinical implications. AIDS Rev. 2008;10(3):172–189.

[75] Lv Z, Chu Y, Wang Y. HIV protease inhibitors: a review of molecular selectivity and toxicity. HIV/AIDS (Auckland, NZ). 2015;7:95.

[76] Perelson AS, Neumann AU, Markowitz M, Leonard JM, Ho DD. HIV-1 dynamics in vivo: virion clearance rate, infected cell life-span, and viral generation time. Science. 1996;271(5255):1582–1586.

[77] Perelson AS. Modelling viral and immune system dynamics. Nat Rev Immunol. 2002;2(1):28–36.

[78] Ramratnam B, Bonhoeffer S, Binley J, Hurley A, Zhang L, Mittler JE, et al. Rapid production and clearance of HIV-1 and hepatitis C virus assessed by large volume plasma apheresis. Lancet. 1999;354(9192):1782–1785.

[79] Perelson AS, Essunger P, Cao Y, Vesanen M, Hurley A, Saksela K, et al. Decay characteristics of HIV-1-infected compartments during combination therapy. Nature. 1997;387:188–191.

[80] Markowitz M, Nguyen BY, Gotuzzo E, Mendo F, Ratanasuwan W, Kovacs C, et al. Rapid and durable antiretroviral effect of the HIV-1 integrase inhibitor raltegravir as part of combination therapy in treatment-naive patients with HIV-1 infection: results of a 48-week controlled study. J Acquir Immune Defic Syndr. 2007;46(2):125–133.

[81] Murray JM, Emery S, Kelleher AD, Law M, Chen J, Hazuda DJ, et al. Antiretroviral therapy with the integrase inhibitor raltegravir alters decay kinetics of HIV, significantly reducing the second phase. AIDS. 2007;21(17):2315–2321.

[82] Sedaghat AR, Dinoso JB, Shen L, Wilke CO, Siliciano RF. Decay dynamics of HIV-1 depend on the inhibited stages of the viral life cycle. PNAS. 2008;105(12):4832–4837.

[83] von Kleist M, Menz S, Huisinga W. Drug-class specific impact of antivirals on the reproductive capacity of HIV. PLoS Comput Biol. 2010;6(3):e1000720.

[84] Duwal S, Schütte C, von Kleist M. Pharmacokinetics and pharmacodynamics of the reverse transcriptase inhibitor tenofovir and prophylactic efficacy against HIV-1 infection. PLoS One. 2012;7(7):e40382.

[85] von Kleist M, Menz S, Stocker H, Arasteh K, Schütte C, Huisinga W. HIV Quasispecies Dynamics during Pro-active Treatment Switching: Impact on Multi-Drug Resistance and Resistance Archiving in Latent Reservoirs. PLoS One. 2011;6(3):e18204.

[86] Chou TC. Theoretical basis, experimental design, and computerized simulation of synergism and antagonism in drug combination studies. Pharmacolog Rev. 2006;58(3):621–681.

[87] Shen L, Peterson S, Sedaghat AR, McMahon MA, Callender M, Zhang H, et al. Dose-response curve slope sets class-specific limits on inhibitory potential of anti-HIV drugs. Nat Med. 2008;14(7):762–766.

[88] von Kleist M, Menz S, Stocker H, Arasteh K, Schütte C, Huisinga W. HIV Quasispecies Dynamics during Pro-active Treatment Switching: Impact on Multi-Drug Resistance and Resistance Archiving in Latent Reservoirs. PLoS One. 2011;6:e18204.

[89] Schuette C, Metzner P. Markov Chains and Jump Processes. 2009 [Accessed on 30-April-2018], Available from: `http://www.hamilton.ie/ollie/Downloads/Mark.pdf`;.

[90] Munsky B, Khammash M. The finite state projection algorithm for the solution of the chemical master equation. J Chem Phys. 2006;124(4):044104.

[91] Nordsieck A, Lamb W, Uhlenbeck G. On the theory of cosmic-ray showers I the furry model and the fluctuation problem. Physica. 1940;7(4):344–360.

[92] Menz S. Hybrid stochastic-deterministic approaches for simulation and analysis of biochemcal reaction networks. Doctoral Thesis. Freie Universtät Berlin, Germany. 2013;.

[93] Gillespie DT. Stochastic simulation of chemical kinetics. Annu Rev Phys Chem. 2007;58(1):35–55.

[94] Kingman JFC. Poisson processes. Wiley Online Library; 1993.

[95] Gillespie DT. Exact stochastic simulation of coupled chemical reactions. J Phys Chem. 1977;81:2340–61.

[96] Wilkinson DJ. Stochastic Modelling for Systems Biology. Chapman & Hall/CRC; 2006.

[97] Kurtz TG. The relationship between stochastic and deterministic models for chemical reactions. The Journal of Chemical Physics. 1972;57(7):2976–2978.

[98] Kurtz TG. Solutions of ordinary differential equations as limits of pure jump Markov processes. Journal of applied Probability. 1970;7(1):49–58.

[99] Kurtz T. Limit theorems for sequences of jump Markov processes. J Appl Probab. 1971;8(2):344–356.

[100] Waage P, Gulberg CM. Studies concerning affinity. J Chem Educ. 1986;63(12):1044.

[101] Alfonsi A, Cancès E, Turinici G, Di Ventura B, Huisinga W. Adaptive simulation of hybrid stochastic and deterministic models for biochemical systems. In: ESAIM: proceedings. vol. 14. EDP Sciences; 2005. p. 1–13.

[102] Thanh VH, Zunino R, Priami C. On the rejection-based algorithm for simulation and analysis of large-scale reaction networks. J Chem Phys. 2015;142(24):06B617_1.

[103] Lewis PA, Shedler GS. Simulation of nonhomogeneous Poisson processes by thinning. Naval Research Logistics (NRL). 1979;26(3):403–413.

[104] Ogata Y. On Lewis' simulation method for point processes. IEEE Trans Inf Theory. 1981;27(1):23–31.

[105] Thanh VH, Priami C, Zunino R. Efficient rejection-based simulation of biochemical reactions with stochastic noise and delays. J Chem Phys. 2014;141(13):10B602_1.

[106] Thanh VH, Priami C. Simulation of biochemical reactions with time-dependent rates by the rejection-based algorithm. J Chem Phys. 2015;143(5):08B601_1.

[107] Brémaud P. Point processes and queues: martingale dynamics. vol. 50. Springer; 1981.

[108] Rowland M, Tozer TN. Clinical pharmacokinetics/pharmacodynamics. Lippincott Williams and Wilkins Philadelphia; 2005.

[109] Bonate PL, Steimer JL. Pharmacokinetic-pharmacodynamic modeling and simulation. Springer, New York; 2011.

[110] Tarantola A. Inverse problem theory and methods for model parameter estimation. SIAM; 2005.

[111] Stigler SM. Gauss and the invention of least squares. Ann Stat. 1981; p. 465–474.

[112] Bauer RJ, Guzy S, Ng C. A survey of population analysis methods and software for complex pharmacokinetic and pharmacodynamic models with examples. AAPS J. 2007;9(1):E60–E83.

[113] Aldrich J, et al. RA Fisher and the making of maximum likelihood 1912-1922. Statistical Science. 1997;12(3):162–176.

[114] Edwards AW. Statistical methods in scientific inference. Nature. 1969;222(5200):1233.

[115] Carson E, Cobelli C. Modelling methodology for physiology and medicine. Newnes; 2013.

[116] MATLAB help page on nonlinear regression [accessed 12-Jan-2018]. Available from: `https://de.mathworks.com/help/simbio/ug/nonlinear-regression.html`;.

[117] Burnham KP, Anderson DR. Multimodel inference: understanding AIC and BIC in model selection. Sociol Methods Res. 2004;33(2):261–304.

[118] Burnham KP, Anderson DR. Kullback-Leibler information as a basis for strong inference in ecological studies. Wildl Res. 2001;28(2):111–119.

[119] Wagenmakers EJ, Farrell S. AIC model selection using Akaike weights. Psychon Bull Rev. 2004;11(1):192–196.

[120] Kirk P, Thorne T, Stumpf MP. Model selection in systems and synthetic biology. Curr Opin Biotechnol. 2013;24(4):767–774.

[121] Ette EI, Williams PJ. Population pharmacokinetics II: estimation methods. Ann Pharmacother. 2004;38(11):1907–1915.

[122] Sheiner LB, Beal SL. Evaluation of methods for estimating population pharmacokinetic parameters. I. Michaelis-Menten model: routine clinical pharmacokinetic data. J Pharmacokinet Biopharm. 1980;8(6):553–571.

[123] Sheiner LB. The population approach to pharmacokinetic data analysis: rationale and standard data analysis methods. Drug Metab Rev. 1984;15(1-2):153–171.

[124] Vonesh EF, Carter RL. Mixed-effects nonlinear regression for unbalanced repeated measures. Biometrics. 1992; p. 1–17.

[125] Steimer JL, Mallet A, Golmard JL, Boisvieux JF. Alternative approaches to estimation of population pharmacokinetic parameters: comparison with the nonlinear mixed-effect model. Drug Metab Rev. 1984;15(1-2):265–292.

[126] De Cock RF, Piana C, Krekels EH, Danhof M, Allegaert K, Knibbe CA. The role of population PK–PD modelling in paediatric clinical research. Eur J Clin Pharmacol. 2011;67(1):5–16.

[127] Owen JS, Fiedler-Kelly J. Introduction to population pharmacokinetic/pharmacodynamic analysis with nonlinear mixed effects models. John Wiley & Sons; 2014.

[128] Kloft C. Lecture note on population approach, A3 Module, PharMetrX, 2015;.

[129] Davidian M, Giltinan DM. Nonlinear models for repeated measurement data: an overview and update. J Agric Biol Environ Stat. 2003;8(4):387–419.

[130] Huisinga W. Lecture notes on Nonlinear Mixed Effect Modeling, A5 Module, PharMetrX, 2016;.

[131] Wu L. Exact and approximate inferences for nonlinear mixed-effects models with missing covariates. J Am Stat Assoc. 2004;99(467):700–709.

[132] Wang Y. Derivation of various NONMEM estimation methods. J Pharmacokinet Pharmacodyn. 2007;34(5):575–593.

[133] Lindstrom MJ, Bates DM. Nonlinear mixed effects models for repeated measures data. Biometrics. 1990; p. 673–687.

[134] Pinheiro JC, Bates DM. Approximations to the log-likelihood function in the nonlinear mixed-effects model. J Comput Graph Stat. 1995;4(1):12–35.

[135] Pinheiro JC, Bates DM. Mixed-effects model in S and S-Plus. Springer; 2009.

[136] Reference page for Matlab nlmefit. [accessed on 15-Jan-2018] Available from: `https://de.mathworks.com/help/stats/nlmefit.html`;.

[137] Smith DA, Van de Waterbeemd H. Pharmacokinetics and metabolism in drug design. John Wiley & Sons; 2012.

[138] Hacker M, Messer WS, Bachmann KA. Pharmacology: principles and practice. Academic Press; 2009.

[139] Kloft C. Lecture note on introduction to pharmacokinetics and pharmacodynamics, A1 Module, PharMetrX, 2015;.

[140] Scaglione F, Berrino L. Cytosine deoxyribonucleoside anti-HIV analogues: a small chemical substitution allows relevant activities. Int J Antimicrob Agents. 2012;39(6):458–463.

[141] Cihlar T, Ray AS. Nucleoside and nucleotide HIV reverse transcriptase inhibitors: 25 years after zidovudine. Antiviral Res. 2010;85(1):39–58.

[142] Anderson PL, Kiser JJ, Gardner EM, Rower JE, Meditz A, Grant RM. Pharmacological considerations for tenofovir and emtricitabine to prevent HIV infection. J Antimicrob Chemother. 2010;66(2):240–250.

[143] Droste J, Verweij-van Wissen C, Kearney B, Buffels R, Hekster Y, Burger D, et al. Pharmacokinetic study of tenofovir disoproxil fumarate combined with rifampin in healthy volunteers. Antimicrob Agents Chemother. 2005;49(2):680–684.

[144] Chittick GE, Zong J, Blum MR, Sorbel JJ, Begley JA, Adda N, et al. Pharmacokinetics of tenofovir disoproxil fumarate and ritonavir-boosted saquinavir mesylate administered alone or in combination at steady state. Antimicrob Agents Chemother. 2006;50(4):1304–1310.

[145] Barditch-Crovo P, Deeks SG, Collier A, Safrin S, Coakley DF, Miller M, et al. Phase I/II trial of the pharmacokinetics, safety, and antiretroviral activity of tenofovir disoproxil fumarate in human immunodeficiency virus-infected adults. Antimicrob Agents Chemother. 2001;45(10):2733–2739.

[146] Hawkins T, Veikley W, St Claire RL 3rd, Guyer B, Clark N, Kearney BP. Intracellular pharmacokinetics of tenofovir diphosphate, carbovir triphosphate, and lamivudine triphosphate in patients receiving triple-nucleoside regimens. J Acquir Immune Defic Syndr. 2005;39(4):406–411.

[147] Wang LH, Begley J, St Claire RL 3rd, Harris J, Wakeford C, Rousseau FS. Pharmacokinetic and pharmacodynamic characteristics of emtricitabine support its once daily dosing for the treatment of HIV infection. AIDS Res Hum Retroviruses. 2004;20(11):1173–1182.

[148] Rousseau FS, Kahn JO, Thompson M, Mildvan D, Shepp D, Sommadossi JP, et al. Prototype trial design for rapid dose selection of antiretroviral drugs: an example using emtricitabine (Coviracil). J Antimicrob Chemother. 2001;48(4):507–513.

[149] Blum MR, Chittick GE, Begley JA, Zong J. Steady-State Pharmacokinetics of Emtricitabine and Tenofovir Disoproxil Fumarate Administered Alone and in Combination in Healthy Volunteers. J Clin Pharmacol. 2007;47(6):751–759.

[150] Zong J, Chittick GE, Wang LH, Hui J, Begley JA, Blum MR. Pharmacokinetic evaluation of emtricitabine in combination with other nucleoside antivirals in healthy volunteers. J Clin Pharmacol. 2007;47(7):877–889.

[151] Kearney B, Zong J, Begley J, Shah J. Bioequivalence of combination tenofovir DF/emtricitabine tablets for one-pill once daily administration. In: 5th International Workshop on Clinical Pharmacology of HIV Therapy; 2004.

[152] Jackson A, Moyle G, Watson V, Tjia J, Ammara A, Back D, et al. Tenofovir, emtricitabine intracellular and plasma, and efavirenz plasma concentration decay following drug intake cessation: implications for HIV treatment and prevention. J Acquir Immune Defic Syndr. 2013;62(3):275–281.

[153] Rousseau FS, Wakeford C, Mommeja-Marin H, Sanne I, Moxham C, Harris J, et al. Prospective randomized trial of emtricitabine versus lamivudine short-term monotherapy in human immunodeficiency virus–infected patients. J Infect Dis. 2003;188(11):1652–1658.

[154] Moore KH, Barrett JE, Shaw S, Pakes GE, Churchus R, Kapoor A, et al. The pharmacokinetics of lamivudine phosphorylation in peripheral blood mononuclear cells from patients infected with HIV-1. AIDS. 1999;13(16):2239–2250.

[155] von Kleist M, Huisinga W. Pharmacokinetic-pharmacodynamic relationship of NRTIs and its connection to viral escape: an example based on zidovudine. Eur J Pharm Sci. 2009;36(4-5):532–543.

[156] Sharma PL, Nurpeisov V, Hernandez-Santiago B, Beltran T, Schinazi RF. Nucleoside inhibitors of human immunodeficiency virus type 1 reverse transcriptase. Curr Top Med Chem. 2004;4(9):895–919.

[157] Chapman EH, Kurec AS, Davey FR. Cell volumes of normal and malignant mononuclear cells. J Clin Pathol. 1981;34(10):1083–1090.

[158] Bisset LR, Lung TL, Kaelin M, Ludwig E, Dubs RW. Reference values for peripheral blood lymphocyte phenotypes applicable to the healthy adult population in Switzerland. Eur J Haematol. 2004;72(3):203–212.

[159] Baheti G, Kiser JJ, Havens PL, Fletcher CV. Plasma and intracellular population pharmacokinetic analysis of tenofovir in HIV-1-infected patients. Antimicrob Agents Chemother. 2011;55(11):5294–5299.

[160] Madrasi K, Burns RN, Hendrix CW, Fossler MJ, Chaturvedula A. Linking the population pharmacokinetics of tenofovir and its metabolites with its cellular uptake and metabolism. CPT Pharmacometrics Syst Pharmacol. 2014;3:e147.

[161] Hendrix CW, Chen BA, Guddera V, Hoesley C, Justman J, Nakabiito C, et al. MTN-001: randomized pharmacokinetic cross-over study comparing tenofovir vaginal gel and oral tablets in vaginal tissue and other compartments. PloS one. 2013;8(1):e55013.

[162] Valade E, Tréluyer JM, Bouazza N, Ghosn J, Foissac F, Benaboud S, et al. Population pharmacokinetics of emtricitabine in HIV-1-infected adult patients. Antimicrob Agents Chemother. 2014;58(4):2256–2261.

[163] Hirt D, Urien S, Rey E, Arrivé E, Ekouévi DK, Coffié P, et al. Population pharmacokinetics of emtricitabine in human immunodeficiency virus type 1-infected pregnant women and their neonates. Antimicrob Agents Chemother. 2009;53(3):1067–1073.

[164] Saag MS. Emtricitabine, a new antiretroviral agent with activity against HIV and hepatitis B virus. Clin Infect Dis. 2006;42(1):126–131.

[165] Modrzejewski KA, Herman RA. Emtricitabine: a once-daily nucleoside reverse transcriptase inhibitor. Ann Pharmacother. 2004;38(6):1006–1014.

[166] Paff MT, Averett DR, Prus KL, Miller WH, Nelson DJ. Intracellular metabolism of (-)-and (+)-cis-5-fluoro-1-[2-(hydroxymethyl)-1, 3-oxathiolan-5-yl] cytosine in HepG2 derivative 2.2. 15 (subclone P5A) cells. Antimicrobial agents and chemotherapy. 1994;38(6):1230–1238.

[167] Darque A, Valette G, Rousseau F, Wang LH, Sommadossi JP, Zhou XJ. Quantitation of intracellular triphosphate of emtricitabine in peripheral blood mononuclear cells from human immunodeficiency virus-infected patients. Antimicrob Agents Chemother. 1999;43(9):2245–2250.

[168] Moore KH, Yuen GJ, Hussey EK, Pakes GE, Eron JJ, Bartlett JA. Population pharmacokinetics of lamivudine in adult human immunodeficiency virus-infected patients enrolled in two phase III clinical trials. Antimicrob Agents Chemother. 1999;43(12):3025–3029.

[169] Li X, Liu B, Sun Y, Chen H, Chen H, Zhang H, et al. Single-Dose Pharmacokinetic Properties, Bioavailability, and Tolerability of Two Lamivudine 100-mg Tablet Formulations: A Randomized Crossover Study in Healthy Chinese Male Subjects. Clin Ther. 2013;35(10):1546–1556.

[170] Zhou Z, Rodman JH, Flynn PM, Robbins BL, Wilcox CK, D'Argenio DZ. Model for intracellular Lamivudine metabolism in peripheral blood mononuclear cells ex vivo and in human immunodeficiency virus type 1-infected adolescents. Antimicrob Agents Chemother. 2006;50(8):2686–2694.

[171] Yuen GJ, Lou Y, Bumgarner NF, Bishop JP, Smith GA, Otto VR, et al. Equivalent steady-state pharmacokinetics of lamivudine in plasma and lamivudine triphosphate within cells following administration of lamivudine at 300 milligrams once daily and 150 milligrams twice daily. Antimicrob Agents Chemother. 2004;48(1):176–182.

[172] Heald AE, Hsyu PH, Yuen GJ, Robinson P, Mydlow P, Bartlett JA. Pharmacokinetics of lamivudine in human immunodeficiency virus-infected patients with renal dysfunction. Antimicrob Agents Chemother. 1996;40(6):1514–1519.

[173] Yuen GJ, Morris DM, Mydlow PK, Haidar S, Hall ST, Hussey EK. Pharmacokinetics, absolute bioavailability, and absorption characteristics of lamivudine. J Clin Pharmacol. 1995;35(12):1174–1180.

[174] Johnson MA, Moore KH, Yuen GJ, Bye A, Pakes GE. Clinical pharmacokinetics of lamivudine. Clin Pharmacokinet. 1999;36(1):41–66.

[175] Else LJ, Jackson A, Puls R, Hill A, Fahey P, Lin E, et al. Pharmacokinetics of lamivudine and lamivudine-triphosphate after administration of 300 milligrams and 150 milligrams once daily to healthy volunteers: results of the ENCORE 2 study. Antimicrob Agents Chemother. 2012;56(3):1427–1433.

[176] Dumond JB, Yang KH, Kendrick R, Reddy YS, Kashuba AD, Troiani L, et al. Pharmacokinetic modeling of lamivudine and zidovudine triphosphates predicts differential pharmacokinetics in seminal mononuclear cells and peripheral blood mononuclear cells. Antimicrob Agents Chemother. 2015;59(10):6395–6401.

[177] Else LJ, Jackson A, Puls R, Hill A, Fahey P, Lin E, et al. Pharmacokinetics of lamivudine and lamivudine-triphosphate after administration of 300 milligrams and 150 milligrams once daily to healthy volunteers: results of the ENCORE 2 study. Antimicrob Agents Chemother. 2011;56(3):1427–1433.

[178] Linnankoski J, Mäkelä JM, Ranta VP, Urtti A, Yliperttula M. Computational prediction of oral drug absorption based on absorption rate constants in humans. J Med Chem. 2006;49(12):3674–3681.

[179] Gagnieu MC, Barkil ME, Livrozet JM, Cotte L, Miailhes P, Boibieux A, et al. Population pharmacokinetics of tenofovir in AIDS patients. J Clin Pharmacol. 2008;48(11):1282–1288.

[180] Drug Bank Entry for Dolutegravir [accessed on 28-June-2017] Available from `https://www.drugbank.ca/drugs/DB08930`;.

[181] Dow DE, Bartlett JA. Dolutegravir, the second-generation of integrase strand transfer inhibitors (INSTIs) for the treatment of HIV. Infect Dis Ther. 2014;3(2):83–102.

[182] Elliot E, Amara A, Jackson A, Moyle G, Else L, Khoo S, et al. Dolutegravir and elvitegravir plasma concentrations following cessation of drug intake. J Antimicrob Chemother. 2016;71:1031–1036.

[183] Bracchi M, Pagani N, Clarke A, Adams T, Waters L, Bolton M, et al. Multicentre open-label pilot study of switching from efavirenz to dolutegravir for central nervous system (CNS) toxicity. In: International Congress of Drug Therapy in HIV Infection, Glasgow, UK, Abstract P209; 2016.

[184] Pirana Software [accessed on 28-June-2017] Available from: `http://www.pirana-software.com/`;.

[185] Castellino S, Moss L, Wagner D, Borland J, Song I, Chen S, et al. Metabolism, excretion, and mass balance of the HIV-1 integrase inhibitor dolutegravir in humans. Antimicrob Agents Chemother. 2013;57(8):3536–3546.

[186] Zhang J, Hayes S, Sadler BM, Minto I, Brandt J, Piscitelli S, et al. Population pharmacokinetics of dolutegravir in HIV-infected treatment-naive patients. Br J Clin Pharmacol. 2015;80(3):502–514.

[187] Schmidt S, Post TM, Peletier LA, Boroujerdi MA, Danhof M. Coping with time scales in disease systems analysis: application to bone remodeling. J Pharmacokinet Pharmacodyn. 2011;38(6):873–900.

[188] Jordheim LP, Durantel D, Zoulim F, Dumontet C. Advances in the development of nucleoside and nucleotide analogues for cancer and viral diseases. Nat Rev Drug Discov. 2013;12(6):447.

[189] PubChem Entry for DeoxyThymidine [accessed on 28-June-2017] Available from: `https://pubchem.ncbi.nlm.nih.gov/compound/5789`;.

[190] PubChem Entry for Zidovudine [accessed on 28-June-2017] Available from: `https://pubchem.ncbi.nlm.nih.gov/compound/35370`;.

[191] Smith AJ, Scott WA. The influence of natural substrates and inhibitors on the nucleotide-dependent excision activity of HIV-1 reverse transcriptase in the infected cell. Curr Pharm Des. 2006;12(15):1827–1841.

[192] Zhou Y, Zhang H, Siliciano JD, Siliciano RF. Kinetics of human immunodeficiency virus type 1 decay following entry into resting CD4+ T cells. J Virol. 2005;79(4):2199–2210.

[193] Durand-Gasselin L, Da Silva D, Benech H, Pruvost A, Grassi J. Evidence and possible consequences of the phosphorylation of nucleoside reverse transcriptase inhibitors in human red blood cells. Antimicrob Agents Chemother. 2007;51(6):2105–2111.

[194] Smith DA, Di L, Kerns EH. The effect of plasma protein binding on in vivo efficacy: misconceptions in drug discovery. Nat Rev Drug Discov. 2010;9(12):929–939.

[195] Watkins WJ, Desai MC. HCV versus HIV drug discovery: Déjà vu all over again? Bioorg Med Chem Lett. 2013;23(8):2281–2287.

[196] Boffito M, Back DJ, Blaschke TF, Rowland M, Bertz RJ, Gerber JG, et al. Protein binding in antiretroviral therapies. AIDS Res Hum Retroviruses. 2003;19(9):825–835.

[197] von Kleist M, Huisinga W. Physiologically based pharmacokinetic modelling: a sub-compartmentalized model of tissue distribution. J Pharmacokinet Pharmacodyn. 2007;34:789–806.

[198] Sandkovsky U, Swindells S, Robbins BL, Nelson SR, Acosta EP, Fletcher CV. Measurement of plasma and intracellular concentrations of raltegravir in patients with HIV infection. AIDS. 2012;26:2257–2259.

[199] Wang L, Soon GH, Seng KY, Li J, Lee E, Yong EL, et al. Pharmacokinetic modeling of plasma and intracellular concentrations of raltegravir in healthy volunteers. Antimicrob Agents Chemother. 2011;55:4090–4095.

[200] Petropoulos CJ, Parkin NT, Limoli KL, Lie YS, Wrin T, Huang W, et al. A novel phenotypic drug susceptibility assay for human immunodeficiency virus type 1. Antimicrob Agents Chemother. 2000;44(4):920–928.

[201] Bazzoli C, Jullien V, Tiec CL, Rey E, Mentré F, Taburet AM. Intracellular Pharmacokinetics of Antiretroviral Drugs in HIV-Infected Patients, and their Correlation with Drug Action. Clin Pharmacokinet. 2010;49(1):17–45.

[202] Hertogs K, de Béthune MP, Miller V, Ivens T, Schel P, Van Cauwenberge A, et al. A rapid method for simultaneous detection of phenotypic resistance to inhibitors of protease and reverse transcriptase in recombinant human immunodeficiency virus type 1 isolates from patients treated with antiretroviral drugs. Antimicrob Agents Chemother. 1998;42(2):269–276.

[203] Qari SH, Respess R, Weinstock H, Beltrami EM, Hertogs K, Larder BA, et al. Comparative analysis of two commercial phenotypic assays for drug susceptibility testing of human immunodeficiency virus type 1. J Clin Microbiol. 2002;40(1):31–35.

[204] Ping LH, Joseph SB, Anderson JA, Abrahams MR, Salazar-Gonzalez JF, Kincer LP, et al. Comparison of viral Env proteins from acute and chronic infections with subtype C human immunodeficiency virus type 1 identifies differences in glycosylation and CCR5 utilization and suggests a new strategy for immunogen design. J Virol. 2013;87(13):7218–7233.

[205] Zhang ZQ, Schuler T, Zupancic M, Wietgrefe S, Staskus K, Reimann K, et al. Sexual transmission and propagation of SIV and HIV in resting and activated CD4+ T cells. Science. 1999;286(5443):1353–1357.

[206] Li H, Bar KJ, Wang S, Decker JM, Chen Y, Sun C, et al. High Multiplicity Infection by HIV-1 in Men Who Have Sex with Men. PLoS Pathog. 2010;6(5):e1000890.

[207] Haase AT. Perils at mucosal front lines for HIV and SIV and their hosts. Nat Rev Immunol. 2005;5(10):783–792.

[208] Isaacman-Beck J, Hermann EA, Yi Y, Ratcliffe SJ, Mulenga J, Allen S, et al. Heterosexual transmission of human immunodeficiency virus type 1 subtype C: Macrophage tropism, alternative coreceptor use, and the molecular anatomy of CCR5 utilization. J Virol. 2009;83(16):8208–8220.

[209] Joseph SB, Swanstrom R, Kashuba AD, Cohen MS. Bottlenecks in HIV-1 transmission: insights from the study of founder viruses. Nat Rev Microbiol. 2015;13(7):414–425.

[210] Tan WY, Wu H. Stochastic modeling of the dynamics of CD4+ T-cell infection by HIV and some Monte Carlo studies. Math Biosci. 1998;147(2):173–205.

[211] Stafford MA, Corey L, Cao Y, Daar ES, Ho DD, Perelson AS. Modeling plasma virus concentration during primary HIV infection. J Theor Biol. 2000;203(3):285–301.

[212] Tuckwell HC, Shipman PD, Perelson AS. The probability of HIV infection in a new host and its reduction with microbicides. Math Biosci. 2008;214(1-2):81–86.

[213] Conway JM, Konrad BP, Coombs D. Stochastic analysis of Pre- and postexposure prophylaxis against HIV infection. SIAM J Appl Math. 2013;73(2):904–28.

[214] Perelson AS, Kirschner DE, De Boer R. Dynamics of HIV infection of CD4+ T cells. Math Biosci. 1993;114(1):81–125.

[215] Pearson JE, Krapivsky P, Perelson AS. Stochastic theory of early viral infection: continuous versus burst production of virions. PLoS Comput Biol. 2011;7(2):e1001058.

[216] Pierson TC, Zhou Y, Kieffer TL, Ruff CT, Buck C, Siliciano RF. Molecular characterization of preintegration latency in human immunodeficiency virus type 1 infection. J Virol. 2002;76(17):8518–8531.

[217] Allen LJS. An introduction to stochastic processes with applications to biology. Chapman & Hall/CR; 2011.

[218] Edwards A. Pascal's problem: The'Gambler's Ruin'. Int Stat Rev. 1983; p. 73–79.

[219] Parzen E. Modern probability theory and its applications. John Wiley & Sons, Incorporated; 1960.

[220] Heffernan JM, Smith RJ, Wahl LM. Perspectives on the basic reproductive ratio. J R Soc Interface. 2005;2:281–293.

[221] Dietz K. The estimation of the basic reproduction number for infectious diseases. Stat Methods Med Res. 1993;2(1):23–41.

[222] Laskey SB, Siliciano RF. Quantitative evaluation of the antiretroviral efficacy of dolutegravir. JCI Insight. 2016;1(19):e90033.

[223] Chun TW, Engel D, Berrey MM, Shea T, Corey L, Fauci AS. Early establishment of a pool of latently infected, resting CD4(+) T cells during primary HIV-1 infection. PNAS. 1998;95:8869–8873.

[224] Chun TW, Moir S, Fauci AS. HIV reservoirs as obstacles and opportunities for an HIV cure. Nat Immunol. 2015;16(6):584–589.

[225] Whitney JB, Hill AL, Sanisetty S, Penaloza-MacMaster P, Liu J, Shetty M, et al. Rapid seeding of the viral reservoir prior to SIV viraemia in rhesus monkeys. Nature. 2014;512:74–77.

[226] Finzi D, Blankson J, Siliciano JD, Margolick JB, Chadwick K, Pierson T, et al. Latent infection of CD4+ T cells provides a mechanism for lifelong persistence of HIV-1, even in patients on effective combination therapy. Nat Med. 1999;5(5):512–517.

[227] Zhang L, Ramratnam B, Tenner-Racz K, He Y, Vesanen M, Lewin S, et al. Quantifying residual HIV-1 replication in patients receiving combination antiretroviral therapy. N Engl J Med. 1999;340:1605–1613.

[228] Chun TW, Justement JS, Moir S, Hallahan CW, Maenza J, Mullins JI, et al. Decay of the HIV reservoir in patients receiving antiretroviral therapy for extended periods: implications for eradication of virus. J Infect Dis. 2007;195:1762–1764.

[229] Ho YC, Shan L, Hosmane NN, Wang J, Laskey SB, Rosenbloom DIS, et al. Replication-competent noninduced proviruses in the latent reservoir increase barrier to HIV-1 cure. Cell. 2013;155:540–551.

[230] Boily MC, Baggaley RF, Wang L, Masse B, White RG, Hayes RJ, et al. Heterosexual risk of HIV-1 infection per sexual act: systematic review and meta-analysis of observational studies. Lancet Infect Dis. 2009;9(2):118–129.

[231] Baeten JM, Kahle E, Lingappa JR, Coombs RW, Delany-Moretlwe S, Nakku-Joloba E, et al. Genital HIV-1 RNA predicts risk of heterosexual HIV-1 transmission. Sci Transl Med. 2011;3(77):77ra29.

[232] Chakraborty H, Sen PK, Helms RW, Vernazza PL, Fiscus SA, Eron JJ, et al. Viral burden in genital secretions determines male-to-female sexual transmission of HIV-1: a probabilistic empiric model. AIDS. 2001;15(5):621–627.

[233] Hart CE, Lennox JL, Pratt-Palmore M, Wright TC, Schinazi RF, Evans-Strickfaden T, et al. Correlation of human immunodeficiency virus type 1 RNA levels in blood and the female genital tract. J Infect Dis. 1999;179(4):871–882.

[234] Kovacs A, Wasserman SS, Burns D, Wright DJ, Cohn J, Landay A, et al. Determinants of HIV-1 shedding in the genital tract of women. Lancet. 2001;358(9293):1593–1601.

[235] Goulston C, McFarland W, Katzenstein D. Human immunodeficiency virus type 1 RNA shedding in the female genital tract. J Infect Dis. 1998;177(4):1100–1103.

[236] Iversen AK, Larsen AR, Jensen T, Fugger L, Balslev U, Wahl S, et al. Distinct determinants of human immunodeficiency virus type 1 RNA and DNA loads in vaginal and cervical secretions. J Infect Dis. 1998;177(5):1214–1220.

[237] Quinn TC, Wawer MJ, Sewankambo N, Serwadda D, Li C, Wabwire-Mangen F, et al. Viral load and heterosexual transmission of human immunodeficiency virus type 1. Rakai Project Study Group. N Engl J Med. 2000;342(13):921–929.

[238] Hughes JP, Baeten JM, Lingappa JR, Magaret AS, Wald A, de Bruyn G, et al. Determinants of per-coital-act HIV-1 infectivity among African HIV-1-serodiscordant couples. J Infect Dis. 2012;205(3):358–365.

[239] Keele BF, Giorgi EE, Salazar-Gonzalez JF, Decker JM, Pham KT, Salazar MG, et al. Identification and characterization of transmitted and early founder virus envelopes in primary HIV-1 infection. PNAS. 2008;105(21):7552–7557.

[240] Abrahams MR, Anderson JA, Giorgi EE, Seoighe C, Mlisana K, Ping LH, et al. Quantitating the multiplicity of infection with human immunodeficiency virus type 1 subtype C reveals a non-poisson distribution of transmitted variants. J Virol. 2009;83(8):3556–3567.

[241] Fischer W, Ganusov VV, Giorgi EE, Hraber PT, Keele BF, Leitner T, et al. Transmission of single HIV-1 genomes and dynamics of early immune escape revealed by ultra-deep sequencing. PloS one. 2010;5(8):e12303.

[242] Royce RA, Seña A, Cates W Jr, Cohen MS. Sexual transmission of HIV. N Engl J Med. 1997;336(15):1072–1078.

[243] Levy JA. The transmission of HIV and factors influencing progression to AIDS. Am J Med. 1993;95(1):86–100.

[244] Wilson DP, Law MG, Grulich AE, Cooper DA, Kaldor JM. Relation between HIV viral load and infectiousness: a model-based analysis. Lancet. 2008;372(9635):314–320.

[245] Mellors JW, Rinaldo C Jr, Gupta P, White RM, Todd JA, Kingsley LA. Prognosis in HIV-1 infection predicted by the quantity of virus in plasma. Science. 1996;272(5265):1167–1170.

[246] Duwe S, Brunn M, Altmann D, Hamouda O, Schmidt B, Walter H, et al. Frequency of genotypic and phenotypic drug-resistant HIV-1 among therapy-naive patients of the German Seroconverter Study. J Acquir Immune Defic Syndr. 2001;26(3):266–273.

[247] Yousef KP, Meixenberger K, Smith MR, Somogyi S, Gromöller S, Schmidt D, et al. Inferring HIV-1 transmission dynamics in Germany from recently transmitted viruses. J Acquir Immune Defic Syndr. 2016;73(3):356–363.

[248] Powers KA, Poole C, Pettifor AE, Cohen MS. Rethinking the heterosexual infectivity of HIV-1: a systematic review and meta-analysis. Lancet Infect Dis. 2008;8(9):553–563.

[249] Keele BF, Estes JD. Barriers to mucosal transmission of immunodeficiency viruses. Blood. 2011;118(4):839–846.

[250] Ray AS. Intracellular interactions between nucleos (t) ide inhibitors of HIV reverse transcriptase. AIDS Rev. 2005;7(2):113–125.

[251] Anderson PL, Zheng JH, King T, Bushman LR, Predhomme J, Meditz A, et al. Concentrations of zidovudine- and lamivudine-triphosphate according to cell type in HIV-seronegative adults. AIDS. 2007;21(14):1849–1854.

[252] Kiser JJ, Aquilante CL, Anderson PL, King TM, Carten ML, Fletcher CV. Clinical and genetic determinants of intracellular tenofovir diphosphate concentrations in HIV-infected patients. JAIDS Journal of Acquired Immune Deficiency Syndromes. 2008;47(3):298–303.

[253] Becher F, Landman R, Mboup S, Kane CNT, Canestri A, Liegeois F, et al. Monitoring of didanosine and stavudine intracellular trisphosphorylated anabolite concentrations in HIV-infected patients. AIDS. 2004;18(2):181–187.

[254] Anderson PL, Glidden DV, Liu A, Buchbinder S, Lama JR, Guanira JV, et al. Emtricitabine-tenofovir concentrations and pre-exposure prophylaxis efficacy in men who have sex with men. Sci Transl Med. 2012;4(151):151ra125.

[255] Bartmeyer B, Kuecherer C, Houareau C, Werning J, Keeren K, Somogyi S, et al. Prevalence of transmitted drug resistance and impact of transmitted resistance on treatment success in the German HIV-1 Seroconverter Cohort. PLoS One. 2010;5(10):e12718.

[256] Menéndez-Arias L. Mechanisms of resistance to nucleoside analogue inhibitors of HIV-1 reverse transcriptase. Virus Res. 2008;134(1-2):124–146.

[257] Menéndez-Arias L. Molecular basis of human immunodeficiency virus drug resistance: an update. Antiviral Res. 2010;85(1):210–231.

[258] Molina JM, Capitant C, Spire B, Pialoux G, Cotte L, Charreau I, et al. On-demand preexposure prophylaxis in men at high risk for HIV-1 infection. N Engl J Med. 2015;373(23):2237–2246.

[259] Nicol MR, Emerson CW, Prince HMA, Nelson JAE, Fedoriw Y, Sykes C, et al. Models for predicting effective HIV chemoprevention in women. J Acquir Immune Defic Syndr. 2015;68(4):369–376.

[260] Kakuda TN, Abel S, Davis J, Hamlin J, Schöller-Gyüre M, Mack R, et al. Pharmacokinetic interactions of maraviroc with darunavir/ritonavir, maraviroc with etravirine, and maraviroc with etravirine/darunavir/ritonavir in healthy volunteers: results of two drug interaction trials. Antimicrob Agents Chemother. 2011;55:2290–6.

[261] Crauwels HM, van Heeswijk RP, Vandevoorde A, Buelens A, Stevens M, Hoetelmans RM. The effect of rilpivirine on the pharmacokinetics of methadone in HIV-negative volunteers. J Clin Pharmacol. 2014;54(2):133–140.

[262] Haberer JE, Bangsberg DR, Baeten JM, Curran K, Koechlin F, Amico KR, et al. Defining success with HIV pre-exposure prophylaxis: a prevention-effective adherence paradigm. AIDS (London, England). 2015;29(11):1277.

[263] Grant R, Anderson P, McMahan V, Liu A, Amico K, Mehrotra M, et al. Results of the iPrEx open-label extension (iPrEx OLE) in men and transgender women who have sex with men: PrEP uptake, sexual practices, and HIV incidence. AIDS. 2014; p. 20–25.

[264] McCormack S, Dunn DT, Desai M, Dolling DI, Gafos M, Gilson R, et al. Pre-exposure prophylaxis to prevent the acquisition of HIV-1 infection (PROUD): effectiveness results from the pilot phase of a pragmatic open-label randomised trial. Lancet. 2016;387(10013):53–60.

[265] Marrazzo JM, Ramjee G, Richardson BA, Gomez K, Mgodi N, Nair G, et al. Tenofovir-based preexposure prophylaxis for HIV infection among African women. N Engl J Med. 2015;372:509–518.

[266] Van Damme L, Corneli A, Ahmed K, Agot K, Lombaard J, Kapiga S, et al. Preexposure prophylaxis for HIV infection among African women. N Engl J Med. 2012;367(5):411–422.

[267] Sagaon-Teyssier L, Suzan-Monti M, Demoulin B, Capitant C, Lorente N, Préau M, et al. Uptake of PrEP and condom and sexual risk behavior among MSM during the ANRS IPERGAY trial. AIDS Care. 2016;28(sup1):48–55.

[268] Velter A, Barin F, Bouyssou A, Guinard J, Léon L, Le Vu S, et al. HIV Prevalence and Sexual Risk Behaviors Associated with Awareness of HIV Status Among Men Who Have Sex with Men in Paris, France. AIDS Behav. 2012;17(4):1266–1278.

[269] Louissaint NA, Cao YJ, Skipper PL, Liberman RG, Tannenbaum SR, Nimmagadda S, et al. Single Dose Pharmacokinetics of Oral Tenofovir in Plasma, Peripheral Blood Mononuclear Cells, Colonic Tissue, and Vaginal Tissue. AIDS Research and Human Retroviruses. 2013;29(11):1443–1450.

[270] Baeten JM, Donnell D, Mugo NR, Ndase P, Thomas KK, Campbell JD, et al. Single-agent tenofovir versus combination emtricitabine plus tenofovir for pre-exposure prophylaxis for HIV-1 acquisition: an update of data from a randomised, double-blind, phase 3 trial. The Lancet Infectious Diseases. 2014;14(11):1055–1064.

[271] The Clinton Health Access Initiative. Antiretroviral (ARV) Ceiling Price List. 2011 [accessed 22-Sept-2014]. Available from: `http://www.clintonfoundation.org`);.

[272] Gulick RM, Wilkin TJ, Chen YQ, Landovitz RJ, Amico KR, Young AM, et al. Phase 2 study of the safety and tolerability of maraviroc-containing regimens to prevent HIV infection in men who have sex with men (HPTN 069/ACTG A5305). Journal Infect Dis. 2017;215:238–246.

[273] McGowan I, Nikiforov A, Young A, Cranston R, Landovitz RJ, Bakshi R, et al. PrEP Impact on T-Cell Activation and Explant Infection: HPTN 069/ACTG 5305 Substudy. In: CROI2016, Boston. Oral presentation 104; 2016.

[274] De Cock KM, Fowler MG, Mercier E, de Vincenzi I, Saba J, Hoff E, et al. Prevention of mother-to-child HIV transmission in resource-poor countries: translating research into policy and practice. JAMA. 2000;283:1175–1182.

[275] Stringer EM, Ekouevi DK, Coetzee D, Tih PM, Creek TL, Stinson K, et al. Coverage of nevirapine-based services to prevent mother-to-child HIV transmission in 4 African countries. JAMA. 2010;304(3):293–302.

[276] Dickinson L, Amin J, Else L, Boffito M, Egan D, Owen A, et al. Pharmacokinetic and pharmacodynamic comparison of once-daily efavirenz (400 mg vs. 600 mg) in treatment-naïve HIV-infected patients: results of the ENCORE1 study. Clin Pharmacol Ther. 2015;98:406–416.

[277] Josephson F, Albert J, Flamholc L, Gisslén M, Karlström O, Lindgren SR, et al. Antiretroviral treatment of HIV infection: Swedish recommendations 2007. Scand J Infect Dis Suppl. 2007;39(6-7):486–507.

[278] Fernández-Montero JV, Vispo E, Anta L, de Mendoza C, Soriano V. Rilpivirine: a next-generation non-nucleoside analogue for the treatment of HIV infection. Expert opinion on pharmacotherapy. 2012;13(7):1007–1014.

[279] Hughes CA, Robinson L, Tseng A, MacArthur RD. New antiretroviral drugs: a review of the efficacy, safety, pharmacokinetics, and resistance profile of tipranavir, darunavir, etravirine, rilpivirine, maraviroc, and raltegravir. Expert Opin Pharmacother. 2009;10(15):2445–2466.

[280] McGowan I, Dezzutti CS, Siegel A, Engstrom J, Nikiforov A, Duffill K, et al. Long-acting rilpivirine as potential pre-exposure prophylaxis for HIV-1 prevention (the MWRI-01 study): an open-label, phase 1, compartmental, pharmacokinetic and pharmacodynamic assessment. Lancet HIV. 2016;3:e569–e578.

[281] Whitfield T, Torkington A, van Halsema C. Profile of cabotegravir and its potential in the treatment and prevention of HIV-1 infection: evidence to date. HIV/AIDS (Auckland, NZ). 2016;8:157.

[282] Markowitz M, Frank I, Grant RM, Mayer KH, Elion R, Goldstein D, et al. Safety and tolerability of long-acting cabotegravir injections in HIV-uninfected men (ECLAIR): a multicentre, double-blind, randomised, placebo-controlled, phase 2a trial. Lancet HIV. 2017;4:e331–e340.

[283] Else LJ, Taylor S, Back DJ, Khoo SH. Pharmacokinetics of antiretroviral drugs in anatomical sanctuary sites: the male and female genital tract. Antivir Ther. 2011;16:1149–1167.

[284] Avery LB, Bakshi RP, Cao YJ, Hendrix CW. The male genital tract is not a pharmacological sanctuary from efavirenz. Clin Pharmacol Ther. 2011;90:151–156.

[285] Cottrell ML, Yang KH, Prince HMA, Sykes C, White N, Malone S, et al. A translational pharmacology approach to predicting HIV pre-exposure prophylaxis outcomes in men and women using tenofovir disoproxil fumarate +/- emtricitabine. J Infect Dis. 2016;.

[286] Aceijas C, Stimson GV, Hickman M, Rhodes T, et al. Global overview of injecting drug use and HIV infection among injecting drug users. AIDS. 2004;18(17):2295–2303.

[287] Wei X, Ghosh SK, Taylor ME, Johnson VA, Emini EA, Deutsch P, et al. Viral dynamics in human immunodeficiency virus type 1 infection. Nature. 1995;373(6510):117–122.

[288] Sedaghat AR, Siliciano RF, Wilke CO. Constraints on the dominant mechanism for HIV viral dynamics in patients on raltegravir. Antivir Ther. 2009;14(2):263–271.

[289] Markowitz M, Louie M, Hurley A, Sun E, Mascio MD, Perelson AS, et al. A novel antiviral intervention results in more accurate assessment of human immunodeficiency virus type 1 replication dynamics and T-cell decay in vivo. J Virol. 2003;77:5037–5038.

[290] Curlin ME, Iyer S, Mittler JE. Optimal timing and duration of induction therapy for HIV-1 infection. PLoS Comput Biol. 2007;3(7):e133.

[291] Callaway DS, Perelson AS. HIV-1 infection and low steady state viral loads. Bull Math Biol. 2002;64:29–64.

[292] Koelsch KK, Liu L, Haubrich R, May S, Havlir D, Günthard HF, et al. Dynamics of total, linear nonintegrated, and integrated HIV-1 DNA in vivo and in vitro. J Infect Dis. 2008;197(3):411–419.

[293] Almond LM, Hoggard PG, Edirisinghe D, Khoo SH, Back DJ. Intracellular and plasma pharmacokinetics of efavirenz in HIV-infected individuals. J Antimicrob Chemother. 2005;56(4):738–744.

[294] Cheng CL, Smith DE, Carver PL, Cox SR, Watkins PB, Blake DS, et al. Steady-state pharmacokinetics of delavirdine in HIV-positive patients: Effect on erythromycin breath test. Clin Pharmacol Ther. 1997;61(5):531–543.

[295] Brown KC, Patterson KB, Jennings SH, Malone SA, Shaheen NJ, Prince HMA, et al. Single and multiple dose pharmacokinetics of darunavir plus ritonavir and etravirine in semen and rectal tissue of HIV-negative men. J Acquir Immune Defic Syndr. 2012;61(2):138.

[296] Schöller-Gyüre M, Kakuda TN, Raoof A, De Smedt G, Hoetelmans RM. Clinical pharmacokinetics and pharmacodynamics of etravirine. Clinical pharmacokinetics. 2009;48(9):561–574.

[297] Dickinson L, Bracchi M, Elliot E, Else L, Khoo S, Back D, et al. Population pharmacokinetics (PK) of dolutegravir (DTG) alone and following treatment switch. In: Journal of the International AIDS Society. vol. 19. INT AIDS SOCIETY AVENUE DE FRANCE 23, GENEVA, 1202, SWITZERLAND; 2016.

[298] Delille CA, Pruett ST, Marconi VC, Lennox JL, Armstrong WS, Arrendale RF, et al. Effect of protein binding on unbound atazanavir and darunavir cerebrospinal fluid concentrations. J Clin Pharmacol. 2014;54(9):1063–1071.

[299] Letendre SL, Capparelli EV, Ellis RJ, McCutchan JA, Group HNRC, et al. Indinavir population pharmacokinetics in plasma and cerebrospinal fluid. Antimicrob Agents Chemother. 2000;44(8):2173–2175.

[300] Holladay JW, Dewey MJ, Michniak BB, Wiltshire H, Halberg DL, Weigl P, et al. Elevated alpha-1-acid glycoprotein reduces the volume of distribution and systemic clearance of saquinavir. Drug Metab Dispos. 2001;29(3):299–303.

[301] Veldkamp AI, van Heeswijk RP, Mulder JW, Meenhorst PL, Schreij G, van der Geest S, et al. Steady-state pharmacokinetics of twice-daily dosing of saquinavir plus ritonavir in HIV-1-infected individuals. JAIDS. 2001;27(4):344–349.

[302] Jilek BL, Zarr M, Sampah ME, Rabi SA, Bullen CK, Lai J, et al. A quantitative basis for antiretroviral therapy for HIV-1 infection. Nat Med. 2012;18(3):446–451.

[303] Dickinson L, Bracchi M, Elliot E, Else L, Khoo S, Back D, et al. Population pharmacokinetics (PK) of dolutegravir (DTG) alone and following treatment switch. In: International Congress of Drug Therapy in HIV Infection, Glasgow, UK. Abstract P094; 2016.

[304] Drug Bank [accessed on 28-June-2017] Available from: `https://www.drugbank.ca`;.

[305] PubChem Website [accessed on 28-June-2017] Available from: `https://pubchem.ncbi.nlm.nih.gov/`;.